Investigation of Temperature, Magnetic Field and Time Dependent Electrical Transport in Phase Separated Manganite Thin Films

A Thesis

Submitted to Delhi Technological University

For the Award of the Degree of

Doctor of Philosophy

in

Applied Physics

By

Sandeep Singh

(**Reg. No. 2K12/PhD/AP/08**)

Under the Supervision of

Dr. Pawan Kumar Tyagi
(Supervisor)
Assistant Professor
Department of Applied Physics
Delhi Technological University,
Delhi-110042

Dr. Hari Krishna Singh
(Co-supervisor)
Principal Scientist
Associate Professor, AcSIR
CSIR-National Physical Laboratory
New Delhi-110012

Delhi Technological University

Delhi-110042

October 2018

DECLARATION

This is to certify that the research work embodied in the thesis entitled ***"Investigation of Temperature, Magnetic Field and Time Dependent Electrical Transport in Phase Separated Manganite Thin Films"*** being submitted for the award of degree of **Doctor of Philosophy** to Delhi Technological University, India, represents the original and authentic research work carried out by me under the supervision of **Dr. Pawan Kumar Tyagi**, Department of Applied Physics, Delhi Technological University and **Dr. Hari Krishna Singh,** CSIR-National Physical Laboratory, New Delhi.

The results obtained in this thesis have not been submitted in a part or fully to any other University or Institute for the award of any degree or diploma.

Date: …….. **Sandeep Singh**

Place: ……. (Reg. No. - 2K12/PhD/AP/08)

Dr. Pawan Kumar Tyagi
(Supervisor)
Assistant Professor
Department of Applied Physics
Delhi Technological University,
Delhi-110042

Dr. Hari Krishna Singh
(Co-supervisor)
Principal Scientist
Associate Professor, AcSIR
CSIR-National Physical Laboratory
New Delhi-110012

DELHI TECHNOLOGICAL UNIVERSITY
(Formerly Delhi College of Engineering)
Shahbad Daulatpur, Bawana Road, Delhi-110042

CERTIFICATE

This is to certify that the research work embodied in the thesis entitled ***"Investigation of Temperature, Magnetic Field and Time Dependent Electrical Transport in Phase Separated Manganite Thin Films"*** submitted by **Mr. Sandeep Singh** with registration number **2K12/Ph.D./AP/08** is the result of his original research carried out in the Department of Applied Physics, Delhi Technological University, and CSIR-National Physical Laboratory, New Delhi for the award of **Doctor of Philosophy** under the supervision of **Dr. Pawan Kumar Tyagi** & **Dr. Hari Krishna Singh.**

It is further certified that this work is original and has not been submitted in part or fully to any other University or Institute for the award of any degree or diploma.

This is to certify that the above statement made by the candidate is correct to the best of our knowledge.

Sandeep Singh
Research Scholar
(Reg. No. 2K12/Ph.D/AP/08)

Dr. Pawan Kumar Tyagi
Supervisor,
Assistant professor
Department of Applied Physics
Delhi Technological University
Delhi-110042, India

Dr. Hari Krishna Singh
(Co-supervisor)
Principal Scientist
Associate Professor, AcSIR
CSIR-National Physical Laboratory
New Delhi-110012

Prof. Rinku Sharma
HOD, Applied Physics
Department of Applied Physics
Delhi Technological University
Delhi-110042, India

Acknowledgement

The completion of my PhD became possible with the support and encouragement of numerous people including my well-wishers, friends and colleagues. I take this opportunity to extend my sincere gratitude and appreciation to all those who supported me to achieve this success.

First and foremost, I would like to extend my sincere gratitude to my ***research supervisor(s) Dr. Pawan Kumar Tyagi*** *and* ***Dr. Hari Krishna Singh*** *for their dedicated help, advice, inspiration, encouragement and continuous support, throughout my Ph.D. work. I specially thank* ***Dr. Pawan Kumar Tyagi*** *who provided me the gateway to achieve this highest degree in academics. His enthusiasm, continuous support and his faith motivated me to accomplish this honourable degree.*

My sincere gratitude to ***Dr. Hari Krishna Singh*** *who introduced me in the world of research in science. His unconditional support, advice and encouragement inspired me to take up challenge of Ph.D. and accomplish it successfully. I am grateful for all his contributions of time, suggestions, constructive criticism and facilities to make my Ph.D. experience productive and stimulating.*

I owe a sincere debt of gratitude to ***Prof. Rinku Sharma****, Head, Department of Applied Physics and* ***Prof. S. C Sharma,*** *DRC Chairman****,*** *Department of Applied Physics for providing opportunity to register as research fellow in Department of Applied Physics, DTU Delhi. My heartfelt recognitions for my SRC/DRC committee members for their enduring support and appropriate propositions.*

I am also thankful to ***Hon'ble Vise-Chancellor****, Delhi Technological University and* ***Director NPL*** *for providing me opportunity to work and utilize the infrastructure and facilities towards the accomplishment of my Ph.D.*

My sincere thanks to ***Dr. Praveen K. Siwach****, Scientist, CSIR- National Physical Laboratory, whose valuable suggestions, support in experiments and discussion at different stages of this Ph.D., improved my understanding and knowledge towards the subject thereby supported me in completing the work in time.*

I am also grateful to persistent support and encouragement of ***Dr. Ramadhar Singh****,* ***Dr. Rajiv K. Singh*** *and* ***Dr. Mahesh K. Sharma*** *for completing my Ph.D. work.*

I am thankful to ***Dr. Anurag Gupta****,* ***Dr. V. P. S. Awana*** *and* ***Dr. K. K. Maurya*** *for providing MPMS, PPMS and HRXRD facilities at CSIR-NPL.*

I am grateful to the Delhi Technological University for extending all the necessary facilities and ***Council of Scientific and Industrial Research (CSIR) (AQUARIUS, 12th five year plan project, Grant No. PSC0110)*** *for providing financial support for the completion of work. I am thankful to the administrative staff of CSIR NPL and DTU for their cooperation.*

Every result described in this thesis was accomplished with the help and support of lab mates and friends. It is my pleasure to thank my lab mates and friends ***Dr. Manoj K Srivastava, Dr. Vasudha Aggarwal, Dr. Pawan Kumar, Ms. Barsha, Ms. Suman, Ms. Shital Chauhan, Ms. Shalini Singh, Mr. Arya Singh, Ms. Lucky Krishnia, Mr. Vinay Kumar, Ms. Ritu Singh*** *and many more for having good time all the way. I acknowledge their unconditional help and moral support whenever needed.*

My special regards to my teachers because of whose teaching at different stages of education has made it possible for me to see this day.

Last but not least, I express my very profound gratitude to my ***parents*** *who mean world to me and formed part of my vision and taught me lessons of life. Their unconditional love and support has always been my strength. Their patience and sacrifice will remain my inspiration throughout my life. I owe my gratitude towards my* ***wife*** *for her support in completing my Ph.D. I also thank my younger sister and other family members for their good wishes.*

A special thanks to my lovely daughter ***Akshita*** *whose smile always gave motivation to complete this task.*

Finally, I thank the "Almighty" for giving me the strength and patience to work through all these years.

Sandeep Singh

Abstract

Manganites generically represented by $RE_{1-x}AE_xMnO_3$, where RE and AE are rare earth and alkaline earth cations have engaged the interest of the physics community because of their highly enriched nature regarding the electronic phases. The presence of various phases is demonstrated by the existence paramagnetic insulator (PMI), ferromagnetic metal (FMM), a ferromagnetic insulator (FMI), an antiferromagnetic insulator (AFMI) and charge ordered/orbital ordered (CO/OO) phases. Various parameters (i.e. RE/AE ratio, their average cationic size and thermomagnetic variables etc.) in such materials make the interphase boundaries permeable and cross boundary electronic phase diffusion noticeable. This cross-boundary phase diffusion is called phase separation (PS), which is the axial attribute of the physics of manganites. PS has been recognized as the most striking intrinsic property of doped rare earth manganites. The $La_{1-x-y}Pr_yCa_xMnO_3$ has emerged as the generic representative of the manganites showing mesoscale phase separation with coexisting AFMI/CO and FMM cluster.

This thesis is devoted on the investigation of temperature, magnetic field and time dependent electrical transport in phase separated manganite thin film. Here, the study of dependence of the insulator metal transition (IMT) of the relative fraction of the two competing phases, nature of the hysteresis in the electrical transport as a function of the thermomagnetic variables temperature (T) and magnetic field (H), temporal evolution of the electrical resistivity, especially near the IMT, and scaling of the hysteresis loop area with temperature and magnetic field on RF magneton sputtered good quality thin films of $La_{1-x-y}Pr_yCa_xMnO_3$ on (001) oriented $SrTiO_3$ substrates has been presented.

The present thesis is divided into seven chapters the contents of which are summarized in the following paragraphs.

Chapter 1 introduces to the basic aspects of doped rare earth manganites like crystal structure, phase diagrams, charge, spin, orbital, and lattice degrees of freedom and the associated competing interactions, magnetic-electrical transitions, observation of colossal magnetoresistance, etc. Popular mechanisms responsible for the exotic phenomena in these compounds such as double exchange interaction, Jahn–Taller induced electron–lattice distortion and phase competition induced phase separation have also been presented. In the later section emergence of phase separation in low bandwidth manganites due to competing phases has been discussed. Following this the prototype phase separated manganite, i.e. $La_{1-x-y}Pr_yCa_xMnO_3$ has been discussed in detail with optimal literature survey. This chapter ends with the motivation for the present work.

Chapter 2 gives brief description of experimental techniques used during the present study like thin films growth, structural/microstructural and magneto transport characterization techniques. The preparation technique of LPCMO sputtering target (~ 2″ diameter) by solid state reaction route and the thin films growth by RF magnetron sputtering has been discussed in detail. The high-resolution X-ray diffraction (HRXRD, PANalytical PRO X'PERT MRD, Cu-Kα1 radiation $\lambda = 1.5406$ Å) techniques like X-ray reflectivity (XRR), $2\theta/\omega$ scan and ω-scan measurements have been described. The surface topological characteristics were probed by and therefore atomic force microscopy (AFM, VEECO Nanoscope V), has also been discussed briefly. The SQUID magnetometry (MPMS XL, Quantum Design) technique used for magnetic characterization through temperature and magnetic field dependent magnetization measurements is briefly discussed. (The magnetotransport properties were measured by a commercial physical property measurements system (PPMS, Quantum Design) and a temperature controlled closed cycle refrigerator (ARS Cryo, 350 – 6 K). All the electrical transport measurements have been carried out in the standard linear geometry. The current was supplied through

the two outer probes and the voltage was measured across the two inner electrodes. The contacts were made by 50 μm diameter Pt coated Cu wires and EPO-TEK (Epoxy Technology) conductive epoxy.

Chapter 3 reports the study of the impact of variation in the relative fractions of the ferromagnetic metallic and antiferromagnetic/charge ordered insulator phases on the supercooling/superheating transition in thin film of the strongly phase separated system, $La_{5/8-y}Pr_yCa_{3/8}MnO_3$ (LPCMO) (y ~ 0.4). The thin film has been studied in detail employing electrical transport measurements. Our study clearly shows that the supercooling transition temperature is non-unique and strongly depends on the magneto-thermodynamic path through which the low temperature state is accessed. In contrast, the superheating transition temperature remains constant. Our study also establishes that the electrical transport in such a strongly phase separated manganite thin film is extremely sensitive to the relative fraction of the coexisting phases (FMM and AFM/COI) and has inherent non-ergodicity. The phase separation tendency is weakened when the fraction of AFM/COI phase is reduced. Time dependence of the resistivity shows that in the vicinity of the IMT, the resistivity relaxation is of the non-Debye type.

Major part of this work is published in ***Applied Physics Letter*****,** 104, 212403 **(2014).**

Chapter 4 describes the detailed study on the effect of phase separation induced supercooling on magnetotransport properties of epitaxial $La_{5/8-y}Pr_yCa_{3/8}MnO_3$ (y ~ 0.4) thin film grown by RF magnetron sputtering on (001) oriented SrTiO3 (STO) substrate. In the previous chapter investigation on the tunability of the insulator to metal transition (IMT) in terms of the variation in the relative fraction of the coexisting FMM and AFM/COI phases in $La_{5/8-y}Pr_yCa_{3/8}MnO_3$ (y ~ 0.4) thin films have been presented. HRXRD reveals that the films are epitaxial but may contain high density of lattice defects such as dislocation networks which are responsible for relaxation of substrate induced strain. These

observations are also supported by AFM measurements. The competition between coexisting FMM and AFM/COI phases governs the temperature dependent magnetic and transport properties of LPCMO. The protocol (ZFC, FCC and FCW) dependent FM transitions, strong divergence between the ZFC and FCW M(T) and prominent irreversibility between the FCC-FCW M(T) provide evidence in favour of the non-ergodic behavior of the magnetic state in this film. This non-ergodicity, the origin of which could be traced to the delicate coexistence of FMM and AFM/COI phases leads to the existence of a liquid like behaviour. This liquid like state gets frozen into strain glass (SRG). M – H measurements also confirmed the frozen glassy states at low temperatures and unblocking of these frozen states with increasing temperature. The ρ-T measurements also confirm the liquid like behaviour and frozen glassy state at low temperatures. The liquid like behaviour is also confirmed by the large drop in resistivity under moderate magnetic fields. The small polaron activation energy decreases nonlinearly with increase in H and the variation of TIM with the activation energy remains nearly linear in the warming cycle, but it becomes nonlinear in the cooling cycle. The analysis of the low temperature ρ-T data reveals the weakening of the electron-lattice coupling under the influence of an external magnetic field as well as during the warming cycle. The devitrification of the frozen glassy state gives rise to Kondo like resistivity minimum. This work is published in ***AIP Advances*** 5, 027131 **(2015).**

Chapter 5 describes the quantification of phase separation in terms of magnetoresistive hysteresis loops in strongly phase-separated $La_{0.21}Pr_{0.42}Ca_{0.37}MnO_3$ (LPCMO) grown on STO (110) substrate. The supercooling of the magnetic liquid during the cooling cycle and the near equilibrium behaviour during warming cycle results in a pronounced ρ–T hysteresis. The zero-magnetic field (H=0) insulator-metal transition temperature (IMT) measured in warming cycle (T_{IM}^{W}~163 K) is higher than that in the

cooling cycle (T_{IM}^{C}~116 K) and the difference between the two IMTs shrinks as H is increased. The magnetic field dependence of the two IMTs is well well described by an empirical relation given by the eq. $T_{IM} = T_{IM}^{0} + \beta H^{\alpha}$. Here T_{IM}^{0} is the H-independent contribution and the constants, pre-factor β and exponent α determine the H-dependent part of the IMT. The fitting parameters β and α are related to the strength of the phase separation and the H induced AFMI to FMM transition. The ρ-T loop area diminishes with the increasing H and its scaling with H in the regime which is akin to a magnetic liquid and unstable towards external H (H<30 kOe) is nicely described by $A_T = A_{T_0} e^{-\Gamma H}$. Here, A_{T_0} is the zero-field normalized area and Γ is a constant related to the degree of phase separation. The isothermal ρ - H loop area is found to follow a scaling law of the type$A(H) = A_H (H - H_{IM})^{\eta}$. The constant H_{IM} is the magnetic field at which the induced IMT occurs due to AFMI – FMM phase transition and the exponent η measures the strength of phase separation; being close to unity in the weakly phase separated regimes and ~0.5 in the strongly phase separated or the magnetic liquid regime. We emphasize that the critical ingredients of the phenomenological models used to explain the observed hysteresis in temperature and magnetic field dependent [(ρ-T) and (ρ-H)] loops are the mesoscale phase separation, appearance of magnetic liquid during the cooling cycle, and nearly equilibrium magnetic solid like behavior while warming. This research work is published in ***Applied. Physics A*** 123:677, **(2017).**

Chapter 6 describes the systematic study of the consequences of in-plane tensile strain on the correlation between structure/microstructure and magneto-electrical properties of RF sputtered $La_{0.23}Pr_{0.41}Ca_{0.36}MnO_3/SrTiO_3$ (001) thin films. For present study composition is so selected that the electronic phase balance is tilted slightly in favor of FM metal. Such a selection gives a possibility of the occurrence of FM-metallic behavior even

at sufficiently small film thickness where the tensile strain is very large. In this chapter, it appears quite pertinent to mention that at very small film thickness (d≤27 nm) such thin films generally show strong insulator behavior and the dominant tensile strain supports layered morphology. At slightly higher thickness (d≥41 nm) structural/microstructural crossover takes place and defects like dislocations are generated due to relaxation induced tilt and dilations of the lattice, which in turn transforms the layer by layer growth into disordered brick type morphology. It appears that the relaxation even at higher thickness (~81 nm) is partial only and the strain may have a self-sustained nature. The dominance of the tensile strain suppresses the ferromagnetic-metallic phase due to the possible electronic reconstruction which could give rise to a magnetically disordered insulator 'dead' layer and a sizeable non-magnetic insulator state at d≤27 nm. Analysis of the rocking curve broadening shows at lower film thickness (~13 and 27 nm) the microstructure is dominated by the strain, which in this case is due to the lattice mismatch. At higher film thickness the mosaic broadening starts dominating due to the dislocation induced tilt and dilations of the lattice. The insulator region electrical conduction in all the films is well described by the Emin-Holstein small polaron hopping, wherein the lower thickness films possess higher activation energies. The magnetization scaling with the film thickness shows the possible existence of a spin disordered insulator layer, the associated electronic reconstruction and a sizeable non-ferromagnetic insulator state at d≤27 nm. This research work has been accepted for publication in ***AIP Advances 8, 095002 (2018)*****.**

Chapter 7 provides the summary of the work done during the course of the doctoral research work. It is also suggests and outlines open issues and the future course of research in the area of manganites.

List of publications (included in thesis)

[1] Supercooling transition in phase separated manganite thin films: An electrical transport study.
Sandeep Singh, Pawan Kumar, P. K. Siwach, Pawan Kumar Tyagi, H. K. Singh
Appl. Phys. Lett 104, 212403 (2014). (Impact Factor - 3.411)

[2] Effect of phase separation induced supercooling on magnetotransport properties of epitaxial $La_{5/8-y}Pr_yCa_{3/8}MnO_3$ ($y \approx 0.4$) thin film."
Sandeep Singh, Geetanjali Sharma, Mukesh K. Thakur, P. K. Siwach, Pawan Kumar Tyagi, K. K. Maurya, and H. K. Singh
AIP Advances 5, 027131 (2015). (Impact factor – 1.568)

[3] Quantifying phase separation in terms of magnetoresistive hysteresis loops in strongly phase-separated manganite thin films.
Sandeep Singh, Pawan Kumar Tyagi and H. K. Singh
Appl. Phys. A 123:677, (2017) (Impact factor – 1.455)

[4] Structure, magnetism and electrical transport in epitaxial $La_{0.23}Pr_{0.41}Ca_{0.36}MnO_3$ thin films: Consequences of film thickness.
Sandeep Singh, Pawan Kumar Tyagi and H. K. Singh
AIP Advances 8, 095002 (2018). (Impact factor – 1.568)

List of Publications: (Not included in thesis)

[1] Magnetic anisotropy and anisotropic magnetoresistance in strongly phase separated manganite thin films
Lalit M. Kandpal, **Sandeep Singh**, Pawan Kumar, P.K. Siwach, Anurag Gupta, V.P.S. Awana and H.K. Singh **J. of Magnetism and Magnetic Materials 408, 60-66, (2016).**

[2] Understanding thermomagnetic hysteresis in $La_{1-x-y}Pr_y Ca_xMnO_3$ thin films
Akash Yadav, **Sandeep Singh**, Amit Vashist, Gyanendra Sharma, P K Siwach and H K Singh **Mater. Res. Express** 4 066102 **(2017).**

[3] Evolution of Intrinsic and Magnetic Field-Induced Magnetic Anisotropies in Strongly Phase-Separated Manganite Thin Films
Akash Yadav, Suman Kumari, Shital Chauhan, **Sandeep Singh**, P. K. Siwach Anurag Gupta and H. K. Singh **J. Supercond. Nov. Magn. (2018)**.

Abbreviations

TMO	Transition Metal Oxide
CMR	Colossal magnetoresistance
GMR	Giant magnetoresistance
MR	Magnetoresistance
T	Temperature
H	Magnetic field
RE	Rare earth
AE	Alkaline earth
JT	Jahn-Teller
SE	Superexchange
DE	Double Exchange
FM	Ferromagnetic
AFM/AF	Antiferromagnetic
FMM	Ferromagnetic Metal
FMI	Ferromagnetic Insulator
AFMI	Antiferromagnetic Insulator
CO	Charge Ordered
COI	Charge Ordered Insulator
OO	Orbital Ordered
PI	Paramagnetic Insulator
CAF	Canted Antiferromagnetic
IMT	Insulator to metal transition
T_{IM}	Insulator to metal transition temperature
T_C	Curie temperature
T_{CO}	Charge ordering transition temperature
PS	Phase Separation
BW	Band width
LCMO	$La_{1-x}Ca_xMnO_3$
LSMO	$La_{1-x}Sr_xMnO_3$
LBMO	$La_{1-x}Ba_xMnO_3$
SSMO	$Sm_{1-x}Sr_xMnO_3$
NSMO	$Nd_{1-x}Sr_xMnO_3$

PCMO	$Pr_{1-x}Ca_xMnO_3$
LPCMO	$La5/_{8-y}Pr_yCa_{3/8}MnO_3$/ $La_{1-x-y}Pr_xCa_yMnO_3$
LAO	$LaAlO_3$
STO	$SrTiO_3$
NGO	$NdGaO_3$
SRG	Strain Glass
CVD	Chemical Vapor Deposition
APCVD	Atmospheric pressure Chemical Vapor Deposition
LPCVD	Low-pressure Chemical Vapor Deposition
PECVD	Plasma-enhanced Chemical Vapor Deposition
LECVD	laser-enhanced Chemical Vapor Deposition
MOCVD	Metal-organic Chemical Vapor Deposition
PVD	Physical Vapor Deposition
PLD	Pulsed Laser Deposition
MBE	Molecular Beam Epitaxy
ALD	Atomic Layer deposition
SPM	Scanning Probe Microscope
STM	Scanning Tunneling Microscope
AFM*	Atomic Force Microscope
XRD	X-ray Diffraction
HRXRD	High Resolution X-Ray Diffractometer
XRR	X-Ray Reflectivity
MPMS	Magnetic Property Measurement System
SQUID	Superconducting Quantum Interference Device
VSM	Vibrating Sample Magnetometer
PPMS	Physical Property Measurement System
EDS/EDX	Energy Dispersive X-Ray Spectroscopy
SEM	Scanning Electron Microscope
TEM	Transmission Electron Microscope
ZFC	Zero Filed Cooled
FCW	Field Cooled Warming
FCC	Field Cooled Cool
M-T	Temperature dependent magnetization
ρ-T	Temperature dependent resistivity

Table of Contents

List of Figures

1 Introduction to Phase Separation in Manganites

1.1 Introduction

Material science has always been at the forefront of all technological advancements which results in smaller and smarter devices. The present information era fully depends on smaller and smarter magnetic devices for memory, storage and processing. Therefore, it is necessary to explore new age magnetic materials for such applications. Perovskite structured transition metal oxides (TMOs) are one of the classical example of new age magnetic materials which show wide range of properties i.e. high T_C superconductivity in copper based compounds, ferroelectricity in the Titanium based perovskites, phase separation and associated colossal magnetoresistance (CMR) in manganese based systems etc. **[1–3]**. TMOs are the compounds composed of oxygen atoms bound to transition metals that offer a broad spectra of exotic and still incompletely understood structural, magnetic and electronic properties **[4–6]**. One-electron band theory, usually works well for most solids, does not explains the exotic properties of TMOs and this demonstrates the urge to understand the strong electron-electron and electron-lattice correlations in such compounds **[7]**. Many transition metals are regarded as strongly correlated materials because of the incompletely filled d electron shell and narrow band and consequently the TMOs exhibit phenomena, e.g. high-Tc superconductivity, magnetism, ferroelectricity, thermoelectricity, anomalous insulator (paramagnet)-metal (ferromagnet) transitions, occurrence of multiple electronic phases and phase separation, etc. **[8–11].** Various proposed theoretical approximations could solve complicated correlated systems to some extent but a standard theory has yet to be established to explain the behaviour of correlated system. The complex electron interactions in transition metal oxides give rise to various

exotic phenomena and therefore make such materials one of the most interesting material families **[12].**

During last few decades, Mn based TMOs having ABO_3 structure and judicious divalent (alkaline earth) doping generally represented chemically by $RE_{1-x}AE_xMnO_3$ (RE = trivalent rare earth cation, AE = divalent alkaline earth cation), have drawn considerable attention due to a broad spectra of technological important and physically/theoretically intriguing phenomena. The prominent ones are insulator/paramagnetic to metal/ferromagnetic phase transition, huge drop in resistivity under external magnetic field (negative magnetoresistance, often called CMR), coexistence of multiple electronic phases, etc. **[13–16]**. Since AE doping causes mixed valence of Mn, these compounds are often referred to as mixed valence manganites and in absence of any structural distortion have structure similar to that of perovskite $CaTiO_3$. The magnetoresistance of this family of compounds is much higher than that for artificial heterostructures as well as granular systems **[17]** and hence it is extremely interesting. Apart from this, this class of materials due to the intimate coupling among the lattice, charge, orbital and spin degree of freedom like ferromagnetic (FM) and anti-ferromagnetic (AFM) ordering, charge ordering (CO), orbital ordering (OO), etc. Interestingly, these electronic orders coexist and compete with each other giving rise to phase separation and the ground state of the system depends on the relative fraction of RE and AE cations and their average cationic radius. Thus the associated phase transitions have also emerged as an interesting feature of manganites **[7]**. The earliest studies on these materials systems led to the phenomenological concepts like the double exchange (DE) **[18,19]** and Jahn-Teller Polaron **[20]** to account for the observed magneto-electric phase transitions. After a long pause the work on these materials restarted and yield several new and exotic aspects like CMR, phase coexistence, phase separation, and optically induced magnetic phase transitions, etc. as mentioned earlier **[21,22]**. The

development of insulating ferromagnets for high frequency applications was the driving force for the early research in 1950s in this area. However, the second phase of the research started in mid 1990s was motivated by the urge to achieve larger and larger magnetoresistance initially, which was later pushed back to the back seat by the quest to understand the fundamentals aspects like electronic phase coexistence and the associated intrinsic electronic phases separation varying over a wide range from nanoscale to the microscales. The broad features of $La_{1-x}Ca_xMnO_3$ (LCMO), the first compound of the series to be studied were reported by Jonker and Van Santen **[23,24]** and Jonker **[25]**. Similar studies on $La_{1-x}Sr_xMnO_3$ (LSMO) and $La_{1-x}Ba_xMnO_3$ (LBMO) were limited to $x < 0.7$ and $x < 0.5$, respectively **[23,24].** In 1954 Volger **[26]** first showed the glimpse of unique magnetotransport which yielded negative magnetoresistance in $La_{0.8}Sr_{0.2}MnO_3$ with a peak near T_C. Later, based on their neutron diffraction study, Wollan and Koehler **[27]** put forward the magnetic structure of LCMO for all x-values. This phase diagram showed the existence of AFM phase in addition to the FM one and also the appearance of charge order (CO) and in a way it proved to be the first experimental proof of magnetic phase coexistence. The structure-property correlation in the flux grown LBMO single crystal with $0.2<x<0.44$ was carried out by several groups **[28–31]**. At the onset of the second phase in 1990s was due to the preparation of high quality thin films with large magnetoresistance independently by Jin et al **[21]**, Von Helmholt et al **[14]** and Chahara et al **[13]** in materials having different combinations of RE and AE cations. The optimized thin films showed remarkably high magnetoresistance in the proximity of the T_C, which was termed as colossal magnetoresistance (CMR) by Jin et al **[21]**.

1.2 Salient Features of Manganites

The characteristic features of AE doped manganites are determined by the average ionic radius of RE/AE cations and the relative fraction (and hence the Mn^{3+}/Mn^{4+} ratio). Some of the silent features of the manganites are summarized in the following subsections.

1.2.1 Crystal Structure

The manganites with the chemical representation $RE_{1-x}AE_xMnO_3$, have a ABO_3 type perovskite structure. The ideal unit cell of this structure is a cube with the RE and AE cations at the vertices with 12-fold oxygen coordination, and the smallest of the cations, viz., Mn at the centre of the cube with 6-fold coordination. Six O^{2-} situated in the centre of the faces of the cube surround each Mn cation hence forming an octahedron (shown in **Fig 1.1**). An alternate representation of this structure is the one in which the Mn cation remains at the centre of the octahedron and the RE/AE cations are located at the cube centre. Raveau **[32]** has emphasized the role and importance of the ReO_3 type framework as a host structure for deriving numerous structures of metal oxides. Under ideal conditions the structure is cubic **[33]** it is distorted by RE/AE cation size mismatch as well as by the Jahn-Teller effect. This results in rhombohedral or orthorhombic unit cells. Manganites with a large deformation can become structurally unstable. One possible lattice distortion arises from the connective pattern of the MnO_6 octahedral and is given by the Goldschmidt tolerance factor **[34]** given as:

$$t = \frac{r_B + r_O}{\sqrt{2}\,(r_A + r_O)} \qquad (1.1)$$

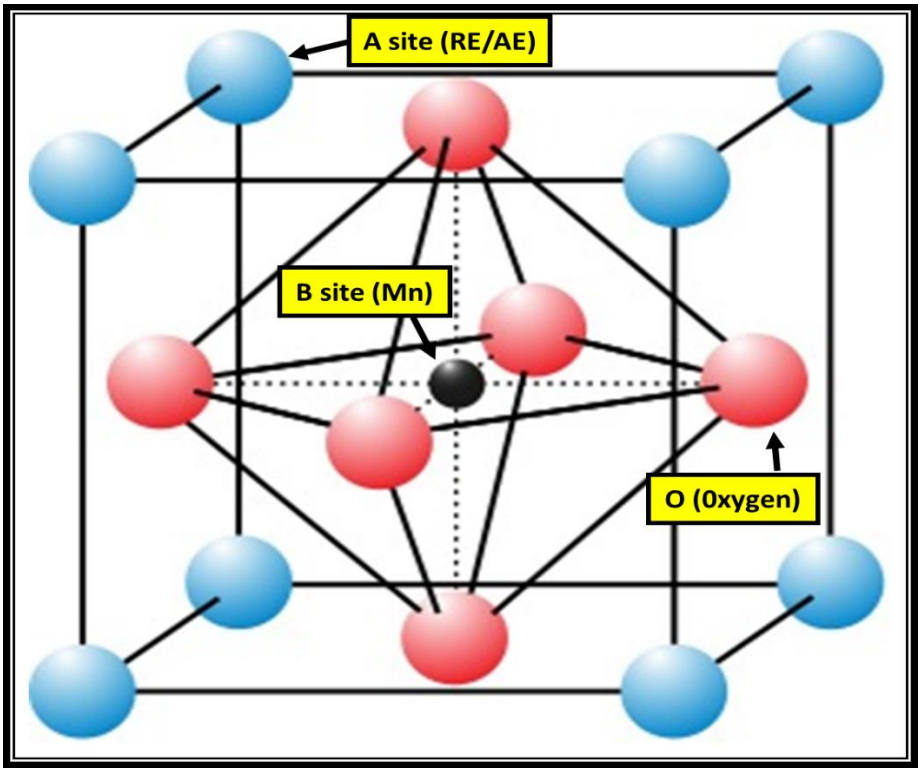

Figure 1.1: Schematic structure of cubic perovskite ABO_3 where A stands for RE/AE and B for Mn ions

where r_A, r_B and r_O are the ionic radius of A, B and oxygen in ABO_3 perovskite **[35]**. Ideally, t = 1 for cubic perovskite structure but there is deviation from ideal structure and distorted rhombohedral or orthorhombic structures may exist at room temperature. $La_{1-x}Ca_xMnO_3$ (LCMO) is the most studied perovskite where both terminal end compounds, viz., $LaMnO_3$ (x = 0) and $CaMnO_3$ (x = 1) are A-type and G-type antiferromagnetic insulators having Mn^{3+} ($3d^4$, $t^3_{2g}\ e^1_g$) and Mn^{4+} ($3d^3$, $t^3_{2g}e^0_g$) ions, respectively **[27]**. Partial substitution of the RE^{3+} by AE^{2+} yields a mixture of Mn^{3+} and Mn^{4+} cations **[23]** whose relative fraction may also be tuned by adjusting the oxygen stoichiometry **[36,37]**. The AE substitution for RE causes size mismatch induced structural distortion and gives rise to the Jahn–Teller effect **[38]**. A detailed investigation of the structure–property correlation in temperature and tolerance factor t realm has been reported by Hwang et al. for $RE_{0.7}AE_{0.3}MnO_3$ compound for different RE /AE combinations **[39].**

This study unambiguously demonstrated the existence of (i) a high temperature paramagnetic insulator (PMI) state for all 't' values, (ii) low temperature ferromagnetic metallic (FMM) state at large 't' values and (iii) low temperature charge ordered ferromagnetic insulator (CO/FMI) at small 't'

1.2.2 Jahn Teller (JT) Effect

The degeneracy of a spatially degenerate electronic ground state is removed by geometrical distortions that lower the overall energy od all the species **[38]**. Such distortions, which occur in organic compounds as well as transition metal complexes, are called the JT distortion. Jahn and Teller formulated a theorem in this regard and JT-theorem says that "systems with degenerate orbital energy ground states are usually unstable and there is a tendency to lower the symmetry and to remove the degeneracy" **[38]**. In manganites the Mn^{3+} ion with electron configuration $3d^4$ is surrounded by six oxygen forming an octahedron. The JT distortion is more effective in manganites with a large concentration of Mn^{3+} ions (small values of x). The $3d_{x^2-y^2}$ and $3d_{3z^2-r^2}$ orbitals are directed towards surrounding oxygen ions known as e_g level whereas $3d_{xy}$,$3d_{yz}$ and $3d_{zx}$ orbitals lies around respective planes (t_{2g} level) as shown in **Fig. (1.2).** The 3d energy levels of cations of transition metals surrounded by oxygen ions creating octahedron are split by the crystal field into doubly degenerated e_g level and triply degenerate t_{2g} level **[40]**. According to the JT theorem, this electronic situation unstable and the MnO_6 octahedron must distort in such a way that the degeneracy of the two electronic configurations is removed.

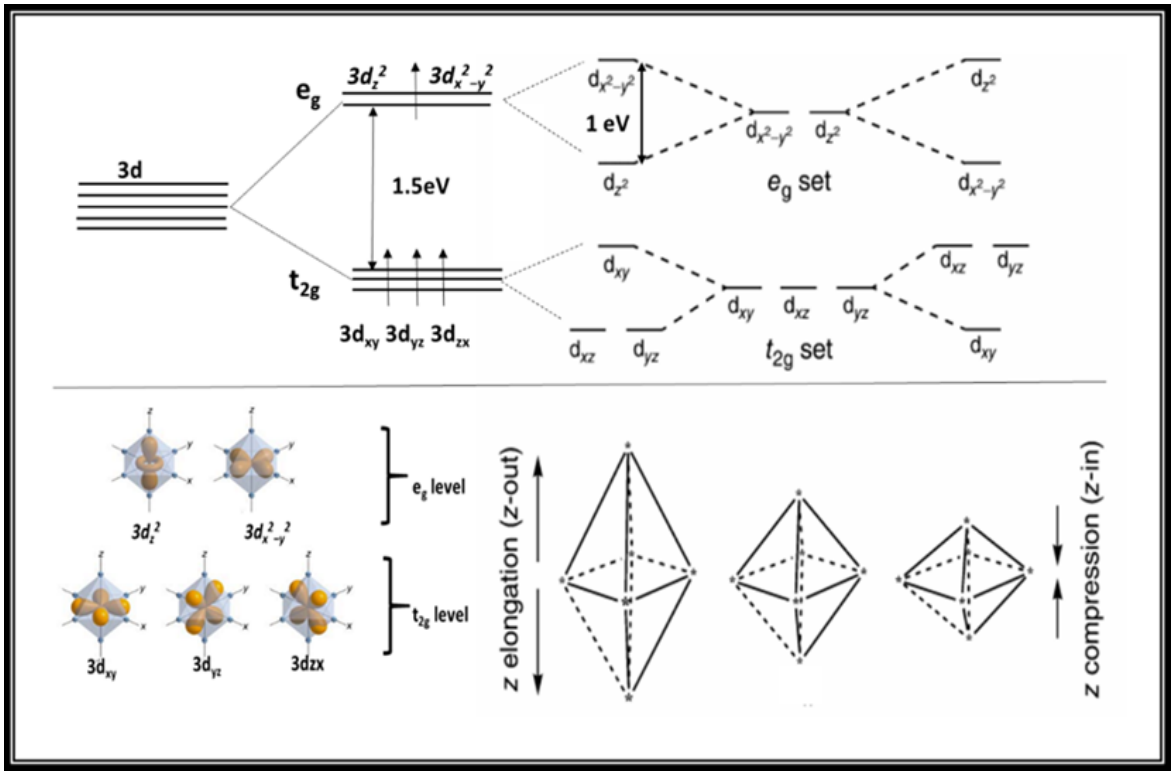

Figure 1.2: Splitting of 3d orbital due to crystal field of oxygen octahedra along with the z- elongation and z-compression Jahn−Teller distortion [42]

In configuration of ($d^0{}_{x^2-y^2}$, $d^1{}_{z^2}$) (d^4), most of the electron density is concentrated in the d_{z^2} orbital between the metal and two ligands on z-axis therefore, the ligands along z-axis are much more screened from the charge of the central metal than other four ligands along x and y axis **[41]**. As a consequence of this the electrons in the d_{z^2} orbital and the ligands along z axis would have greater electrostatic repulsion than between the electrons in t_{2g} set of orbitals pointing between the axis and the ligands and the ligands on x and y axes itself. Thus, the ligands on z axis will move further away from the central metal ion and thus acquire the stability by lowering the energy of d_{z^2} orbital than $d_{x^2-y^2}$ orbital. This results in '*elongated JT distortion'*. For the other configuration ($d^1{}_{x^2-y^2}$, $d^0{}_{z^2}$), the $d_{x^2-y^2}$ is more stable having lower energy than d_{z2} giving rise to '*compression JT distortion'* [42] as shown in **Fig (1.2)**.

1.2.3 Exchange Interactions

The fundamental physical aspects of manganites are generally dominated by different types of exchange interactions which are at play between the Mn ions. The extent of the overlapping of the d-orbitals of Mn and p- orbitals of O determines the nature and strength of these interactions. The Mn3+ ions have four electrons in 3d shell surrounded by O2- octahedron. The crystal field splits d orbitals into eg and t2g levels and in compliance of Hund's rule three of the four electrons of Mn^{3+} occupy t_{2g} level while the fourth one is in e_g level. The t_{2g} electrons are always localized while the e_g electrons behave as itinerant ones with a certain band of the AE fraction (x). The e_g electrons use Op-orbital as a bridge between Mn^{3+} and Mn^{4+} ions. Such exchange of electron between Mn ions via O-2p orbital is explained in the framework of superexchange (SE) interaction and double exchange (DE) interactions. An indirect (second nearest neighbour) magnetic coupling between the magnetic ions of the same valency in an ionic solid through an occupied Oxygen 2p orbital is referred to as the superexchange interaction. The name superexchange is given due to the fact that this interaction takes place over relatively large distances. In $REMnO_3$ case (x=0), e_g degeneracy is split due to JT distortion **[38]**. This splitting localizes e_g electrons thus making the AE free material as insulator and minimizes the energy by stabilizing the antiferromagnetic ordering. The virtual hopping process describe the exchange interactions between half-filled orbitals. In view of this the superexchange (SE) is a virtual exchange between Mn-electrons and electrons from the same 2p orbital of oxygen. Since the electrons in these oxygen orbitals have antiparallel spins therefore the orientation of spins of magnetic ions is also antiparallel leading to antiferromagnetic coupling as shown in **Fig (1.3)**. In general, the exchange interaction in Mn^{4+}-O-Mn^{4+} is antiferromagnetic (AFM) whereas it may be ferromagnetic metallic (FM) or antiferromagnetic (AFM) in Mn^{4+}-O-Mn^{3+} **[43]**. This is seen in $LaMnO_3$, which has both FM as well as AFM exchanges **[44].**

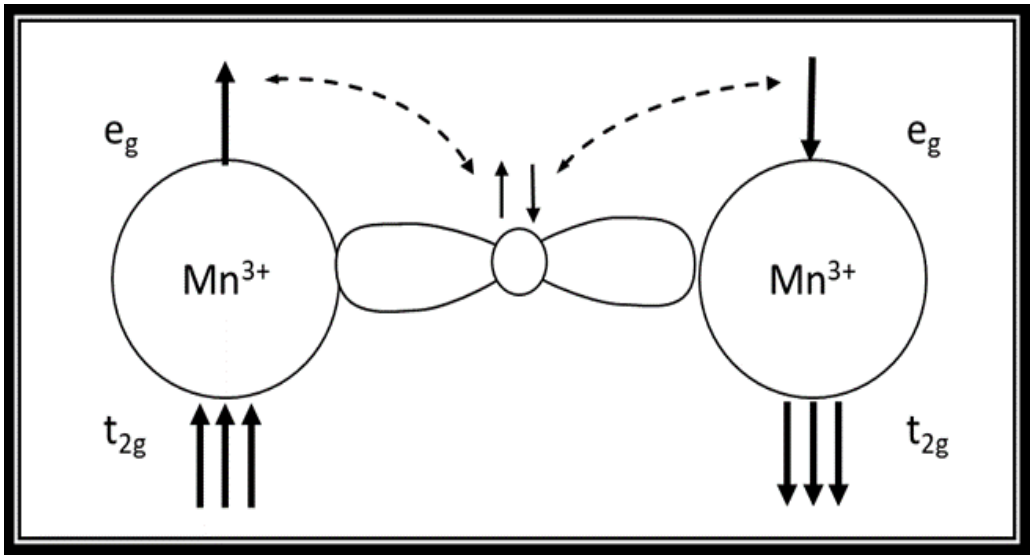

Figure 1.3: Schematic for Superexchange interactions

In the absence of any AE doping each the lattice contains only Mn^{3+} which has 4 electrons (three d-electrons in t_{2g} orbitals and one in e_g orbital) with total spin S = 2. The Mott correlation effect forbid the electron hopping motion. Consequent to the AE doping (or oxygen deficiency) x-fraction of Mn^{3+} ions lose additional electron and hence transform to Mn^{4+} (ionic state t_{2g} with total spin, S=3/2). This provides the e_g electrons itineracy to roam around the lattice in a random fashion and results in large conductivity. Such motion of the e_g electrons in the backdrop of t_{2g} core is described by the Zener double exchange mechanism **[27]** which ensures a strong ferromagnetic-type interaction through the coupling of Mn^{3+} and Mn^{4+}cations via oxygen anions. The e_g electron jumps from 3d energy level of Mn ion to the 2p orbital of oxygen from which there is simultaneous transfer of one electron to 3d level of the second Mn cation. The noticeable feature of this process is the preservation of the spin sign and this leads to ferromagnetic order of magnetic cations as shown in **Fig. (1.4)**. However, a restriction on this hopping is the fulfilment of the Hund rule, and therefore it occurs only when this rule is satisfied. This interaction is observed when Mn^{3+}–O–Mn^{4+} bonding angle is close to 180^o.

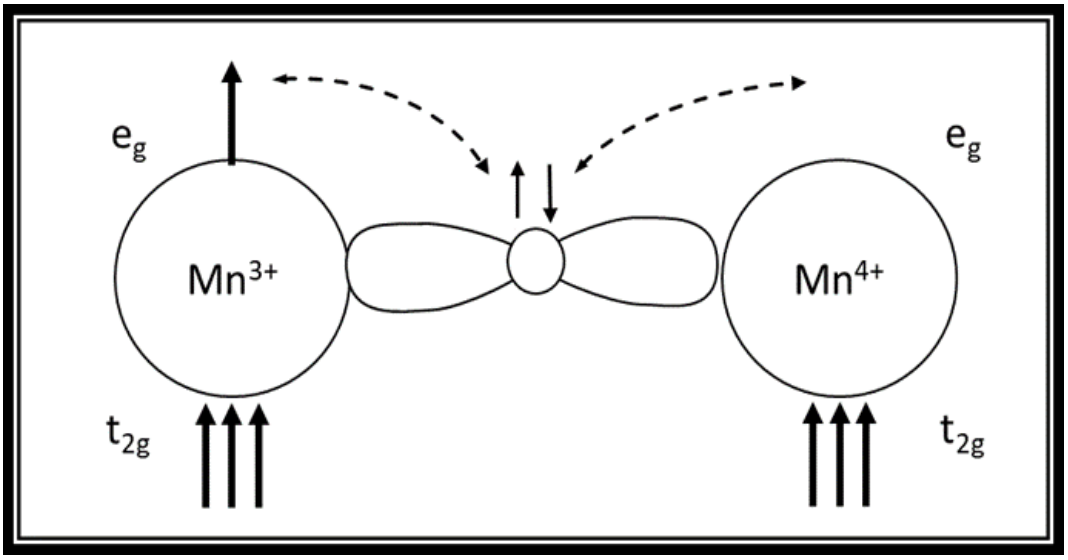

Figure 1.4: Schematic for double exchange interactions

Further, Anderson and Hasegawa **[45]** confirmed this approach by deriving the probability of the e_g electron transfer from Mn^{3+} to neighbouring Mn^{4+}, which is given by $t_{et} = t_0 \cos\frac{\theta}{2}$. Here, θ is the angle between the Mn^{4+} and Mn^{3+}. The degeneracy of the two possible hoping configuration in Mn^{4+}-O-Mn^{3+} and Mn^{3+}-O-$Mn^{4+}$is lifted by process of electron transfer and which leads to two energy levels $E = E_{t=0} \pm E(t_0 \cos\frac{\theta}{2})$. The $\theta = \pi$ corresponds to antiparallel spins while θ = 0, which maximizes the transfer integral, corresponds to parallel spin configuration and hence DE **[44]**. The insulating phase is driven by the coupling/interplay between e_g electrons and JT distortions of the MnO_6 octahedra **[46,47].** Such a coupling leads to some exotic charge and orbital orders as discussed in the next section.

1.2.4 Spin, Charge-Orbital Ordering

The affluent phase diagram of manganites is a direct revelation of the intimately coupled lattice, charge, orbital and spins degrees of freedom. Their long range spatial replication in manganites results in orbital ordering, charge ordering and spin ordering,

respectively at Mn sites **[17,46,48,49].** These orderings are very sensitive to the average size of the RE/AE in $RE_{1-x}AE_xMnO_3$ and consequently the extent of ordering on the x-T phase diagram can vary from low bandwidth ($Sm_{1-x}Sr_xMnO_3$), intermediate bandwidth ($Nd_{1-x}Sr_xMnO_3$ and $La_{1-x}Ca_xMnO_3$) to large-bandwidth ($La_{1-x}Sr_xMnO_3$) **[17,46,48,49].** Interaction of charged cations in specific lattice with neighboring atoms make their electron spin to align in a particular fashion and give rise to different types of spin orders like ferromagnetism and antiferromagnetism (A, C, and G type) as shown in **Fig. (1.5)**.

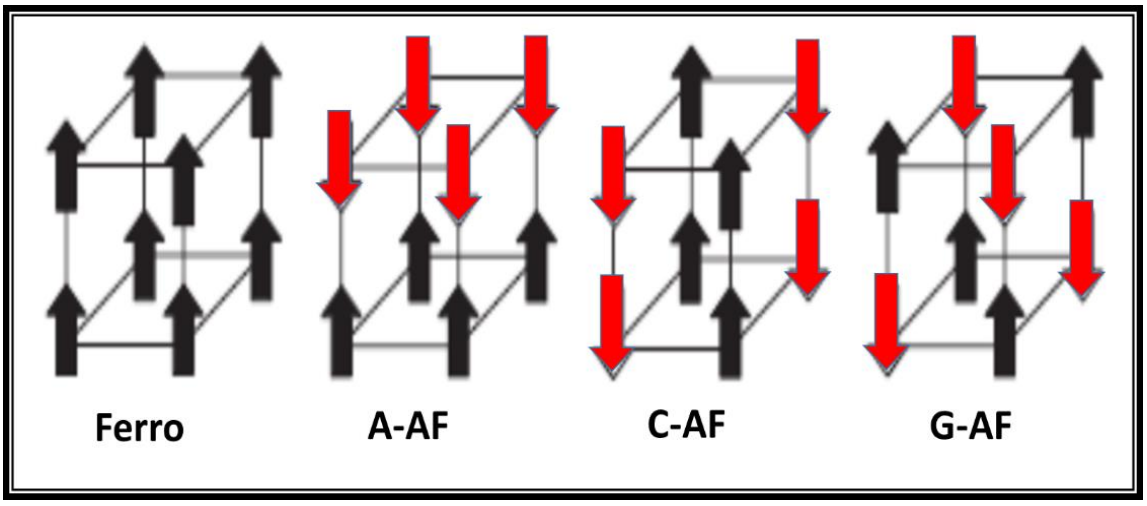

Figure 1.5: Alignment of electron spin due to interaction of charged cations

A-type antiferromagnetism, the intra-plane coupling is FM while inter-plane coupling is AFM. In other words two FM planes (two dimensional FM) are coupled in AFM manner. For C-type antiferromagnetism, the intra-plane coupling is AFM while inter-plane coupling is FM, that is one dimensional FM chains are coupled in AFM manner whereas for G-type antiferromagnetism, both the intra-plane and inter-plane coupling are AFM, that is, all neighbouring spins are coupled in an AFM manner. For $LaMnO_3$, the parent compound of large and intermediate bandwidth manganites, A-type and C-type AFM phase appears **[27,50,51]**. In 'A-type' AFM structure, 2-dimensional ferromagnetic sheets are coupled antiferromagnetically along the normal. The C-type comprises of AFM

coupling of 1-dimensional nearest neighbour ferromagnetic chains, while the coupling of the chains along the diagonal is always FM **[27].**

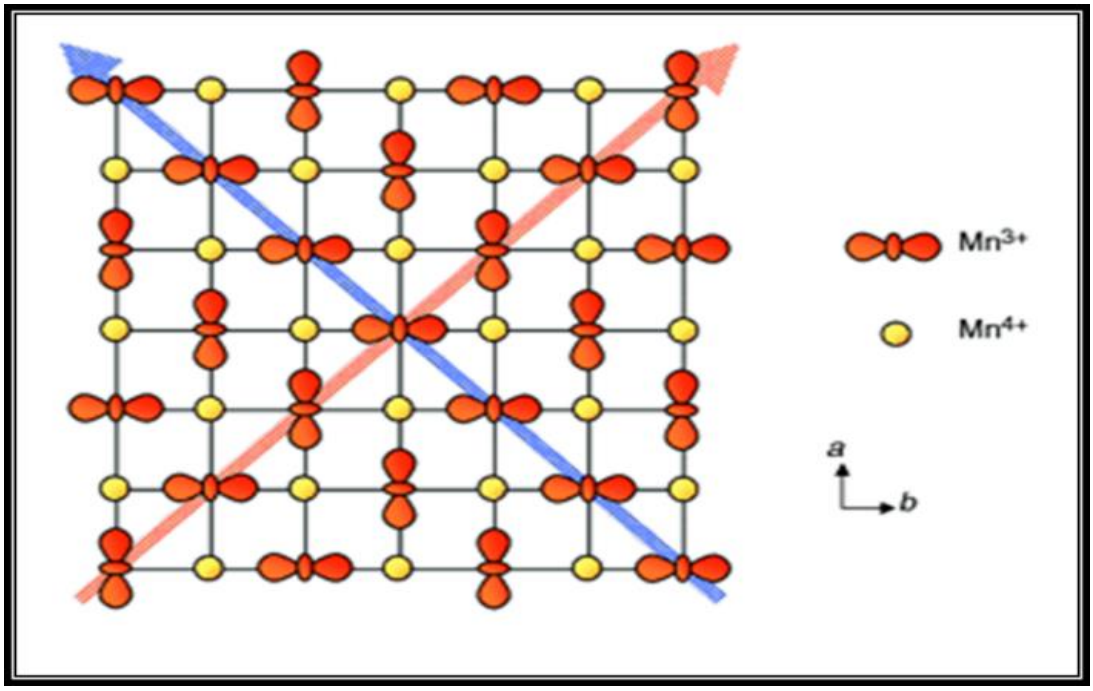

Figure1.6: The orbital and charge order of the CE type projected on the MnO_2 sheet (ab plane) [52]

Charge ordering (CO), is another distinctive feature in which the ordering of differently charge cations on specific lattice sites and renders the material insulating or semiconducting nature **[46,49,53–57]**. The ratio Mn^{3+}/Mn^{4+} is responsible for this and in general, CO consists of a periodic distribution of electric charge (i.e. e_g electrons of Mn^{3+} ions), driven by standard electrostatic interaction. Such a distribution localizes the e_g electrons of Mn ion positions in the lattice, forming an ordered sublattice as shown in **Fig. 1.6.** The charge ordered insulator (COI) state is favoured by small size cations at RE/AE-site **[58]**. As discussed in the earlier sections, the earliest experimental evidence of charge ordering was put forth by Wollan and Koehler **[27]** and Jirak et al, **[59].** More recently, Chen and Cheong [60] [61] used electron diffraction to experimentally illustrate such order in $La_{0.5}Ca_{0.5}MnO_3$ ($T_C \approx 220$ K). Mori et al **[62]** employed low temperature transmission

electron microscopy to demonstrate the existence of stripe phase in which the JT effect driven distorted $Mn^{3+}O_6$ and non-distorted $Mn^{4+}O_6$ octahedral stripes alternate periodically. The antiferromagnetic charge/orbital ordered (AFM-CO/OO) phase under the action of external perturbations like electromagnetic field/radiation as well as can transform into the ferromagnetic-metallic one **[63–67]**electric field **[68]**. Low temperature Lorentz electron microscopy has also been used to illustrate the coexistence of different electronic orders in manganites **[69]**. This shows consistency with the complex and extremely delicate phase coexistence unriddled by Mori et al **[70]** in $La_{0.25}Pr_{0.375}Ca_{0.375}MnO_3$. The transition to the charged ordered (CO) phase is a first order phase transition and it is closely related to the orbital ordering through the Jahn Teller (JT) effect of Mn^{3+} **[71,72]**

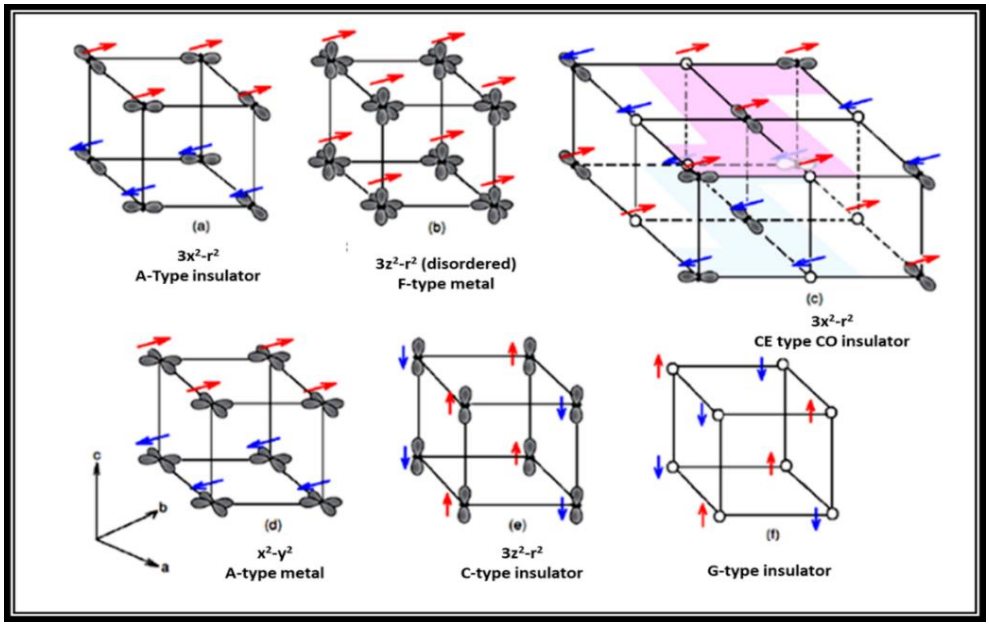

Figure 1.7: Schematic of different types of spin ordering and orbital ordering in manganites [73]

Another distinctive particularity of manganites is existence of orbital order which is crucial for decoding the magnetic orders not only in manganite but in other TMO based systems also **[12,47,55,73].** The Spatially ordered arrangement of d orbitals in the crystal is termed as the orbital ordering (OO). **Fig. 1.7** shows various types of depicted orbital

ordering in manganites. Generally, the orbital ordering is responsible anisotropy in various electronic interaction and gives rise to a mosaic spin orbital coupled state **[73,74]**

1.3 Relevant Phase Diagrams

The electronic phase diagrams of manganites is extremely opulent and the phases become mosaic and entangled with reducing bandwidth **[75–77].** Complexity of the phase diagrams is implicit in the strongly coupled multiple degrees of freedom and hence is intrinsic to such systems. Since the coupling between the various degrees is correlated to the RE/AE size and fraction (this determines the bandwidth) therefore the nature and extent of the phases on the x – T diagram differs from system to system **[78].** $La_{1-x}Ca_xMnO_3$ (LCMO) is considered as canonical representative of the mixed valent perovskite manganites (**Fig. 1.8**) and therefore is among the most studied compound of the manganite family because of its robust magneto-resistance which is larger than other much-studied materials i.e. $La_{1-x}Sr_xMnO_3$ (LSMO) (large bandwidth manganite) or $Pr_{1-x}Ca_xMnO_3$ (PCMO) (low bandwidth manganite) **[79].** The earliest magnetic phase diagram of LCMO on the x – T plane was elucidated by Schiffer et al. for limited x-range **[15]** and later on Cheong and Hwang (2000) **[80]** presented the complete phase diagram of LCMO. **Fig. (1.8)** shows the phase diagram of the intermediate bandwidth manganite i.e. LCMO. From the phase diagram it is clear that at both the ends ($x \leq 0.07$ and $x \geq 0.875$) the high temperature phase is a paramagnetic insulator, while the low temperature spin order is a canted-AFM (C-AFM). A low temperature CO phase appears approximately in the range x~0.07 – 0.175, which transforms to a FM insulator as the temperature increases. The composition range x~0.175 – 0.5 has FM metallic phase at the low temperatures with the maximum of the insulator-metal/paramagnetic-ferromagnetic phase transition around x~3/8.

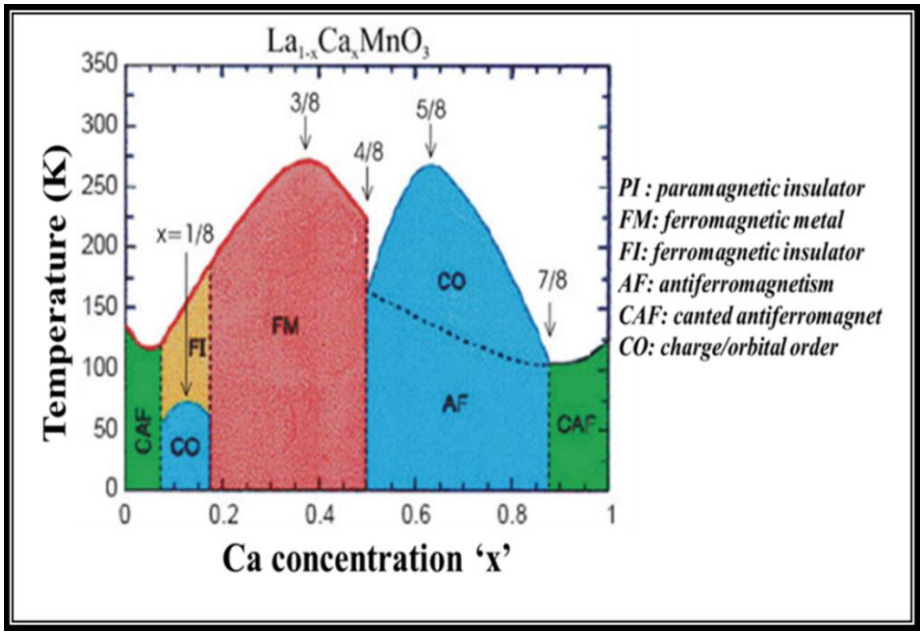

Figure 1.8: Phase diagram of $La_{1-x}Ca_xMnO_3$ [81]

In the range x~0.5 – 0.875 the lower temperature is dominated by AFM spin order, which on warming transforms to a CO one and finally to the high temperature PM phase. The CO temperature (T_{CO}) maximizes in the vicinity of x~5/8. The above clearly outlines the affluence of the LCMO phase diagram **[15,80]**. It is also clear that only the hole doped regime is conducive to the FM order, while the CO order remains confined to the electron doped regime. Further, the C-AFM insulator is present, both in the lightly hole doped as well as lightly electron doped regimes. It is important to understand the importance of electron lattice coupling leading to charge localization in the mixed-valent manganites at the terminal compositions **[61,82].**

Another low bandwidth pristine $PrMnO_3$ manganite system exhibits an orthorhombic distorted structure (Pbnm) at room temperature which transforms to antiferromagnetic order at T_N = 91 K **[83]**. Its Ca-doped variant, viz., $Pr_{1-x}Ca_xMnO_3$ (PCMO) is rather uncommon among manganites because of the fact that it exhibits AFM ground state over the entire range of x and the CO appears as the high temperature phase at x>0.3. Further, it

remains insulating over the entire doping range (x) and temperature range as shown in **Fig. 1.9**.

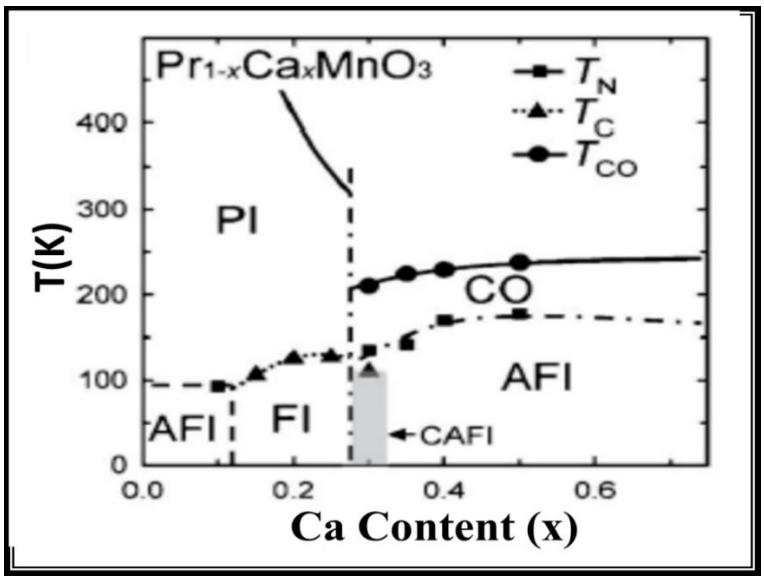

Figure 1.9:The magnetic and electronic phase diagrams of PCMO [84]

Sha *et. al.* **[84]** showed that in PCMO, AFM and FM spin clusters coexist with a canted antiferromagnetic insulating (C-AFI) structure and the CO state at $T<T_{CO}$ has an inhomogeneous nature. The CO state having AFM spin flavor is generally a homogeneous state and a critical composition in proximity to x=0.35, separates the homogeneous and inhomogeneous states. This is generally ascribed to small ionic radius of Ca (~ 1.34 Å), which produces a sizeable orthorhombic distortion favoring strong charge localization. The AFMI is stable at T<100 K for $0 \leq x \leq 0.1$. This is followed by a FMI with $T_C \leq 140$ K for $0.15 \leq x \leq 0.3$. In the range $0.3 \leq x \leq 0.75$, a prominent J-T distortion is seen and this stabilizes the CO at $T \leq 240$ K. At $T \leq 175$ K, an insulating AFM spin order appears **[84].** All these phases related to the presence of distorted $Mn^{3+}O_6$ octahedra and their elastic interaction. At $x \geq 0.3$ COI-AFM is the ground state in PCMO.

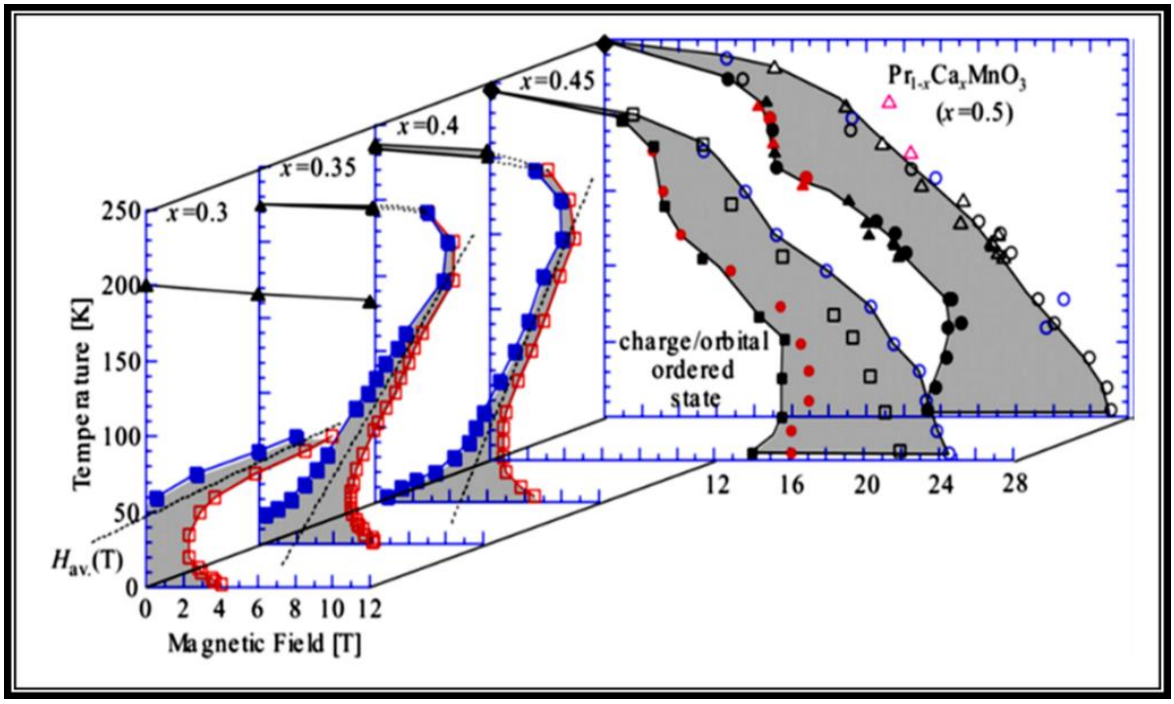

Figure 1.10: The CO-OO state of $Pr_{1-x}Ca_xMnO_3$, plotted on the magnetic field temperature plane. The shaded area shows the hysteresis region. [3,85]

The stability of the CO/OO states in PCMO vis-à-vis external perturbations like a magnetic field depends on the deviation from half doping (x ≈ 0.5) (shown in **Fig. 1.10**). On lowering the divalent concentration from x = 0.5 towards x = 0.3, the CO-melting magnetic fields come down significantly from about H=27 T for x = 0.5 to few Tesla at x = 0.3 **[49,66,67,86,87]** . The true phase of PCMO is a mixture of AFMI and FMI and at sufficiently large magnetic fields the former transforms through a first order transition into the latter and hence the magnetic phase becomes more homogeneous. Burgy et al. **[88]**, suggested the intrinsic inhomogeneities in PCMO and the competing degrees of freedom gives rise to charge-exchange (CE) type charge and orbital ordering that coexist FMI.

In this compound the relatively smaller size of the Pr^{3+}/Ca^{2+} cations yield a small tolerance factor/lower bandwidth x thus leading to the stabilization of the CO phase over a broad x-range. The low temperature electronic phase at the low hole concentrations (0.15

< x < 0.3) O is a FMI, wherein an OO ground state akin to that in $LaMnO_3$ and the cooperative JT distortion yield $(3x^2-r^2)/(3y^2-r^2)$-type OO in the a-b plane. The Mn^{4+} ions are disordered. Antiferromagnetic spin order with insulating flavor (AFMI) dominates the lower temperature span at low temperatures and the CO/OO takes over at the higher temperatures. The CO state is unstable against external perturbations such as magnetic and electric fields and electromagnetic radiations **[66,67,86,87,89–91]**.

1.4 Phase Separation

Phase separation (PS) is now a well-established and fundamental attribute of the manganites and has origin in the complex interplay between the various intimately coupled degrees of freedom **[55,92]**. The strongly interacting charge, spin, orbital, and lattice degrees leads to affluence in the structural and magneto-electric phases which often coexist and compete with one another leading to PS **[55,57,92,93]** . PS is well known in strongly correlated electron systems such as TMOs **[73,94]**, doped manganite **[95,96],** high T_c oxides **[97,98]** etc., which have microscopically and intrinsically inhomogeneous states. Phase separation in manganites occurs at various length scales ranging from sub-nm to up to even few microns and also referred to as mesoscale phase separation **[95,96]**. The occurrence of PMI, FMM, AFMI, AFMM, FMI and CO/OO phases and their coexisting tendencies clearly validate the electronic and magnetic phase affluence **[55,57,63,85,92,93]**. The nature, relative strength and the degree and composition-temperature range of coexistence of these phases are fixed by two prominent factors, viz., (i) the RE/AE ratio and their average cationic size, and (ii) thermomagnetic variables like temperature (T) and magnetic field (H) **[99–102]**. When average RE/AE cation radii is small, a reduced electronic bandwidth (BW) results and the interphase boundaries become permeable making the phase boundary prone to diffusion. Nagaev **[103]** discovered the phase separation in semiconductors and showed FM phase

was embedded in an AFM matrix results in percolative transport. The PS is entirely reversible and competing charge localized and delocalized states or coexisting phases results in contrasting electronic and magnetic properties. The competing phases give rise to strong coulomb interaction and results in conducting FM and insulating AFM phases to form assemblage of one phase embedded into another in order to minimize the electrostatic energy. The clusters size depends on competing DE and the Coulomb interactions. The neutron diffraction experiments of Wollan and Koehler **[27]** while confirming the coexistence of the coexistence of FM and A-type AFM yielded the earliest evidence of phase separation.

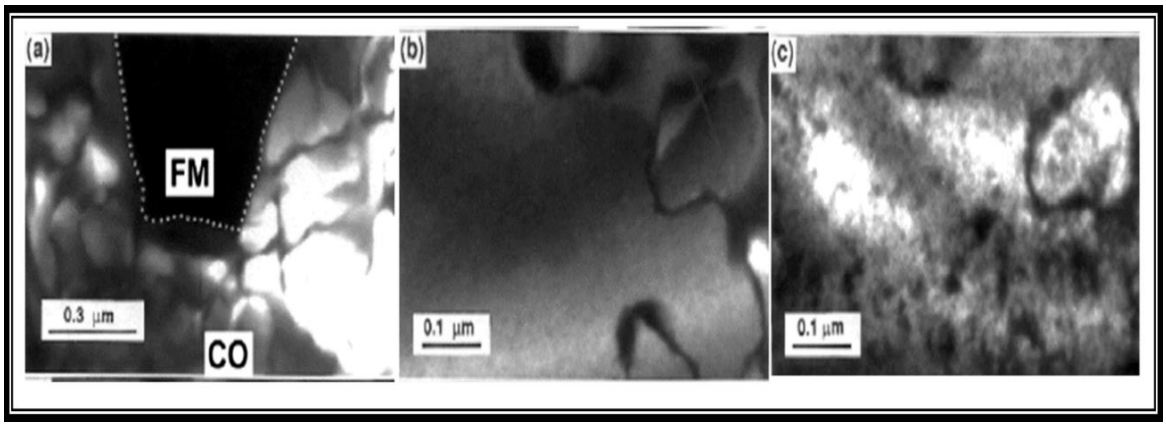

Figure1.11: Dark field images for $La_{5/8-y}Pr_yCa_{3/8}MnO_3$ (a) shows the coexisting insulating (CO) and metallic (FM) phases at 20 K for y = 0.375. Dark area with in dotted line highlights metallic phase. (b) and (c), show the development of nanoscale charge-disordered domains at $T > T_C$ obtained at same area for y = 0.4 at 17 K and 120 K, respectively, [63].

Uehara et al. [63] gave the most convincing proof of coexisting insulating and metallic phases in manganites through the transport, magnetic and electron microscopy studies in La5/8−yPryCa3/8MnO3 (y~0.4) (LPCMO). They validated the coexistence of two magneto-electric phases exhibiting percolative transport and found PS clusters as large as ~500 nm for y ~ 0.375 at 20 K by transmission electron microscopy and these clusters reduce to few nanometers at 120 K as shown in **Fig 1.11.**

These results align well with the disorder-induced phase transition model of Moreo et al. **[104]**, in which a first order transition is transformed into two-phase coexisting regions by the disorder embodied in the system. Phase separation can be envisioned as a repercussion of the disorder due to cation size mismatch as observed in the LPCMO system **[104]**. Fath et al. **[105]** employed scanning tunneling spectroscopy (STS) to unearth the intrinsic PS in single crystalline bulk and thin film $La_{0.7}Ca_{0.3}MnO_3$. For $T < T_C$, phase separation was observed and the cluster size was found to be quite large and strongly depends on magnetic field. Other groups have also shown phase separation by scanning tunneling spectroscopy STS **[106]**, scanning tunneling microscopy (STM) **[99]** and low temperature microscopy (MFM) **[100]**. Nanometer scale 'red cabbage' FM clusters embedded in an AFMI matrix have been exposed using polarized small angle neutron scattering technique by Viret et al. **[101]** and Saurel et al. **[102]**. The simultaneous existence of the occupied and vacant states in LPCMO epitaxial thin film has been confirmed by *in-situ* STM experiments of Ma et al. **[107].** Various theories based on effective medium approach, Monte Carlo simulation of random resistor network **[108,109]** etc., put forward a two-phase model of competing FMM and AFM/COI phases. Lyuksyutov and Pokrovsky **[110]** proposed better and realistic model based on magnetic polaron formation theory of C. M. Varma **[111]**. In this model the polaron density continues to increases with temperature till an overlap of magnetic polarons is achieved. The mean field theories like the dynamical one due to Millis et al. **[112]** and much simpler approach pursued by Jaime et al. **[113]** provided only a approximate treatment of phase separation. Ahn et al. **[114]** has rightly outlined the importance of the strongly coupled electro-elastic degrees of freedom in accounting for the inhomogeneities of different phases. The modified ℓ-b model which includes (i) long range electrostatic (Columbic) interaction and (ii) the disorder due to the dopant ion **[115,116]** adopted by Shenoy et al. **[117]** has shown that the nanoscale

inhomogeneities in doped manganites arise due to the long range electrostatic interactions. The various aspects of PS in manganites have been reviewed by several authors **[95,96,118–120]** Among the doped rare-earth manganites $La_{1-x-y}Pr_xCa_yMnO_3$ (LPCMO) has been recognized as the prototypical of the phase separated doped rare-earth manganite. The literature survey and various properties of LPCMO have been discussed in detail in next section.

1.5 Literature Survey on $La_{1-x-y}Pr_xCa_yMnO_3$ (LPCMO)

$La_{1-x-y}Pr_yCa_xMnO_3$ (LPCMO) has emerged as emblematic of the narrow bandwidth (BW) manganites showing mesoscale phase separation wherein the major coexisting electronic phases are the charge ordered antiferromagnetic insulator (CO/AFMI) and the ferromagnetic metallic (FMM) **[63,121–123].** As the BW is reduced, the tendency towards phase separation has been observed due to the occurrence of multiple magnetic phases coexisting on a limited span of the x-T plane. LPCMO has emerged as the most widely investigated phase separated manganite system and has been studied in bulk as well as thin films form. Its bulk exhibits (magnetic and electronic) phase **[54,63,114,124,125]** coexistence/separation **[121,124,126–128]** typically between cubic FMM, orthorhombic AFM–COI, and pseudo-cubic PMI phases. Although the favored length scale of PS is the 'nanometer', but it has shown sub nanometer to micrometer scale PS over a broad x- and y- compositions. The magneto-electrical properties of LPCMO are very sensitive to compositional variations. The electronic properties in general and various electric and magnetic transitions in particular become extremely sensitive to external perturbations like hydrostatic pressure, magnetic field, electric field, substrate induced strain, etc. **[121,122]**. The size and fraction of the competing phases has been found to be extremely sensitive to various extrinsic factors external electromagnetic radiation, substrate induced strain, crystallite size, dimensional confinement, etc. In narrow BW compounds FMM and

AFM/COI are the two phases demonstrating simultaneousness. When larger RE/AE cations are substituted by the smaller ones (e.g. La by Pr and Sr by Ca) the pseudocubic FMM phase transforms into a pseudotetragonal distorted AFM/ COI phase having free energy close to the former. Uehara et al., showed sub micrometer scale FM and AFM/COI coexists over a broad range of the phase diagram in $La_{5/8-y}Pr_yCa_{3/8}MnO_3$ and that the transport through this two phase mixture is percolative. The ionic radii mismatch induced quenched disorder also leads to the coexistence of two competing phases and this results in the phase separated state in manganites which has been described as "electronic soft matter" state **[125,129]**.

Wu et al. **[126]** studied the lattice strain effects in the pulsed laser deposition (PLD) deposited epitaxial $La_{0.67-x}Pr_xCa_{0.33}MnO_3$ (x = 0.12, 0.2, 0.27) thin films of varying thickness on $LaAlO_3$ (LAO) (compressive strain), $SrTiO_3$ (STO) (tensile strain) and $NdGaO_3$ (NGO) (negligible strain) substrates. No hysteresis was observed in the films (shown in **Fig. 1.12**), having higher T_{IM} or less strain whereas it dominates in low T_{IM} and strained films. Low magnetic field (~ 1 T) melts the CO in STO films but on LAO and NGO it enhances the T_{IM}. A first order IM transition accompanied by hysteresis and significant low field MR was reported by Ogale et al. **[124]** in oxygen-deficient $La_{0.42}Pr_{0.28}Ca_{0.3}MnO_{3-\delta}$ thin films. In another interesting work on $La_{0.375}Pr_{0.25}Ca_{0.375}MnO_3$ films deposited on NGO substrates by PLD. Tsai et al. **[130]** showed that phase separation plays very important role in the occurrence of persistent magnetic memory effect (PMME). Sarma et al. **[131]** reported CO transition at low temperature (~ 30 K) in addition to the occurrence of CO at ~ 210 K in single- and poly- crystalline $La_{5/8-x}Pr_xCa_{3/8}MnO_3$ (x ~ 0.41) manganite. The presence of coexisting CO and FMM phases at low temperature is also accompanied with spin-glass-like magnetism.

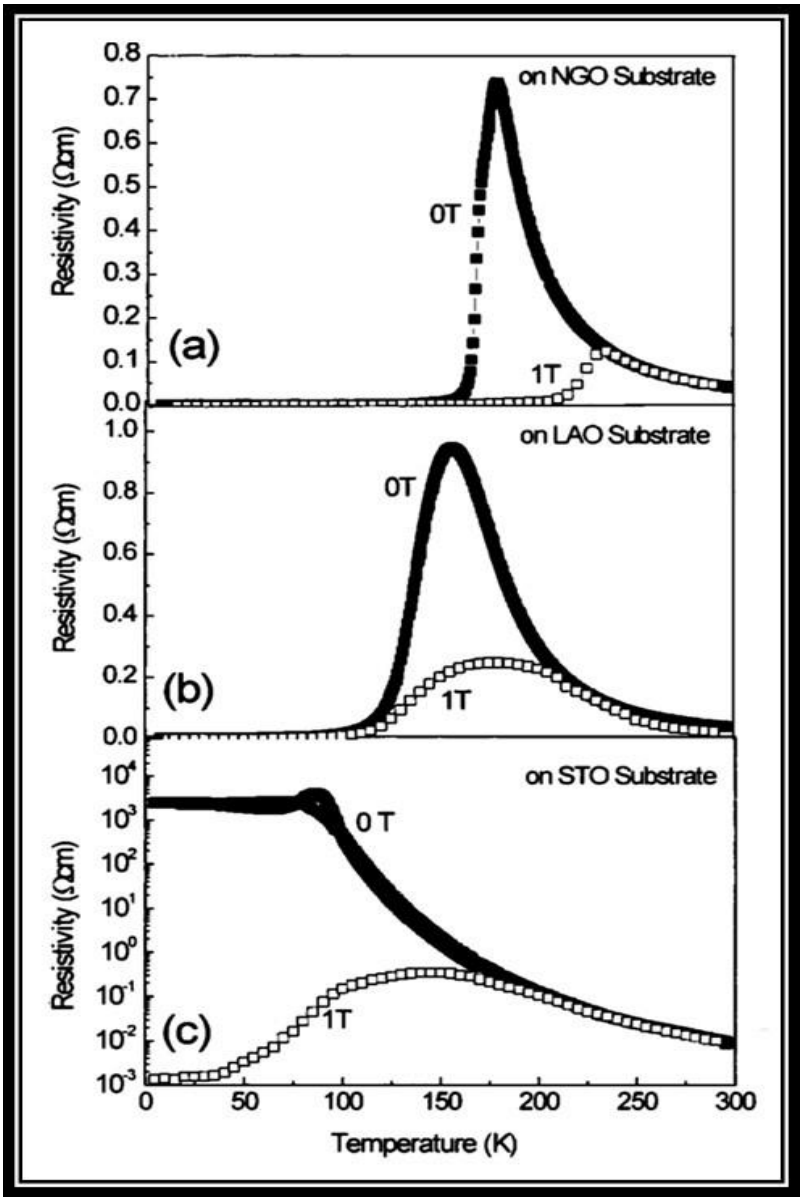

Figure 1.12: Resistivity vs temperature of 600 Å $La_{0.4}Pr_{0.27}Ca_{0.33}MnO_3$ films on (a) NGO (b) LAO (c) STO substrate at 0 and 1T magnetic field [126]

The dynamic nature of phase separation in polycrystalline $La_{5/8-y}Pr_yCa_{3/8}MnO_3$ (y = 0.1, 0.2, and 0.3) is shown by Ghivelder et al. **[121]** (Fig. **1.13**). They observed homogeneous FM state at low temperatures for y = 0.1, 0.2, 0.3, 0.5 and 0.625 with CO transition at ~ 230 K, and the AFM ordering (a small peak that marks) at lower temperature, T_N ~ 180 K. For y = 0.4 sample, a disorder induced "glass" state is observed in addition to T_{CO} and T_N.

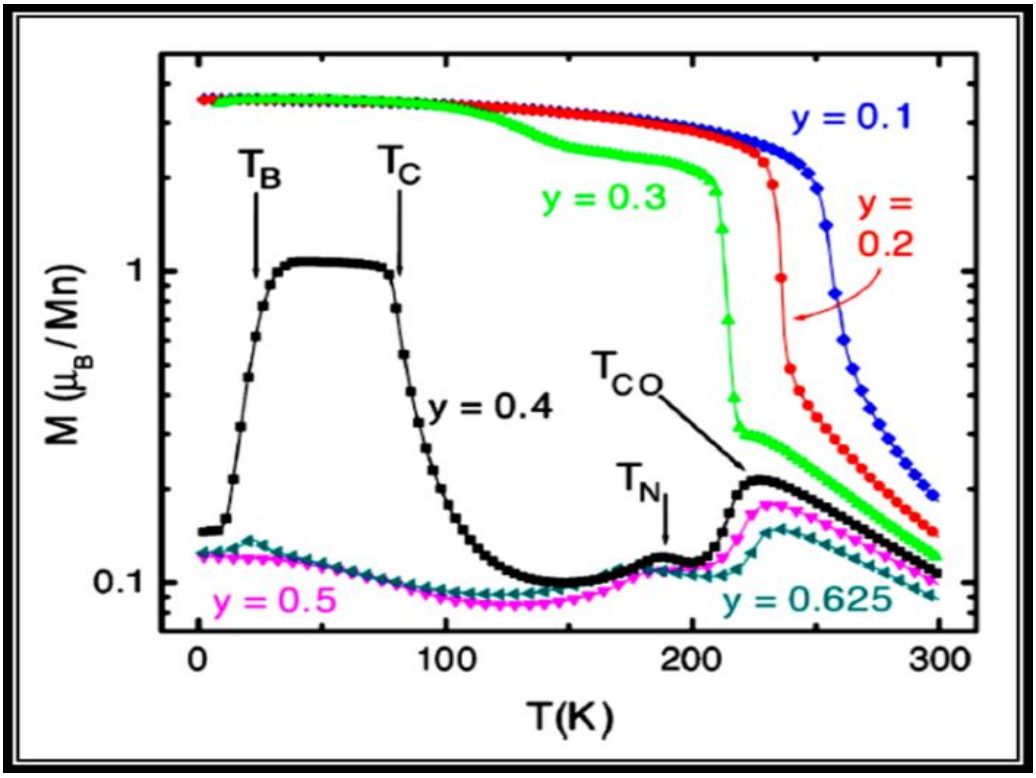

Figure 1.13: The temperature dependence magnetization of $La_{5/8-y}Pr_yCa_{3/8}MnO_3$. For the y=0.4 sample there exist charge-order transition temperature (T_{CO}), antiferromagnetic transition (T_N), ferromagnetic transition (T_C), and blocking temperature (T_B) [121]

Sharma et al. **[122]** also investigated $La_{5/8-y}Pr_yCa_{3/8}MnO_3$ (y~0.4) in bulk single crystalline as well as polycrystalline form and they characterized the low temperature state below which the magnetization has a reversible behavior as the strain glass (SRG). This study ingrained the existence of a magnetically soft liquid like magnetic state spanning the phase separated regime. This soft magnetic phase makes a cooperatively transition to a randomly frozen glass like phase at low temperature. The frozen glass like phase is termed as strain glass (SRG). According to Podzorov et al. **[132]** martensitic accommodation strains caused by different structural symmetries of the COI (orthorhombic) and FM (pseudo cubic) phases are believe to stabilize the large-scale PS. In contrast, Sharma et al. **[122]** suggest that PS regime at low temperature can be transformed by martensitic accommodation strains giving rise to a cooperative transition from a dynamic liquid like to

randomly frozen glasslike state. Deac et al. **[133]** have investigated the relaxation properties of a series of LPCMO (y~0.38) in which the relative fraction of FM and AFM/COI was varied through variation in the sintering temperature. Their study unraveled two distinctive relaxation channels, viz., the relaxation of moment orientation and the relaxation of phase fraction. The magnetic and magnetotransport impacts of substrate-provided strain in $(La_{1-y}Pr_y)_{0.67}Ca_{0.33}MnO_3$, (y = 0.4-0.6) thin films on the NGO and STO substrates have been studied by Dhakal et al **[125]**. They have shown that similar to the strain liquid state in bulk compounds **[128],** a phase-separated state that mimics a fluid appears at intermediate temperatures in these films. In this state the magnetic fluid is transformed into a FMM state when an external electric field is applied. Jeon et. al. **[134]** in their thickness dependent study on the compressive and tensile strained $La_{0.35}Pr_{0.35}Ca_{0.3}MnO_3$ films grown on LAO and STO substrates, respectively found a correlation between the film surface roughness and FMM and AFM/COI inhomogeneity, e.g., at lower film thickness, the static phase separated regions are more inhomogeneous than the fluid phase separated ones. Zhai et al. **[135]** investigated the effect of dimensional confinement and observed ultra-sharp jumps of resistivity as a function of the temperature and magnetic field in the vicinity of the MIT in a $(La_{5/8-0.3}Pr_{0.3})Ca_{3/8}MnO_3$ wire fabricated using optical lithography from an epitaxial thin film grown on LAO substrate. As shown by Ward et al. **[127],** the dimensional confinement in single crystalline $La_{0.391}Pr_{0.234}Ca_{0.375}MnO_3$ thin film yields a robust re-entrant MIT in the lower temperature regime. Singh et al. **[123]** while probing the correlation between the chemical and magnetic depth profiles of a single crystalline $(La_{1-x}Pr_x)_{1-y}Ca_yMnO_3$ thin films grown on NGO substrate using various techniques demonstrated that there is a direct correlation between the magnetic non uniformity across the film's thickness and the chemical non-uniformity

across the corresponding film depth. These chemically non- uniform regions have lower magnetization and hence different regions have different ordering temperatures.

The hysteresis loops are believed to be the materialization of non-equilibrium states, observed in the vicinity of first order phase boundaries. Interesting memory effects are seen in systems embodying non-equilibrium states and such effects are generally not present in in equilibrium state. The dynamic scaling behavior i.e. study of hysteresis loop area in various magnetic systems provides the information regarding energy loss per cycle in terms of external influences like applied magnetic field strength (H_0), frequency (Ω, in case of AC fields) and temperature (T) and internal parameters like the system dimensionality and associated magnetic anisotropy. The magnetic hysteresis loops (like the M-H loop) emulate the irreversibility in the domain wall motion in pinning fields have shown scaling power laws in their hysteresis parameters. The dynamic hysteresis also unravels the characteristic times of domain nucleation and domain boundary motion as concurrent process during the domain reversal. For ferromagnetic thin films, dynamic hysteresis loop area (A) have shown relation with applied field strength (H_0), frequency (Ω) and temperature (T) as [**136]** (and ref therein): $A \propto H_0^{\alpha} \Omega^{\beta} T^{-\gamma}$, where α, β and γ and are exponents that depend on the system symmetry and dimensionality. The empirical Steinmetz law **[137]** relates static loop area with applied field is generally applicable to bulk ferromagnetic systems. Despite the growing interest in magnetic materials, very little experimental work is reported on the study of scaling behavior of the hysteresis loops. The study of hysteresis loops by Kobayashi et al. **[138]** in a helical incommensurate magnetic phase established that the irreversibility related hysteresis loss in such materials is related with remnant flux density as power law with same scaling exponent of 1.05 ± 005 as that in ferromagnetic materials. Santi et al **[139]** have studied the dynamic hysteresis loops in Finemet

$Fe_{73.5}Cu_1Nb_3Si_{18.5}B_4$ thin films showed logarithmic dependence on the frequency of applied field. Zhong Fan et al. **[140]** emphasized the irreversible nature of the hysteretic behavior. Thomas et al. **[141]** showed that the power-law dependence of hysteresis loop area manifests the self-organized criticality in continuous spin systems. They observed that for small frequencies (Ω), and small field amplitude (H_0), the area of loop scales as $(H_0\ \Omega)^{1/2}$ with logarithmic corrections. Dahmen et al. **[142]** while studying the non-equilibrium zero temperature random field Icing model for hysteretic behaviour in the first order transformation and found transition in the shape of associated loop. They showed that rectangular shaped hysteresis loops and big discontinuity (Barkhausen) are characteristics of the system with lower disorder vis-à-vis the coupling strength, while smooth hysteresis loops without macroscopic jumps are associated with systems with large disorder. *Kobayashi et al.* **[143]** observed that the scaling power law with an exponent of ≈1.35 holds true for several ferromagnets (Fe–Si, Ni, and Co as well as Co single crystal) in the wide magnetization range, while the magnetization range where the Steinmetz law **[137]** is valid is only limited in the intermediate range and strongly depends both on materials and temperature.

Kim et al. **[145]** discussed the possibility of both ferroelectric and ferromagnetic systems belonging to a common universality class of polarization/magnetization reversal dynamics. They studied the dependence of applied field amplitude (H_0) and frequency (Ω) on scaling region of hysteresis loop area of ferroelectric crystal with scaling behaviour $A \propto H_0^{1.55}\Omega^{0.20}$ in the region of small H_0 and Ω. Liu et al. **[144]** studied frequency dependence of hysteresis area for Nd substituted $Bi_4Ti_3O_{12}$ thin film expressed as $A \propto H_0^{2/3}\Omega^{1/3}$ for low frequency and $A \propto H_0^{2}\Omega^{-2/3}$ for high frequency (**shown in Fig 1.14**). Singh et al. **[146]**

studied conductive AFM characteristics of $(La_{0.4}Pr_{0.6})_{0.67}Ca_{0.33}MnO_3$/NGO films to unravel non-uniform distribution of metallic and insulating regions on the film surface around the IMT.

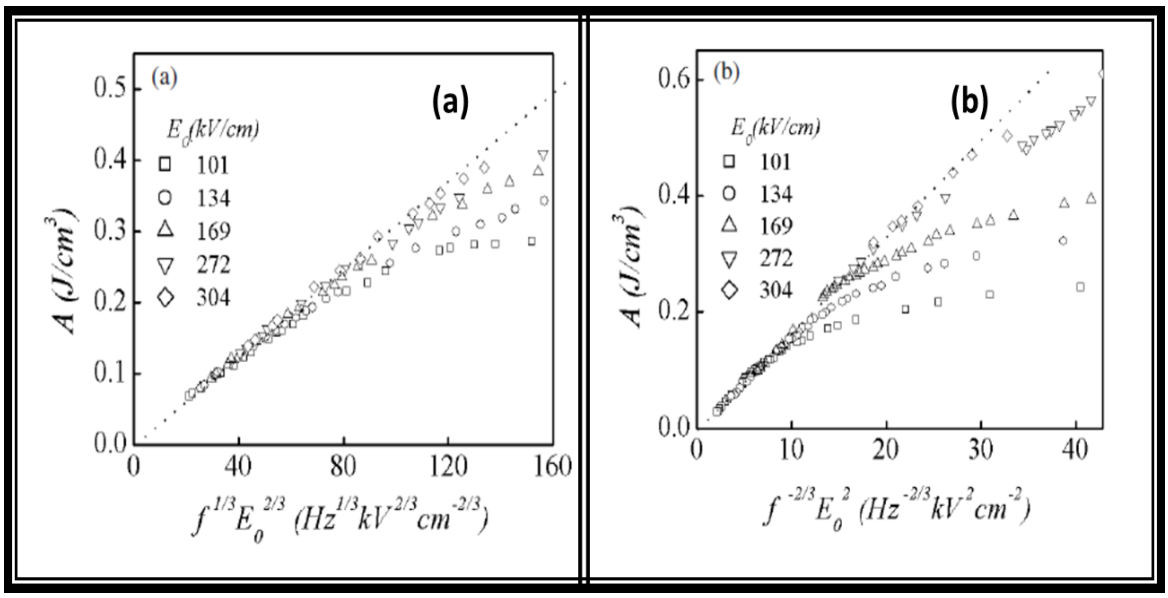

Figure 1.14: Scaling of ferroelectric hysteresis for Nd-substituted $Bi_4Ti_3O_{12}$. Frequency response of hysteresis area A plotted against (a) $f^{1/3}E_0^{2/3}$ over the low frequency range and (b) $f^{-2/3}E_0^2$ over the high-frequency range. [144]

Phase separated manganites also show unique property of anisotropic magnetoresistance (AMR) where strong correlation and complex interplay between the various degrees of freedom are believed to affect the spin orbit coupling and hence magnitude of AMR **[123].** Alagoz et al. **[147]** has probed the different aspects of AMR in LPCMO thin films and showed that (i) a metastable irreversible state exists in the films at the temperature corresponding to the strongest phase separation and the resistivity attains large time dependence. In another study Alagoz et al. **[148]** also showed the resistance measured as a function of angle between magnetic field direction and direction of current in the plane of LPCMO film does not follow the standard oscillatory dependence**.** Zhou et al **[149]** have revealed the effect of various degrees of freedom using magnetic force

microscopy and imaged phase transitions at microscopic scales. Du et. al. [150] employing magnetic force microscopy have showed the existence of edge states in LPCMO with the appearance of distinct FMM phase along the edge of manganite strips. The resistivity in LPCMO films also show sensitivity to electric field which is manifested in form of CER effect. Wei et al. **[151]** showed that FMM domains remain virtually unchanged after passing electric current and tiny fractions of FMM bridges which are responsible for CER effect appear. Zhu et. al. **[152]** in their study on the consequences of chemical ordering in LPCMO system observed that it markedly reduces electronic phase separation length scale. Zhang et. al. **[153]** through their terahertz (THz) optical conductivity measurements on $La_{0.33}Pr_{0.34}Ca_{0.33}MnO_3$/LAO thin film demonstrated that the optical conductivity in the metallic phase region exhibits a non-Drude-like response. Nguyen et. al. **[154]** carried out terahertz (THz) time domain spectroscopy of LPCMO nanowires to decipher the change in the conductivity from metallic to dielectric/insulating behaviour as the electric field of the THz pulse was varied from parallel to perpendicular to the nanowires.

1.6 Motivation to the Work

The above survey clearly brings out that $La_{1-x-y}Pr_yCa_xMnO_3$ (LPCMO) is a canonical low BW compound showing mesoscopic phase separation wherein the major coexisting electronic phases are the charge ordered antiferromagnetic insulator (CO/AFMI) and the ferromagnetic metal (FMM). There are several issues which are not well understood yet. Typical of them are (i) systematic thickness dependence of the magnetic phases and the nature of electrical transport, (ii) dependence of the insulator metal transition (IMT) of the relative fraction of the two competing phases, (iii) the nature of the hysteresis in the electrical transport as a function of the thermomagnetic variables temperature (T) and magnetic field (H), (iv) temporal evolution of the electrical resistivity, especially near the IMT and in the magnetically soft regions, and (v) scaling of the hysteresis loop area with

temperature and magnetic field. In the current work an attempt has been made towards understanding of the above issues in good quality thin films of $La_{1-x-y}Pr_yCa_xMnO_3$. The films have been grown by RF magnetron sputtering on (001) oriented $SrTiO_3$ substrates.

1.7 References

[1] B. R. C. N. R. Rao, *Transition Metal Oxides: Structure, Properties, and Synthesis of Ceramic Oxides*, 2nd Editio (Wiley, 1998, 1998).

[2] C. W. Chu, P. H. Hor, R. L. Meng, L. Gao, Z. J. Huang, and and Y. Q. Wang, Phys. Rev. Lett. **58**, 405 (1987).

[3] Y. Tokura and Y. Tomioka, J. Magn. Magn. Mater. **200**, 1 (1999).

[4] J. B. Goodenough, *Magnetism And The Chemical Bond* (John Wiley And Sons, 1963).

[5] A. T. Howe and P. J. Fensham, Q. Rev. Chem. Soc. **21**, 507 (1967).

[6] David Adler, Solid State Phys. **21**, 1 (1968).

[7] D. Paquet and P. Leroux-Hugon, Phys. Rev. B **22**, 5284 (1980).

[8] H. Schmid, Ferroelectrics **162**, 317 (1994).

[9] J. G. Bednorz and K. A. Müller, Zeitschrift Für Phys. B Condens. Matter **64**, 189 (1986).

[10] C. W. Chu, P. H. Hor, R. L. Meng, L. Gao, Z. J. Huang, Wang, and Y. Q., Phys. Rev. Lett. **58**, 405 (1987).

[11] S. N. Putilin, E. V Antipov, O. Chmaissem, and M. Marezio, Nature **362**, 226 (1993).

[12] M. Imada, A. Fujimori, and Y. Tokura, Rev. Mod. Phys. **70**, 1039 (1998).

[13] K. Chahara, T. Ohno, M. Kasai, and Y. Kozono, Appl. Phys. Lett. **63**, 1990 (1993).

[14] R. von Helmolt, J. Wecker, B. Holzapfel, L. Schultz, and K. Samwer, Phys. Rev. Lett. **71**, 2331 (1993).

[15] P. Schiffer, A. P. Ramirez, W. Bao, and S.-W. Cheong, Phys. Rev. Lett. **75**, 3336 (1995).

[16] P. G. Radaelli, D. E. Cox, M. Marezio, S.-W. Cheong, P. E. Schiffer, and A. P. Ramirez, Phys. Rev. Lett. **75**, 4488 (1995).

[17] J. M. D. Coey, M. Viret, and S. von Molnár, Adv. Phys. **48**, 167 (1999).

[18] C. Zener, Phys. Rev. **81**, 440 (1951).

[19] C. Zener, Phys. Rev. **82**, 403 (1951).

[20] G. Zhao, Nat. **381**, 676 (1996).

[21] S. Jin, T. H. Tiefel, M. McCormack, R. A. Fastnacht, R. Ramesh, and L. H. Chen, Science (80-.). **264**, 413 (1994).

[22] H. Y. Hwang, S.-W. Cheong, N. P. Ong, and B. Batlogg, Phys. Rev. Lett. **77**, 2041 (1996).

[23] G. H. Jonker and J. H. Van Santen, Physica **16**, 337 (1950).

[24] J. H. Van Santen and G. H. Jonker, Physica **16**, 599 (1950).

[25] G. H. Jonker, Physica **22**, 707 (1956).

[26] J. Volger, Physica **20**, 49 (1954).

[27] EO Wollan and WC Koehler, Phys. Rev. **100**, 545 (1955).

[28] C. W. Searle and S. T. Wang, Can. J. Phys. **47**, 2703 (1969).

[29] C. W. Searle, Can. J. Phys. **48**, 2023 (1970).

[30] A. H. Morrish, Can. J. Phys. **47**, 2691 (1969).

[31] L. K. Leung, A. H. Morrish, and C. W. Searle, Can. J. Phys. **47**, 2697 (1969).

[32] B. Raveau, Proc. Indian Acad. Sci.(Chem. Sci.).–1986.–52.–P 67 (1986).

[33] M. A. Peña and J. L. G. Fierro, Chem. Rev. **101**, 1981 (2001).

[34] V. M. Goldschmidt, Naturwissenschaften **14**, 477 (1926).

[35] R. D. T. Shannon and C. T. Prewitt, Acta Crystallogr. Sect. B Struct. Crystallogr. Cryst. Chem. **25**, 925 (1969).

[36] W. Prellier, A. M. Haghiri-Gosnet, B. Mercey, P. Lecoeur, M. Hervieu, C. Simon, and B. Raveau, Appl. Phys. Lett. **77**, 1023 (2000).

[37] Y. G. Zhao, M. Rajeswari, R. C. Srivastava, A. Biswas, S. B. Ogale, D. J. Kang, W. Prellier, Z. Chen, R. L. Greene, and T. Venkatesan, J. Appl. Phys. **86**, 6327 (1999).

[38] H. A. Jahn and E. Teller, Proc. R. Soc. A Math. Phys. Eng. Sci. **161**, 220 (1937).

[39] H. Y. Hwang, S.-W. Cheong, P. G. Radaelli, M. Marezio, and B. Batlogg, Phys. Rev. Lett. **75**, 914 (1995).

[40] P. A. Cox, Transition Metal Oxides: An Introduction to Their Electronic Structure and Properties (OUP Oxford, 2010).

[41] P. L. G. F. Albert Cotton, Geoffrey Wilkinson, *Basic Inorganic Chemistry, 3rd Edition*, 3rd Editio (1995).

[42] R. Freitag and J. Conradie, J. Chem. Educ. **90**, 1692 (2013).

[43] J. B. Goodenough, Phys. Rev. **100**, 564 (1955).

[44] A.-M. Haghiri-Gosnet and J.-P. Renard, J. Phys. D. Appl. Phys. **36**, R127 (2003).

[45] P. W. Anderson and H. Hasegawa, Phys. Rev. **100**, 675 (1955).

[46] Y. Tokura, *Colossal Magnetoresistive Oxides* (CRC Press, 2000).

[47] T Hotta and E Dagotto, in *Colossal Magnetoresistive Manganites*, edited by T. Chatterji (Springer Netherlands, Dordrecht, 2004).

[48] P. K. Siwach, H. K. Singh, and O. N. Srivastava, J. Phys. Condens. Matter **20**, 273201 (2008).

[49] C. N. R. Rao and B. Raveau, Colossal Magnetoresistance, Charge Ordering and Related Properties of Manganese Oxides (WORLD SCIENTIFIC, 1998).

[50] M. Gen, J. Phys. Soc. Japan **29**, 606 (1970).

[51] Y. Murakami, J. P. Hill, D. Gibbs, M. Blume, I. Koyama, M. Tanaka, H. Kawata, T. Arima, Y. Tokura, K. Hirota, and Y. Endoh, Phys. Rev. Lett. **81**, 582 (1998).

[52] Y. Tokura, Science (80-.). **288**, 462 (2000).

[53] M. K. Srivastava, A. Kaur, K. K. Maurya, V. P. S. Awana, and H. K. Singh, Appl. Phys. Lett. **102**, 32402 (2013).

[54] A. Moreo, Science (80-.). **283**, 2034 (1999).

[55] E. Dagotto, T. Hotta, and A. Moreo, Phys. Rep. **344**, 1 (2001).

[56] E. Dagotto, New J. Phys. **7**, 67 (2005).

[57] E. Dagotto, *Nanoscale Phase Separation and Colossal Magnetoresistance* (Springer Berlin Heidelberg, Berlin, Heidelberg, 2003).

[58] Y. Tokura, J. Appl. Phys. **79**, 5288 (1996).

[59] Z. Jirák, S. Krupička, Z. Šimša, M. Dlouhá, and S. Vratislav, J. Magn. Magn. Mater. **53**, 153 (1985).

[60] C. H. Chen and S.-W. Cheong, Phys. Rev. Lett. **76**, 4042 (1996).

[61] C. H. Chen, S.-W. Cheong, and H. Y. Hwang, J. Appl. Phys. **81**, 4326 (1997).

[62] S. Mori, C. H. Chen, and S.-W. Cheong, Nature **392**, 473 (1998).

[63] M. Uehara, S. Mori, C. H. Chen, and S.-W. Cheong, Nature **399**, 560 (1999).

[64] H. Kuwahara, Science (80-.). **270**, 961 (1995).

[65] Y. Moritomo, H. Kuwahara, Y. Tomioka, and Y. Tokura, Phys. Rev. B **55**, 7549 (1997).

[66] V. Kiryukhin, D. Casa, J. P. Hill, B. Keimer, A. Vigliante, Y. Tomioka, and Y. Tokura, Nature **386**, 813 (1997).

[67] A. Asamitsu, Y. Tomioka, H. Kuwahara, and Y. Tokura, Nature **388**, 50 (1997).

[68] S. Parashar, E. E. Ebenso, A. R. Raju, and C. N. R. Rao, Solid State Commun. **114**, 295 (2000).

[69] J. C. Loudon, N. D. Mathur, and P. A. Midgley, Nature **420**, 797 (2002).

[70] S. Mori, T. Asaka, and Y. Matsui, Microscopy **51**, 225 (2002).

[71] P. G. Radaelli, M. Marezio, H. Y. Hwang, S.-W. Cheong, and B. Batlogg, Phys. Rev. B **54**, 8992 (1996).

[72] K. H. Ahn and A. J. Millis, Phys. Rev. B **58**, 3697 (1998).

[73] Y. Tokura, Science (80-.). **288**, 462 (2000).

[74] J. Orenstein, Science (80-.). **288**, 468 (2000).

[75] J. Dho, W. S. Kim, and N. H. Hur, Phys. Rev. Lett. **87**, 187201 (2001).

[76] H. Kawano, R. Kajimoto, M. Kubota, and H. Yoshizawa, Phys. Rev. B **53**, R14709 (1996).

[77] H. Kawano, R. Kajimoto, M. Kubota, and H. Yoshizawa, Phys. Rev. B **53**, 2202 (1996).

[78] R. Kajimoto, H. Yoshizawa, Y. Tomioka, and Y. Tokura, Phys. Rev. B **66**, 180402 (2002).

[79] Y. Tomioka, A. Asamitsu, H. Kuwahara, and Y. Tokura, in *Phys. Manganites* (Kluwer Academic Publishers, Boston, n.d.), pp. 155–175.

[80] S. Cheong and H. Y. Hwang, in *Colossal Magnetoresistive Oxides*, edited by Y. Tokura (London, UK: Gordon and Breach, 2000), pp. 237–280.

[81] A. Moreo, J. Phys. Chem. Solids **67**, 32 (2006).

[82] J. M. D. Coey, M. Viret, L. Ranno, and K. Ounadjela, Phys. Rev. Lett. **75**, 3910 (1995).

[83] S. Quezel-Ambrunaz, Bull. Soc. Fr. Minéral. Cristal. B **91**, 339 (1968).

[84] H. Sha, F. Ye, P. Dai, J. A. Fernandez-Baca, D. Mesa, J. W. Lynn, Y. Tomioka, Y. Tokura, and J. Zhang, Phys. Rev. B **78**, 52410 (2008).

[85] Y. Tokura, Rep. Prog. Phys. **69**, 797 (2006).

[86] Y. Tomioka, A. Asamitsu, H. Kuwahara, Y. Moritomo, and Y. Tokura, Phys. Rev. B **53**, R1689 (1996).

[87] Y. Tomioka, J. Phys. Soc. Jpn. **64**, 3626 (1995).

[88] J. Burgy, M. Mayr, V. Martin-Mayor, A. Moreo, and E. Dagotto, Phys. Rev. Lett. **87**, 277202 (2001).

[89] D. E. Cox, P. G. Radaelli, M. Marezio, and S.-W. Cheong, Phys. Rev. B **57**, 3305 (1998).

[90] K. Miyano, T. Tanaka, Y. Tomioka, and Y. Tokura, Phys. Rev. Lett. **78**, 4257 (1997).

[91] T. Mori, K. Ogawa, K. Yoshida, K. Miyano, Y. Tomioka, and Y. Tokura, J. Phys. Soc. Japan **66**, 3570 (1997).

[92] M. B. Salamon and M. Jaime, Rev. Mod. Phys. **73**, 583 (2001).

[93] E. Dagotto, Science (80-.). **309**, 257 (2005).

[94] E. Sigmund and K. A. Muller, *Phase Separation in Cuprate Superconductors* (Springer Berlin Heidelberg, 1994).

[95] C. N. R. Rao, A. K. Kundu, M. M. Seikh, and L. Sudheendra, Dalt. Trans. 3003 (2004).

[96] E. Dagotto, J. Burgy, and A. Moreo, Solid State Commun. **126**, 9 (2003).

[97] J. M. Tranquada, B. J. Sternlieb, J. D. Axe, Y. Nakamura, and S. Uchida, Nature **375**, 561 (1995).

[98] E. Sigmund and K. A. Müller, Phase Separation in Cuprate Superconductors: Proceedings of the Second International Workshop on "Phase Separation in Cuprate Superconductors" September 4–10, 1993, Cottbus, Germany (Springer Science & Business Media, 2012).

[99] M. Bibes, L. Balcells, S. Valencia, J. Fontcuberta, M. Wojcik, E. Jedryka, and S. Nadolski, Phys. Rev. Lett. **87**, 67210 (2001).

[100] L. Zhang, C. Israel, A. Biswas, R. L. Greene, and A. de Lozanne, Science **298**, 805 (2002).

[101] M. Viret, F. Ott, J. Renard, H. Glättli, L. Pinsard-Gaudart, and A. Revcolevschi, Phys. Rev. Lett. **93**, 217402 (2004).

[102] D. Saurel, A. Brûlet, A. Heinemann, C. Martin, S. Mercone, and C. Simon, Phys. Rev. B **73**, 94438 (2006).

[103] E. L. Nagaev, *Colossal Magnetoresistance and Phase Separation in Magnetic Semiconductors* (PUBLISHED BY IMPERIAL COLLEGE PRESS AND DISTRIBUTED BY WORLD SCIENTIFIC PUBLISHING CO., 2002).

[104] A. Moreo, M. Mayr, A. Feiguin, S. Yunoki, and E. Dagotto, Phys. Rev. Lett. **84**, 5568 (2000).

[105] M. Fäth, Science (80-.). **285**, 1540 (1999).

[106] V. N. Smolyaninova, A. Biswas, X. Zhang, K. H. Kim, B.-G. Kim, S.-W. Cheong, and R. L. Greene, Phys. Rev. B **62**, R6093 (2000).

[107] J. Ma, D. Gillaspie, E. Plummer, and J. Shen, Phys. Rev. Lett. **95**, 237210 (2005).

[108] P. J. M. Bastiaansen and H. J. F. Knops, J. Phys. Chem. Solids **59**, 297 (1998).

[109] M. Mayr, A. Moreo, J. Vergés, J. Arispe, A. Feiguin, and E. Dagotto, Phys. Rev. Lett. **86**, 135 (2001).

[110] I. F. LYUKSYUTOV and V. L. POKROVSKY, Mod. Phys. Lett. B **13**, 379 (1999).

[111] C. Varma, Phys. Rev. B **54**, 7328 (1996).

[112] A. J. Millis, Nature **392**, 147 (1998).

[113] M. Jaime, P. Lin, S. Chun, M. Salamon, P. Dorsey, and M. Rubinstein, Phys. Rev. B **60**, 1028 (1999).

[114] K. H. Ahn, T. Lookman, and A. R. Bishop, Nature **428**, 401 (2004).

[115] T. V Ramakrishnan, J. Phys. Condens. Matter **19**, 125211 (2007).

[116] T. Ramakrishnan, H. Krishnamurthy, S. Hassan, and G. Pai, Phys. Rev. Lett. **92**, 157203 (2004).

[117] V. Shenoy, T. Gupta, H. Krishnamurthy, and T. Ramakrishnan, Phys. Rev. Lett. **98**, 097201 (2007).

[118] F. Y. Genin, MRS Proc. **389**, 83 (1995).

[119] B. D. Gates, Q. Xu, M. Stewart, D. Ryan, C. G. Willson, and G. M. Whitesides, Chem. Rev. **105**, 1171 (2005).

[120] E. Dagotto, Nanoscale Phase Separation and Colossal Magnetoresistance (Berlin: Springer, 2002).

[121] L. Ghivelder and F. Parisi, Phys. Rev. B **71**, 184425 (2005).

[122] P. A. Sharma, S. B. Kim, T. Y. Koo, S. Guha, and S.-W. Cheong, Phys. Rev. B **71**, 224416 (2005).

[123] S. Singh, J. W. Freeland, M. R. Fitzsimmons, H. Jeen, and A. Biswas, J. Appl. Phys. **116**, 222205 (2014).

[124] A. S. Ogale, S. R. Shinde, V. N. Kulkarni, J. Higgins, R. J. Choudhary, D. C. Kundaliya, T. Polleto, S. B. Ogale, R. L. Greene, and T. Venkatesan, Phys. Rev. B **69**, 235101 (2004).

[125] T. Dhakal, J. Tosado, and A. Biswas, Phys. Rev. B **75**, 92404 (2007).

[126] T. Wu, S. B. Ogale, S. R. Shinde, A. Biswas, T. Polletto, R. L. Greene, T. Venkatesan, and A. J. Millis, J. Appl. Phys. **93**, 5507 (2003).

[127] T. Z. Ward, S. Liang, K. Fuchigami, L. F. Yin, E. Dagotto, E. W. Plummer, and J. Shen, Phys. Rev. Lett. **100**, 247204 (2008).

[128] N. S. Bingham, P. Lampen, M. H. Phan, T. D. Hoang, H. D. Chinh, C. L. Zhang, S. W. Cheong, and H. Srikanth, Phys. Rev. B **86**, 64420 (2012).

[129] E. Dagotto, Science (80-.). **309**, 257 (2005).

[130] Y. T. Tsai, W. J. Chang, C. C. Hsieh, C. W. Luo, K. H. Wu, T. M. Uen, J. Y. Juang, and J. Y. Lin, J. Appl. Phys. **105**, 13705 (2009).

[131] D. D. Sarma, D. Topwal, U. Manju, S. R. Krishnakumar, M. Bertolo, S. La Rosa, G. Cautero, T. Y. Koo, P. A. Sharma, S.-W. Cheong, and A. Fujimori, Phys. Rev. Lett. **93**, 97202 (2004).

[132] V. Podzorov and B. G. Kim, Phys. Rev. B **64**, 140406 (2001).

[133] I. G. Deac, S. V. Diaz, B. G. Kim, S.-W. Cheong, and P. Schiffer, Phys. Rev. B **65**, 174426 (2002).

[134] J. Jeon, H. S. Alagoz, J. Jung, and K. H. Chow, J. Appl. Phys. **115**, 233907 (2014).

[135] H.-Y. Zhai, J. X. Ma, D. T. Gillaspie, X. G. Zhang, T. Z. Ward, E. W. Plummer, and J. Shen, Phys. Rev. Lett. **97**, 167201 (2006).

[136] W. Y. Lee and J. A. C. Bland, J. Korean Phys. Soc. **39**, 661 (2001).

[137] C. P. Steinmetz, Trans. Am. Inst. Electr. Eng. **IX**, 1 (1892).

[138] S. Kobayashi, Phys. Rev. Lett. **106**, 057207 (2011).

[139] L. Santi, L. . Dorneles, R. . Sommer, F. Colaiori, S. Zapperi, A. Magni, and G. Durin, J. Magn. Magn. Mater. **272**–**276**, E913 (2004).

[140] F. Zhong and J. Zhang, Phys. Rev. Lett. **75**, 2027 (1995).

[141] P. B. Thomas and D. Dhar, J. Phys. A. Math. Gen. **26**, 3973 (1993).

[142] K. Dahmen and J. P. Sethna, Phys. Rev. B **53**, 14872 (1996).

[143] S. Kobayashi, S. Takahashi, T. Shishido, Y. Kamada, and H. Kikuchi, J. Appl. Phys. **107**, 023908 (2010).

[144] J.-M. Liu, B. Pan, H. Yu, and S. T. Zhang, J. Phys. Condens. Matter **16**, 1189 (2004).

[145] D.-H. Kim and J.-J. Kim, Ferroelectrics **222**, 285 (1999).

[146] S. Singh, M. R. Fitzsimmons, H. Jeen, A. Biswas, and M. E. Hawley, Appl. Phys. Lett. **101**, 22404 (2012).

[147] H. S. Alagoz, J. Jeon, S. T. Mahmud, M. M. Saber, B. Prasad, M. Egilmez, K. H. Chow, and J. Jung, Appl. Phys. Lett. **103**, 232402 (2013).

[148] H. S. Alagoz, J. Jeon, R. Boos, R. H. Ahangharnejhad, K. H. Chow, and J. Jung, Appl. Phys. Lett. **105**, 162409 (2014).

[149] H. Zhou, L. Wang, Y. Hou, Z. Huang, Q. Lu, and W. Wu, Nat. Commun. **6**, 8980 (2015).

[150] K. Du, K. Zhang, S. Dong, W. Wei, J. Shao, J. Niu, J. Chen, Y. Zhu, H. Lin, X. Yin, S.-H. Liou, L. Yin, and J. Shen, Nat. Commun. **6**, 6179 (2015).

[151] W. Wei, Y. Zhu, Y. Bai, H. Liu, K. Du, K. Zhang, Y. Kou, J. Shao, W. Wang, D. Hou, S. Dong, L. Yin, and J. Shen, Phys. Rev. B **93**, 035111 (2016).

[152] Y. Zhu, K. Du, J. Niu, L. Lin, W. Wei, H. Liu, H. Lin, K. Zhang, T. Yang, Y. Kou, J. Shao, X. Gao, X. Xu, X. Wu, S. Dong, L. Yin, and J. Shen, Nat. Commun. **7**, 11260 (2016).

[153] C. Zhang, F. Su, J. Dai, L. Pi, H. Mei, P. Zhang, and W. Xu, Jpn. J. Appl. Phys. **55**, 031101 (2016).

[154] T. V. A. Nguyen, A. N. Hattori, M. Nagai, T. Nakamura, M. Ashida, and H. Tanaka, J. Appl. Phys. **119**, 125102 (2016).

2 Experimental and Characterization Techniques

2.1 Thin Films and its Basic Aspects:

A thin film is a low dimensional material formed by condensation of one by one atomic, molecular or ionic species of matter on a chosen base material called the substrate. In thin film, one of the dimension is reduced to range from few atomic/molecular layers to hundreds/thousands of such layers so that the length of reduced dimension is of the order of mean free path of the material under consideration **[1–5]**. Thin films have high surface to volume ratio with unique structure and other properties which are direct result of the growth mechanism and they show deviation from the corresponding bulk. The high surface to volume ratio influences various phenomena such as electrical transport, thermal transport, chemical transport/diffusion, catalytic activity, gas adsorption, etc. **[6,7]**. Similarly, thin films of certain materials show enhancement of corrosion resistance, hardness, superconducting transition temperature, and optical adsorption having metastable disordered structure **[8**]. A very natural consequence of small thickness are electronic tunneling through an intermediate separator insulating layer, Josephson effect, optical interference, , planar magnetization, high resistivity, low temperature coefficient of resistance, and increment in critical magnetic field as well as critical temperature of super conductors etc. **[7]**. Thin film materials have variety of application in semiconductor industry such as integrated circuits, transistors, solar cells, light-emitting diodes (LEDs), magneto-optic memories, photoconductors, compact discs, electro-optic coatings, flat-panel displays, smart windows, computer chips, micro electromechanical devices etc., as well as various other emerging technologies in areas like telecommunication and wireless communication systems **[9–11].** The innovation and development of computer technology

strongly demand for very high density data storage devices and motivated the research on new age magnetic thin films. The understanding of growth process of thin film and its tunability to film thickness is very important for the development of thin film technology. The film thickness ultimately determines the physical properties of thin film material. A thin film growth process has three stages: ((i) creation of appropriate species, (ii) the transportation of these species to desired substrate through an appropriate medium and (iii) condensation of these species on suitable substrate. General schematic for thin film growth process is represented in **Fig. 2.1**.

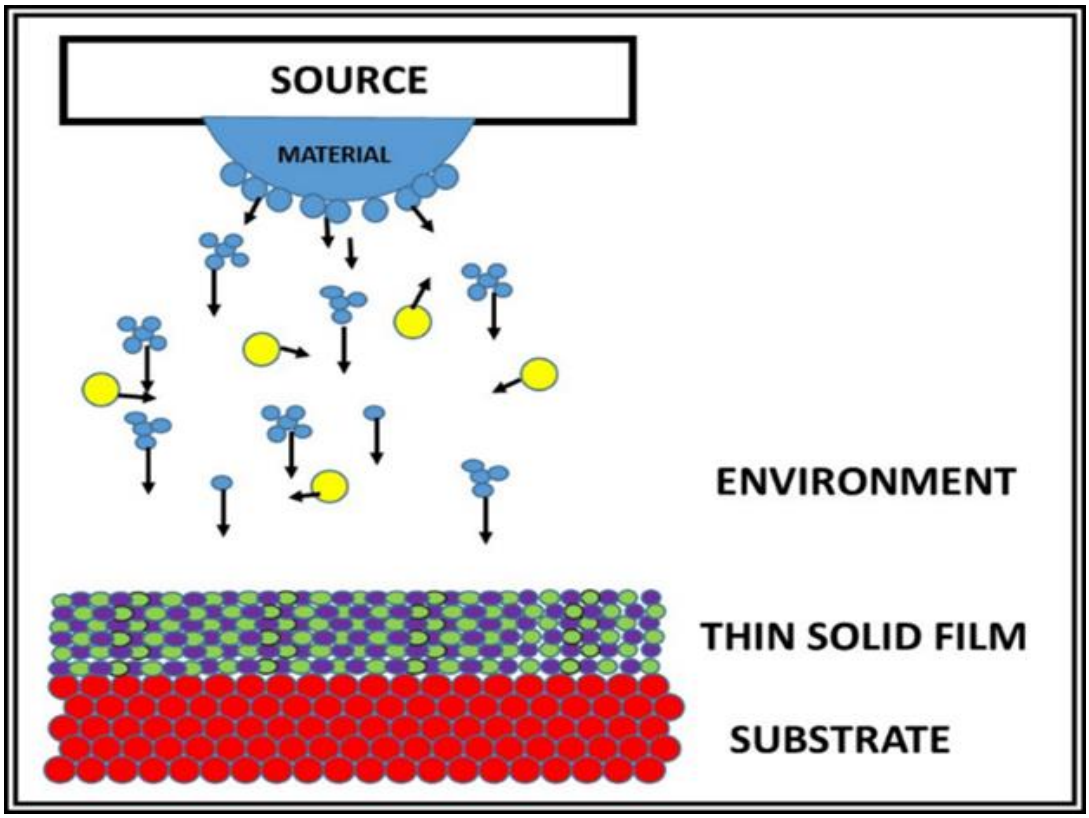

Figure 2.1: Schematic of thin film growth process

In general the gradual-growth stages of thin films are summarized as follows **[7]**:

(1) The deposit species impinging the substrate retain velocity component along substrate surface but lose normal to it on collision. This way they are adsorbed on the substrate.

(2) Post adsorption, the deposit species are under random motion and intract with each other and coalesce to form bigger clusters called “nuclei"**.**

(3) Further collision between the nuclei and the adsorbed species results in further enhancement in size to “nucleation stage”.

(4) Nuclei further increase their number and size till saturation is achieved. The formed nuclei at saturation is called “islands”**.**

(5) Small islands coalesce with each other to form bigger islands called “***agglomerates***”. These agglomerates grow together and create channels and holes of uncoverd substrate and make porous network like structure of film.

(6) The growth proceeds further by gradually filling of porous networks and yiels continuous film

Hence, in the nutshell the growth process consists of (i) statistical process of nucleation, (ii) surface diffusion, (iii) controlled growth of 3D nuclei, and (iv) formation of network structure and its subsequent filling to give a continuous film. The growth state and the initial nucleation is governed by the thermal parameters of the material, the nature of the substrates and the growth conditions. **[1–5].**

2.1.1 Volmer–Weber or Island Growth

The Volmer–Weber (or Island Growth) growth mode is a three-dimensional island formation through the nucleation of the smallest stable clusters on the substrate as shown in **Fig. 2.2(a) [12].** Here unit species of deposited material are more strongly bonded to each other as compared to the substrate. This mode is more common in hetero-epitaxial growth where the film and substrate are of different materials. This growth mode is more frequently observed for metal and semiconductor films on oxide substrates.

2.1.2 Frank–Van der Merwe (or Layer-by-Layer Growth):

The Frank–Van der Merwe or commonly known as layer-by-layer growth of film where smallest nucleus join together in two dimensions resulting in planar sheet like structure as shown in **Fig. 2.2(b) [13].** Here, depositing atoms or molecules are more strongly bonded to the substrate than each other. Also, each progressive layer is less strongly bonded to the previous layers..

2.1.3 Stranski–Krastanov Mode (or Mixed Growth):

Stranski–Krastanov mode is the combination of the layer-by-layer and island growth **[14]** as shown in **Fig. 2.2(c).** In this growth mode first few monolayers are formed in layer-by-layer fashion then further it becomes energetically unfavourable and islands growth begin to form. This growth mode is fairly common and is observed in various metal-metal and metal-semiconductor systems.

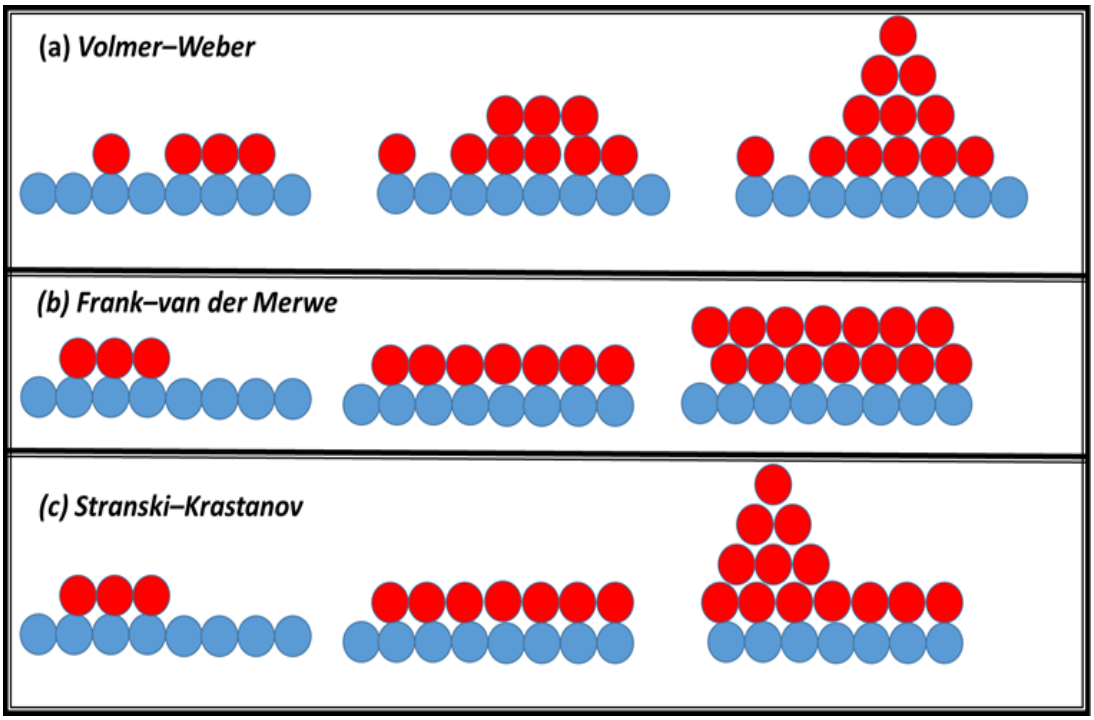

Figure 2.2: Modes of growth (a) Volmer–Weber (or Island Growth) (b) Frank–van der Merwe (or Layer-by-Layer Growth) and (c) Stranski–Krastanov Mode (or Mixed Growth)

Generally, the growth of thin film adopts island formation mode. Initially, a continuous thin layer of film forms on the substrate. This is followed by the growth of cylindrical columns along the substrate normal the ensuing island growth. The crystallite size and lateral grain size during the formation of film depends on the initial nucleation density. For further deposition, re-nucleation starts and multi-granular vertical column grows on previous grown layers for thicker films and shows deviation from normal growth **[15]**.

Various defects (point and line) and grain boundaries are introduced in the film during growth process due to crystallographic and geometrical configuration mismatch. Epitaxial films also have possibility of different structural faults like, twin boundaries, dislocation lines, stacking faults, multiple positioning boundaries and other minor defects arises due to conglomeration of point defects. The dislocations and defects arise due to (i) lattice mismatch of film and substrate causing strain in film (ii) large inherent stress in thin films, (iii) different coefficients of thermal expansion of film and substrate and (iv) dislocations on the substrate surface which apparently transfer to the film during growth process **[5]**. Such defects are most commonly observed in perovskite oxide films on mismatched substrate.

2.2 Consequences of Film Growth Parameters

The film topography and its microstructure is controlled by the kinetics of of growth process, chemical and topographical nature of substrate, gas environment and substrate temperature etc. Such parameters influence the kinetic energy of incident species, surface mobility of adsorbed species, deposition rate, condensation coefficient, level of impurities and super-saturation **[5]**. Structural/microstructural consequences of these parameters are described in ensuing subsections

2.2.1 Effect on Microstructure

The lateral grain size depends on super-saturation and surface mobility of the adsorbed species. It increases with decreasing super-saturation and increasing surface mobility. Larger grains with high surface mobility are formed for high source and substrate temperatures. Surface mobility of adsorbed species shows an increase with the increase in kinetic energy of incident species and at sufficiently high kinetic energies incident species could penetrate into the substrate. This reduces the surface mobility resulting in smaller grains. The kinetic energy effects acquire more prominence at (i) high substrate temperatures and (ii) high film thickness. The grain size of the deposit also shows dependence on post annealing process. It generally increases for annealing temperatures higher than deposition temperature.. This effect of post annealing is prominently observed in higher thickness films.

High good quality epitaxial films can be also be obtained by various deposition techniques under controlled conditions. The epitaxial growth is favoured by (1) high surface mobility of adsorbed species on high substrate temperature (2) clean and smooth surface (3) low supersaturation and (4) crystallographic matching of the material and substrate. Thin films with particular crystallographic directivity (orientation along certain direction) are called oriented films. Single crystalline substrates are necessary for the growth of epitaxial films, while amorphous substrates are suffice for the growth of oriented films **[5]**.

2.2.2 Effect on Surface Roughness and Density

A fine grained and continuous smooth film is formed due to low nucleation barrier and high super-saturation at smaller thickness. On the other side, the large nucleation barrier and low super-saturation result in the grain coarsening and higher film roughness.

Such films become continuous only at relatively higher thicknesses. The coarse grained rough films have cavities and porosities which are prominently filled by high surface mobility of adsorbed species and results in smoother films. Preferential films along certain direction can also be formed on substrates having large anisotropic surface energy or faceted rough substrate.

Surface roughness of films show dependence on various factors like the oblique angle incidence, which generally enhances the surface roughness, different chemical composition of the deposit also changes the roughness in compound thin films. The growth modes of thin film essentially influence the surface roughness of deposited films. Comparatively smoother films are formed by Frank-van der Merwe mode (layered growth) whereas, Volmer-Weber Island growth yields higher film roughness. The thermal expansivity of the interface materials, that is, the substrate and the film also affect the surface microstructure **[16,17]**.

Density is another important parameter that determines the physical structure of thin film. Density shows dependence on film thickness which generally decreases with the decreasing thickness of deposited film.

2.2.3 Effect on Adhesion

The adhesion of a film to the substrate is determined by several factors, viz. (i) the cleanliness, (ii) chemical nature (iii) thermal compatibility (iv) crystallographic structure of the substrate and the materials, and (v) the growth conditions. Better adhesion is achieved with the highly energetic impinging species, high adsorption energy and faster initial nucleation density. The fine-grained substrates or buffered substrate provide more nucleation centres on the substrate and hence improve adhesion **[5]**.

2.2.4 Effect on Metastable Structure

A variety of metastable structures are, possibly as a result of (i) deposition conditions, (ii) the presence of some impurity and (iii) the substrate structural, chemical and thermal nature **[5].** Generally, a deviation in lattice constants of ultrathin films is observed as compared with their corresponding bulk material. This change in lattice constant is determined by surface energy and hence the nature of the strain which depends on whether the surface energy is negative or positive.

2.3 Thin Film Deposition Processes

Thin films play a key role in the growing technological advancement in the fields of photonics, opto-electronics, electrical and magnetic devices **[6,8].** The properties of thin films are significantly different from their corresponding bulk variants. The processing of bulk materials into thin films provide easy access for developing different types of devices. There are few vital process variables that play a crucial role in deposition of thin film such as deposition conditions, nature of substrate, post deposition treatment and passivation etc. The individual atomic, molecular or ionic species of matter may be in vapor phase or liquid phase. Therefore, depending on the phase, thin film deposition process can be broadly classified into two main categories: (1) Vapor phase deposition (2) Liquid phase deposition.

Vapor phase deposition includes "evaporation, molecular beam epitaxy (MBE), sputtering, chemical vapor deposition (CVD), atomic layer deposition (ALD) techniques whereas *liquid phase deposition* includes electrochemical deposition, chemical solution deposition (CSD), Langmuir-Blodgett films, self-assembled monolayers (SAMs) etc" **[8]**.

In general, vapor phase is the most common method used for deposition of film atomically on a suitable substrate and is classified as "Physical Vapor Deposition (PVD) and Chemical Vapor Deposition (CVD)". Many variants in vapor deposition methods have

been developed based on the requirements of film deposition such as purity, structural quality, growth rate, and other factors. **Fig. 2.3** show schematic of typical vapor deposition processes.

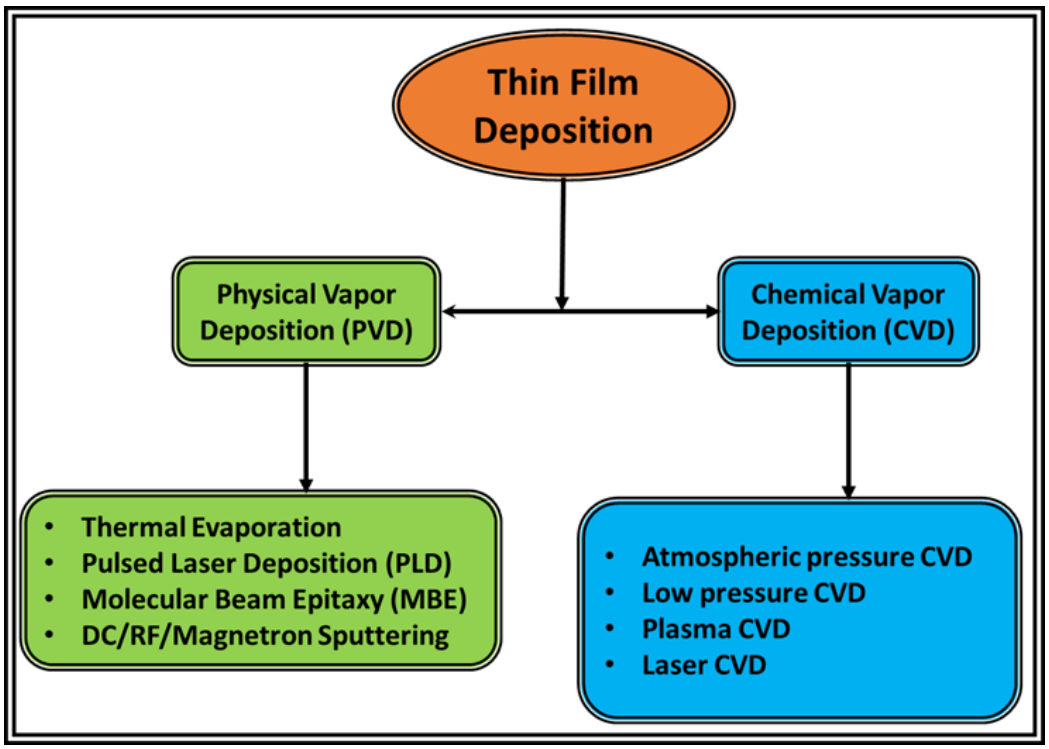

Figure 2.3: Schematic of different processes of thin-film deposition

2.3.1 Chemical Vapor Deposition Methods

Chemical vapor deposition (CVD) is one of the most common technique used to coat metallic or ceramic compound which includes elements, metals and their alloys and intermetallic compounds. In this process, volatile compounds react chemically with other gasses and produce a non-volatile solid that deposits atomically on suitable substrate. The CVD technique employ various chemical reactions such as oxidation, reduction and hydrolysis and pyrolysis etc. and emerged as one of the powerful techniques for thin film growth. CVD has application for the production of variety of films with varying stoichiometry, purity and other desirable properties **[18]**. Material with wide range of

physical, and chemical properties can be grown with the varying experimental conditions in CVD i.e. substrate material, substrate temperature, gas mixture and its pressure etc. CVD is a low cost deposition technique and involves low operating expenses which makes it a suitable technique for large scale production of thin film devices.

There are many variants of CVD that includes low pressure CVD (LPCVD), atmospheric pressure CVD (APCVD), plasma enhanced CVD (PECVD), laser enhanced CVD (LECVD) and metal organic CVD (MOCVD) **[19–21]**. Out of all variants MOCVD has come with considerable importance for the deposition of epitaxial semiconductor thin films. This technique has been utilized to grow different compositions of thin CMR manganite films **[22]**. MOCVD plays an important role for large scale production of oxide thin films as well as depositing decorated complex organic molecules on a desired material. Lange et al. **[23]**, have described thorough reviews of the MOCVD process, precursors and specific details in reference to ferroelectric materials.

CVD technique has characteristic feature of its exceptional throwing power which enables large scale coatings of uniform thickness and low porosity, CVD is also capable of localized and selective depositions on patterned substrates. CVD has variety of applications in dielectrics, conductive oxides passivation layers, corrosion resistance coatings, heat resistance coatings and epitaxial layers for microelectronics **[19]**. This technique also finds application in preparation of high temperature materials, solar cells, high temperature fibre composites etc. Recently, this technique is exceptionally used for the production of high temperature superconductors and carbon nanotubes **[24]**. Another advantage of CVD technique is that oxygen activity in vapor can be easily and precisely controlled therefore, post deposition annealing in oxygen environment is not required to achieve optimum oxygen stoichiometry. CVD technique allows uniform distribution of deposited film over a large area without compositional gradient across the substrate.

2.3.2 Physical Vapor Deposition (PVD)

PVD involves atom by atom transfer of material on suitable substrate at desired temperature by undergoing transfer of atoms from solid phase to vapor phase then back to solid phase. The PVD technique takes place under vacuum and a controlled atmosphere. This allows controllable high-purity film deposition from high-purity source material. ***Thermal evaporation*** is one of the oldest PVD methods widely employed for thin film deposition. In this process material to be coated is thermally vaporized then moved to the desired substrate by means of potential applied to the substrate. Thermal evaporation under vacuum conditions reduces the evaporation temperature as well as reduces the amount of impurities. Here, thermal energy is provided to the source material in a vacuum chamber evacuated below ~10^{-5} torr then evaporated particles condense on the **[25]**. In this process, resistive heating through filament or boat is commonly used for deposition of film. Electron beam deposition is employed for refractory metals due to their high melting point. Recently, laser beam evaporation is introduced in thermal evaporation. The laser source is kept outside of the evaporation system and beam penetrates through a window and focused on fine powdered evaporate material **[26]**.

Pulsed laser deposition (PLD) is one of the refined PVD techniques employed for controlled compositional deposition of variety of materials. In this method the source (deposit) material is irradiated by a high pulse laser ~ 1J/shot through a quartz window. Generally, KrF (248 nm) **[27]**, ArF (193 nm) **[27]** and Nd-YAG (266 or 355 nm) **[28]** are the commonly used laser sources for deposition of manganite thin films. The target material is heated in a confined manner to its melting point using highly energetic laser beam and the molecules/atoms evaporated from the target surface. These molecular/atomic species are transported on a suitable substrate to form a thin film **[29]**. The laser pulse also provides photo-electrons from target to form plume in between target and substrate. The desired

deposition rate and structural quality of deposited film can be obtained by optimizing various process parameters such as base vacuum level, background gas pressure, ablation energy, distance between target and substrate and temperature of substrate etc. PLD technique has advantage of direct monitoring cell by cell growth by reflective high energy electron diffraction (RHEED) pattern **[30]**. A major drawback of this otherwise excellent technique is the small are uniform deposition and ejection of small particulates from target during deposition.

Molecular Beam Epitaxy (MBE) is another most reliable deposition technique among various evaporative methods **[20]**. It is highly controlled process and can provide extraordinarily high quality thin films ideally required for research purpose and have potential for best possible device fabrication. However, slow growth rate in comparison to other techniques makes it limited for production of devices. Here, the deposition is precisely controlled at atomic level in ultra-high vacuum environment and widely used for deposition of the highest quality thin film of elemental and compound semiconductors (GaAs, AlGaAs and related structures), all oxide superlattices and 2DEGs. The MBE consist of three major compartments, viz., growth, analysis, and sample chamber. The substrate is placed in ultra-high vacuum chamber and sputtered with low energy ion beam for short time to clean the surface This step is followed by substrate preparation by high temperature annealing (to relax any damage to the growth surface during cleaning) and then gradually cooled to the desired growth temperature. After this growth commences by directing atomic beams of film material and dopant material (if required) towards the substrate. The film composition can be properly selected by accurate control of atomic ratio of each metallic electron beam sources. O'Donnell et al. have used MBE to prepare very high quality epitaxial manganite thin films and investigated anisotropic magneto-transport **[31]**. Another reliable and the most widely used (even at industrial level) PVD

technique for deposition of good quality thin film is ***sputtering*** which has been used for thin film deposition in the present work. The detailed description of sputtering is discussed in subsequent sections.

2.3.2.1 Sputtering

When target of the material which is to be deposited is bombarded with highly energetic gaseous species like ions, momentum transfer to the surface atoms takes place and consequently they are ejected out of the surface. This process is called sputtering. The ejected atoms are accelerated towards a substrate surface electrically and then condensed to form a thin film **[5,32]**. The sputter yield is an important parameter to characterize sputtering is the ratio of the number of emitted particles and the number of incident particles:

$$S = \frac{\text{number of particles emmited}}{\text{number of particles incident}}$$

Sputtering virtually occurs with various incident species e.g., like atoms, ions, electrons, neutrons, photons, as well as inert gas ions Kr^+ and Ar^+, or other smaller molecular ions like N^{2+} and O^{2+} and so on. Sputtering yield depends on energy and angle of incident particles, target material and its crystal structure. A schematic of the generally observed variation of the sputtering yield with incident ion energy is depicted in **Fig 2.4**. There exist a threshold energy for the occurrence of sputtering phenomenon and it is typically 20 ~ 30 eV for most of metallic targets. Above threshold value sputtering yield 'S' follows direct dependence to the √E up to the ion energy of E ~ 100 eV. In between 100 eV and few k eV ion energy the 'S' follows direct dependence on the incident ion energy E **[5]**.

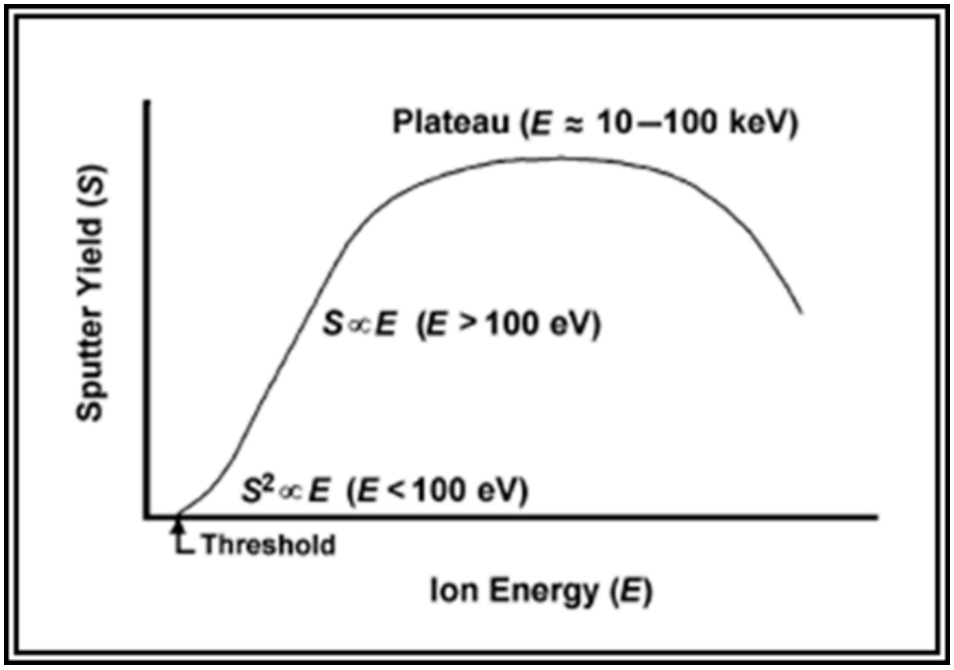

Figure 2.4: Variations of sputter yield with incident ion energy [5]

Here, the number of sputtered atoms are proportional to the incident atoms. As energy is increased further i.e. above 10eV, the incident ions penetrate the surface and reduces the sputtering yield. Therefore, the sputter yield decreases for high energy ions as energy is dissipated deep inside the target. Different models has been proposed for the collision mechanisms in sputtering process. The "elastic-collision theory" was the earliest, where it was assumed that the energy transfer is maximum in the first collision only. The second called "linear cascade collision theory" based on the ground breaking work of Sigmund, Thomson, and Wehner **[33–36]** assumed that the cascades of atomic collisions are responsible for sputtering of target by energetic particles **[33]**. Currently it is the most widely accepted theory for the understanding of sputtering in the keV range of the incident energy **[33]**.

Sputter yield shows angle dependence as well as target material dependence. The metals such as Gold, Silver, Copper and Platinum, having high sputtering yield, shows very

small angle dependence. In contract low yield materials like Iron, Tantalum, etc. show very pronounced angle dependence. The yield maximizes at angles between 60° and 80° and then it decreases rapidly for larger angles. Wehner et al proposed that the sputtered atoms are ejected along the close-packed atoms near threshold; as in in fcc Ag, the sputtering yield is maximum along close-packed direction which corresponds to ⟨110⟩. He also suggested that surface structure of target also influence the angle dependent sputtering **[34,35]**.

In sputtering, the whole target acts like a source and this suggests a higher coverage area for the erosion of surface and further deposition of film as compared to other deposition techniques. The ejected atoms strike the surface of the substrate and undergo kinetics changes to rearrange and subsequently condense on the substrate to form thin film. A better adhesion of sputtered particles to the substrate as a result of high kinetic energy of sputtered particles leads to the deposition of highly uniform and dense thin film over large surface area. The higher melting point elements/targets can also be used for sputtering by incorporating target cooling provision in sputtering. Different classes of sputtering are discussed in next section.

2.3.2.2 DC or RF Sputtering

Depending on the power supply, the sputtering process may be classified as DC or RF sputtering. **Fig. 2.5** shows the schematic of RF/DC sputtering system. The process gas will breakdown into a spatially uniform plasma discharge under the adequate conditions of voltage and gas pressure and will form a dark space or sheath near the cathode where electric field is very large. The ions in plasma are accelerated rapidly to strike the cathode and ejects energetic particles (secondary electrons) from the surface. These energetic particles are accelerated back and gain significant energy to form more particles for sustaining the discharge. The ejected particles are then accelerated to the anode or substrate to deposit in the form of thin film. This process is called as *dc sputtering*. Historically,

sputtering was first used to erode the surface and then sputter deposition of thin film. At higher voltages there is increase of energy of incident ions which in turn decreases the sputtering rate. In addition, dc sputtering phenomena fails if the cathode surface is insulating. This is typically the case of insulating target or a case of oxygen ambience which makes the surface insulating which results in extremely low discharge currents and low sputtering. This technique is mainly confined for metal depositions.

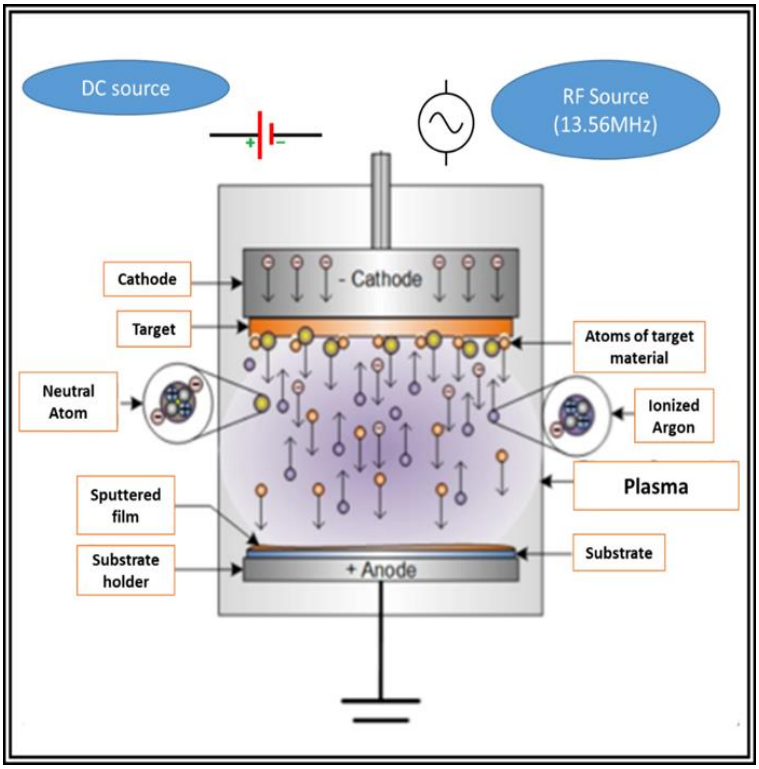

Figure 2.5: The schematic diagram of RF and DC sputtering system.

For insulating surfaces the charge localizes as the ions strike the surface and with passage of time a sheath of positive charge builds up on the target surface, making it difficult for further sputtering. This sheath of positive charges can be prevented by bombarding of positive ions and electrons simultaneously to the insulator which is generally achieved by applying a RF potential to the target. The alternating filed of RF potential provide sufficient energy to the electrons to cause ionizing collisions and results

in a self-sustained discharge. More number of electrons will reach the insulating target surface due to higher electron mobility during the positive half cycle. As the target becomes self-biased negatively due to RF power supply, it repels the electrons from the neighbourhood of the target material and forms a enriched sheath of positive ions in front the target surface which further supports the sputtering. Typically, 13.56 MHz (**I**ndustrial, **S**cientific and **M**edical frequency band) is the most general frequency used for RF-sputtering. Such systems require an impedance matching network between the power supply and sputtering chamber. This network provides an optimal matching of the load to the RF generator in order to deliver sufficient power to the sputtering chamber **[37–39].**

2.3.2.3 Magnetron Sputtering

Schematic of magnetron sputtering is shown in **Fig 2.6**. The crossed electric field and magnetic field, $\overrightarrow{E} \times \overrightarrow{B}$, confines the electrons and increase the sputter yield. In the presence of a magnetic field effective path length of electrons is increased as they trace helical paths This results in more ionizing collisions between them and the neutral gaseous species close to target surface **[40]**. The collision between the helical electrons and neutral gas species, which is mostly Argon, leads to the creation of ionic species. This results in a higher deposition rate. The ejected atoms are mostly neutral and much heavier. Due to this they are not affected by the magnetic trap and a sustained plasma even at a lower gas (Ar) pressure is achieved.

RF magnetron sputtering facilitate the use of an insulator oxide as a target material in a more efficient manner. The sputtering gas pressure controls the growth and nature of the oxide materials **[41].** In is interesting to note that one of the major issues that leads to morphological changes such as formation of pits, ripples, cones and craters on the film surfaces is the re-sputtering of the layer by negative ions and reflected neutrals [**42,43]**. The

use of off axis geometry and higher pressures are able to tackle the problem of re-sputtering to fairly good extent.

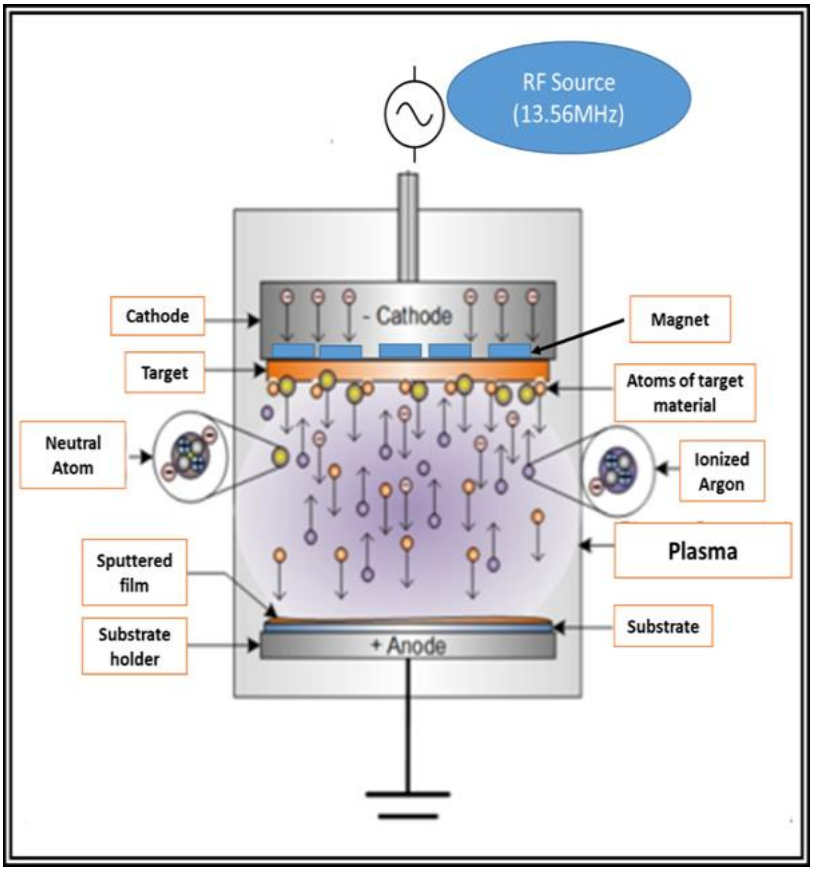

Figure 2.6: Magnetron sputtering set up schematic.

In the growth of oxide thin films by sputtering of oxide targets the major issues needing proper attention are (i) chemical composition control, (ii) epitaxial nature, (iii) selection of suitable substrates, and (iv) oxygen stoichiometry control during the deposition etc, **[44]**. Studies shows that films with good structural quality and composition control within an accuracy of 0.1% can be grown under reasonably controlled and optimized deposition conditions, particularly temperature, oxygen pressure, substrate-target distance and periodically cleaning/polishing of the sputtering target, etc. **[45–47].** Method adopted for the thin film deposition in the present investigation

The deposition of all the LPCMO thin films on differently oriented STO substrates has been carried out employing RF magnetron sputtering. Prior to the film deposition processes, a two inch diameter *target* (as per the shape of the cathode) was prepared. Targets was then mounted on a water-cooled backing plate which also acts as cathode. Water is circulated to overcome the heating effects of input power. In the present study, solid state route has been employed for the preparation of $La_{1-x-y}Pr_yCa_xMnO_3$ (LPCMO) target for thin film deposition. The detail of target preparation and film deposition are discussed in later sections.

2.3.3 Target Preparation by Solid State Route

Solid state reaction method, which is a direct reaction of mixture of solids used as a starting material, is one of the more common of the techniques employed for the synthesis of polycrystalline solids **[6,48]**. Heat treatment at higher temperatures for long duration is done to achieve high quality bulk. Typically a temperature of 1200 – 1400 °C has been found to be reasonably good for a target. During the high temperature and high duration heat treatment the atoms diffuse in between grains/particles to form a stable compound of minimum free energy. The ultimate quality depends on temperature, pressure or the composition of the gas atmosphere. The conditions of solid state reaction route plays a crucial role to prepare a single-phase sample. The different $La_{1-x-y}Pr_yCa_xMnO_3$ (LPCMO) targets have been prepared by pursuing the following the protocol enlisted below.

- High purity (99.9% or better) powders of oxides/carbonates, viz., La_2O_3, Pr_2O_3, $CaCO_3$, and MnO_2 have been used the raw materials.
- Powders were weighed in desired stoichiometry and mixed thoroughly using pestle-mortar. Care must be taken to avoid any contamination during mixing, especially any magnetic impurity.

- Homogeneous powder is calcined at 900 ºC for 24 hours in air to facilitate thermal decomposition to liberate the CO_2 and other undesirable gaseous entities.
- The calcined powder is again mixed/grind thoroughly and then further heated at 1000 ºC for 24 hours in air. This heating facilitates beginning of the phase formation. High temperature facilitate the diffusion of constituents to enable their reaction with each other and also reduces the diffusion requirements and shrinkage that occur during final sintering and densification stage.
- Using a die and hydraulic press powder was pressed in the form of disc of ~2″ diameter and ~3 mm thickness.
- Finally, ~2″ disc was sintered at 1200 °C for 24 hrs. This process yields a phase pure LPCMO with reasonably good grain size. We have used higher sintering temperatures also but the film composition and film quality remains unaffected for the targets sintered at 1400 °C.

The solid state reaction method is most suitable for depositing reproducible thin films of CMR manganites. Pictures of target (LPCMO) before deposition and after deposition shown in **Fig 2.7**

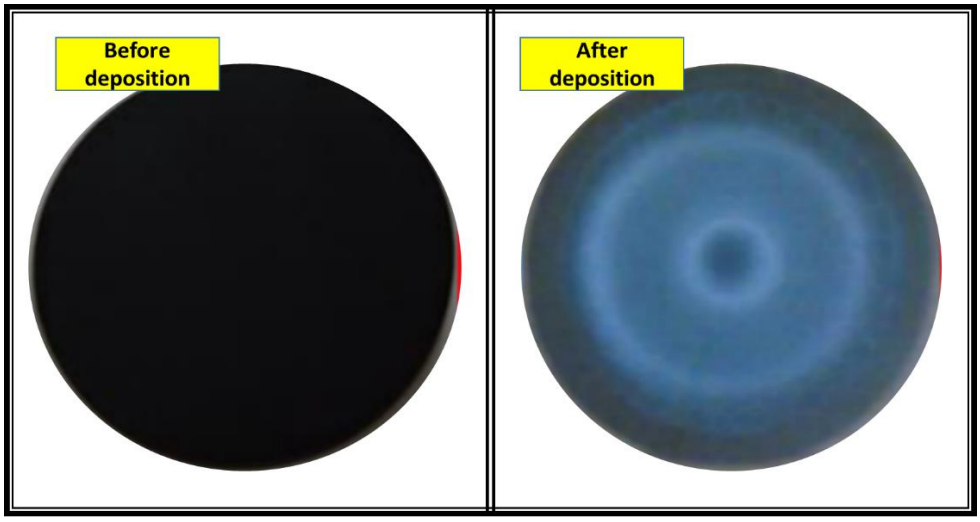

Figure 2.7: LPCMO target before deposition and after deposition

2.3.4 Thin Film Preparation Procedure

The magnetron sputtering system used for the deposition of LPCMO thin films in the present study is shown in **Fig. 2.8**.

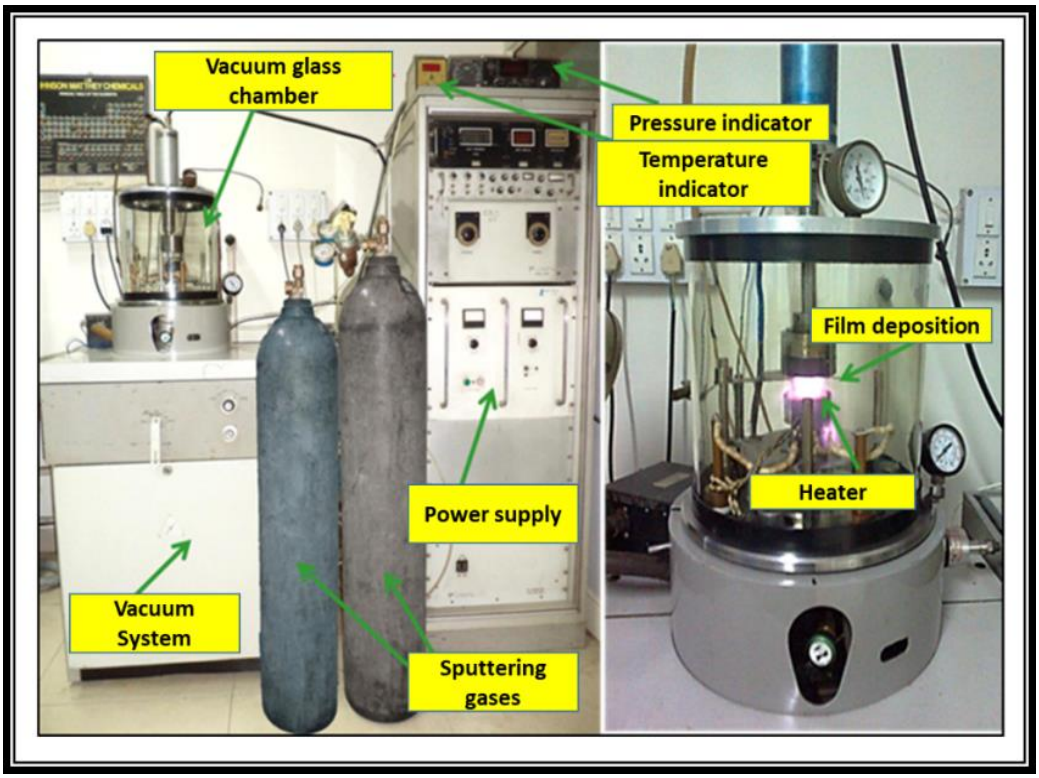

Figure 2.8: The Magnetron Sputtering system which is used in the present investigation.

The procedure used for thin film preparation in the present study is described in the following.

- The target is placed on the cathode and mounted properly in the chamber. The substrates are cleaned and placed over heater.
- The sputtering chamber is evacuated using the rotary pump. Sidewise, the diffusion pump is turned on bring it into optimum condition to carry out further evacuation of the chamber. These processes roughly take more than two hours to attain pressure ~ $5x10^{-6}$ torr.

- During the evacuation process, the heater is heated to desired temperature (~ 750 °C – 870 °C) through pre-set program (temperature and time) using proportional–integral–derivative (PID) controller (temperature controller).
- The chamber is flushed twice during the evacuation with premixed gas mixture consisting of Argon ~ 80 % and Oxygen ~ 20 %. This gas mixture is also used during the sputtering.
- Once desired temperature is reached, the Argon ~ 80 % and Oxygen ~ 20 % mixture is put into vacuum chamber and a dynamic pressure of ~200 mTorr is maintained throughout the deposition.
- Then the RF power (Incident power ~100-150 watt, reflected power ~5 watt or lower) to the cathode is applied and the parameters such as incident power and reflected power are adjusted to maintain the self-sustain plasma.
- After the plasma formation a pre-deposition sputtering of target was done for ~10 minutes and the shutter is removed from the substrate. The f film gets deposited on the plasma exposed surface of the substrate. The deposition continues to the optimized time to obtain the desired thickness of film under the given set of experimental conditions.
- After the deposition, the film is kept at ~ 900 °C and 0.6 torr oxygen pressure for optimized time to get optimum oxygen content in thin film then cooled to room temperature slowly.

The $La_{1-x-y}Pr_yCa_xMnO_3$ thin films were deposited on differently oriented single [(001) and (110)] crystalline $SrTiO_3$ (STO) substrates. Various techniques used for the structural, electrical and magnetic characterization in the present study have been discussed below in detail.

2.4 Characterization of Thin Films

2.4.1 Energy Dispersive X-Ray Spectroscopy (EDS)

Energy Dispersive X-Ray Spectroscopy (EDS or EDX) is a chemical microanalysis technique based on the principle of detection of X-rays by after the sample under investigation is attacked by an energetic stream of electrons. Scanning/Transmission Electron Microscopy systems incorporate this analytical technique. The electrons from higher energy states fill the electronic vacancies left by the ejected electrons due to bombardment thus emitting a *characteristic x-radiation*. The interaction between the host nucleus and the impinging electrons give rise to lower energy continuous x-rays **[49].**

A solid state detector based on the Lithium-drifted silicon detects the relative affluence of the x-rays thus emitted and analyses as a function of the energy. The detector is based on the principle of generation of a charge pulse commensurate to the individual energies as the characteristic x-rays strike the detector. A charge-sensitive preamplifier transforms into a voltage pulse. From this voltage the energy is computed and fed to a PC for display and further data evaluation, which is evaluated to determine the elemental composition. The EDS spectrum appears in the form of a plot on which x-axis representing x-ray energy (usually in channels 10 or 20 eV wide) and the y-axis representing the number of counts per channel. An EDS spectrum plot also distinguishes the type of x-ray (K-α, K-β) (**Fig. 2.9**).

EDS uses the comparison method in which x-ray energies from the specimen under study are compared with known characteristic/standard x-ray energy values. In genera the EDS detection limit ranges from the atomic number Z=4 (Be) to Z=92 (U). The minimum detection limits vary from approximately 0.1 to a few atom percent, depending on the element and the sample matrix **[50].**

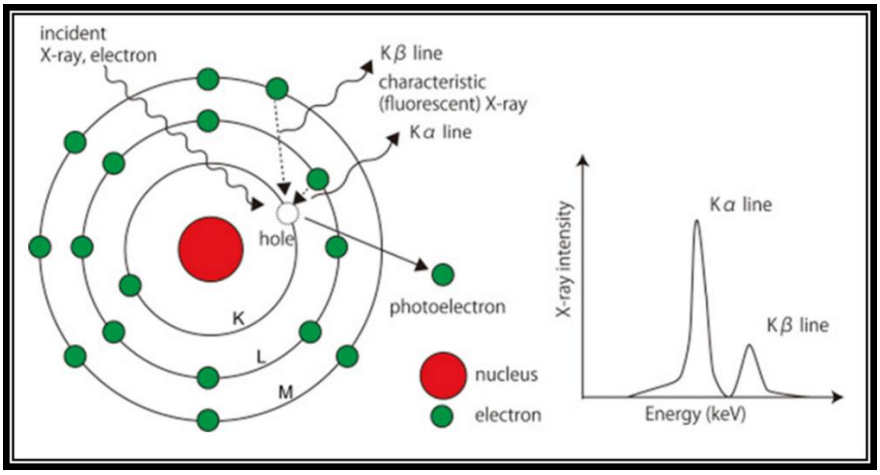

Figure 2.9: Schematic for atomic shell showing the generation of characteristic x-rays

In the present study the energy dispersive spectroscopy has been done using ***Carl Zeiss supra 40VP*** SEM and a typical EDS spectrum of the LPCMO on STO substrate is shown in Fig. 10.

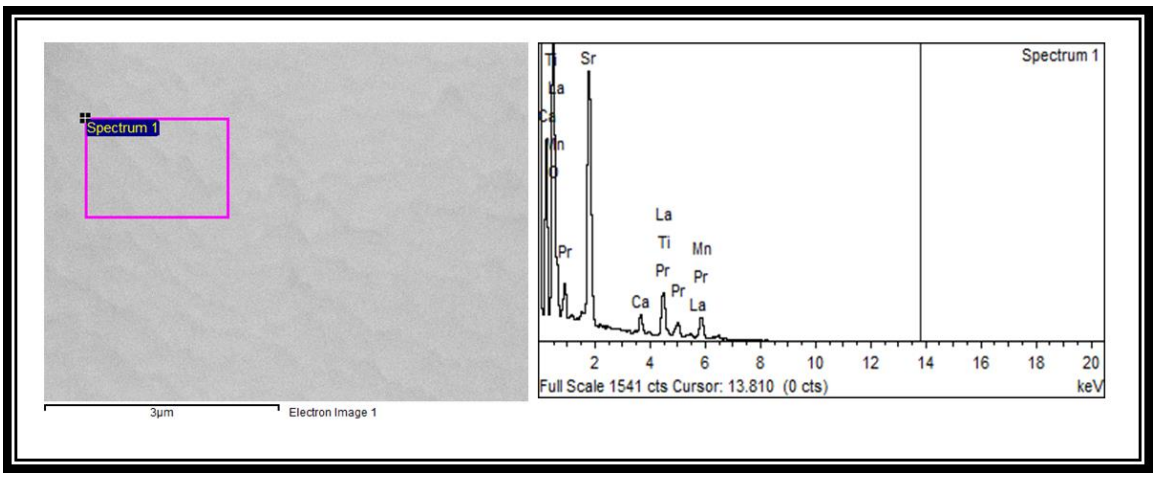

Figure 2.10: A representative EDS spectrum of the LPCMO on STO substrate.

2.4.2 Scanning Probe Microscopy (SPM)

In Scanning probe microscopy (SPM), a physical probe scans the surface of the specimen to image. It has two types (i) Scanning Tunneling Microscope (STM) and (ii) Atomic Force Microscope (AFM*). STM was developed in 1981, and was limited for the

imaging of electrically conductive surfaces at the atomic level. Later in 1986, Binnig and Quate employed an ultra-sharp tip placed at end of a cantilever [**51]** to investigate the surface of non-conductive materials. This technique is referred to as "**Atomic Force Microscope (AFM*)**". In AFM* the sharp tip scanning the surface can be moved in X-, Y-, and Z- directions by piezoelectric scanner and feedback loop controls the distance between tip and the surface. The data thus acquired is analyzed by a PC to to get the map of the surface. This characterization tool is extremely useful in surface analysis by measuring roughness, size, thickness, local friction, surface forces, and local elasticity profiles **[52].**

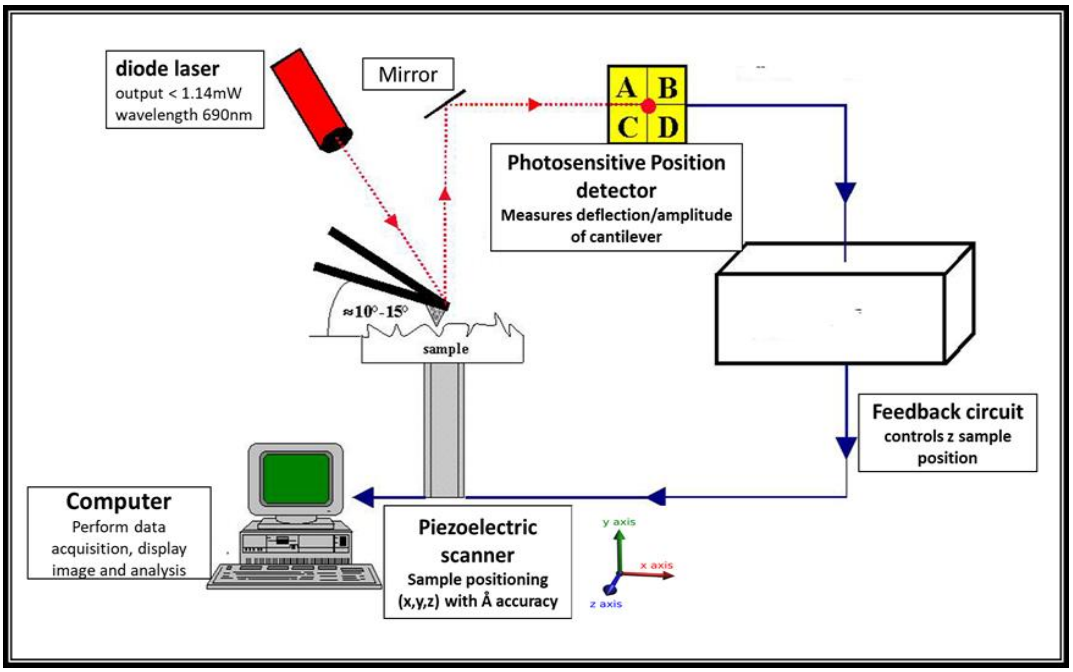

Figure 2.11: Schematic of the basic principle of AFM*

The tip surface interaction is described by Lenard-Jones potential [53] given by

$$\mathbf{V(r) = 4\,\varepsilon \left[\left(\frac{\sigma}{r}\right)^{12} - \left(\frac{\sigma}{r}\right)^{6}\right]} \qquad \mathbf{(2.1)}$$

where, ε is potential well depth , σ is the atomic diameter and r is the interatomic distance. The term ~ $1/r^6$ approximates the **i**nteraction between the cantilever's outermost atom and surface atoms for large interatomic distance r. At smaller r, electron shells of atoms overlap giving rise to repulsive exchange and electrostatic interaction given by the term ~ $1/r^{12}$. The variation of the typical force with the tip-sample distance is shown in **Fig. 2.12**.

AFM* has three operational modes (i) contact Mode, (ii) tapping/intermittent mode and (iii) non-contact mode. All these imaging modes are classified in terms of the tip/sample distance as shown in **Fig 2.12.**

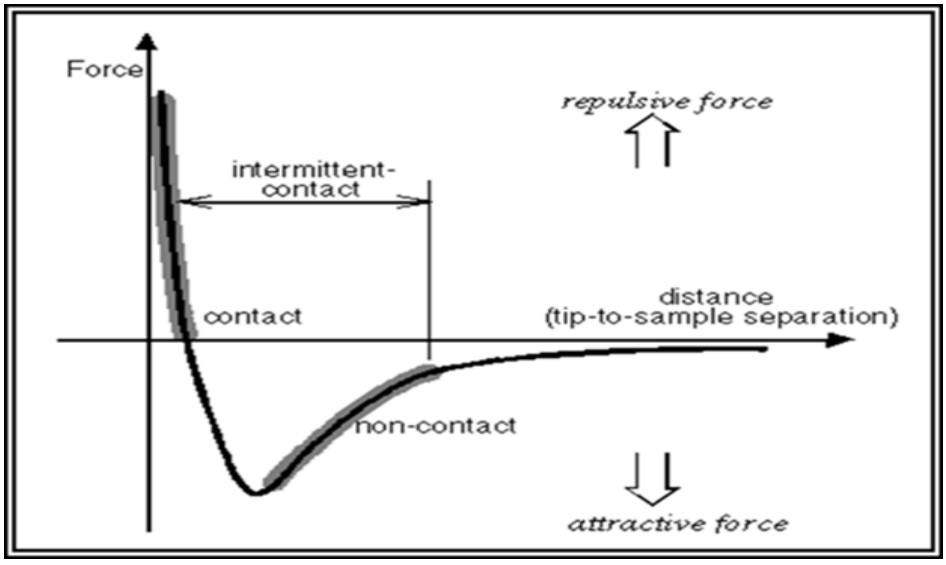

Figure 2.12. The schematic of the variation of the force as function of the tip/sample distance and different AFM* modes [53]

In **contact mode**, which works in the repulsive region, the tip apex is in close proximity of surface, and the tip sample forces are counter balanced by the elastic force due to the deflected cantilever in accordance with Hooke's law. Contact mode cantilevers have relatively low stiffness which makes them high sensitive for measurement. This mode permits high scan speed for imaging and is the only AFM* mode to obtain atomic resolution. However, lateral (shear) forces in contact mode can distort surface features in

the image and can reduced spatial resolution of soft surfaces like biological samples, polymers etc. The ***Tapping/ intermittent mode*** works in attractive region where the cantilever is oscillated at or slightly below its resonance frequency with an amplitude ranging typically from 20 nm to 100 nm. In this mode the tip frequency is used for acquiring topograpical information. This mode has higher lateral resolution and lateral forces in this mode are almost eliminated, so there is no scraping. However, one of the drawbacks that this mode has is the slower scan speed as compared to contact mode. In the third mode, viz., the ***non-contact mode***, which too works in the attractive region, the cantilever is oscillated at a frequency which is slightly above the cantilever's resonance frequency with an amplitude of a few nanometers (< 10 nm). This mode has relatively lower lateral resolution and slower scan speed than tapping mode/intermittent mode and contact mode. Non-contact mode usually preferred for extremely hydrophobic samples with very thin layer of adsorbed fluid. The surface characterization of presently studied LPCMO thin films was done by employing the VEECO Multimode V (**Fig. 2.13).**

Figure 2.13: Atomic force Microscope (Multimode V, Veeco Instruments)

2.4.3 X-Ray Diffraction (XRD)

X-ray diffraction (XRD) is the most widely and frequently used crystallographic techniques to determine structure and properties of materials ranging from metals, semiconductors to highly complex biological and medicinal molecules. To get the detailed information of structural phase of thin film, certain modifications to diffractometer used for bulk is needed **[54,55].** The excellent resolution of the X-rays is attributed to their charge less nature and the fact that they have wavelengths of the order of interatomic distances in crystalline solids. Each crystalline solid has a unique crystalline structure (differentiated in terms of the nature of the unit cell, space group, etc.) and hence each of them has distinct XRD pattern. Hence XRD is considered as the 'fingerprints' for materials structural phase identification.

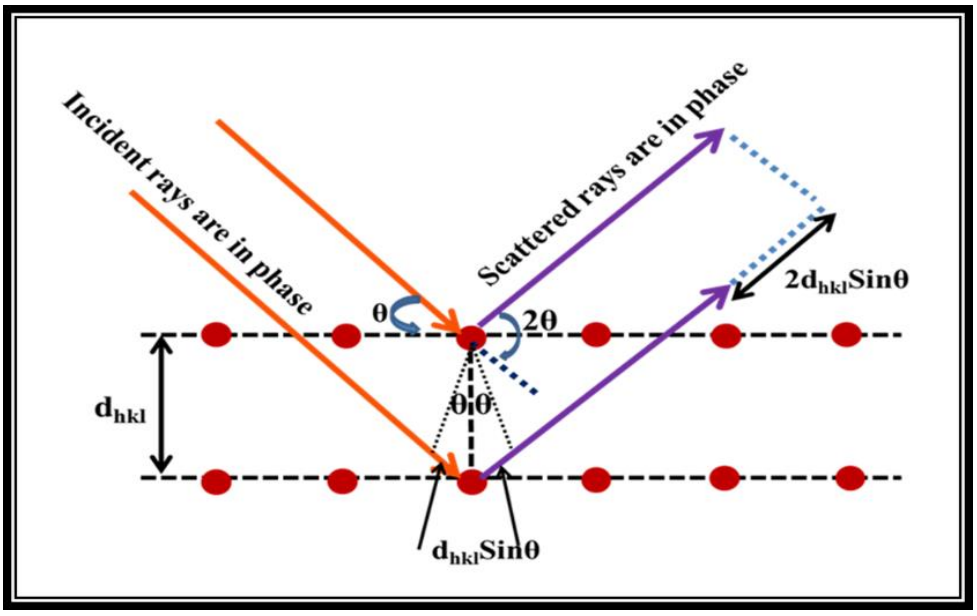

Figure 2.14: Schematic of of X-rays diffraction by crystallographic plane (Bragg's Law).

The basic theoretical frame work of XRD is the Bragg law, which provides the basic relationship among the interplaner spacing (d_{hkl}), the X-ray the wavelength (λ) and the

angle (θ) of incidence (shown in **Fig 2.14**). In a diffraction experiment for constructive Bragg's law is given by the equation:

$$\mathbf{n\lambda = 2d_{hkl} \sin\theta} \qquad \mathbf{(2.2)}$$

Here, 'n' denotes the order of diffraction, λ is the wavelength of the X-rays, d_{hkl} is the inter planar spacing and θ is the angle between the incoming X-ray and the atom layer. The detail of the basics of X-ray crystallography are discussed in several standard books and reviews **[56–60].**

The θ–2θ scan in which the angle between X-ray and sample plane is varied up to θ and simultaneously the detector is moved up to 2θ is used to determine crystal structure, symmetry and phase purity. The θ–2θ scan of a polycrystalline sample results in numbers of possible diffracted peak at angles where the Bragg's law is satisfied. The θ–2θ scan of single crystalline sample also results in numbers of peak but of higher intensity as compared to the polycrystalline sample. In epitaxial/single crystalline/oriented thin films, θ–2θ scan results in only few diffraction peaks depending on the plane orientation of the substrate. The high intensity peak in epitaxial thin film results from the substrate and along with it low intensity peak correspond to the thin film of same orientation. Using the Bragg law it is possible to calculate the length of the out–of–plane lattice parameter for the different layers.

High Resolution X-Ray Diffractometer (HRXRD) employs high quality X-ray sources, in conjunction with the highly efficient optoelectronics and hence yields the desired resolution needed to characterize epitaxial thin films and single crystals. HRXRD enables characterization of not only structure but various types of crystal defects, non-localized deformations, and the relationship between the substrate and overlaying thin film, etc.. Hence, information regarding macroscopic defects like mismatch, curvature,

inhomogeneity, relaxation, dislocation density, misorientation, mosaic spread, surface damage, etc. is easily retrieved. Different types of scans used for the structural analysis of the specimen are summarized below and shown in **Fig 2.15**.

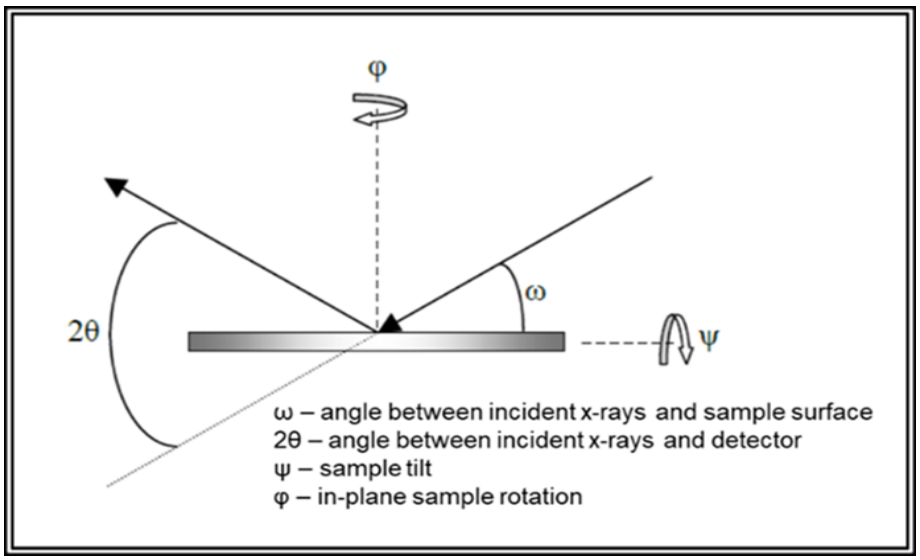

Figure 2.15: Schematic diagram depicting – θ, ψ and φ angles in HRXRD characterization

- **Lattice constants and ω-2θ scan:** Employing this mode information relating to the relative crystal orientation of the thin film and the substrate, lattice parameter and film thickness is obtained. The sharpest and intense peak belongs to the substrate and another low intensity sister peak belongs to the deposited film. Using Bragg's law the lattice parameters of substrate and film can be calculated and gives information about composition and strain or relaxation of film.
- **Rocking curve or ω-scan:** This mode yield information about the crystalline texture or mosaicity of thin films. The broadening of the rocking curve is generally attributed to the presence of strain, dislocation density, mosaic spread and curvature.

- **Texture measurements φ- scan:** This mode is used to unravel the orientation relationship between the film and the substrate and nature of the growth. Oblique planes of layer and substrate were commonly used to determine in-plane orientation. The texture measurements are performed on thin films at a fixed scattering angle and consist of a series of φ–scans (in-plane rotation around the centre of the sample) at different chi-angles (ψ).
- **X-ray reflectivity (XRR)** technique is used to characterize multilayer structures to determine the thickness, roughness and density of the crystalline as well as amorphous film. It is a non-destructive and non-contact technique used for thickness determination between 2-200 nm with a precision of about 1-3 Å. In addition, density and roughness of films and multilayers with a high precision can also be determined by XRR. It involves monitoring the intensity of the x-ray beam reflected by a sample at grazing angles.

In present thesis, the structural characterization of LPCMO thin films has been done by using high-resolution X-ray diffraction (HRXRD, PANalytical PRO X'PERT MRD (Shown in **Fig. 2.16**, Cu-Kα1 radiation λ = 1.5406 Å) to record the X-ray reflectivity (XRR), 2θ/ω scan and ω-scan.

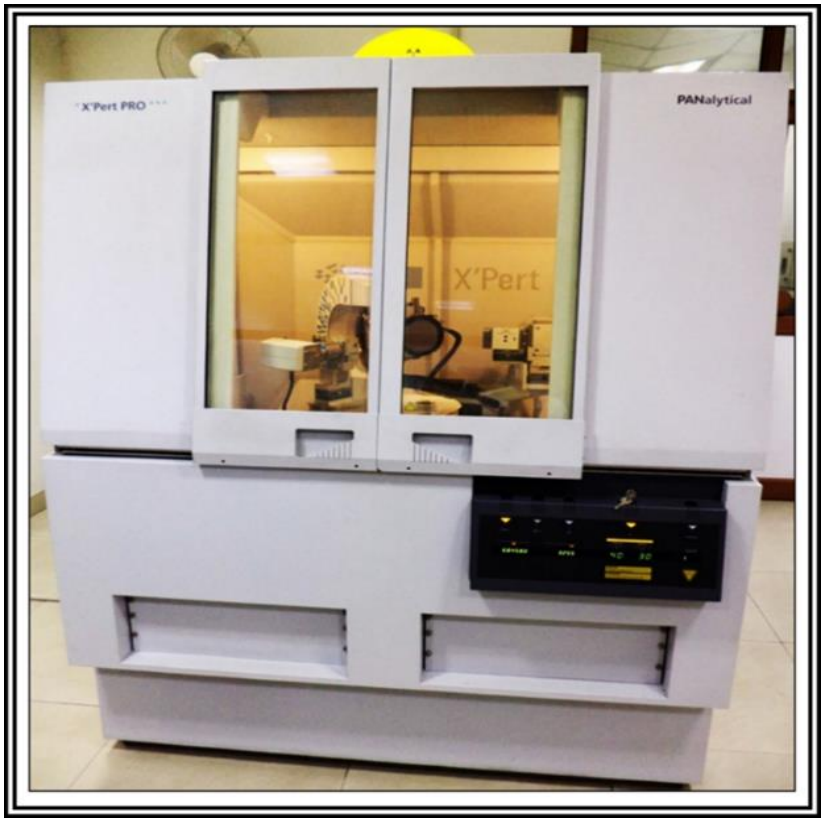

Figure 2.16: The typical HRXRD system employed in the present investigation.

2.4.4 Magnetic Property Measurement System (MPMS)

Generally, Vibrating Sample Magnetometer (VSM) is employed for the magnetic characterization of bulk magnetic materials with resolution of the order of 10^{-4} ~ 10^{-6} emu/gm. However, such instrument is not capable of measuring magnetic moment of the order of ~ 10^{-7} emu/gm or more, which is the typically observed in low dimensional system such as magnetic thin films. Since, thin films have small volume fraction available for the analysis therefore, it is difficult to have magnetic characterization as there will be appreciable contribution of the substrate in measurement. A Superconducting Quantum Interference Device (SQUID) magnetometer achieves the highest precision magnetic moment measurements. The magnetic measurements (temperature and field dependent magnetization) of the films in present thesis were performed by using magnetic property measurement system (MPMS-Quantum Design) having SQUID magnetometer with the

provision of temperature (1.8–400 K) and field (0–7 T) variation. The typical MPMS system used in present investigation is presented in **Fig. 2.17.**

Figure 2.17: The Quantum Design (USA) Magnetic Property Measurement System (MPMS-7T).

In the SQUID magnetometer (refereed to magnetic property measurement systems, MPMS), the heart of the system like the superconducting magnet and the SQUID are at generally 4.2 K and the temperature can be lowered down to 2 K. Superconducting magnet is used for high field magnetic fields is in the form of a superconducting closed loop which is charged with up to specific current value then operate in persistent mode during measurement without any external current source or power supply. Thus liquid Helium is used to cool down the system (ever cool variants with closed cycle refrigerators are also available). The SQUID measures changes in the magnetic flux as sample moves through the superconducting detection coil thereby, make it a very sensitive magnetometer. It is configured to detect the magnetic moment of material, especially, thin films, which

determines the magnetization and magnetic susceptibility of that material. MPMS can measure the magnetic moment with the range of sensitivity from 10^{-8} emu to 2 emu in standard configuration and over 300 emu with extended range option. The main reason for the high sensitivity of a MPMS is the fact the SQUID is very sensitive for measuring weak magnetic fields as low as 10^{-18} T. It consists of superconducting loop containing one or more Josephson junctions made of two pieces of superconductors separated by a thin barrier layer as shown in **Fig. 2.18 (a)**. SQUIDs are of two type; (1) rf-SQUID, consisting of one Josephson junction and (2) dc- SQUID, consisting of two or more Josephson junctions. Pure niobium or lead alloys are used in low temperature SQUIDS **[61–63]**.

The SQUID is connected with superconducting detection coil through superconducting wires. The detection coil consists of a single piece of superconducting wire looped in a set of three coil configuration like second order gradiometer. In this configuration the upper coil is single turn loop in clockwise direction, the centre coil comprises of two turn loops counter clockwise direction and bottom coil is again single turn loop clockwise direction as shown in **Fig. 2.18(b).**

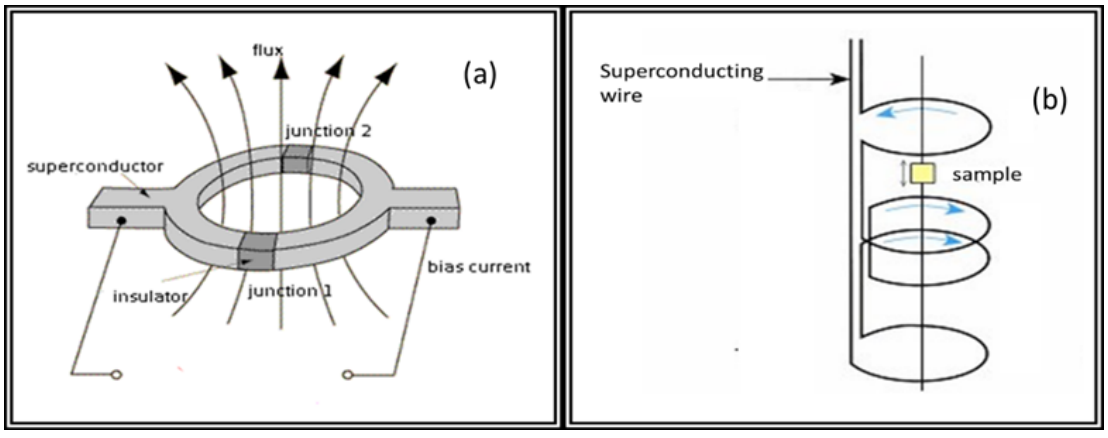

Figure 2.18: Schematic of (a) Superconducting QUantum Interference Device (SQUID and (b) Second order gradiometer configuration of detection coil in MPMS

For magnetization measurements the sample mounted on sample holder attached to is inserted in specially designed chamber. Sample is moved in series of discrete steps through detection coil using stepper motor attached to the sample rod. Flux with in the detection coil changes with the change in sample position thereby changing the current in superconducting circuit. During the measurement sample is stopped at number of positions and at each stop several readings of SQUID voltage are recorded and averaged to improve signal-to-noise ratio. The sample must be much smaller than the detection coil so that its motion in between gradiometer is observable to measure the change of flux **[61]**. There are two principal magnetic measurements using SQUID magnetometer: (1) Magnetization as function of applied field (M–H) (2) Magnetization as function of temperature (M–T).

2.4.5 Physical Property Measurement System (PPMS)

The physical property measurement system (PPMS) is an automated low-temperature and magnet system that offers a wide range of magnetic, electrical and thermal measurement capabilities to understand material properties as function of temperature and magnetic field. It gives the information of material properties like specific heat, magnetic AC and DC susceptibility and both electrical and thermal transport properties (like Hall Effect, thermoelectric figure of merit and Seebeck Effect). The temperature can be varied continuously between 1.9 K and 400 K, while a magnetic field of up to ±14 Tesla can be applied. In present thesis, Quantum Design, PPMS 6000 (14 Tesla) (shown in **Fig. 2.19**) has been used for electrical transport study of LPCMO thin films.

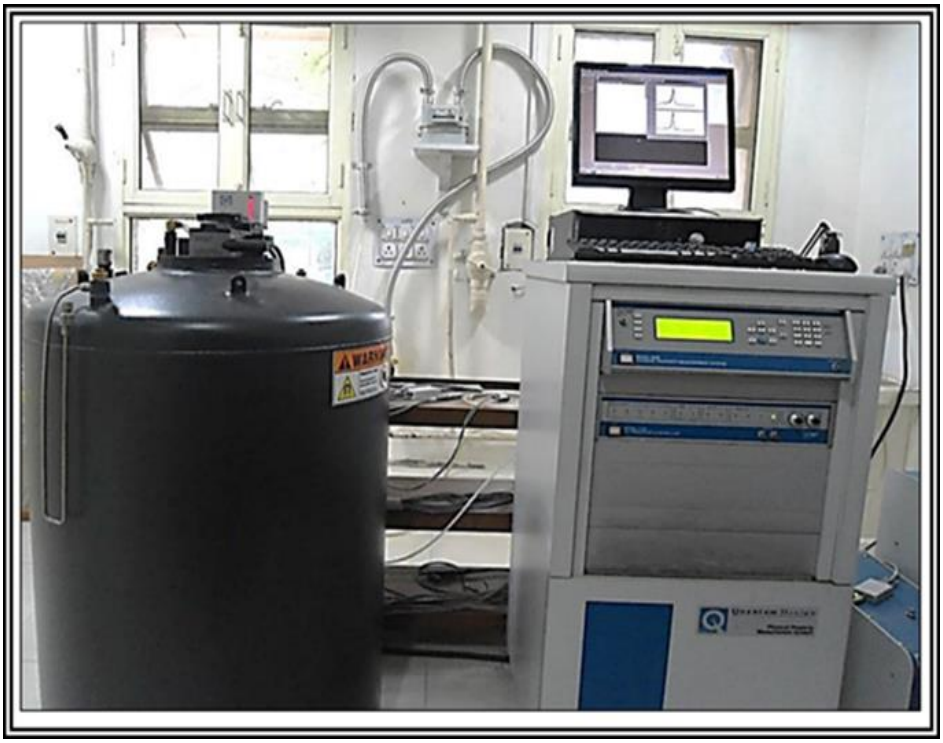

Figure 2.19: Quantum Design, Physical Property Measurement System, PPMS 6000 (14 Tesla)

Sample is mounted in "puck" with 12 pin connector which is connected at the bottom of the PPMS sample chamber on specially designed probe as shown in **Fig. 2.20.** The probe includes basic temperature-control hardware, superconducting magnet, helium-level meter, gas lines, sample puck connectors, and various electrical connections. It is immersed in the liquid-helium bath inside the dewar. Dewar is primarily constructed by aluminium and its outer layer has reflective superinsulation to minimize the helium loss. The outer layer is evacuated through a valve on the top of the dewar. The PPMS used in the present study uses Nitrogen-jacketed dewar which consumes significantly less liquid helium than those without nitrogen jackets.

Temperature control system of PPMS enables extreme temperature sweep capability such as 0.01-6 K/min. The Continuous Low-Temperature Control (CLTC) maintains temperatures below 4.2 K indefinitely and offers smooth temperature transitions when

warming and cooling through 4.2 K. Different types of measurements, e.g., temperature and magnetic field dependent resistance (R-T-H), current-voltage (IV) characteristics, thermoelectric power, heat capacity, AC/DC magnetization, and AC susceptibility, are the hallmark of a typical full PPMS.

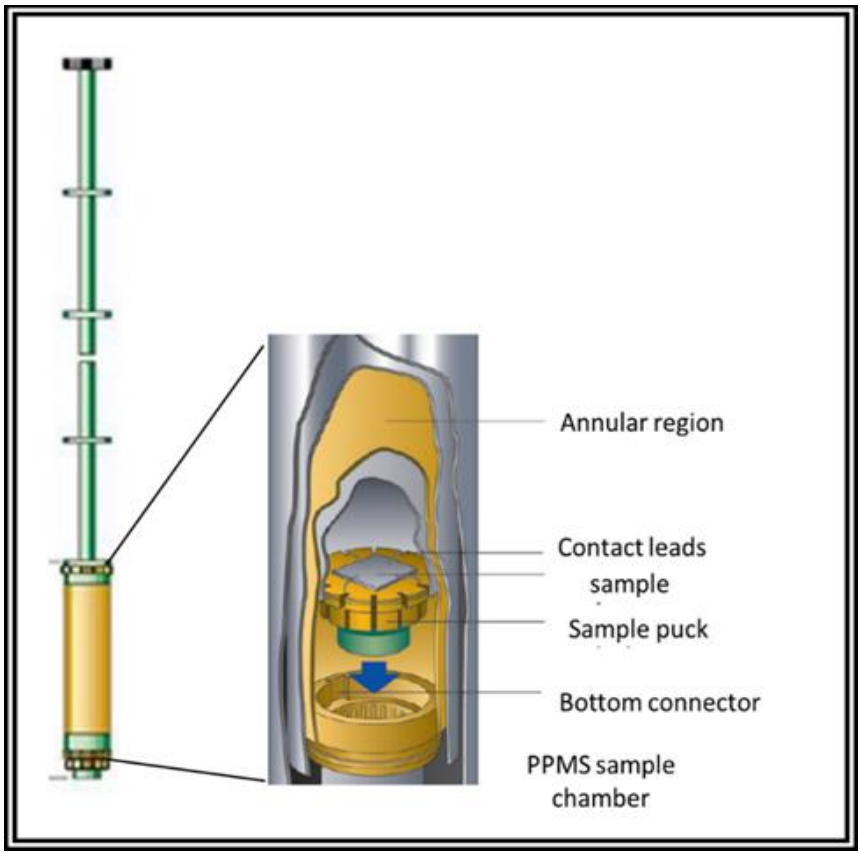

Figure 2.20: PPMS sample probe

The AC measurement system in PPMS provides the capability to perform both AC susceptibility and DC magnetization in a single automated measurement. AC susceptibility measurement can be done with magnetic moment sensitivity of 10-11 A-m^2 (10^{-8} emu). The excitation field ranges from 0.4 A/m – 1.2 kA/m (0.005 Oe – 15 Oe) at frequencies of 10 Hz-10 kHz. The four probe mode which consists of four wires in linear configuration **[64,65]** is the preferred for R-T-H and IV measurements. In this mode current is passed through outer two probes and voltage is measured through inner two

probes. The voltmeter measuring voltage through inner probes has high impedance so voltage leads draw negligible current. A schematic diagram of four-point collinear probe resistivity measurement is shown in **Fig. 2.21(a).** The resistivity of the films is calculated by using following formula:

$$\rho = \left(\frac{V}{I}\right)\left(\frac{w \times t}{l}\right) \qquad (2.3)$$

Where, ρ = resistivity in ohm-cm, V = voltage in volts, I = current in ampere, w = width of the film in cm, t = thickness of the film in cm, and l = distance between inner two probes. Resistivity sample pucks have four contacts - one positive and one negative each for current and voltage. There is provision of up to three sample mounting on resistivity puck as shown in **Fig. 2.21 (b).**

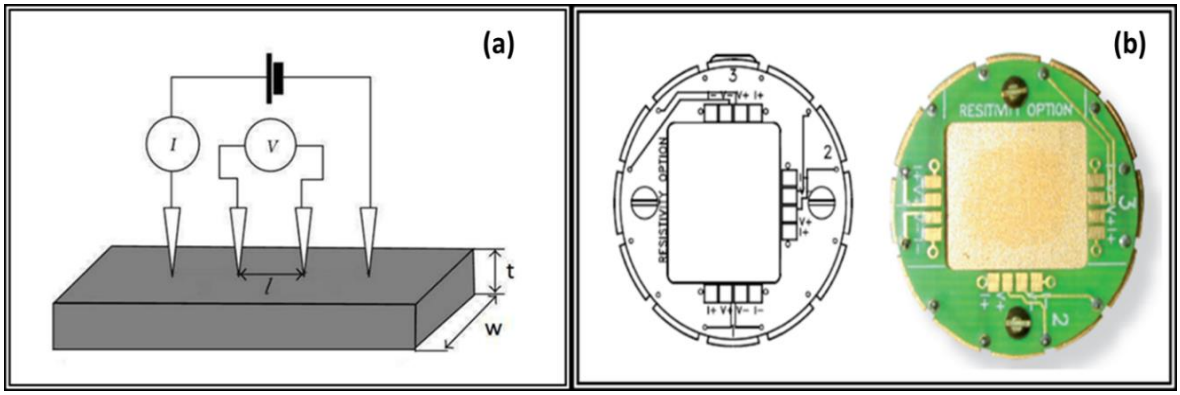

Figure 2.21: (a) A schematic diagram of resistivity measurement setup using a four-point collinear probe on film. (b) Four probe resistivity measurement arrangement on resistivity sample puck

2.5 References

[1] C. A.Neugebauer, in *Handb. Thin Film Technol.*, edited by L. I. Maissel and R. Glang (New York : McGraw-Hill, 1970).

[2] Rointan F. Bunshah, *Handbook of Deposition Technologies for Films and Coatings*, 2nd Editio (William Andrew, 1994).

[3] Milton Ohring, *Materials Science of Thin Films : Deposition and Structure*, Ed., 2nd (Academic Press, c2002., San Diego, 2002).

[4] JOHN A. VENABLES, *Introduction to Surface and Thin Film Processes* (Cambridge University Press, 2003).

[5] K. Wasa, M. Kitabatake, and Hideaki Adachi, *THIN FILM MATERIALS TECHNOLOGY Sputtering of Compound Materials* (William Andrew, Inc. and Springer-Verlag GmbH & Co. KG, 2004).

[6] Anthony R. West, *Solid State Chemistry and Its Applications*, 2nd Editio (John Wiley And Sons, 2014).

[7] K. L. Chopra and I. Kaur, in *Thin Film Device Appl.* (Springer US, Boston, MA, 1983), pp. 1–54.

[8] K. L. Chopra, *Thin Film Phenomena* (McGraw-Hill, 1969).

[9] G. S. Kino and R. S. Wagers, J. Appl. Phys. **44**, 1480 (1973).

[10] K. M. Lakin and J. S. Wang, in *1980 Ultrason. Symp.* (IEEE, 1980), pp. 834–837.

[11] P. K. Tien, Appl. Opt. **10**, 2395 (1971).

[12] M Volmer and A Weber, Z. Phys. Chem. **119**, 277 (1926).

[13] F. C. Frank and J. H. van der Merwe, Proc. R. Soc. A Math. Phys. Eng. Sci. **198**,

216 (1949).

[14] I. N. Stranski and L. Krastanov, Acad. Wiss. Math.-Naturw. Klasse IIb **146**, 797 (1938).

[15] T. Fukuda and H. J. Scheel, *Crystal Growth Technology* (Wiley, New York, 2003).

[16] C. P. Burmester, L. T. Wille, and R. Gronsky, Mat. Res. Symp. Proc **389**, 59 (1995).

[17] F. Y. Genin, MRS Proc. **389**, 83 (1995).

[18] W. A. Bryant, J. Mater. Sci. **12**, 1285 (1977).

[19] J.-O. Carlsson and P. M. Martin, in *Handb. Depos. Technol. Film. Coatings* (Elsevier, 2010), pp. 314–363.

[20] J. L. Zilko, in *Handb. Thin Film Depos. Process. Tech. (Second Ed.*, edited by K. Seshan, Second Edi (William Andrew Publishing, Norwich, NY, 2001), pp. 151–203.

[21] Krishna Seshan, editor , *HANDBOOK OF THIN-FILM DEPOSITION PROCESSES AND TECHNIQUES Principles, Methods, Equipment and Applications*, Second Edi (NOYES PUBLICATIONS WILLIAM ANDREW PUBLISHING Norwich, New York, U.S.A., 2002).

[22] O. Y. Gorbenko, A. R. Kaul, A. A. Molodyk, V. N. Fuflyigin, M. A. Novozhilov, A. A. Bosak, U. Krause, and G. Wahl, J. Alloys Compd. **251**, 337 (1997).

[23] F. F. Lange, Science (80-.). **273**, 903 (1996).

[24] A. Eftekhari, P. Jafarkhani, and F. Moztarzadeh, Carbon N. Y. **44**, 1343 (2006).

[25] M. Donald Mattox, *Vacuum Deposition, Reactive Evaporation, and Gas Evaporation* (ASM Handbook Volume 5, Surface Engineering (ASM International),

556, 1994).

[26] R. Acosta, Thin Solid Films **95**, 131 (1982).

[27] D.-W. Kim, T. . Noh, H. Tanaka, and T. Kawai, Solid State Commun. **125**, 305 (2003).

[28] M. Baran, S. L. Gnatchenko, O. Y. Gorbenko, A. R. Kaul, R. Szymczak, and H. Szymczak, Phys. Rev. B **60**, 9244 (1999).

[29] R. Eason, *Pulsed Laser Deposition of Thin Films: Applications-Led Growth of Functional Materials* (Wiley, 2007).

[30] C. Cantoni, D. K. Christen, M. Varela, J. R. Thompson, S. J. Pennycook, E. D. Specht, and A. Goyal, J. Mater. Res. **18**, 2387 (2003).

[31] J. O'Donnell, M. Onellion, M. S. Rzchowski, J. N. Eckstein, and I. Bozovic, J. Appl. Phys. **81**, 4961 (1997).

[32] S. Rossnagel, in *Handb. Thin Film Depos. Process. Tech. (Second Ed.*, edited by K. Seshan, Second Edi (William Andrew Publishing, Norwich, NY, 2001), pp. 319–348.

[33] P. Sigmund, Phys. Rev. **184**, 383 (1969).

[34] G. K. Wehner and D. Rosenberg, J. Appl. Phys. **31**, 177 (1960).

[35] G. K. Wehner, Phys. Rev. **102**, 690 (1956).

[36] D. Rosenberg and G. K. Wehner, J. Appl. Phys. **33**, 1842 (1962).

[37] Hari S Nalwa, editor , *Handbook of Thin Films, Five-Volume Set*, 1st Editio (Academic Press, 2001).

[38] K. Wasa, in *Handb. Sputtering Technol. (Second Ed.*, edited by K. Wasa, I. Kanno,

and H. Kotera, Second Edi (William Andrew Publishing, Oxford, 2012), pp. 41–75.

[39] K. Wasa, in *Handb. Sputtering Technol. (Second Ed.*, edited by K. Wasa, I. Kanno, and H. Kotera, Second Edi (William Andrew Publishing, Oxford, 2012), pp. 77–139.

[40] P. . Kelly and R. . Arnell, Vacuum **56**, 159 (2000).

[41] Y. M. Boguslavsky and A. P. Shapovalov, Supercond. Sci. Technol. **4**, 149 (1991).

[42] J. M. Gregoire, M. B. Lobovsky, M. F. Heinz, F. J. DiSalvo, and R. B. van Dover, Phys. Rev. B **76**, 195437 (2007).

[43] D. J. Kester and R. Messier, J. Mater. Res. **8**, 1938 (1993).

[44] R. Kossowsky, B. Raveau, D. Wohlleben, and S. K. Patapis, editors , *Physics and Materials Science of High Temperature Superconductors, II* (Springer Netherlands, Dordrecht, 1992).

[45] E. J. Tomlinson, Z. H. Barber, G. W. Morris, R. E. Somekh, and J. E. Evetts, IEEE Trans. Magn. **25**, 2530 (1989).

[46] G. Linker, X. X. Xi, O. Meyer, Q. Li, and J. Geerk, Solid State Commun. **69**, 249 (1989).

[47] O. Auciello, A. I. Kingon, and S. B. Krupanidhi, MRS Bull. **21**, 25 (1996).

[48] Paul Hagenmuller, editor , *Preparative Methods in Solid State Chemistry* (Academic Press, 1972).

[49] R. F. Egerton, *Physical Principles of Electron Microscopy* (Springer US, Boston, MA, 2005).

[50] P. D. Ngo, in *Fail. Anal. Integr. Circuits* (Springer US, Boston, MA, 1999), pp. 205–

215.

[51] G. Binnig, C. F. Quate, and C. Gerber, Phys. Rev. Lett. **56**, 930 (1986).

[52] F. J. Giessibl, Rev. Mod. Phys. **75**, 949 (2003).

[53] P. Klapetek, in *Quant. Data Process. Scanning Probe Microsc.* (Elsevier, 2013), pp. 127–172.

[54] M. K. Srivastava, P. K. Siwach, A. Kaur, and H. K. Singh, Appl. Phys. Lett. **97**, 182503 (2010).

[55] M. K. Srivastava, A. Kaur, and H. K. Singh, Appl. Phys. Lett. **100**, 222408 (2012).

[56] B. D. Cullity, *Elements Of X Ray Diffraction*, SECOND EDI (Addison-Wesley Publishing Company, Inc., 1978).

[57] Thorsten Buzug, in *Comput. Tomogr.* (Springer Berlin Heidelberg, Berlin, Heidelberg, n.d.), pp. 15–73.

[58] B. Capusten, Radiology **161**, 22 (1986).

[59] H. P. Klug and L. E. Alexander, X-Ray Diffr. Proced. Polycryst. Amorph. Mater. 2nd Ed. by Harold P. Klug, Leroy E. Alexander, Pp. 992. ISBN 0-471-49369-4. Wiley-VCH, May 1974. 992 (1974).

[60] R. Guinebretière, *X-Ray Diffraction by Polycrystalline Materials* (ISTE Ltd., London W1T 5DX, London, UK, 2007).

[61] R. Kleiner, D. Koelle, F. Ludwig, and J. Clarke, Proc. IEEE **92**, 1534 (2004).

[62] P. W. Anderson and J. M. Rowell, Phys. Rev. Lett. **10**, 230 (1963).

[63] D. . Drung, C. . Assmann, J. . Beyer, A. . Kirste, M. . Peters, F. . Ruede, and T. . Schurig, IEEE Trans. Appl. Supercond. **17**, 699 (2007).

[64] L. J. VAN DER PAUW, Philips Res. Rep **13**, 1 (1958).

[65] B. J. Horkstra, L. J. VAN DER PAUW, and N. V. Philips, J. Electron. Control **7**, 169 (1959).

3 Impact of Relative Phase Fractions on Supercooling and Superheating Transition Temperature of Phase Separated Manganite Thin Film

3.1 Introduction

Phase separation is the phenomenon of coexistence of different phases on a certain dimensional scale, which is determined by elastic and thermomagnetic parameters like strain, temperature and magnetic field in a single manganite system. Various existing phases play a crucial role in governing the properties of manganite system. $La_{1-x-y}Pr_yCa_xMnO_3$ is a prototype phase separated manganite among all low and intermediate bandwidth manganites. The strong nature of the phase separation has be established by the observation of (i) strong divergence of the zero filed cooled (ZFC) and field cooled warming (FCW) magnetization, (ii) pronounced hysteresis between the field cooled cool (FCC) and FCW magnetization, (iii) prominent hysteresis in the temperature dependent resistivity (ρ-T) measured in cooling-warming cycles **[1–10]** Wu et al. **[4]** have shown the occurrence of a supercooled glass transition in $La_{5/8-y}Pr_yCa_{3/8}MnO_3$ (y≈0.4) thin film. They have attributed it to the accommodation strain arising due to distinct structural symmetries of FM and AFM/COI phase. They have proposed that the low temperature phase-separated states prepared by different thermodynamic paths arise from the cooperative dynamic freezing of the first-order AFM/COI–FM transition, which is frustrated and hindered by the long range cooperative strain interactions **[3,4]**. This demonstrate the non-ergodic nature of the strongly phase separated system $La_{5/8-y}Pr_yCa_{3/8}MnO_3$ (y≈0.4). The FCC-FCW and ρ-T hysteresis are regarded as a signatures of supercooling and superheating transition of the magnetic liquid resulting from competing FMM and AFM phases, presence of martensitic accommodation strain and long range cooperative strain

interactions **[2–4]**. Despite the exhaustive investigations on different variants of the $La_{1-x-y}Pr_yCa_xMnO_3$, the nature of the supercooling/superheating transitions, e.g., their dependence on relative fractions of FMM and AFM phases has not been probed through electrical transport measurements. The different relative fractions of the FM/AFM phases in the phase separated regime could lead to different thermodynamic paths and hence could lead to different supercooling transition temperatures. Hence it is important to investigate the signature of different magneto-thermodynamic paths in electrical transport.

In this chapter the impact of variation in the relative fractions of the ferromagnetic metallic (FMM) and antiferromagnetic/charge ordered insulator (AFM/COI) phases on the supercooling/superheating transition in strongly phase separated system, $La_{5/8-y}Pr_yCa_{3/8}MnO_3$ ($y\approx0.4$), has been presented. The results clearly show that the supercooling transition temperature is non-unique and strongly depends on the magneto-thermodynamic path through which the low temperature state is accessed. In contrast, the superheating transition temperature remains constant. Also, the thermo-magnetic hysteresis, which is the separation of the two transitions and the associated resistivity, are strongly dependent on the relative fractions of the coexisting phases.

The resistivity and henceforth the IMT of such materials is determined by the relative fraction and size of the two coexisting phases and their interconnection, so it is essential to have proper understanding of the time evolution of the electrical transport in such materials is important. Apart from unravelling new aspects of the phase conversion kinetics, this study is expected to provide deeper insight into the temporal nature of the phase separation; a key to unlock mystery of such manganites. The transformation of the coexisting phases, namely AFMI and FMM from one to the other is expected to be a function of time also. In view of this we have conducted a variety of time dependence resistivity evolution under zero magnetic field condition. Major part of this work is published in ***Applied Physics Letter*****, 104, 212403 (2014).**

3.2 Experimental

A stoichiometric (2 inch) target of $La_{5/8-y}Pr_yCa_{3/8}MnO_3$ (y≈0.4), as prepared by solid state route, was used for thin film deposition by RF magnetron sputtering of in 200 mtorr of Ar + O_2 (80% + 20%) mixture on single crystal (001) $SrTiO_3$ (STO) substrates maintained at ~ 800 °C. The detailed description of target preparation and thin film deposition is described in chapter 2. In order to achieve optimum oxygen content the films were annealed at ≈900 °C for 10 hr. in flowing oxygen.

3.3 Result and Discussion

3.3.1 Structural and Surface Analysis

The thickness of the film was estimated from X-Ray reflectivity (XRR) measurements. The experimental and simulated XRR curves are plotted in **Fig. 3.1**.

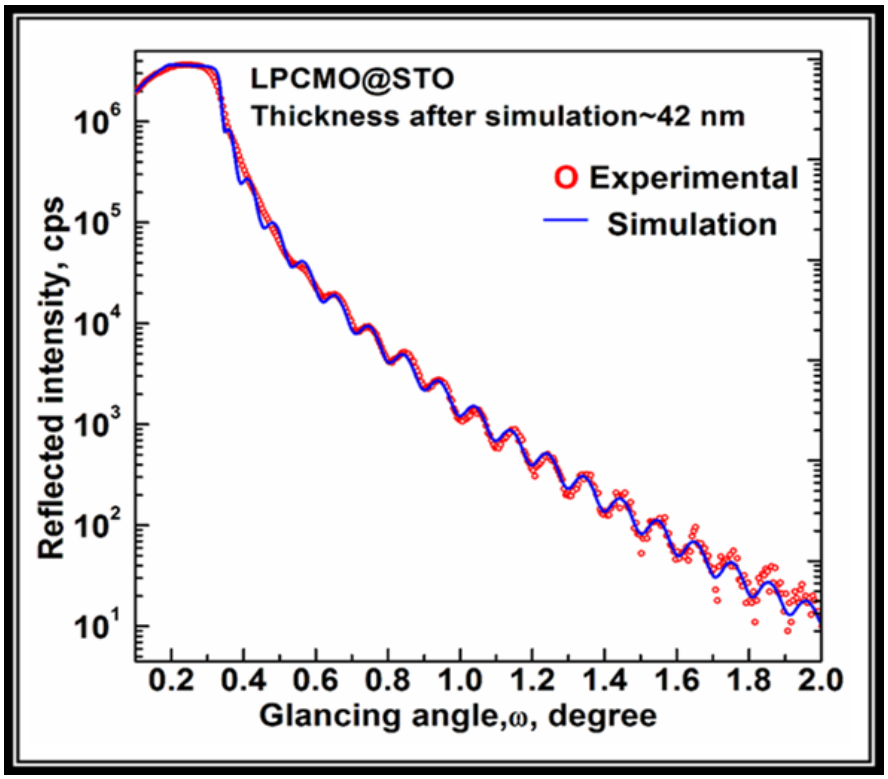

Figure 3.1: Experimental and simulated X-ray reflectivity (XRR) plot of LPCMO film

The measurement yield film thickness ~ 42 nm. The average roughness and density estimated from the XRR simulation is ~ 0.52 nm and ~ 4.5 gm/cm^3, respectively. The density is very close to the theoretical value ~ 4.6 gm/cm^3.

The high resolution X-ray diffraction (HRXRD, 2θ-ω scan) was measured from 20° - 80° and confirms the epitaxial nature of thin film. The lattice mismatch (ε) between the target and substrate is ≈ -1.93 % ($\varepsilon = (a_t - a_{s)x100}/a_s$ where a_t and a_s are the lattice parameters of the bulk target (3.842 Å) and substrate (3.905 Å) respectively), therefore, there is appreciable tensile strain. **Fig. 3.2** clearly shows LPCMO thin film is oriented along c-axis with significantly reduced out-of-plane or the normal lattice parameter of the film, a_f = 3.832 Å (a_{bulk} = 3.842 Å), confirms the presence of appreciable tensile strain in thin film.

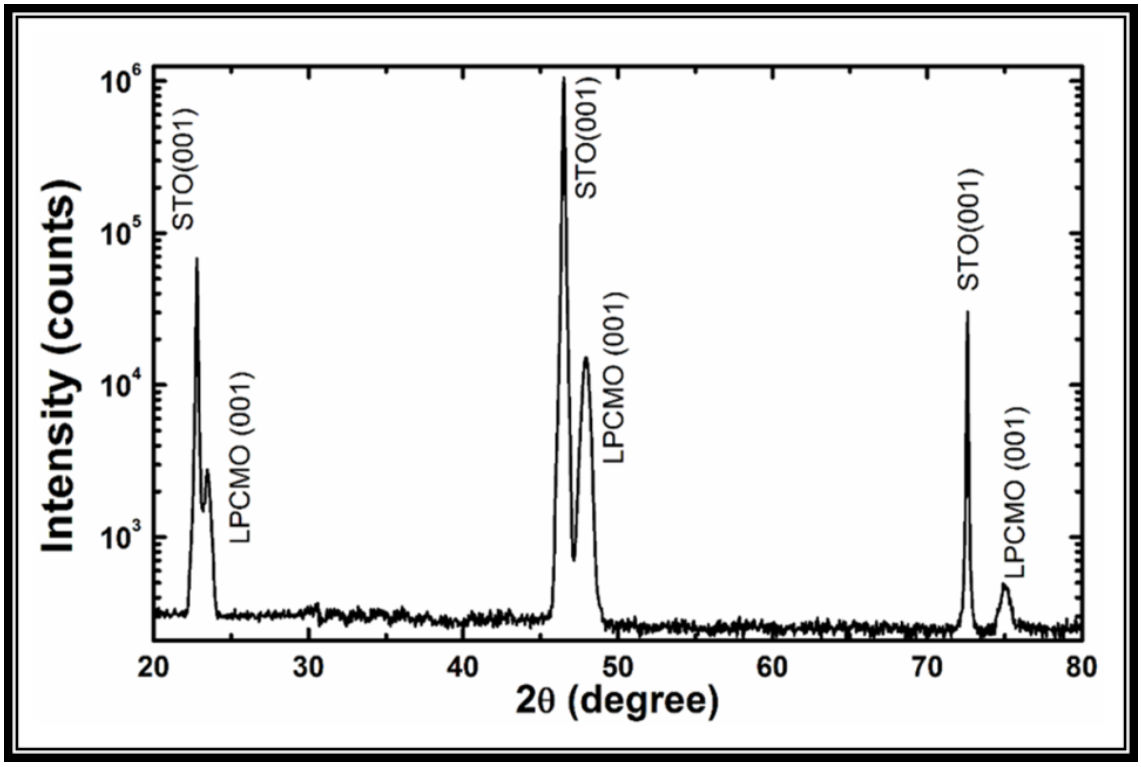

Figure 3.2: X-ray diffraction pattern (2θ–ω scan) of LPCMO film on STO substrate

The epitaxial nature of the film is also reflected in the surface topography. A representative AFM* image of the annealed film is shown in **Fig. 3.3**, which shows step-terrace

growth and further confirms the epitaxial nature of the film. The average roughness of film was found to be ~ 0.58 nm which shows fairly good surface quality of film. The steps and terraces are not well defined and there is appearance of holes and regular discontinuities in the individual layers. This could be regarded as an evidence of the lattice defects which arises due to the relaxation of the large strain between the substrate and the film during the oxygen annealing process.

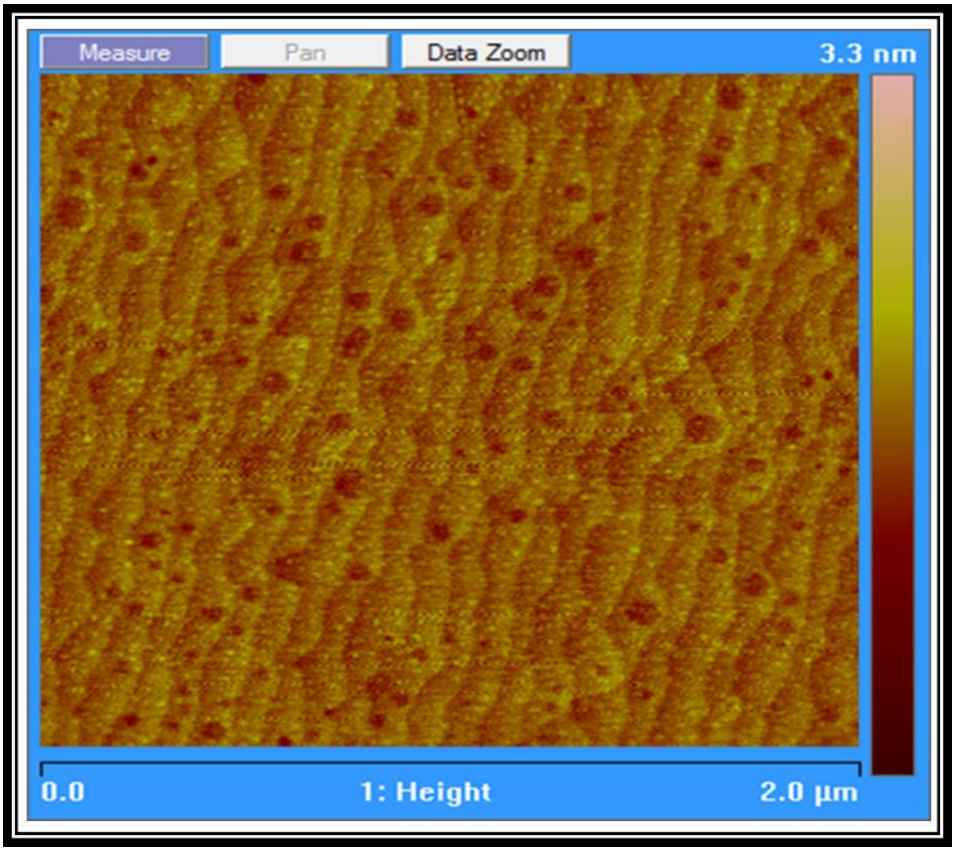

Figure 3.3: Tapping mode AFM* image of annealed LPCMO film

3.1.2 Temperature Dependent Magnetization Analysis

The variation of magnetization with temperature (M-T) was measured using ZFC (zero field cool), FCC (field cooled cooling) and FCW (field cooled warming) protocols. In ZFC protocol the sample was cooled to low temperature in zero field and then magnetization is measured during warming cycle in low external magnetic field. The FCC and FCW is the

measurement of magnetization during cooling and warming cycles respectively in low external magnetic field. The ZFC, FCC and FCW data plotted in **Fig. 3.4** shows several interesting features viz., (i) huge irreversibility in the ZFC and FCW curves, (ii) pronounced hysteresis between the FCC and FCW curves, (iii) reversible behaviour of FCC and FCW curves below T ≈ 26K, (iv) a peak in the FCW M-T around T_P ~ 43 K, and (v) sharp drop in ZFC: M-T curve around T_P. The ZFC-FCW irreversibility, which is distinct from that of a representative spin glass state **[11]** and is invariably observed in phase separated manganites as a signature of cluster glass state **[12–14]** Spin glass is the disordered magnetic state where spins are not aligned in any regular fashion whereas in cluster glass spins are locally ordered creating small domains. The cluster glass state is encountered in case of intermediate bandwidth manganites having x~1/2 **[12]** or over a wide range of divalent doping (x) in low bandwidth manganites **[13,14]**

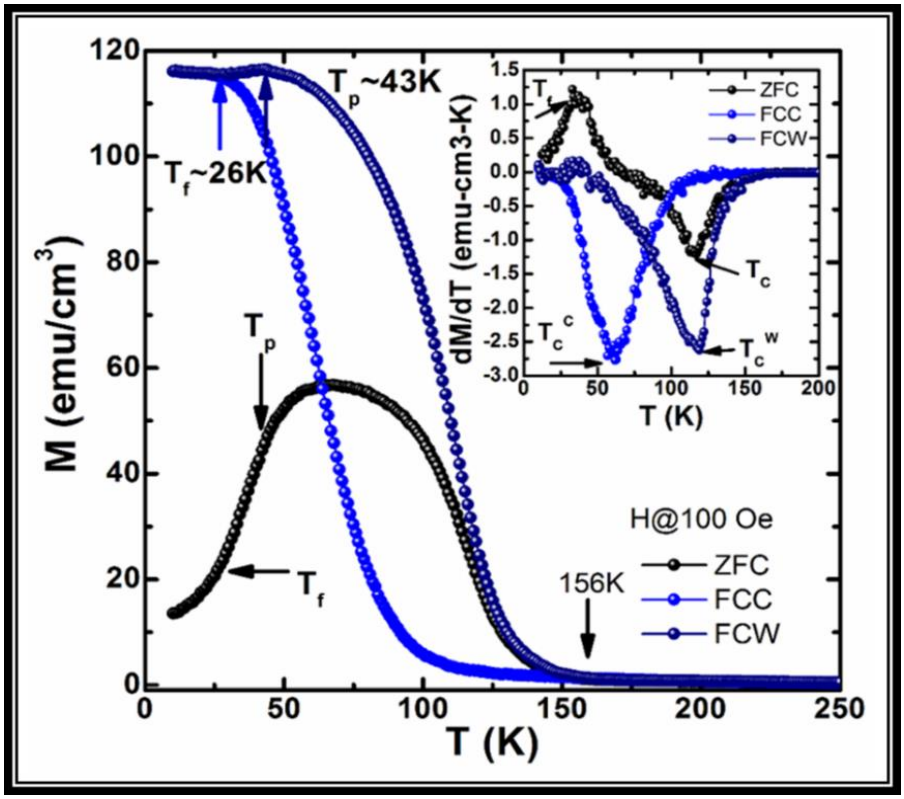

Figure 3.4: The temperature dependence of magnetization measured at H=100 Oe. The inset shows the temperature derivative of the ZFC, FCC and FCW curves.

This state originates from the coexistence of FMM and AFM/COI phases below the Neel temperature T_N. The sharp drop in the ZFC curve observed at temperature marked T_P is a signature of cluster freezing of spins. The prominent FCC-FCW hysteresis is signature of the different magneto-thermodynamics of the system in the two protocols and arises due to the global frustration created by the AFM/COI phase that increases the energy of the system and also the degeneracy of the energy minima. Hence the origin of the non-ergodicity is traceable to the AFM/COI phase, which alone can create frustration. The low temperature (T<26 K) reversible behaviour of the FCC and FCW has been regarded as a signature of an equilibrium state attained in the FCC protocol by Ghivelder and Parisi **[2]** and could be related to the blocking of system or freezing of the cluster glass. The weak temperature dependence of the FCC and FCW at T<26 K suggests that the magnetic clusters may not be frozen completely. AT T>26 K the states are gradually unblocked and the moment increases and peaks at $T_P \sim 43$ K, which can be regarded as the onset of cluster freezing.

The FM transition, determined from the derivative of M-T data (**inset of Fig. 3.4**), occurs at $T_C \approx 117$ K, $T_C^C \approx 63$ K and $T_C^W \approx 120$ K in the ZFC, FCC and FCW protocols, respectively. The protocols dependent T_C could be taken as an evidence of non-ergodicity. A significantly lower $T_C^C \approx 63$ K in FCC protocol can be considered as a consequence of supercooling [4] whereas the $T_C^W \approx 120$ K can be taken as the equilibrium FM transition. The fact that the COI and AFM transitions are not explicit in the M-T data could be regarded as a consequence of defect induced quenching of AFM/COI. In thin films the substrate induced strain and associated defects make the scenario dramatically different and the CO transition, which is explicit in bulk at y > 0.3, is generally quenched in thin films **[4,7–9]**.

The simultaneous existence of distinctive crystallographic structures **[9,15]** of the FMM (pseudocubic) and AFM/COI (orthorhombic) phases gives rise to accommodation strain. This in conjunction with the frustration induced by the AFM could hinder the seeding of a low

temperature equilibrium state through creation of multi-minima configurations in the energy landscape of the system. Such a scenario in turn could give rise to a liquid like magnetic phase, which has been called strain liquid by Sharma et al. **[3]**. Hence the T_{IM} corresponding to liquid like magnetic phase should be non-unique and depend on the relative fractions of FM and AFM/COI phases at the beginning of the magneto-thermodynamic process.

3.3.2 Temperature Dependent Resistivity Analysis

The relative fractions of FM and AFM/COI phases change with temperature across T_C^W and T_{IM} must be a function of the temperature (T^*) corresponding to the start of the magneto thermodynamic process. This was experimentally verified by temperature dependent resistivity (ρ - T) measurement using a protocol in which the thermal cycling was started from a temperature (T^*), which was achieved by cooling the sample from room temperature and then warming up to T^*. In view of the M-T data present above it is obvious that each T^* corresponds to a distinct ratio of FMM and AFM/COI phases. ρ-T was measured during cooling and warming employing the cycle $T^* \rightarrow 6\ K \rightarrow T$ ($T > T_{IM}^W$) at H = 0 and H = 10 kOe. The full cycle (300 K $\rightarrow$ 6 K $\rightarrow$ 300 K) ρ-T taken during cooling and warming (cooling and warming rate 1K/min) is plotted in **Fig. 3.5 (a).** In the cooling cycle insulator-metal transition (IMT) occurs at $T_{IM}^C \approx 64$ K, where ρ drops by more than four orders of magnitude within a narrow temperature window. This is generally attributed to the abrupt enhancement in the FMM fraction at the cost of the AFM/COI. During the warming cycle the ρ-T curve shows a minimum at $T_m \approx 45$ K and IMT appears at $T_{IM}^W \approx 123$ K. The rapid rise in resistivity just below T_{IM}^W corresponds to the enhanced fraction of the AFM/COI. The huge thermo-resistive hysteresis in the ρ - T curve and large $\Delta T_{IM} = T_{IM}^W - T_{IM}^C \approx 59$ K unravels the strongly phase separated nature of the system. The T_{IM}^C almost coincides with the FCC $T_C^C \approx 63$ K, while $T_{IM}^W \approx 123$ K is very close to $T_C^W \approx 120$ K. It is believed that the drastically lowered T_{IM}^C and T_C^C is caused

by supercooling of the phase separated magnetic liquid consisting of FMM and AFM/COI sub-lattices **[1–4,7]**.

The zero filed cooling and warming cycle ρ-T data acquired after cooling from different T^* is plotted in **Fig. 3.4 (b-f).** When the film is cooled down from $T^* \approx 97$ K no IMT is observed. However, for higher values of T^* is increased to higher values, IMT which we denote by T_{IM}^{C*} appears in the cooling cycles. The value of T_{IM}^{C*} for $T^* \approx 105$ K, 113 K, 117 K, 122 K, and 143 K are observed to be 103 K, 95 K, 88 K, 79 K and 69 K, respectively . For values of $T^* \geq 170$ K the IMT saturates to $T_{IM}^{C} \approx 64$ K, the full cycle value. Interestingly, the warming cycle IMT, T_{IM}^{W*} remains independent T^*.

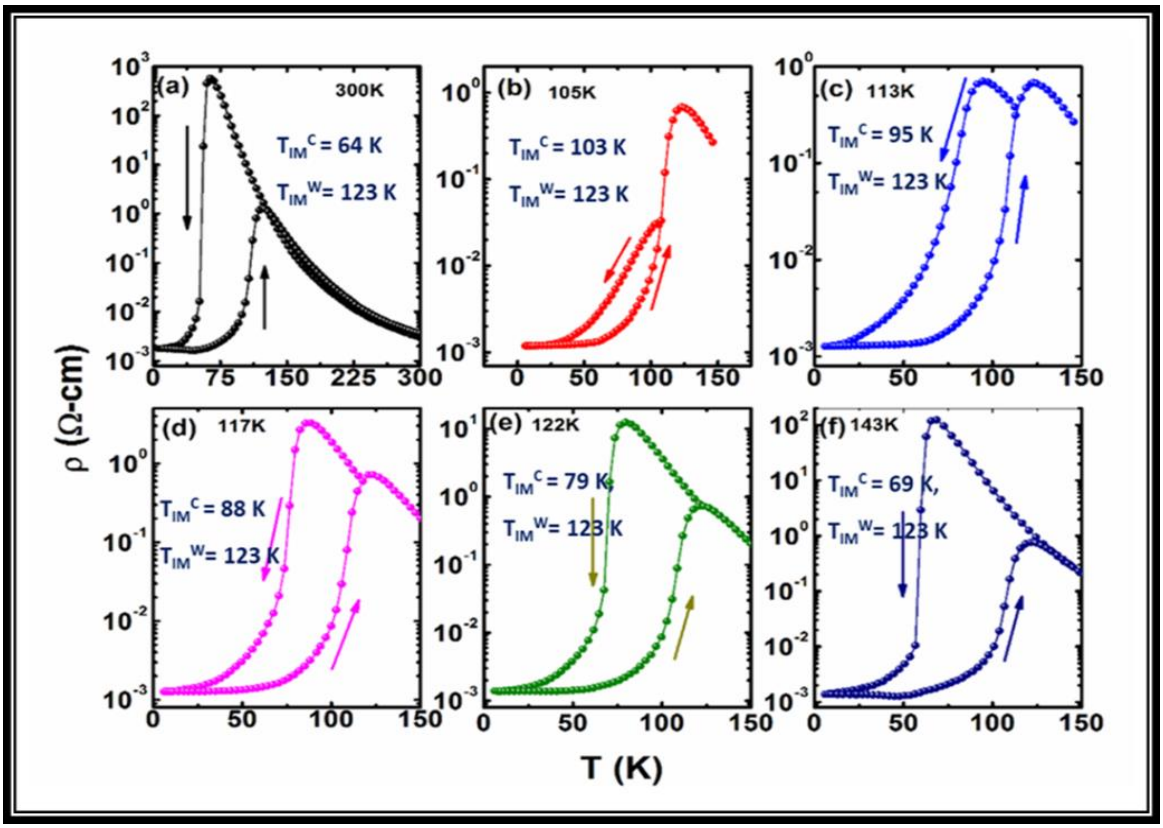

Figure 3.5: Temperature dependence of resistivity measured for H=0 kOe in cooling and warming cycles after initial cooling and subsequent warming to different temperatures T.

In another study, the field (H=10 kOe) cooling and warming cycle ρ-T data acquired after cooling from different T* are plotted in **Fig. 3.6**. The full cycle ρ-T shows $T_{IM}^{C} \approx 104$ K and $T_{IM}^{W} \approx 133$ K. At H = 10 kOe the cooling cycle IMT shows an increase of 40 K, which, however, is only 10 K in the warming cycle. This could be attributed to the substantial suppression of AFM induced frustration in the phase separated regime. For T* = 105 K, no IMT was observed in cooling cycle, while warming cycle showed IMT at $T_{IM}^{W*} \approx 133$ K. The absence of IMT for T* = 105 K shows that at this temperature the film has a dominant FMM fraction. For higher T* (< T_{IM}^{W}), e.g., 120 K and 127 K IMT occurs at $T_{IM}^{C*} \sim 119$ K and 112 K respectively was observed in the cooling cycle but the warming cycle IMT remained constant at $T_{IM}^{W*} \approx 133$ K (**Fig. 3.6**). For further higher values of T* = 150 K, 200 K, and 300 K, both T_{IM}^{C*} and T_{IM}^{W*} remain constant at 104 K and 133 K, respectively.

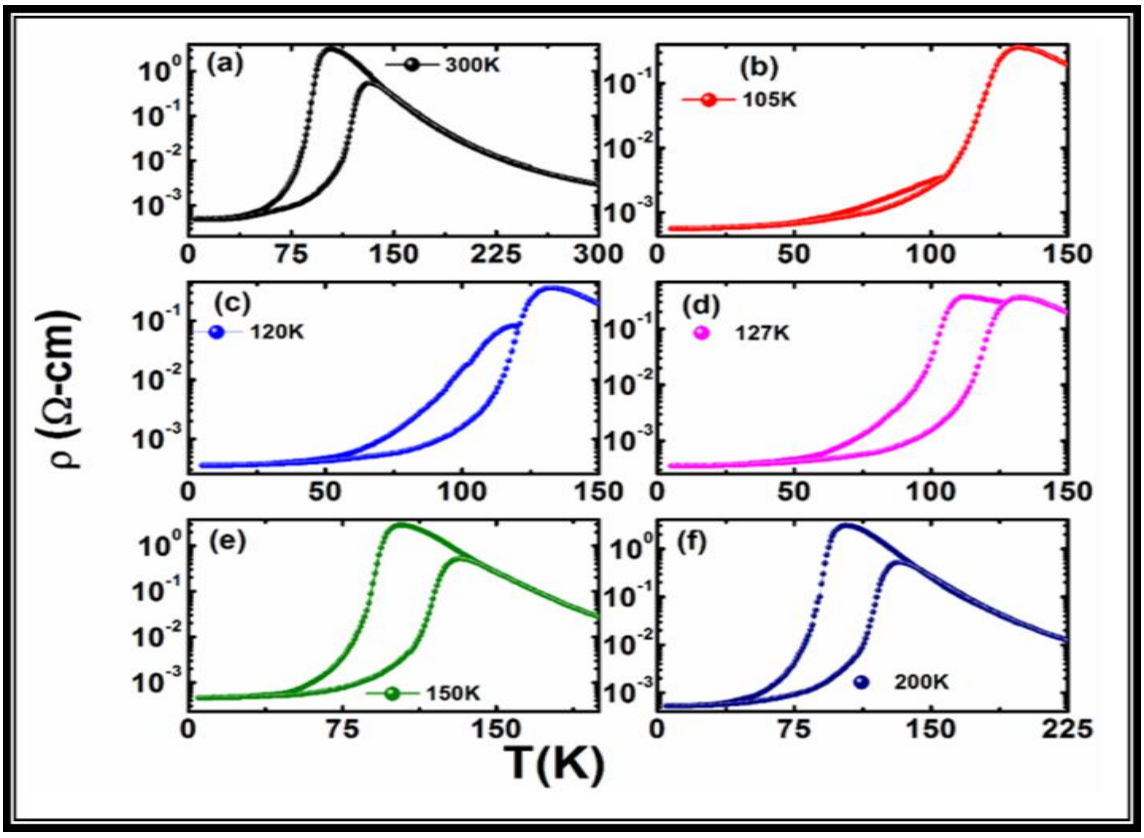

Figure 3.6: Temperature dependence of resistivity measured in a magnetic field of H=10 kOe in cooling and warming cycles after initial cooling and subsequent warming to different temperatures T*.

The variation of T_{IM}^{C*} and the corresponding peak resistivity measured in the cooling cycle are plotted in **Fig. 3.7a** and **3.7b**, respectively. Apart from IMT, the impact of the relative fraction of the FMM and AFM phases on electrical transport is also reflected in the resistivity (ρ_{IMC}) at T_{IM}^{C*}. The variation of ρ_{IMC} with T^* for H=0 and 10 kOe is shown in **Fig. 3.7 (b)**. The difference of more than two orders of magnitude in ρ_{IMC} measured at H=0 and 10 kOe clearly reflects the colossal magnetoresistance effect. Another interesting feature seen in the zero field warming ρ-T data is the appearance (disappearance) of resistivity minimum ρ_m (T_m) for all $T^* \geq 143$ K (≤ 122 K). In the measurements carried out at H=10 kOe, no ρ_m (T_m) is observed at all.

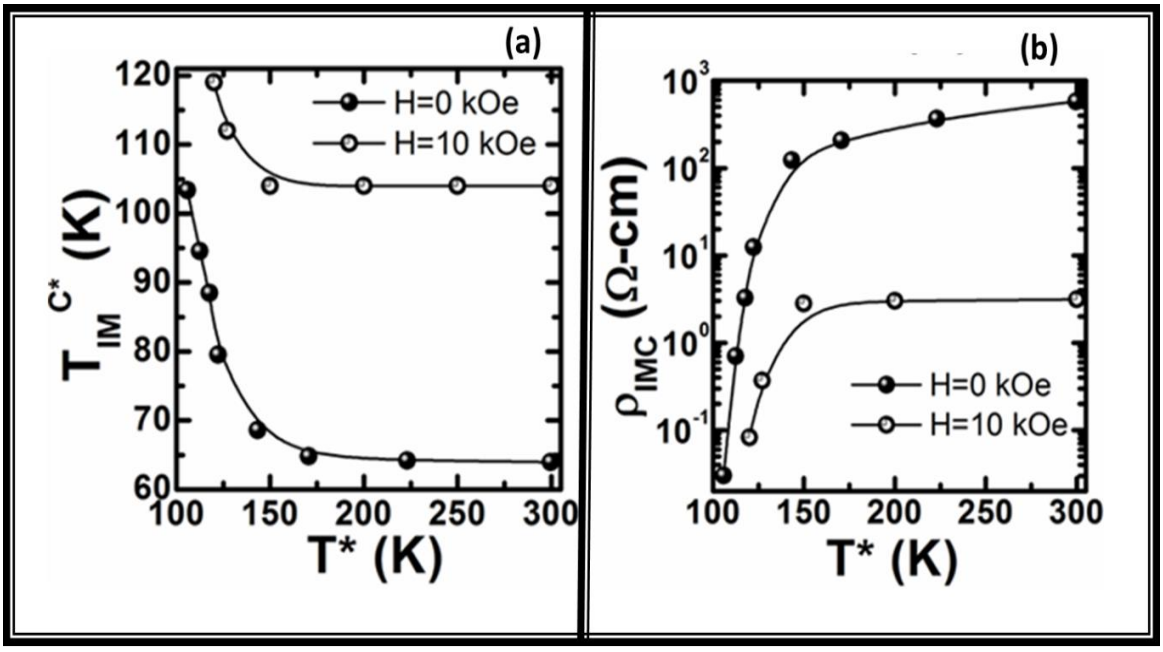

Figure 3.7: (a) The variation of the T_{IM}^{C*} as a function of the characteristic temperature T^* measured at H=0 and 10 kOe. (b) The variation of the peak resistivity measured in the cooling cycle as a function of T^*.

The results presented above clearly show that the supercooling transition temperature is strongly dependent on T^*, i.e., on the relative fraction of the two coexisting phases (FMM and AFM/COI) and hence the degree of magnetic frustration at the temperature from where the

magneto-thermodynamic process is started. The fact that for different $T^* < T_{IM}^W$, that lies on the steepest region of the warming ρ-T curve, the supercooling transition occurs at different temperatures suggests that the system acquires different energy configurations for different T^*. This gives an unambiguous signature of non-ergodicity. When the sample is cooled from a T^* at which the either FMM is in minority or absent, $T_{IM}^C{}^*$ saturates to the lowest value $T_C^C \approx 64$ K and the resistivity minimum reappears. This clearly shows that the AFM fraction is key to the occurrence of resistivity minimum and is probably related to the freezing of the strain glass state. At $T^* > T_{IM}^W$ the fraction of FMM (AFM/COI) phase decreases (or increases) leading to dilution of the phase separation tendency and therefore no modulation of the IMT takes place. At lower AFM/COI fractions and hence reduced magnetic frustration, the nature of IMT is drastically affected. This is obvious from the broadening of the IMT and reduced intensity of the T_{IM}^C for all $T^* \leq T_{IM}^W$. The phase separation tendency, as evidenced by the narrowing of the ρ-T hysteresis, is also weakened at reduced AFM/COI fractions.

3.3.3 Time Dependent Modification in Electrical Transport

Therefore in order to unravel the temporal aspects of the AFMI-FMM and reverse phase transition we carried out time dependent resistivity as a function of temperature as well as isothermally. First we employed different cooling/ warming rates of 0.5 K, 1 K, 2 K and 4 K per minute to measure the temperature dependent resistivity (ρ-T) during cooling and warming. The results are shown in **Fig. 3.8.** As the cooling/ warming rate is changed from 0.5 K/ min to 4 K/ min (i) the cooling IMT decreases from 68.6 K to 53.13 K, (ii) the low temperature resistivity (at 5 K) increase manifold, (iii) the glass transition (Tg) shifts to lower values, (iv) the temperature corresponding to the resistivity minimum increases slightly and (v) the warming IMT remain almost unaffected. The variation of the cooling cycle IMT (T_{IM}^C) is shown in the inset of **Fig. 3.8**.

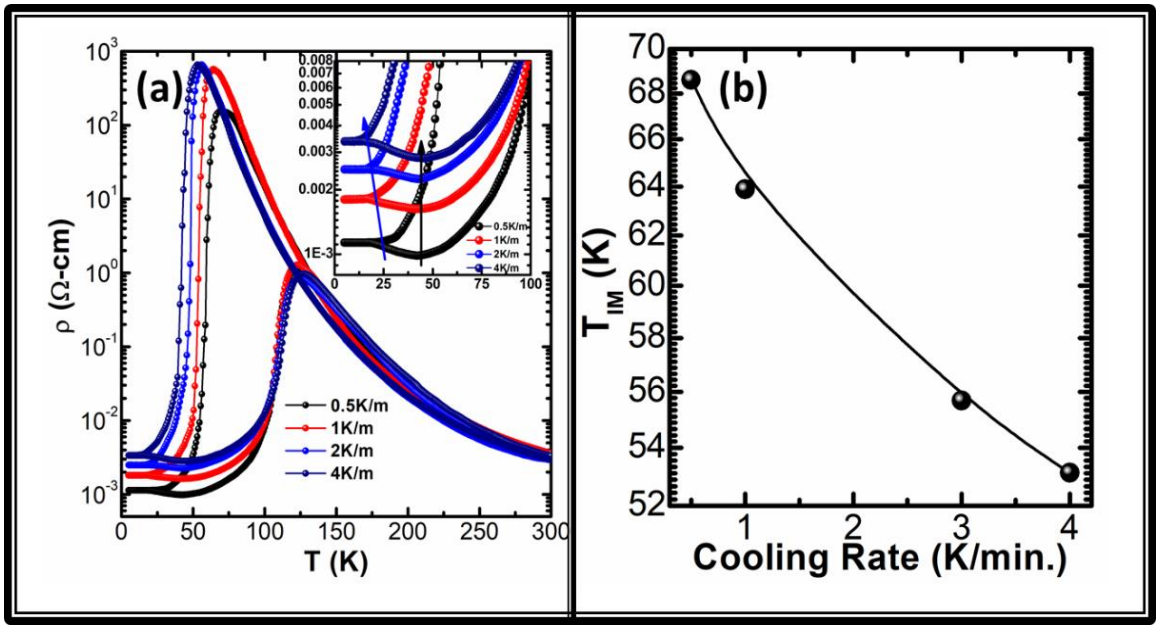

Figure 3.8: (a) The temperature dependent resistivity measured during cooling/warming at different cooling and warming rates (b) The Variation of the cooling cycle IMT with cooling rate.

The decrease in T_{IM}^{C} and in ρ (5 K) with increasing cooling/warming (C/W) rates clearly suggests that the AFMI-FMM phase transition is indeed hindered at higher C/W rates. Hence the slower the C/W the better is the AFMI- FMM phase transition during the cooling cycle. However, the independence of the T_{IM}^{W} from thermal cycling rate confirm that FMM- AFMI, the reverse phase transition remain unaffected. This could be a consequence of the liquid (non-equilibrium) like behaviour of the magnetic phase mixture during cooling. During the warming, system remains close to the equilibrium and hence exhibit no temporal hindrances The C/W ρ-T hysteresis, which also is considered as a measure of the phase coexistence increases sharply as C/W rate is increased from 0.5 K/min to 1 K/min and beyond this the increase is rather slow.

In view of the dynamical effects observed in the phase separated state it would be quite intriguing to investigate the temporal behaviour of the resistivity during the cooling cycle (which shows supercooling) and the warming cycle (which shows behaviour closer to equilibrium). Since the temporal evolution of magnetization and resistivity are due to the

transformation of AFMI metastable (non-equilibrium) phases to the FMM stable state during cooling and the reverse process during warming, therefore the time scale of resistance relaxation should reflect the nature of the phase separation. The resistivity versus time (ρ-t) data was acquired at different temperatures during cooling as well as warming periods. The data measured during the cooling cycle is plotted in **Fig. 3.9**, while the one corresponding to the warming period is shown in **Fig. 3.10**. For better quantitative comparison in both the figures (**Fig. 3.9** and **Fig. 3.10**) we have plotted the time evolution of the normalized resistivity (=ρ (t)/ρ (t=0)). As seen in **Fig. 3.9**, during the cooling cycle huge decrease in the resistivity in very short span of time are clearly seen at temperatures in the vicinity of the IMT. This is due to the generation of large FMM clusters with simultaneous disappearance of the AFMI ones. In the lower temperature region, which is dominated by the glassy state the decrease in the resistivity is very small. This could be due to the frozen nature of the spins.

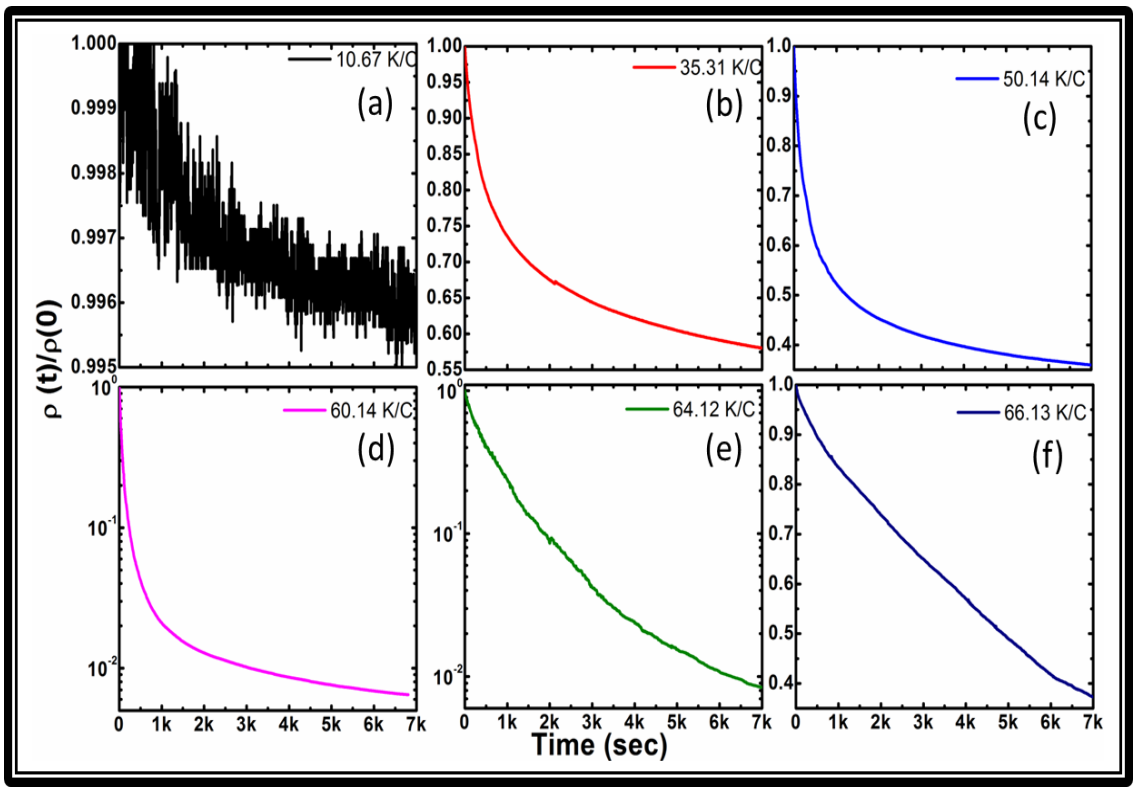

Figure 3.9: Time dependent normalized resistivity measured during cooling at different temperatures.

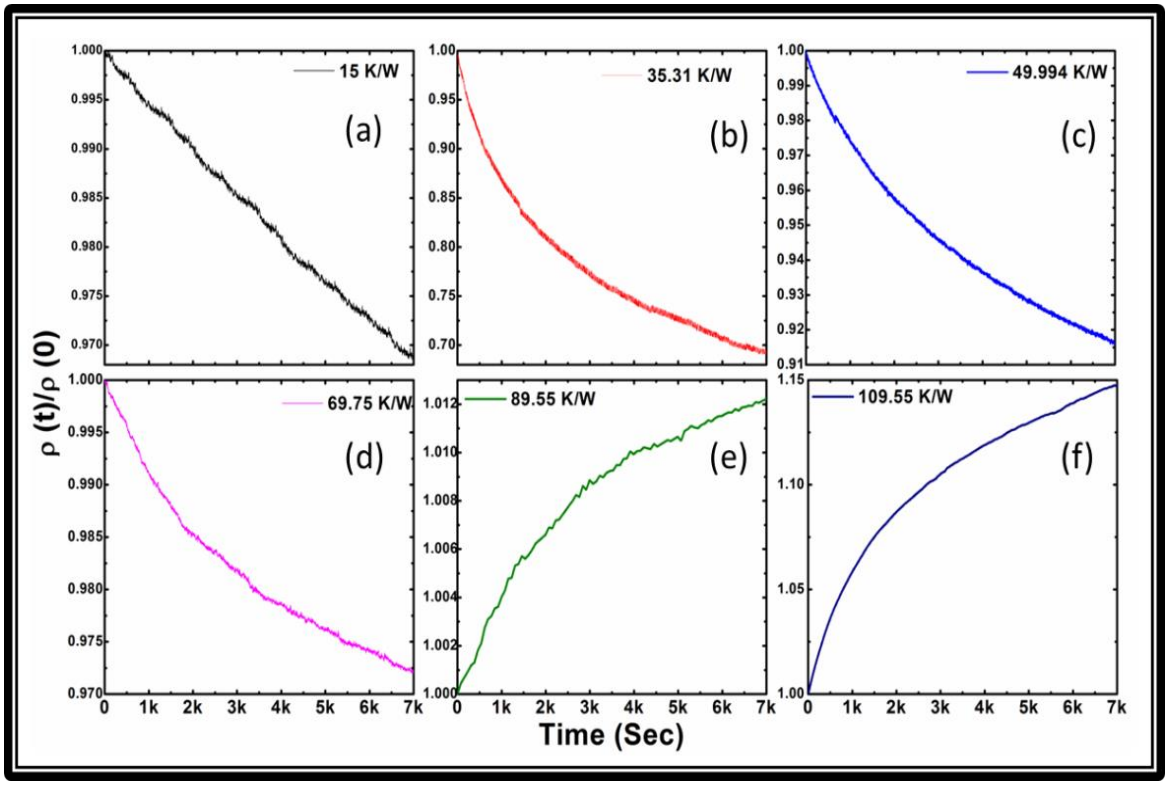

Figure 3.10: Time dependent normalized resistivity measured during warming at different temperatures

The temporal evolution of resistivity changes in the warming cycle is not as pronounced as in the cooling one **(Fig 3.10).** This could be due to the fact that during warming the system contains higher fraction of the FMM than in the cooling cycle i.e., during reverse process of FMM to AFMI conversion is slow enough to be quasi equilibrium process. The resistivity-time behaviour for a time of t= 8×10^3 sec measured at several temperatures during cooling and warming has been analysed in terms of the Debye/non-Debye relaxation. This relaxation model is studied in the transition from liquid to liquid crystal which retain only orientational order, orientationally disordered crystal and an amorphous solid where transitional disorder has been dramatically frozen, quite extensively. This behaviour is a signature of non-ergodicity usually attributed to competing long range interaction, microscopic memory effects or (multi) fractional structure of the phase space. In the present case the non-ergodicity arises (as discussed in relation to the ρ-T data in **Fig. 3.5**) from the competing AFMI and FMM

interaction, which give rise to a magnetic liquid. This relaxation is represented mathematically by the stretched exponential function of the type $\Phi(t) \sim e^{(-t/\tau)^{\beta}}$, where $\beta=1$ for Debye relaxation and $0 < \beta < 1$ for the non-Debye one **[16]**. The ρ-t data has been fitted with an equation of the type

$$\rho(t) = \rho_0 + \rho_0 e^{(-t/\tau)^{\beta}} \qquad (3.1)$$

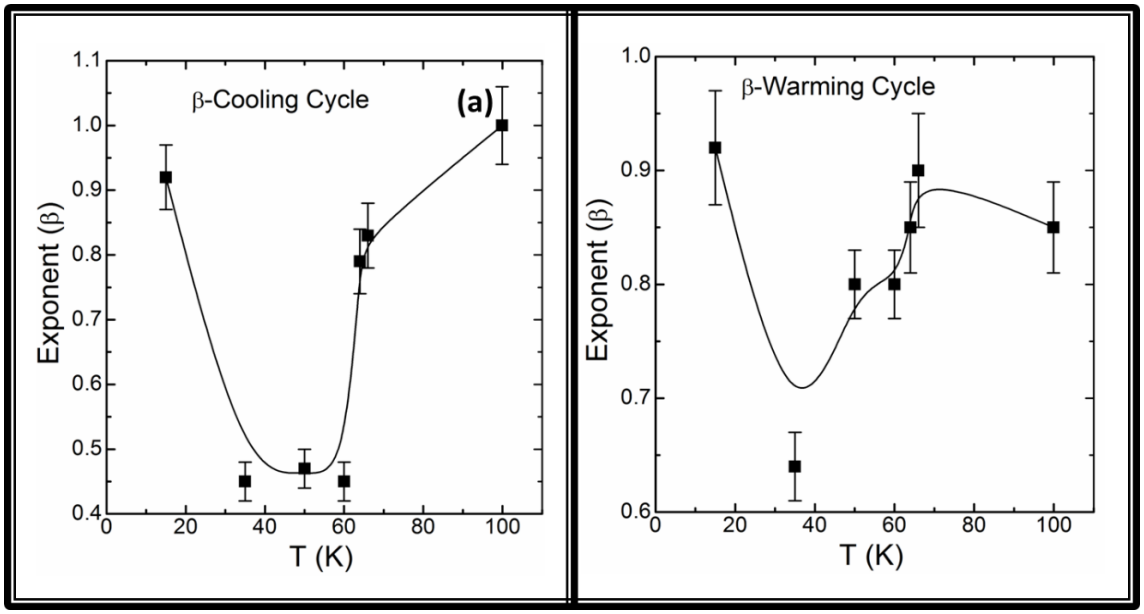

Figure 3.11: fitted ρ - t data in terms of the non-Debye type relaxation model

The solid lines are fit to the experimental curves. The value of the constant τ and β are obtained from the best fit are plotted as a function of temperature in **Fig. 3.11**. From this figure it is clear that in the temperature regime dominated by the magnetic liquid state, the relaxation is fast and behaviour is strongly non-Debye type, while in the lower temperature glassy region it is extremely slow (due to spin freezing) and approaches Debye type. The relaxation behaviour in the present films is generally different from those reported for similar compounds **[17].**

In this chapter it is shown that the electrical transport in a strongly phase separated manganite thin film is extremely sensitive to the relative fraction of the coexisting FMM and AFM/COI phases and has inherent non-ergodic nature. The phase separation tendency is weakened with the reduction of AFM/COI phase fractions. The supercooling insulator-metal transition is non-unique and depends on the relative fractions of the FMM and AFM phases at the start of the magneto-thermodynamic process. In contrast, the superheating transition has equilibrium characteristic and remains independent of the ratio of the two ordered phases. The relaxation behaviour of the resistivity shows a strong non-Debye type character in the temperature region dominated by the magnetic liquid.

3.4 References

[1] M. Uehara, S. Mori, C. H. Chen, and S.-W. Cheong, Nature **399**, 560 (1999).

[2] L. Ghivelder and F. Parisi, Phys. Rev. B **71**, 184425 (2005).

[3] P. A. Sharma, S. B. Kim, T. Y. Koo, S. Guha, and S.-W. Cheong, Phys. Rev. B **71**, 224416 (2005).

[4] W. Wu, C. Israel, N. Hur, S. Park, S.-W. Cheong, and A. de Lozanne, Nat. Mater. **5**, 881 (2006).

[5] V. Podzorov and B. G. Kim, Phys. Rev. B **64**, 140406 (2001).

[6] T. Dhakal, J. Tosado, and A. Biswas, Phys. Rev. B **75**, 92404 (2007).

[7] H. Jeen and A. Biswas, Phys. Rev. B **88**, 024415 (2013).

[8] T. Z. Ward, S. Liang, K. Fuchigami, L. F. Yin, E. Dagotto, E. W. Plummer, and J. Shen, Phys. Rev. Lett. **100**, 247204 (2008).

[9] V. G. Sathe, A. Ahlawat, R. Rawat, and P. Chaddah, J. Phys. Condens. Matter **22**, 176002 (2010).

[10] S. Singh, M. R. Fitzsimmons, H. Jeen, A. Biswas, and M. E. Hawley, Appl. Phys. Lett. **101**, 22404 (2012).

[11] J A Mydosh, *Spin Glasses : An Experimental Introduction*, 2nd editio (Taylor & Francis, 1993., London ; Washington, DC, 1993).

[12] R. Prasad, M. P. Singh, P. K. Siwach, A. Kaur, P. Fournier, and H. K. Singh, Appl. Phys. A **99**, 823 (2010).

[13] M. K. Srivastava, P. K. Siwach, A. Kaur, and H. K. Singh, Appl. Phys. Lett. **97**, 182503 (2010).

[14] V. Agarwal, R. Prasad, M. P. Singh, P. K. Siwach, A. Srivastava, P. Fournier, and H. K. Singh, Appl. Phys. Lett. **96**, 052512 (2010).

[15] P. Littlewood, Nature **399**, 529 (1999).

[16] T. V. Ramakrishnan, M. R. Lakshmi, and M. Rajalakshmi, *Non-Debye Relaxation in Condensed Matter: Proceedings of the Discussion Meeting, Bangalore* (Singapore ; New Jersey : World Scientific, 1987., n.d.).

[17] D. Kumar, K. Kumar, A. Banerjee, and P. Chaddah, J. Phys. Condens. Matter **24**, 386001 (2012).

4 Magnetotransport Properties of Supercooled Phase Separated Manganite Thin Film

4.1 Introduction

Phase separation (PS) has been recognized as the most striking intrinsic property for the thorough understanding of the physical properties of doped rare earth manganites having general formula $RE_{1-x}AE_xMnO_3$ **[1–5].** The relative fraction of the coexisting electronic phases plays a crucial role in understanding the degree of PS, which in turn depend on the interaction between spin, lattice and charge degrees of freedom. These fundamental degrees of freedom are dependent on structural factors like the tolerance factor (t), which is generally determined by the average size of the RE/AE cations, size mismatch between the RE and AE cations and the value of x **[3]** Extensive experimental and theoretical investigations have established PS as the most dominant mechanism on the composition-temperature (x-T) diagram of intermediate and low bandwidth manganites like $Nd_{1-x}Sr_xMnO_3$ **[3,6]**, $Sm_{1-x}Sr_xMnO_3$ **[7,8]** and $La_{1-x-y}Pr_yCa_xMnO_3$ **[9–12].** Amongst these materials, $La_{1-x-y}Pr_yCa_xMnO_3$ (LPCMO) has emerged as the prototypical system among the phase separated manganites. The pronounced nature of the PS with coexistence of sub-micrometer scale ferromagnetic metallic (FMM) and antiferromagnetic/charge ordered insulator (AFM/COI) clusters is well demonstrated in various studies **[9–11,13–15]**. The AFM/COI phase appears explicitly in magnetotransport measurements only at $y \geq 0.3$ with $x \approx 3/8$ and percolative electrical transport have been evidenced by huge residual resistivity (ρ_0) for $y \approx 0.4$ in the metallic regime **[9]**. Bulk-polycrystalline $La_{5/8-y}Pr_yCa_{3/8}MnO_3$ ($y \approx 0.4$) show COI phase at $T_{CO} \approx 230$ K and subsequent transition to AFM and FM spin order at $T_N \approx 180$ K and $T_C \approx 80$ K, respectively and large temporal relaxation

in magnetization and resistivity has also been observed due to the rapid spatial and temporal variations in the relative fraction of FMM and AFM phases **[10]**. LPCMO also show the existence of a liquid like magnetic state in the phase separated regime, which transforms cooperatively to a randomly frozen glass like phase, termed as strain glass (SRG), at low temperature due to the presence of martensitic accommodation strain **[11]** . Various other studies on the properties of LPCMO have been discussed in *chapter 1*.

In the previous chapter tunability of the IMT in terms of the variation in the relative fraction of the coexisting FMM and AFM/COI phases in $La_{5/8-y}Pr_yCa_{3/8}MnO_3$ (y≈0.4) (LPCMO) thin film (~42 nm) have been discussed in detail. Here in this chapter, a detailed investigation of the impact of supercooling/superheating on the electrical transport of similar LPCMO (~42 nm) film on STO substrate in varying magnetic field has been presented. The non-ergodic magnetic state have been established by magnetization measurements and the origin of this non-ergodicity could be traced to the magnetic liquid like state arising from the delicacy of the coexisting magnetic phases, viz., ferromagnetic and antiferromagnetic-charge ordered (FM/AFM-CO). Further, nature of transport below and above insulator to metal transition temperature (T_{IM}) has also been established in this chapter.

4.2 Experimental Details

A stoichiometric (2 inch) target of $La_{5/8-y}Pr_yCa_{3/8}MnO_3$(y≈0.4), as prepared by solid state route, was used for thin film deposition by RF magnetron sputtering of in 200 mtorr of Ar + O_2 (80% + 20%) mixture on single crystal (001) $SrTiO_3$ (STO) substrates maintained at ~ 800 °C. The detailed description of target preparation and thin film deposition is described in chapter 2. In order to achieve optimum oxygen content the films were annealed at ≈900 °C for 10 hrs. in flowing oxygen. The structural and microstructural

characteristics were probed by high resolution X-ray diffraction (HRXRD, PANalytical PRO X'PERT MRD, Cu-Kα1 radiation λ = 1.5406 Å) and atomic force microscopy (AFM, VEECO Nanoscope V), respectively. The temperature and magnetic field dependent magnetic and magnetotransport properties were measured by commercial MPMS and PPMS (both Quantum Design). The transport measurements were done in linear four contact configuration. The current was supplied through the outer probes and the voltage was measured across the two inner electrodes. The contacts were made by 50 μm diameter Cu wires and EPO-TEK (Epoxy Technology) conductive epoxy.

4.3 Results and Discussion

4.3.1 Structural and Microstructural Analysis

The thickness of LPCMO thin film was estimated to be ~ 42 nm from X-ray reflectivity (XRR) as described in chapter 3. The similar film has been used for detailed investigation of the impact of supercooling/superheating on the electrical transport. The structural information was extracted from 2θ–ω scan plotted in **Fig. 4.1**. Appearance of out of plane diffraction maxima (00ℓ) only in the 2θ–ω scan confirms highly oriented nature of the film. Out of plane lattice constant estimated from 2θ–ω scan is found to be $a_{cf} \approx 0.3832$ nm. This value is slightly smaller than average out of plane lattice constant ($a_{cb} \approx 0.3842$ nm) of the bulk used for the sputter deposition of the present film. The observed decrease in the out-of-plane (OP) lattice parameter is due to the in-plane tensile strain due to the larger in-plane lattice constant of substrate (STO, $a_s \approx 0.3905$ nm) as compared to the bulk ($a_b \approx 0.3843$ nm). This tensile strain stretches the MnO_6 octahedron along the plane of the substrate and leads to the decrease in the OP parameter. The tensile strain strengthens the Jahn-Teller distortion and the superexchange interaction which favors AFM/COI phase. However, prolonged oxygen annealing carried out in the present

study is expected to relax the strain to a great extent. This is supported by the fact that there is only moderate difference between the OP parameter of bulk and film. To evaluate in-plane growth nature of the film ϕ scans were measured. The ϕ scans of (001) plane of STO and LPCMO is shown in **inset of Fig. 4.1**. The ϕ scans peak separation of 90° in STO as well as LPCMO confirm the four fold symmetry of the film and cube on cube coherent growth.

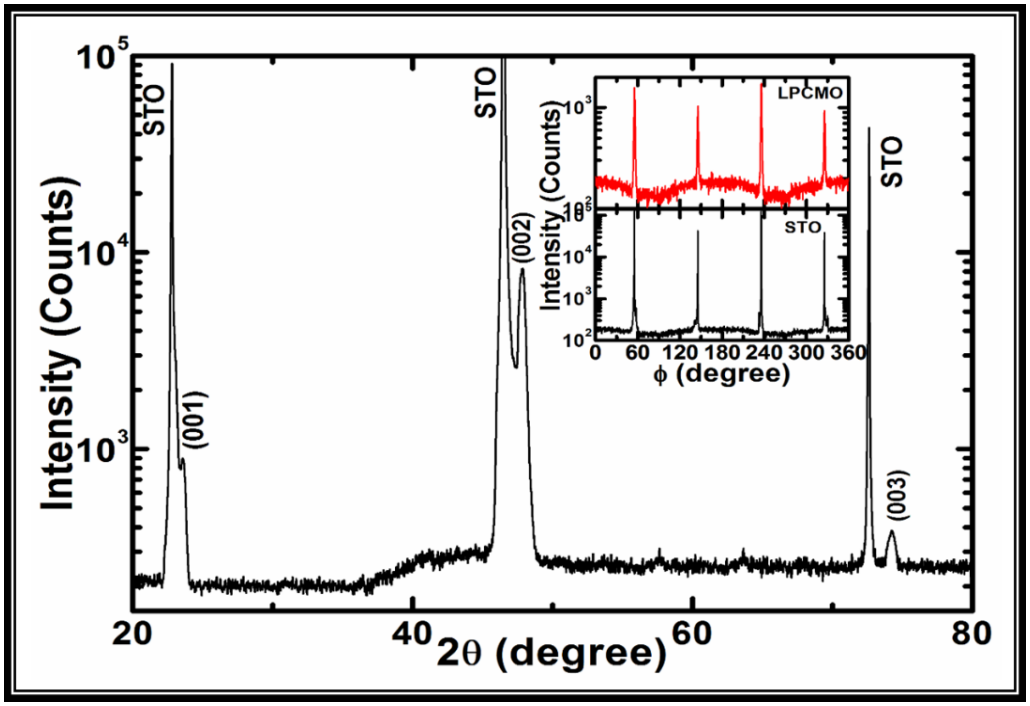

Figure 4.1: X-ray diffraction pattern of LPCMO film on STO. Inset shows ϕ-scan of (001) plane of LPCMO film and STO substrate

In order to acquire qualitative idea about the degree of defects and hence to probe the structural quality of the film, in-plane and out-of-plane rocking curves (ω scan) were measured. For ω scan we have chosen the highest intensity peak, viz. (002). Here we would like to mention that the full width at half maximum (FWHM) increases with the order of reflection. As shown in **Fig. 4.2** the out-of-plane rocking curve of (002) reflection) has FWHM $\Delta\omega \approx 0.63°$, which is higher than generally observed values for manganite films

deposited by magnetron sputtering **[16]**. The in-plane rocking curve of (110) reflection has FWHM $\Delta\omega \approx 0.99°$, which is considerably larger than the out-of-plane value. The symmetry of the two rocking curves suggests that the film is nearly strain free. The long duration oxygen annealing and larger mismatch between the substrate (a = 0.3905 nm) and bulk (a= 0.3842 nm) in plane lattice parameters could be regarded as the major influences causing relaxation of strain.

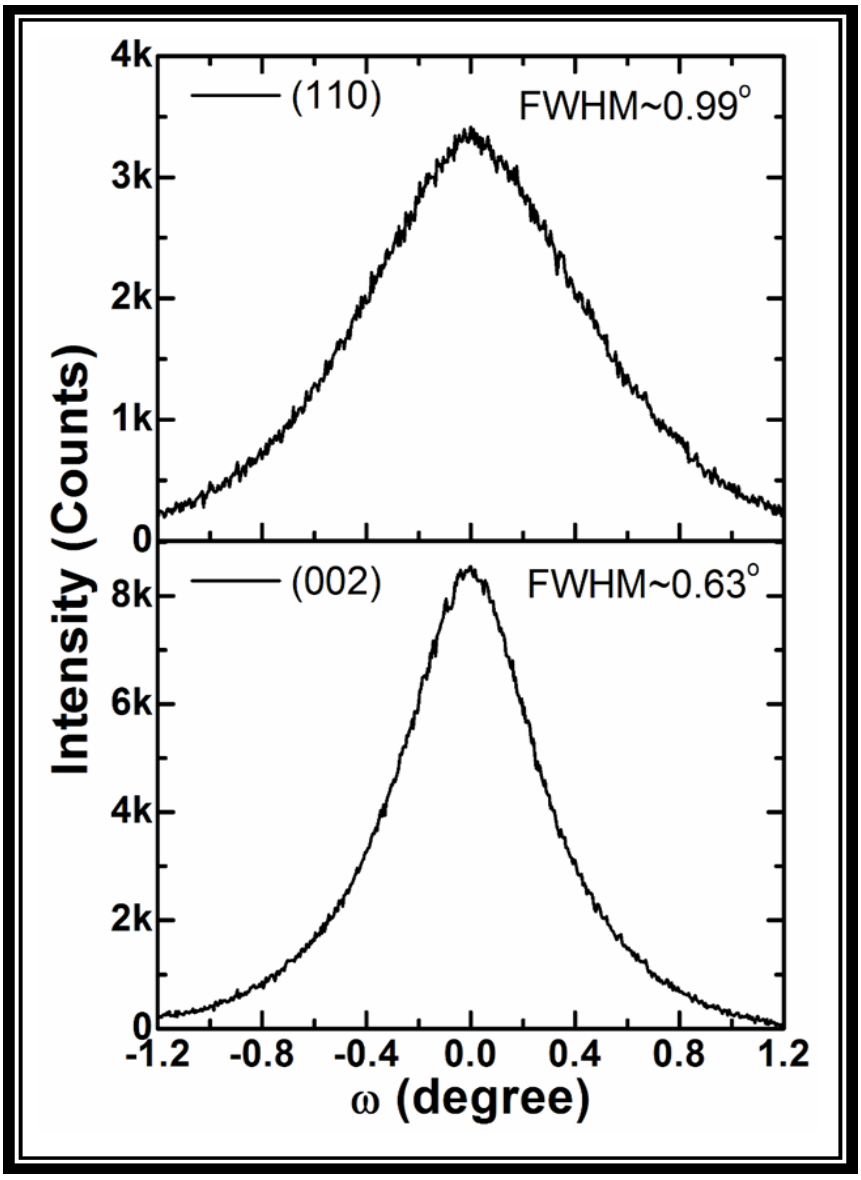

Figure 4.2: Rocking curve (ω-scan) along (110) and (001) planes of LPCMO film.

The broadening of the rocking curve is generally attributed to the presence of (i) strain, (ii) dislocation density, (iii) mosaic spread, and (iv) curvature. As pointed out above the rocking curve broadening due to strain is expected to be very small. Although small variation in the FWHM of the rocking curves was observed as a function of the beam size, no linear dependence could be established between them. This rules out the contribution from curvature induced broadening. Thus the rocking curve broadening in the present case is attributed mainly to the mosaic spread and dislocation density. Since the FWHM variation with the beam size was not appreciable we believe that the dominant contribution to the peak broadening comes from the presence of dislocation arrays/network. The large difference between the FWHMs of (002) and (110) rocking curves suggests that the density of defects and mosaicity are different along the different planes, that is, the density distribution is anisotropic. In this regard it appears that the substrate film interface could have higher density of dislocations as compared to the epitaxial layers above. In fact it is well known that the dislocation networks present at the interface provide relaxation of substrate induced strain. The dislocation in the upper film layers are created due to the non-equilibrium energetic conditions that exist during the growth. The FWHM of the ω-scan of the annealed film is always found to be much higher than that of the as grown film.

The epitaxial nature of the film is also reflected in the surface topography. A representative atomic force microscope (AFM*) image of the annealed film shown in **Fig. 4.3**, further confirms the epitaxial growth. The inset shows the AFM* image of as grown film which is granular in nature with average roughness ~ 1.41 nm. Post deposition annealing in oxygen environment results in layer by layer growth/step terrace growth. This is clearly seen in the surface AFM* image. Although the steps and terraces are not well defined, the average surface roughness is reduced to less than ~ 0.47 nm (nearly one unit cell). This agrees well with the surface roughness estimated from the XRR simulation (as

described in chapter 3). The appearance of holes and regular discontinuities in the individual layers could be regarded as an evidence of the lattice defects. These defects are generated due to the relaxation of the large strain between the substrate and the material during the oxygen annealing.

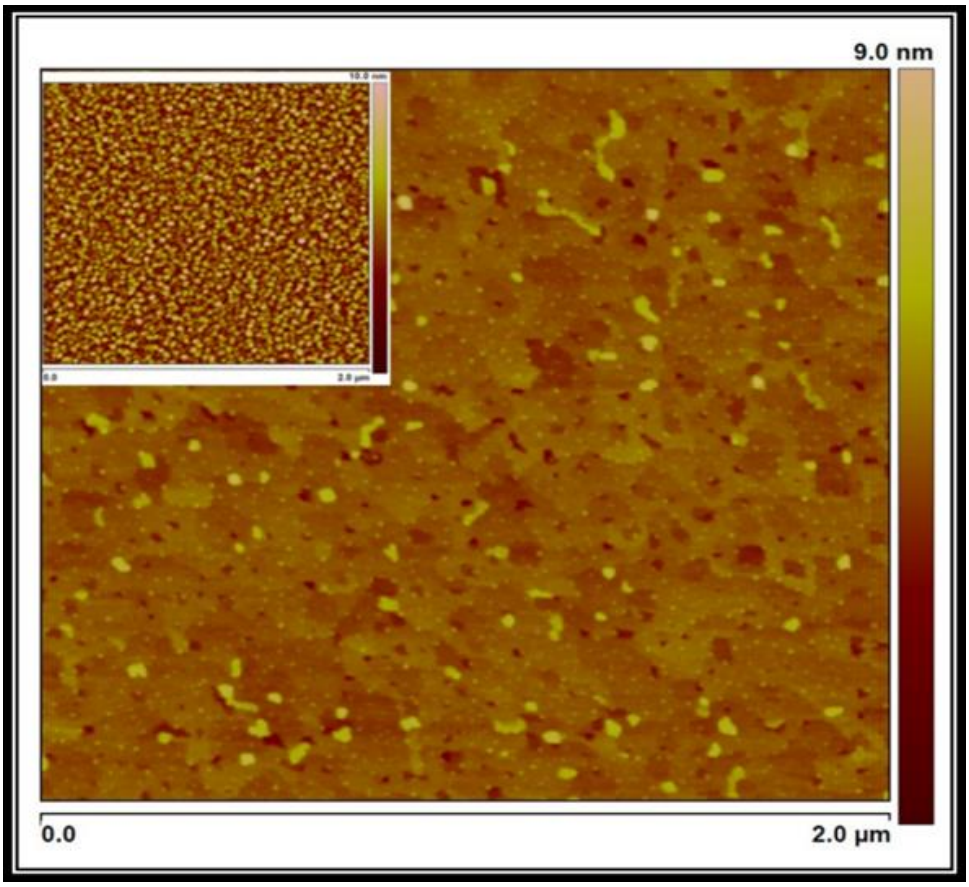

Figure 4.3: Tapping mode AFM image of annealed LPCMO film. Inset shows AFM image of as grown film

4.3.2 Temperature and Magnetic Field Dependent Magnetization Analysis

The temperature dependent magnetization M (T) was measured using zero field cooled (ZFC), field cooled cool (FCC) and field cooled warming (FCW) protocols. The detailed analysis of the M (T) data has already been presented in chapter 3. For the sake of convenience and continuity the main results are summarized here. The FM transition temperature (T_C) occurs at $T_C \approx 117$ K, $T_C^C \approx 63$ K and $T_C^W \approx 120$ K in the ZFC, FCC and

FCW protocols, respectively. The protocol dependence of FM transition evidenced non-ergodicity. A significant difference between the T_C in the FCC and FCW protocols coupled with the huge hysteresis between these two M (T) curves is a consequence of supercooling of the liquid like state due to the magnetic frustration caused by competing FM and AFM/COI interactions. The explicit absence of the COI and AFM transitions could be due to defect induced quenching of AFM/COI in thin film form. Further, the prominent divergence of the ZFC-FCW M (T) is invariably a signature of cluster glass state and originates due to the coexistence of FMM and AFM/COI phases below the Neel temperature T_N. **[11,12,17]**. The sharp drop in the ZFC curve in conjunction with the lower temperature reversibility of the FCC-FCW M (T) is a signature of cluster freezing **[10–12]**. The reversible regime nearly temperature independent M (T) represents the frozen or blocked magnetic clusters and there is unblocking of such clusters with further rise in temperature. A maxima in the FCW M (T) curve was observed where the clusters are completely unblocked.

The magnetic properties were further elucidated by measuring the magnetic field dependence of magnetization (M (H)) at several temperatures. The diamagnetic contribution of the substrate was removed by subtracting the magnetization data of the bare STO substrate from the as-acquired data of the film. The M (H) data measured at 10 K and 50 K is plotted in **Fig. 4.4**. At both temperatures virgin cycle M (H) show nearly identical field dependence and rise sharply up to ~2 kOe (**lower inset in Fig. 4.4).** At H > 2 kOe the M (H) at 10 K bends and then increases linearly up to the highest applied magnetic field (H=50 kOe). In contrast, the M (H) measured at 50 K continues to increase beyond H=2 kOe, albeit with changing slope and then appears to saturate at H>30 kOe. The observed difference in the two virgin M (H) curves could be attributed to the different nature of the magnetic state. At 10 K the magnetic clusters are randomly frozen into a glassy state, while

at 50 K is just above the temperature at which the clusters are unblocked completely (peak in the M-T curve). Hence at T=50 K, the FMM phase is dominant with possibility of AFM/COI droplets embedded into it. It is precisely due to this reason that M (H) at 50 K saturates. Beyond the virgin cycle the M (H) curve traces a typical loop at both the temperatures. In fact such behavior of M (H) curves has been generally attributed to the metamagnetic nature of the magnetic ground state. In the LPCMO films under study, as explained in chapter 3 and summarized above a metamagnetic glassy state is created by the competing FM and AFM/COI phases. The coercivity is observed to decrease from H_C ≈ ± 737 Oe at 10 K to ±502 Oe at 50 K (**upper inset in Fig. 4.4**).

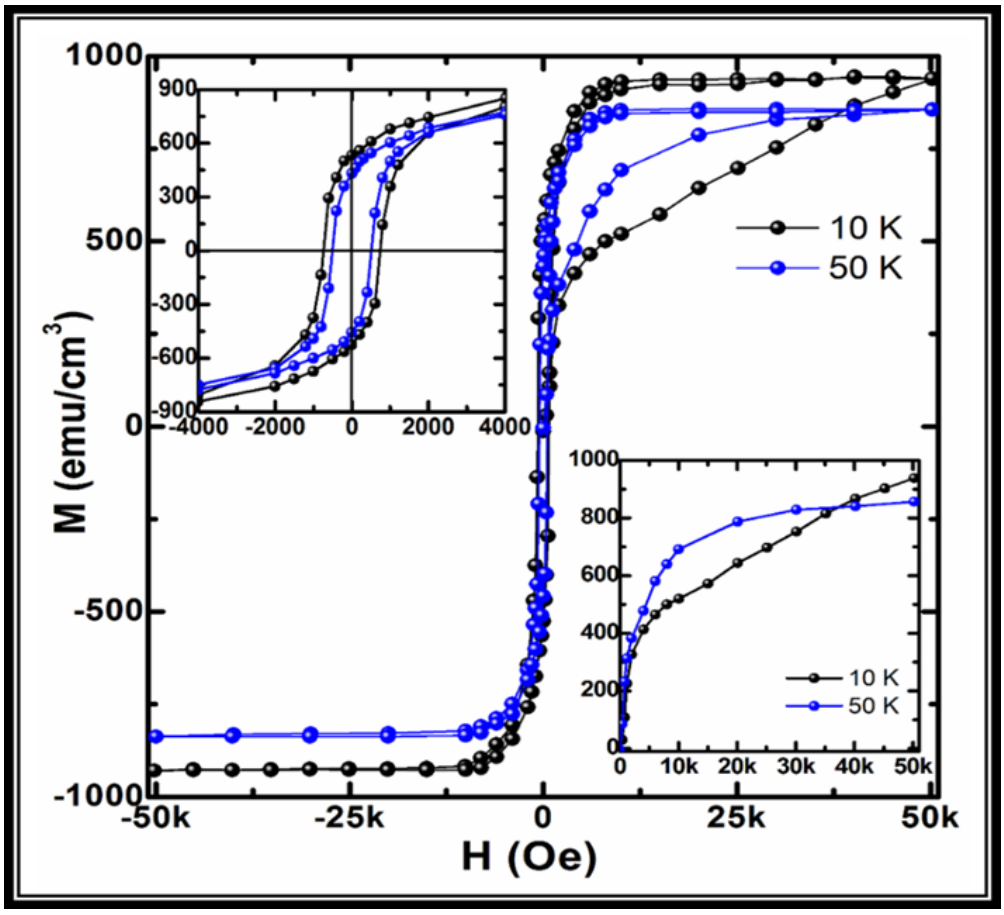

Figure 4.4: Magnetization-Magnetic field loop measured at 10 K and 50 K.

The remanent magnetization decreases from $M_r \pm 550$ emu/cm^3 at 10 K to ±440 emu/cm^3 at 50 K. The M (H) curves shows saturation tendencies at much higher field, around H~10 kOe in both cases. Here it must be pointed out that in the present case the saturation moment (≈ 940 emu/cm^3 of ≈ 5.6 μ_b/Mn) is larger than the theoretical value. The higher value of the magnetic moment could be regarded as the signature of the giant magnetic moment effect, in which due to magnetic field induced polarization effect the AFM/COI phases could be transformed into FM ones. This this effect has been reported for several magnetic glass forming alloys and have been attributed to the field induced magnetic polarization effect, wherein the non-FM phases like AFM are transformed into FM ones **[18]**.

4.3.3 Temperature Dependent Resistivity (ρ -T) Analysis

The temperature dependent resistivity (ρ-T) measured at different values of H was measured in cooling and warming cycles as shown in **Fig. 4.5 (a).** In the cooling cycle ρ-T shows insulating behavior as shown by about six orders of magnitude rise in resistivity between 300 – 65 K and IMT is observed at $T^C_{IM} \approx 64$ K. As T is lowered further down the ρ-T curve appears to saturate. In the warming cycle the ρ-T curve remains reversible with the cooling cycle ρ (T) up to $T_g \approx 15$ K. As T is increased further, ρ (T) decreases, approaching a minimum at $T_M \approx 45$ K (**inset of Fig. 4.5(a)**). In the warming cycle the IMT shifts to a higher temperature and appears at $T^W_{IM} \approx 123$ K. In the PMI regime ρ-T curves overlaps with the one in cooling cycle. The two distinct transitions at T_{IM}^C and T_{IM}^W in cooling and warming cycles are separated by $\Delta T_{IM} \approx 59$ K. The observed thermal hysteresis in ρ (T) is attributed to supercooling and superheating of the magnetic liquid consisting of FMM and AFM-COI phases and is an evidence of a first order phase transition **[6]**. The sharp drop in the ρ-T during the cooling cycle could be regarded as manifestation of

dynamical magnetic liquid behavior. The saturation and reversible behavior of ρ-T at T< T_g is due to the crossover from the liquid like state to the strain glass regime **[11,12,17].** During the warming cycle the ρ-T minimum at $T_M \approx 45$ K has been regarded as a consequence of thermal devitrification of disordered SRG in to an ordered FMM **[15,19]**

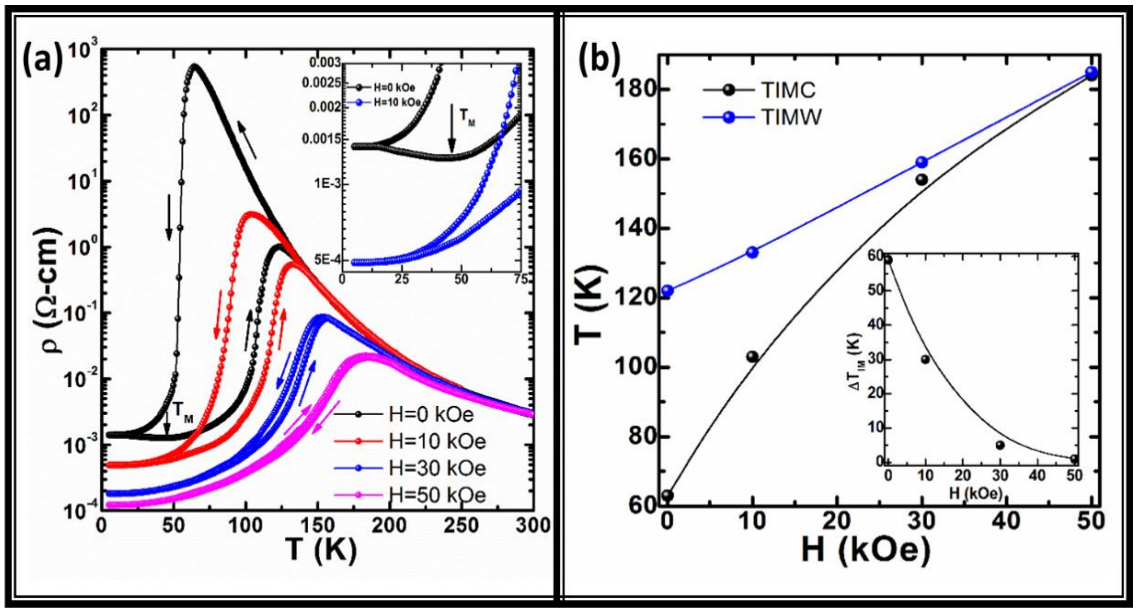

Figure 4.5: (a) Resistivity as a function of temperature (ρ (T) curves) of epitaxial LPCMO film measured at magnetic field (H) of 0, 10, 30 and 50 kOe. (b) Variation T_{IM} as function of applied magnetic field (H) in cooling and warming cycles. Inset shows difference if TIM as a function of H. Lines are guides to the eye.

Application of magnetic field enhances T_{IM}^C/T_{IM}^W, reduces the ρ□T hysteresis, and dilutes the first order nature of the IMT. Another noticeable effect of magnetic field is the disappearance of the ρ-T minimum at H=10 kOe. The observed ρ□T hysteresis and the minimum are related to the magnetic liquid and the SRG, respectively. The application of magnetic field increases the size and fraction of the FMM clusters and simultaneously reduces the size and fraction of the AFM/COI. This magnetic field induced increase in the FMM fraction is expected to (i) reduce the magnetic frustration, (ii) weaken the liquid like behavior and (iii) push the SRG towards a FMM. The variation of the T_{IM}^C and T_{IM}^W with

magnetic is field plotted in **Fig. 4.5(b)** and the variation of ΔT_{IM} with magnetic field is plotted in the inset. The T_{IM}^{C} shows a nonlinear dependence on H, while T_{IM}^{W} increases linearly with applied field. The nonlinearity in the T_{IM}^{C} – H could be regarded as a consequence of the liquid like behavior of the FMM-AFM/COI two phase mixture in the cooling cycle. In the warming cycle the FMM-AFM/COI competition is appreciably weakened and the materials behaves like nearly equilibrium FMM system. This results in linear T_{IM}^{W} – H behavior. Like the M (T) measurements, the cooling and warming cycle ρ-T data do not show any explicit evidence of AFM/COI, the absence of which could be attributed to the presence of lattice defects, such as dislocations. The presence of dislocations could destroy the AFM/COI order by weakening of the J-T distortion and delocalizing the charger carriers **[16]**.

The electron–lattice coupling through the J-T distortion of the MnO_6 octahedron favors an AFM order and in small bandwidth manganites it becomes strong so much so that it challenges the FMM phase and create magnetic frustration even at $T<T_C$. In the present case this is evidenced by the prominent hysteresis and the widely separated magnetic and electrical transition temperatures. Under the influence of a magnetic field the observed modifications in the electrical transport are generally associated with intrinsic nature of carriers and could be probed by the analysis of ρ-T data in the temperature range above T_C. In manganites the electron-lattice coupling often traps the charge carriers and creates polaronic states, which in turn has direct influence on the PM phase electrical transport **[16,20–22].** The ρ-T data at $T>T_C/T_{IM}$ have been analyzed in the framework of adiabatic small polaron hopping model put forth by Emin and Holstein **[23]:**

$$\boldsymbol{\rho\,(T) = ATexp\left(\frac{E_A}{k_B T}\right);\ A = \frac{2k_B}{3ne^2a^2\nu}} \qquad \textbf{(4.1)}$$

Here, the polaronic concentration is given by 'n', site-to-site hopping length is 'a', the attempt frequency for overcoming the potential barrier is given by 'ν', and k_b is the Boltzmann constant. The activation energy, E_a is measured by the potential barrier height and is related to the overlap integral 't' through the relation $t = E_P - 2E_a$. However, in general, the overlap integral is so small that it could be neglected and then $E_P = 2E_a$..

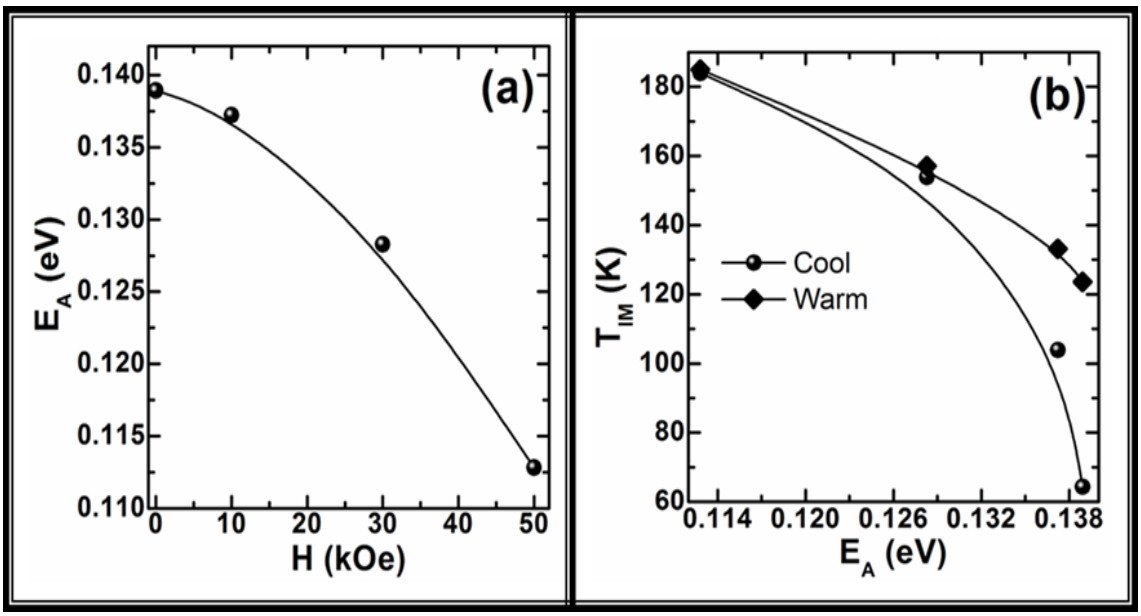

Figure 4.6: (a) Plot of variation of activation energy (E_A) with magnetic field (H) and (b) Plot of variation of T_{IM}^C/T_{IM}^W with E_A. Lines are guides to the eye.

E_A was calculated from the data taken from the best fit (data not plotted here) to eq. (4.1) in the temperature range $T_{IM} \leq T \leq 300$ K. The variation of E_A with magnetic field is plotted in **Fig. 4.6 (a).** In absence of external magnetic field (H=0 kOe) the estimated value of E_A is ≈138 meV. Such high values of the activation energy are typical of the low bandwidth manganite films **[20]** and are significantly larger than that of the large and intermediate bandwidth compounds like $La_{1-x}Sr_xMnO_3$ **[24]**, $Nd_{1-x}Sr_xMnO_3$ **[16]**. Such high value of E_A clearly suggests strong electron-lattice coupling through the J-T distortion. E_A≈138 meV corresponds to $T_{IM}^C/T_{IM}^W \approx 64$ K/123 K in cooling and warming

cycles. As the magnetic field is increased the value of E_A decreases nonlinearly and at H=50 kOe, $E_A \approx 112$ meV corresponds to $T_{IM}^C/T_{IM}^W \approx 184$ K/185 K in cooling and warming cycles. The variation of T_{IM}^C/T_{IM}^W with E_A is plotted in **Fig. 4.6 (b).** The sharp rise in T_{IM}^C at smaller magnetic field, that is, higher values of E_A is a signature of the liquid like behavior of the two phase mixture in the cooling cycle. This liquid like behavior is not retraced in the warming cycle and hence T_{IM}^W - E_A behavior is nearly linear.

In the low temperature FMM regime, the ρ-T is parametrized by (i) sharp decrease in the cooling cycle, (ii) appearance of a minimum at T_M at H=0 kOe in the warming cycle which vanishes at H≥10 kOe, (iii) relatively slower increase in the warming cycle. The low temperature ρ-T behavior is not well studied in strongly phase separated manganites like the present compound. In order to explain the low temperature ρ-T behavior in manganites several mechanisms have been in taken into consideration. The first is the Kondo like scattering given by, $\rho_k(T) \propto \ell nT$. **[25].** The second mechanism, generally observed in a disordered metallic system which changes sign as a function of disorder, arises from the elastic scattering and is given by $\rho_c \propto T^{0.5}$ **[26]** The third term is the electron-electron (e-e) scattering described by a contribution of the type $\rho_{ee} \propto T^2$ **[24,26]**. The fourth contribution is the electron-phonon (e-ph) scattering, which at low temperatures acquires the form $\rho_{eph} \propto T^5$ and in view of the strong electron-lattice coupling through the J-T distortion is expected to make significant contribution to the low temperature resistivity of low bandwidth manganites **[24]**. In the present case we tried to fit the cooling and warming cycle low temperature ρ-T data measured at different magnetic fields using different combination of the above mentioned mechanisms. It is interesting to note that except the zero magnetic field warming data, all the ρ-T curves at $T \ll T_{IM}$ were fitted very well by the following equation:

$$\rho(T) = \rho_0 + \rho_{ee}T^2 + \rho_{ph}T^5 \qquad (4.2)$$

Here, ρ_0 is the residual resistivity arising due to elastic scattering like electron impurity scattering. The ρ-T data of the zero field warming cycle could not be fitted with the eq. (4.2). The appearance of the minimum in the H=0 warming cycle ρ-T prompted us to consider the Kondo like scattering. It has been shown that in inhomogeneous magnetic systems, e. g., those exhibiting glassy behavior like the present films, Kondo like transport may appear in the low temperature regime. **[24]**. The best fit to this was obtained by replacing the e-e scattering by the Kondo term ($\rho_k(T) \propto \ell nT$), that by the equation,

$$\rho(T) = \rho_0 - \rho_k \ell nT + \rho_{ph}T^5 \qquad (4.3)$$

However, the ρ-T data corresponding to the glassy state (T<18 K) could not be fitted even by this equation. If the e-e scattering is included in eq. (4.3) then it does not converge at all**.** The representative low temperature data along with the fitted ones are presented in **Fig. 4.7 (a) & (b).**

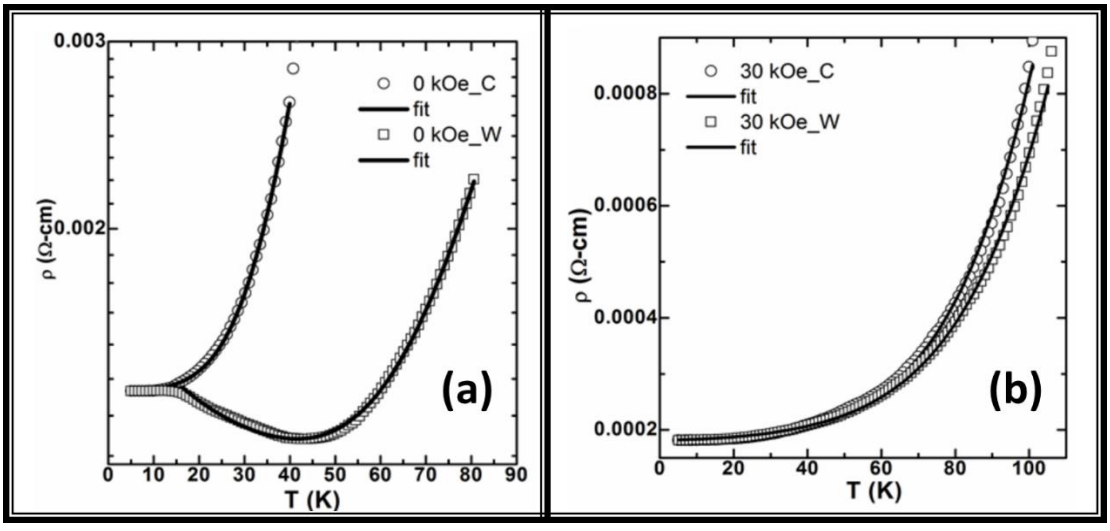

Figure 4.7: The low temperature ρ-T data measured in cooling and warming cycle at (a) H = 0 kOe and (b) H = 30 kOe. The open symbols are the experimental data and the solid line are the fitted data

The fitting parameters ρ_{ee} and ρ_{ph} have been found to depend on the thermal cycling as well as the applied magnetic field. The values of both, ρ_{ee} and ρ_{ph} are found to be higher in the cooling cycle and decrease under the influence of the magnetic field. However, the change in ρ_{ph} as a function of thermal cycle and the magnetic field are much more pronounced.

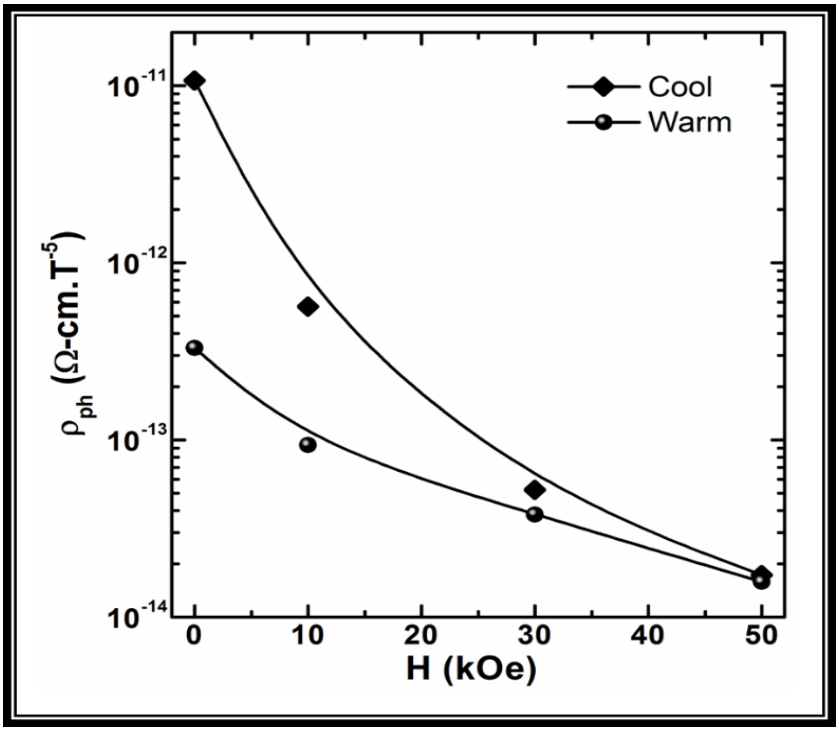

Figure 4.8: Variation of the fitting parameter ρ_{ph} measured in cooling and warming cycle with magnetic field. Lines are guides to the eye.

The variation of the coefficient ρ_{ph} with the H in both the thermal cycles is plotted in **Fig. 4.8**. A sharp decrease in the value of ρ_{ph} in warming cycle as well as with magnetic field in both cooling and warming cycle shows the weakening of the electron-lattice coupling during the warming cycle as well as under magnetic field. This leads to substantially lower resistivity and considerably higher T_C/T_{IM} in the warming cycle as well as at higher values of H. The quantum interference effects can also be taken into account to explain the two temperature transport and the resistivity upturn in intermediate and large

bandwidth manganites **[27–29]**. In low bandwidth manganites like $La_{5/8-y}Pr_yCa_{3/8}MnO_3$ ($y\approx0.4$) the role of phase separation and hence mesoscopic inhomogeneities become more important. This is also clear from the effect of magnetic field on the resistivity minimum. Hence, the Kondo like scattering is the most probable mechanism causing this minimum in strongly phase separated manganites**.**

In this chapter, LPCMO (y=0.4) thin film deposited on STO by RF-magnetron sputtering contains high density of lattice defects such as dislocation networks which are responsible for relaxation of substrate induced strain. Lattice defects such as dislocation networks are confirmed by AFM* measurements. The competing co-existing FMM and AFM/COI phases governs the temperature dependent magnetic and transport properties of LPCMO. The protocol (ZFC, FCC and FCW) dependent FM transitions, strong divergence between the ZFC and FCW M (T) and prominent irreversibility between the FCC-FCW M (T) evidenced the non-ergodic behavior of the magnetic state in this film. This non-ergodicity, the origin of which could be traced to the delicate coexistence of FMM and AFM/COI phases leads to the existence of a liquid like behavior. This liquid like state gets frozen into SRG. M (H) measurements also confirmed the frozen glassy states at low temperatures and unblocking of these frozen states with increasing temperature which are further confirmed by ρ-T measurements at low temperatures. The liquid like behavior is also confirmed by the large drop in resistivity under moderate magnetic fields. The small polaron activation energy decreases nonlinearly with increase in H and the variation of T_{IM} while the activation energy remains nearly linear in the warming cycle, but it becomes nonlinear in the cooling cycle. The analysis of the low temperature ρ-T data reveals the weakening of the electron-lattice coupling under the influence of an external magnetic field as well as during the warming cycle. The devitrification of the frozen glassy state gives rise to Kondo like resistivity minimum.

4.4 References

[1] E. Dagotto, T. Hotta, and A. Moreo, Phys. Rep. **344**, 1 (2001).

[2] E. Dagotto, New J. Phys. **7**, 67 (2005).

[3] Y. Tokura, Rep. Prog. Phys. **69**, 797 (2006).

[4] C. N. R. Rao, A. Arulraj, A. K. Cheetham, and B. Raveau, J. Phys. Condens. Matter **12**, R83 (2000).

[5] P. K. Siwach, H. K. Singh, and O. N. Srivastava, J. Phys. Condens. Matter **20**, 273201 (2008).

[6] H. Kuwahara, Science (80-.). **270**, 961 (1995).

[7] Y. Tomioka, H. Hiraka, Y. Endoh, and Y. Tokura, Phys. Rev. B **74**, 104420 (2006).

[8] M. K. Srivastava, A. Kaur, K. K. Maurya, V. P. S. Awana, and H. K. Singh, Appl. Phys. Lett. **102**, 32402 (2013).

[9] M. Uehara, S. Mori, C. H. Chen, and S.-W. Cheong, Nature **399**, 560 (1999).

[10] L. Ghivelder and F. Parisi, Phys. Rev. B **71**, 184425 (2005).

[11] P. A. Sharma, S. B. Kim, T. Y. Koo, S. Guha, and S.-W. Cheong, Phys. Rev. B **71**, 224416 (2005).

[12] W. Wu, C. Israel, N. Hur, S. Park, S.-W. Cheong, and A. de Lozanne, Nat. Mater. **5**, 881 (2006).

[13] T. Wu, S. B. Ogale, S. R. Shinde, A. Biswas, T. Polletto, R. L. Greene, T. Venkatesan, and A. J. Millis, J. Appl. Phys. **93**, 5507 (2003).

[14] T. Dhakal, J. Tosado, and A. Biswas, Phys. Rev. B **75**, 92404 (2007).

[15] V. G. Sathe, A. Ahlawat, R. Rawat, and P. Chaddah, J. Phys. Condens. Matter **22**, 176002 (2010).

[16] R. Prasad, M. P. Singh, P. K. Siwach, A. Kaur, P. Fournier, and H. K. Singh, Appl. Phys. A **99**, 823 (2010).

[17] V. Podzorov and B. G. Kim, Phys. Rev. B **64**, 140406 (2001).

[18] J A Mydosh, *Spin Glasses : An Experimental Introduction*, 2nd editio (Taylor & Francis, 1993., London ; Washington, DC, 1993).

[19] D. K. Mishra, V. G. Sathe, R. Rawat, and V. Ganesan, J. Phys. Condens. Matter **25**, 175003 (2013).

[20] M. K. Srivastava, P. K. Siwach, A. Kaur, and H. K. Singh, Appl. Phys. Lett. **97**, 182503 (2010).

[21] J. M. D. Coey, M. Viret, and S. von Molnár, Adv. Phys. **48**, 167 (1999).

[22] A. J. Millis, B. I. Shraiman, and R. Mueller, Phys. Rev. Lett. **77**, 175 (1996).

[23] D. Emin and T. Holstein, Ann. Phys. (N. Y). **53**, 439 (1969).

[24] R. Prasad, H. K. Singh, M. P. Singh, W. Prellier, P. K. Siwach, and A. Kaur, J. Appl. Phys. **103**, 083906 (2008).

[25] J. Zhang, Y. Xu, S. Cao, G. Cao, Y. Zhang, and C. Jing, Phys. Rev. B **72**, 054410 (2005).

[26] D. Kumar, J. Sankar, J. Narayan, R. K. Singh, and A. K. Majumdar, Phys. Rev. B **65**, 094407 (2002).

[27] M. Ziese, Phys. Rev. B **68**, 132411 (2003).

[28] L. Maritato, C. Adamo, C. Barone, G. M. De Luca, A. Galdi, P. Orgiani, and A. Y. Petrov, Phys. Rev. B **73**, 094456 (2006).

[29] G. Herranz, F. Sánchez, J. Fontcuberta, V. Laukhin, J. Galibert, M. V. García-Cuenca, C. Ferrater, and M. Varela, Phys. Rev. B **72**, 014457 (2005).

5 Quantification of Phase Separation in Terms of Magnetoresistive Hysteresis Loops in Phase Separated Manganite Thin Films

5.1 Introduction

Manganese incorporating perovskite oxides represented generically by $RE_{1-x}AE_xMnO_3$, where RE and AE are rare earth and alkaline earth cations have engaged the interest of the physics community for nearly a quarter century now because of their highly enriched nature regarding the electronic phases **[1–3]**. The presence of various phases is demonstrated by the existence of paramagnetic insulator (PMI), ferromagnetic metal (FMM), a ferromagnetic insulator (FMI), an antiferromagnetic insulator (AFMI) and charge ordered/orbital ordered (CO/OO) phases **[1–3]**. The RE/AE ratio, their average cationic size and thermomagnetic variables like temperature (T) and magnetic field (H) controls the nature and relative phase fractions in a manganite system. The sufficiently small average RE/AE cation radii manifests reduced one electron bandwidth (BW) by making the interphase boundaries permeable and cross boundary electronic phase diffusion noticeable. This cross-boundary phase diffusion is called phase separation, which is the axial attribute of the physics of manganites **[1–3].** As BW is lowered the nature of the PM and FM phases and the associated phase transition deviates from the canonical one due to the phase separation. In low BW manganites like $Sm_{1-x}Sr_xMnO_3$ and $La_{1-x-y}Pr_yCa_xMnO_3$, the dominant phase separation tendencies are considered as intrinsic having mesoscopic dimensionality **[4–10]**. Among low bandwidth manganites, the $La_{1-x-y}Pr_yCa_xMnO_3$ has emerged as the generic representative of the manganites showing mesoscale phase separation with coexisting AFMI/CO and FMM clusters **[6]**.

Various aspects of prototypical phase separated LPCMO have been discussed in detail in chapter 1. Recently, Agarwal et al. **[9,10]** demonstrated that depending on the growth conditions and the degree of microstructural inhomogeneity the difference between cooling and warming cycle T_C and IMTs can be as large as ~73-75 K in $La_{1-x-y}Pr_yCa_xMnO_3$ (x ~ 0.42, y ~ 0.40) thin films. Such huge difference in the magneto-metallic transitions and the devitrification of the glassy phase during warming yields extraordinary hysteresis in FCC-FCW and cooling and warming cycle IMTs. Pronounced divergence of the zero-filed cooled (ZFC) and field cooled warming (FCW) magnetization, noticeable hysteresis between the field cooled cooling (FCC) and FCW magnetization, and strong thermomagnetic hysteresis in resistivity measured during cooling/warming and H increasing/decreasing cycles are the typical signatures of strongly phases separated manganites **[5–16].**

The hysteresis loops are common manifestations of non-equilibrium states and are generally associated with the first order phase transition in which there is a finite barrier to the nucleation of the new phase. It is also related to a glass phase frozen into a non-equilibrium. In case of low BW manganites like $La_{1-x-y}Pr_yCa_xMnO_3$, the finite barrier to the growth of the low temperature ordered FM phase is provided by the high temperature ordered AFM phase and the non-equilibrium states are manifested in the form of the thermomagnetic hysteresis in ρ - T and ρ - H measured during cooling/warming and H increasing/decreasing cycles. Manganites embodying AFMI/CO or a mixture of FMM and AFMI/CO phases, which exhibit magnetic field induced AFMI/CO to FMM first order phase transition are typical representative of this class. The prominent members of the family are the low BW manganites with intrinsic phase separation like $Pr_{1-x}Ca_xMnO_3$ (x≈0.3-0.5) **[3,17,18]**, $Sm_{1-x}Sr_xMnO_3$ (x≈0.35-0.5) **[3,4,19,20]** and $La_{1-x-y}Pr_yCa_xMnO_3$ (x ≈ 0.3-0.5, y ≈ 0.3-0.5) **[5–16]** Among these, the last member has emerged as the prototypical system to study the magnetic field induced first order phase transition, the supercooling glass transition, and the associated thermomagnetic

hysteresis. The hysteretic behaviour of $La_{1-x-y}Pr_yCa_xMnO_3$ (x ≈ 0.3-0.5, y ≈ 0.3-0.5) (LPCMO) as observed in the ρ - T and ρ - H measurements have been studied in fair detail during the last decade **[5–16]**. Depending on the values of the compositional variables x and y the zero field (H=0) difference between the cooling and warming cycle IMTs (T_{IM}^C and T_{IM}^W) can be as large as 50 K-75 K **[9,10]** and as H is increased, both T_{IM}^C and T_{IM}^W rise up, with simultaneous shrinking of the difference between them and the enclosed loop area. Similar differences are seen in the T_C obtained from the FCC and FCW M-T. The isothermal ρ - H curves of LPCMO also show pronounced hysteresis in the magnetic liquid regime. Despite several detailed studies focused on the phase separation in LPCMO, not much attention has been paid to the scaling behavior of the ρ - T and ρ - H hysteresis loops as a function of thermomagnetic variable T and H. We believe that in view of the mesoscopic cluster coexistence, the scaling behavior of the ρ - T and ρ - H hysteresis loops can prove to be an alternative tool to analyze and understand the intrinsic phase separation. With the growing interest in magnetic materials, very little experimental work is reported on the study of scaling behaviour of the hysteresis loops in magnetic systems with complete measurements of both field amplitude and frequency dependence of the hysteresis loops.

Here in this chapter, the scaling behaviour of thermomagnetic hysteresis in temperature and magnetic field dependent resistivity [(ρ-T) and (ρ-H)] has been demonstrated during cooling/warming and H increasing/decreasing cycles in single crystalline $La_{0.21}Pr_{0.42}Ca_{0.37}MnO_3$ thin films. This work is published in ***Applied. Physics A 123:677, (2017).***

5.2 Experimental Details

A stoichiometric (2 inch) target of $La_{5/8-y}Pr_yCa_{3/8}MnO_3$(y≈0.4), as prepared by solid state route, was used for thin film deposition by RF magnetron sputtering in 200 mtorr of Ar + O_2

(80% + 20%) mixture on single crystal (110) $SrTiO_3$ (STO) substrates (5x3x0.5 mm^3) maintained at ~ 800 °C. The detailed description of target preparation and thin film deposition is described in chapter 2. In order to achieve optimum oxygen content the films were annealed at ≈ 900 °C for 10 hr. in flowing oxygen. The X-ray reflectivity (XRR) measurement was used to estimate the film thickness. The structural and topological characteristics were probed by high-resolution X-ray diffraction (HRXRD, PANalytical PRO X'PERT MRD, Cu-Kα1 radiation λ = 1.5406 Å). The temperature dependent magnetotransport properties were measured by commercial PPMS (Quantum Design) with linear four contact configurations. The current was supplied through the two outer probes and the voltage was measured across the two inner electrodes. The contacts were made by 50 μm diameter Pt coated Cu wires and EPO-TEK (Epoxy Technology) conductive epoxy.

5.3 Results and Discussions

5.3.1 Structural Characterization

The film thickness was estimated in nm/minute from by X-ray reflectivity of films deposited under a given set of growth conditions. In the present case thickness is found to be ≈70 nm. The doped bulk $La_{5/8-y}Pr_yCa_{3/8}MnO_3$ (x~0.42 and y=0.36) used for target has Pbnm symmetry and the lattice constants obtained after the Rietveld refinement are found to be a = 0.548 nm, b = 0.546 nm, and c = 0.772 nm. Thus, the average in-plane lattice parameter is a_{av} = 0.387 nm. The pseudo-cubic lattice of manganites is defined as lattice with a lattice parameter of a_{sc}=c/2=0.386 nm. For the cubic STO substrate, the lattice constants are a_c = 0.3905 nm. As a result, epitaxial deposition of LPCMO film on STO substrate can give rise to an in-plane tensile strain of -1.06 % if we take into account the average in plane lattice constant of the bulk LPCMO or -1.26 % if c/2 of the bulk is taken as the pseudo-cubic lattice constant. Whichever may be the case, the film grown on STO (110) is expected to grow with its (110) plane parallel

to that of the substrate and will experience almost uniform strain because the difference between the orthorhombic 'a' and 'b' lattice constants is very small. A representative HRXRD symmetric 2θ/ω scan of the film deposited on STO (110) substrates is shown in **Fig. 5.1**. The occurrence of the diffraction maxima of the LPCMO film and the substrate in close proximity and absence of any other peaks in the HRXRD pattern clearly demonstrates that the former (LPCMO film) has adopted the structural symmetry of the latter (substrate). The 2θ-ω scan presented in **Fig. 5.1** shows two diffraction peaks corresponding to the LPCMO thin film. The broad low intensity peak corresponds to the cubic lattice parameter of 0.3824 nm. This is appreciably smaller than the lattice parameter of the target used and hence signified a large tensile strain.

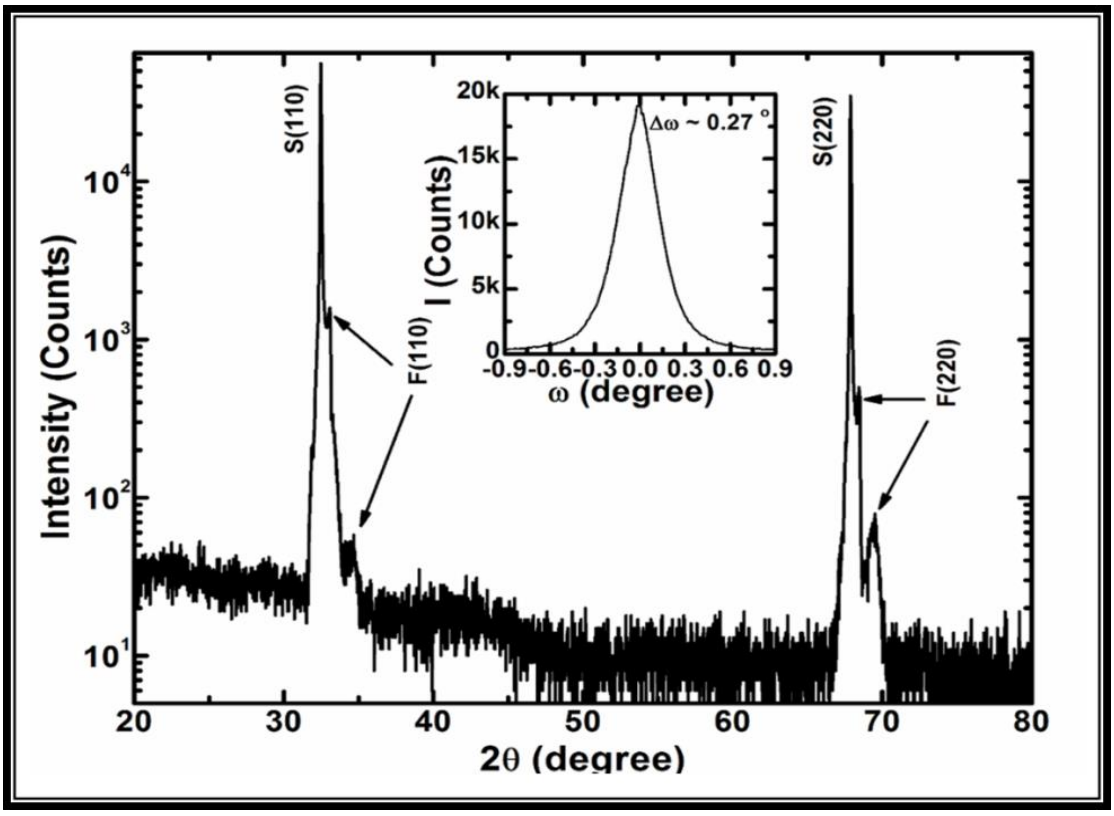

Figure 5.1: 2θ/ω scan of the LPCMO film on STO (110). The arrows indicate the strained and strain relaxed diffraction peaks of the film. The inset shows rocking curve of (220) diffraction peak

The peak with higher intensity, which appears close to that of the substrate yields a cubic lattice constant of 0.3871 nm. This is the same as that of the bulk cubic unit cell and thus corresponds to the strain relaxed part of the film. The rocking curve of the (220) diffraction peak is plotted in the **inset of Fig. 5.1**. The half width at full maximum of the rocking curve is ≈0.27°. This shows that the film has fairly good crystallinity.

Finally we would like to point out that the distribution of the cations is expected to be of disordered type. Ordering of the cationic species (La^{3+}, Pr^{3+} and Ca^{2+}) is indeed important but not a critical factor governing the magnetic and transport behaviour of the strongly phase separated systems like LPCMO. As shown by Zhu et al. **[21]** the ordering of the cations leads to (i) lower resistivity, (ii) higher magnetic moment, (iii) less sharp IMT at higher temperature, and (iv) narrower hysteresis in the cooling and warming cycle ρ-T. Zhu et al. **[21]** achieved the cationic ordering only in the 2 LCMO-PCMO superlattices on (001)-$SrTiO_3$ by laser MBE. But such ordering is extremely difficult to achieve in films prepared from a compound target of LPCMO and the resulting films are generally cation disordered. Here we would like to point out that in contrast to the manganites like different doped variants of $LaMnO_3$, the cationic ordering plays far greater role in determining the properties of double perovskites manganites like $LnBaMn_2O_6$ system (Ln = Y and rare earth ions) **[22,23].**

Apart from the cationic ordering the oxygen vacancies/stoichiometry also play a crucial role in governing the magnetic and magnetotransport properties of manganites. Oxygen vacancies break the symmetry in the arrangement of d-orbitals of manganese ions and hamper the orbital ordering. Through his systematic study of the effect of oxygen stoichiometry in $La_{0.70}Sr_{0.30}MnO_{3-d}$ ($0 \leq d \leq 0.25$), $La_{1-x}Ba_xMnO_{3-x/2}$ and $Pr_{0.70}Ba_{0.30}MnO_{3+\delta}$, Trukhanov has established that decrease in oxygen vacancy (i) lowers the Curie temperature T_C and spontaneous magnetization, (ii) gradually increases the resistivity towards the semiconducting regime, (iii) induces structural changes, and (iv) results in the formation of cluster spin glass

with freezing of magnetic moments at low temperature due to competition between ferromagnetic and antiferromagnetic interactions **[24–26]**. In a study on the large BW manganite $La_{0.5}Ba_{0.5}MnO_3$, Trukhanov et al. have observed a monotonic increase in the T_C and the spontaneous magnetic moment with an increase in the average crystallite size. It has been established that anomalous magnetic properties in large BW manganites could be explained in terms of the two competing size effects, (i) frustration of indirect exchange interaction Mn^{3+}-O-Mn^{4+} on the nanocrystallite surface and (ii) crystal lattice compression due to crystallite surface tension **[27].**

5.3.2 Thermomagnetic Hysteresis and T_{IM} – H Scaling

The temperature dependent resistivity (ρ -T) measured during cooling and warming cycles at several magnetic fields upto H = 70 kOe are shown in **Fig. 5.2 (a).** The resistivity (ρ_{RT} (H = 0 kOe) = 0.048 Ω-cm) increases on lowering the temperature and ρ - T first shows insulator like behaviour and then insulator to metal transition (IMT) appears at T_{IM}^C = 116 K (ρ_{IM}^C (H=0 kOe) =34.921 Ω-cm; an increase of nearly three orders of magnitude). At $T < T_{IM}^C$ the zero field resistivity decreases sharply (ρ_{4K} (H = 0 kOe) = 0.0035 Ω-cm; a decrease by nearly four orders of magnitude). Such sharp IMT is the hall mark of the strongly phase separated manganite families, like $La_{1-x-y}Pr_yCa_xMnO_3$ **[5–16]** and $Sm_{1-x}Sr_xMnO_3$ **[3,4,19,20]** and is caused by the competing mesoscopic FMM and AFMI/CO clusters. During the warming cycle the metal to insulator transition is observed at T_{IM}^W = 163 K (ρ_{IM}^W (H = 0 kOe) = 3.422 Ω-cm) and in the higher temperature regime the resistivity approaches the cooling cycle value. The application of magnetic field (H) pushes the IMT up with concomitant reduction in its sharpness and narrowing of the thermal hysteresis in ρ - T. The drastic difference between the zero field IMT measured during cooling and warming thermal cycles (≈ 47 K) has been understood in terms of the accommodation strain and the energy barrier provided by the AFMI

phase to the nucleation of the lower temperature ordered FMM phase. This results in the formation of a magnetic phase which is akin to a magnetic liquid **[7].** The electrical transport characteristics of the magnetic liquid phase should depend on the relative fractions of FM and AFM/COI phases at the instant from where the low temperature state is approached and consequently IMT temperature corresponding to liquid like magnetic phase should be non-unique (as discussed in chapter 3 in detail). The lower value of the T_{IM}^{C} is caused by the non-equilibrium magnetic liquid and the magnetic frustration is a direct evidence of supercooling of the magnetic liquid formed by the competing AFM and FM phases **[8–10]**. During the warming cycle the system is much closer to the equilibrium due to the dominantly higher fraction of the FMM phase and hence the IMT occurs at almost the actual transition **[28].**

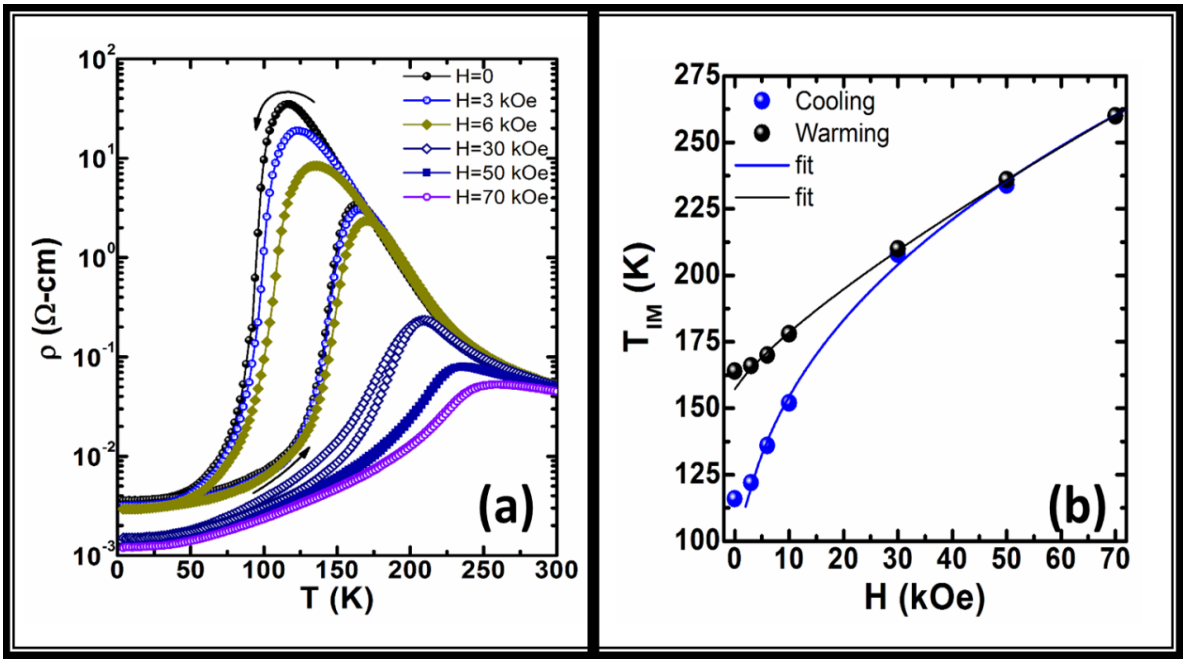

Figure 5.2: (a) ρ - T measured during cooling and warming (2K/min) cycles at different H. (b) Variation of T_{IM}^{C} and T_{IM}^{W} with H. The solid lines are fit to power law eq. (1) (see text).

The ρ - T hysteresis, which is very pronounced in absence of H nearly vanishes at H = 70 kOe and cooling and warming cycle IMTs coincide with $T_{IM}^{C} = T_{IM}^{W} = 262$ K. The evolution of T_{IM}^{C} and T_{IM}^{W} with H plotted in **Fig. 5.2 (b)** shows that during the cooling cycle

the IMT shows a sharp nonlinear rise at H ≤ 45 kOe and above it rises linearly. In contrast, during warming the IMT scales up almost linearly with H. The nonlinear behaviour of T_{IM}^{C} – H is a signature of the non-equilibrium magnetic liquid, which is created by the low energy barrier to the nucleation of the FM phase by the AFM phase. In the warming cycle the system is closer to the equilibrium and hence the T_{IM}^{W} – H is nearly linear. In order to parametrize the IMT-H scaling in terms of some physically relevant empirical law we analysed the data in terms of several power laws. It is found that the scaling of the IMT during the two thermal cycles is well fitted by the power law:

$$\mathbf{T_{IM}(H) = T_{IM}^{0} + \beta H^{\alpha}} \qquad \mathbf{(5.1)}$$

Here T_{IM}^{0} is the characteristic H-independent contribution to the T_{IM}, which can be taken as a measure of the zero field FMM fraction. The second term in eq. (5.1) in which the constant β and the exponent $\boldsymbol{\alpha}$ determine the magnetic field dependent part of the IMT and can be considered as a measure of the relative fraction of the AFMI/CO and FMM phases. The T_{IM}^{C} – H experimental data, except the zero-field value are well fitted by the above equation with, $T_{IM}^{0} = 64.44 \pm 19.50$ K, $\beta = 35.81 \pm 4.02$ K/(kOe)$^{\alpha}$ and $\boldsymbol{\alpha} = 0.40 \pm 0.07$ (R^2=0.99803). During the warming cycle, small deviation is observed for the zero-field data but all other data points are well fitted by the above equation with, $T_{IM}^{0} = 156.41 \pm 1.78$ K, $\beta = 3.53 \pm 0.61$ K/(kOe)$^{\alpha}$, and $\alpha = 0.80 \pm 0.04$ (R^2=0.99803). In **Fig. 5.3** the fit to the experimental data using eq. (5.1) is shown by the solid lines. The large difference in the value of the constants exponent β and α is attribute of the contrasting difference in the nature of the overall magnetic phase realized during the two thermal cycles. The large difference in the cooling and warming cycle values of β in conjunction with fact that it is measure of the H dependent contribution to IMT, suggests that H induced AFMI to FMM phases transition is quite robust during the cooling cycle. As discussed above, in the cooling cycle the magnetic phase is akin to a magnetic

liquid phase and is extremely unstable against the fluctuations arising due to external perturbations like H. This causes the robust H induced AFMI-FMM first order phase transition. At H > 45 kOe, because of the dominance of the FMM over AFMI, the H induced phase transition may not be of the first order and hence the linear behaviour. During the warming cycle the magnetic phase is dominated by FMM fraction and more akin to a solid and hence less sensitive to fluctuations caused by external stimuli such as H. Consequently, the H dependent contribution to T_{IM} is very small and hence a small value of β. The small value of the exponent α for the cooling cycle is consistent with the non-linear behaviour of the non-equilibrium and fluctuation dominated magnetic liquid phase. The nearly equilibrium magnetic phase is manifested by the appreciably larger value of the pre-factor β and exponent α during the warming cycle. Hence the proposed model with a H independent contribution and H dependent part appears to be reasonably successful in explaining the behaviour of T_{IM} – H scaling.

Another interesting feature in the ρ - T data shown in **Fig. 5.2 (a)** is the hysteresis between the cooling and warming cycle curves. The zero field ρ - T curves enclose the largest area, which gradually diminishes as H is increased. Such hysteresis, apart from being signature of the first order AFM/COI–FMM phase transition also manifests the strong magnetic frustration created by the delicate balance between these coexisting phases. At H=70 kOe the area enclosed by the cooling and warming cycle ρ - T curves negligible. The scaling of ρ - T loop area with H can be taken as a signature of the strength of phase separation. The larger loop area signatures stronger phase separation. The decrease in the loop area with increase in H clearly show the weakening of the phase separation tendencies due to H induced AFMI to FMM phase transition. Hence a more detailed analysis of the loop area scaling appears pertinent.

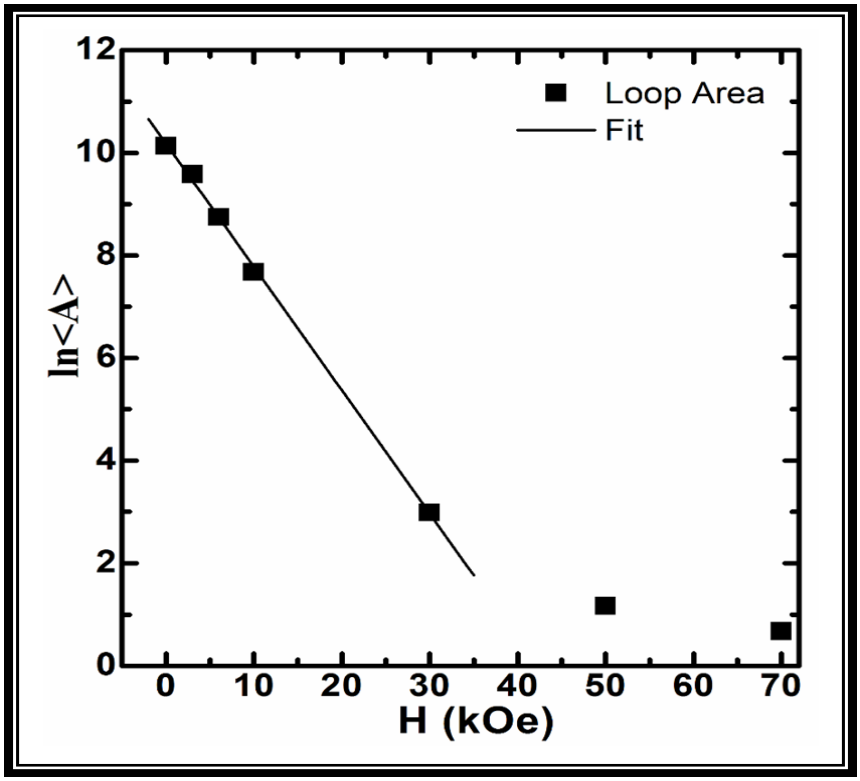

Figure 5.3: Scaling of normalized loop area enclosed by hysteretic (ρ - T) curves at different H. Solid line represent the fit to equation (2) (see text).

For further analysis, the area (A_T) enclosed by the hysteretic ρ - T curves were calculated after normalizing the measured ρ - T data with the room temperature resistivity [ρ (RT)]. The variation of the loop area with H is plotted in **Fig. 5.3.**

While developing models for the scaling of the thermo-magnetic hysteresis in temperature and magnetic field dependent [(ρ-T) and (ρ-H)] loops, (i) the intrinsic mesoscale nature of the phase separation, (ii) non-ergodic and liquid like behaviour of magnetic state during the cooling cycle, and (iii) nearly equilibrium magnetic solid like behaviour of the magnetic state while warming have been taken into account. Our analysis shows that for the $A_T - H$ scaling upto a certain value of H the follows the exponential decay given by

$$\mathbf{A_T(H) = A_{T_0} e^{-\Gamma H}} \qquad \mathbf{(5.2)}$$

Here, A_{T_0} is the zero-field normalized area and Γ is a constant which could be related to the degree of phase separation. The experimental data is well fitted with the above equation up to H ≈ 30 kOe (the solid line in Fig. 4). At H > 30 kOe, the loop area is very small and therefore can be regraded as well outside the strongly phase separated regime with mesoscale magnetic clusters. The value of the constant $\ln(A_{T_0}) = 10.18 \pm 0.06$ and Γ=0.241±0.004/kOe with R^2=0.99887. Thus it is clear that the exponential decay given by eq. (5.2) describes the ρ - T loop area scaling with H quite nicely in the regime which is akin to a magnetic liquid. The linear behaviour of the ln <A> - H curve upto H ~ 30 kOe, is the map of the exponential decrease in the ρ-T loop area with increasing H. This is clearly due to extreme sensitivity of the magnetic liquid phase to the applied magnetic field. The magnetic liquid undergoes a first order AFMI-FMM transition at relatively small H. The deviation from the exponential behaviour at H > 30 kOe is due to the substantial decrease (increase) in the AFMI (FMM) phase fraction which is detrimental to the magnetic liquid like behaviour and favours the appearance of an equilibrium magnetic phase. We believe that the nature of the constant Γ can be ascertained if similar analysis is carried out on thin films having different degree of phase separation that may be induced by either changing the substrate or the composition.

5.3.3 Isothermal Magnetoresistive Hysteresis and ρ - H Scaling

Another hallmark of the manganites exhibiting strong mesoscopic phase separation is the hysteresis in isothermal resistivity versus magnetic field (ρ-H) measurements **[3,8,18,29].** However, the scaling of the ρ-H loop area with the applied DC magnetic field has not be studied so far and hence no scaling laws are existent in the literature. In the present study, we have measured the isothermal ρ - H loops using a protocol, which is used to study the B-H and P-E hysteresis dynamics as function of the field amplitude and frequency in ferromagnetic and ferroelectric materials, respectively **[30–38].** Theoretical and experimental studies spread over

the last two decades have shown that the dynamic M-H loop area scaling follows the following scaling relation:

$$A \propto H^{\eta}\Omega^{\beta}T^{-\gamma} \qquad (5.3)$$

Here, H is the amplitude of the AC magnetic field, Ω is its frequency and T is the temperature. The exponents, α, β and γ depend on the dimensionality and the symmetry of the system and their universality is still under debate. The continuous spin system model predicts α = β =1/2 **[31,32].** In the present case, we assume that the isothermal ρ - H curves would follow the above scaling law with frequency Ω taken as a constant (as there is no AC magnetic field). Since the ρ-H measurements are isothermal, therefore $T = \text{constant}$. Thus in the present case the scaling law should appear like:

$$A \propto H^{\eta} \qquad (5.4)$$

In case of manganites or other magnetoresistive materials, the common practice in ρ - H measurements have been that during the virgin cycle H is varied from zero to the desired value (+H) in the positive field direction, then reversed and brought via H=0 kOe to the same value (-H) in the negative field direction. Afterwards, H is again reversed and allowed to pass via H=0 kOe to the desired value on the positive side (+H). In order to investigate the evolution of the isothermal ρ - H loops measured at different reversal magnetic fields we have employed a measurement protocol in which the loops were traced during the positive cycle only and the reversal magnetic field was increased in the steps of 10 kOe from H=0 to 70 kOe. Thus, for the first ρ - H measurement, the field was varied from 0 to 10 kOe and then reversed back to the initial value. In the next cycle H was increased to 20 kOe and reversed back to H=0 kOe. This procedure was followed for field up to H=70 kOe. All the measurements were done in the cooling cycle. The ρ - H loops measured at different temperatures with the above-mentioned

protocol is shown in **Fig. 5.4 (a)** shows the ρ - H loop measurements at T=185 K. For the first H cycle up to H=10 kOe there is no significant change in resistivity and no hysteresis is observed. However, at all higher H cycles (i) the magnetic field induced drop in resistivity increases successively, (ii) the ρ - H curves show hysteretic behavior with progressively include larger area and (iii) loops traced at smaller H lie inside those traced at higher H.

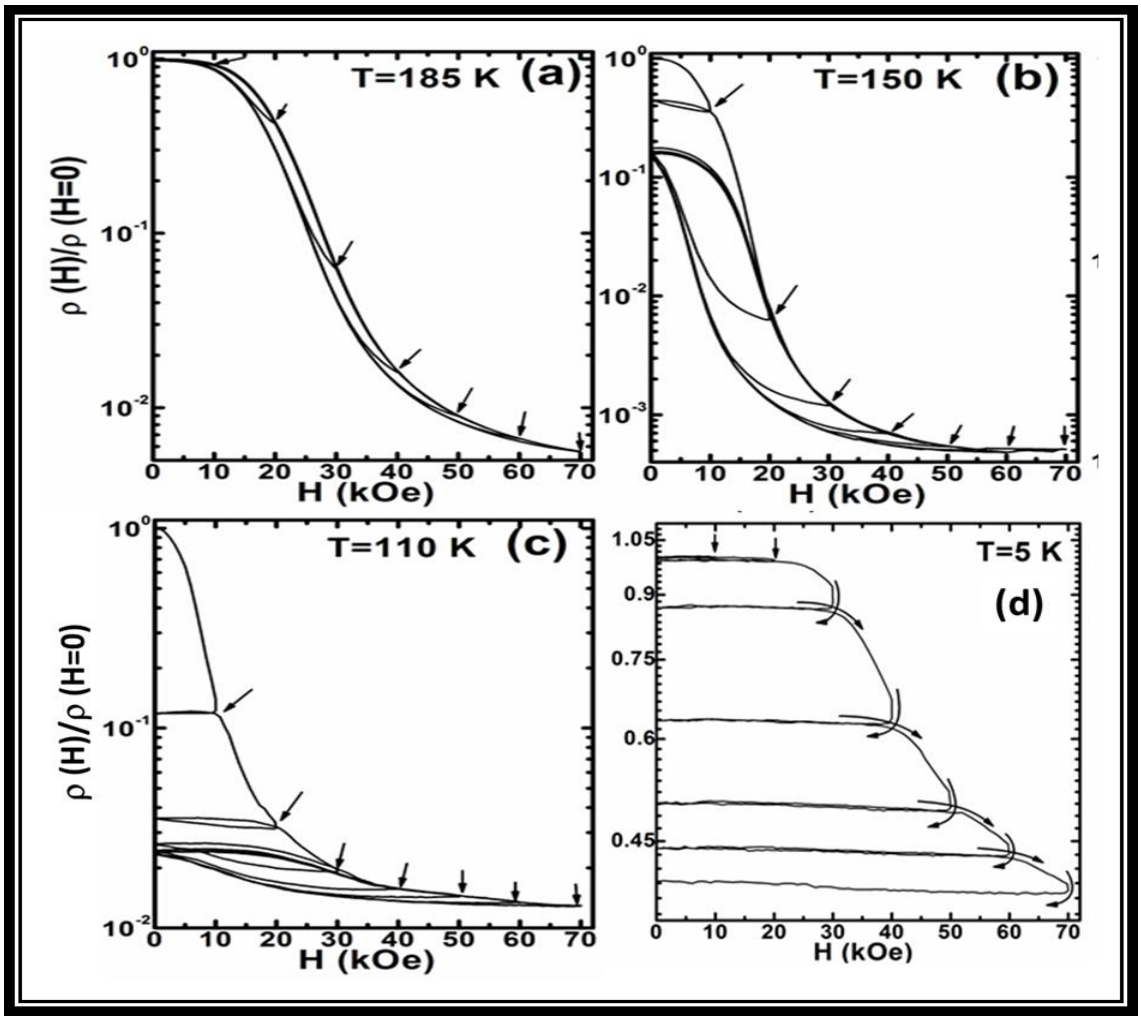

Figure 5.4: Isothermal ρ - H loop measurements at temperatures T = 185 K (a), 150 K (b), 110 K (c) and in the glassy region at 5 K (d).

At H=70 kOe the decrease in resistivity is more than two orders of magnitude. Since the measurement temperature is well above the cooling and warming cycle IMTs and FCC/FCW T_C values therefore this temperature regime consists mainly of AFMI/CO phases. Hence the

decrease in resistivity is principally due to AFMI to FMM phase transition. The hysteretic behaviour, although weak suggests the first order nature of this field induced phase transition. Despite the irreversibility the zero-field value is recovered in all the cycles, confirming a FMM-AFMI/CO transition during the reverse cycle.

The temperature for the second set of measurement (T=150 K) was chosen to be the beginning of the magnetic liquid phase, which is just below T_{IM}^{W} = 163 K and well above T_{IM}^{C}=116 K. This temperature regime is still dominated by the AFMI phase. The ρ - H loops measured at T=150 K are plotted in **Fig. 5.4 (b)**. The resistivity decreases sharply during the first H increasing cycle and when H is reversed the initial state is not recovered. In the H=20 kOe cycle the resistivity drop is even sharper and the initial state is still not recovered after the field is reversed to zero. However, in subsequent cycles the initial resistivity state is recovered and the ρ- H loops lie well within those traced at higher H values.

The behaviour of the ρ - H curves in this case clearly has two contributions; (i) at H ≤ 30 kOe the initial resistivity state is not recovered after reversing H to zero and (ii) at H > 30 kOe, the initial resistivity state is almost fully recovered after reversing H to zero. This clearly shows that during the first two H cycles a fraction of the AFMI phase after the H induced transition to the FMM phase remains permanently in that phase even after reversing the field to zero. Thus, it can be said that the softer magnetic liquid with a higher AFMI fraction is transformed into a stiffer magnetic liquid with a lower fraction of the AFMI phase. At higher H values the induced phase transition is irreversible but with fully recoverable zero field values. The hysteretic behaviour outlines the first order nature of the phase transition.

The next set of measurements was carried out at a temperature T=110 K, which is lower than T_{IM}^{C} = 116 K. The ρ - H loops measured at T = 110 K are plotted in **Fig. 5.4 (c).** The resistivity decreases nearly by an order of magnitude at H= 10 kOe during the first H increasing

cycle and when H is reversed it remain almost constant till H=0 kOe. This clearly shows that appreciable fraction of the AFMI that has been permanently transformed to FMM. During the second H cycle the resistivity first increases and then decreases sharply by nearly seventy percent when H is increased to 20 kOe. After H reversal, the resistivity increases slightly and the H=0 kOe value lies well below the initial value of the second H cycle. Thus in this case too some of the AFMI remains permanently in AFM phase. The next H cycle also shows a similar behaviour. In the subsequently cycles the initial resistivity state is recovered and the ρ- H loops lie well within those traced at higher H values. However, in this case the influence of the magnetic field is much subtle than in case at T=150 K. Nearly similar behaviour is observed around 80 K also. However, at T < 20 K, that is in the glassy region, the behaviour of the ρ - H curves changes dramatically. The ρ - H loops measured at 5 K, which lies well within the glassy region formed by the freezing of the magnetic liquid are shown in **Fig. 5.4 (d).** In this case for all H cycles, the resistivity remains constant and then decreases after a certain H value during each field increasing cycle. During each field decreasing cycle the resistivity remains nearly constant and follows the same path even during the next H increasing cycle. As seen in **Fig. 5.4 (d).** The hysteretic behaviour is conspicuously absent and replaced by a reversible behaviour. Such behaviour appears consistent with the low temperature glassy phase.

To look into the further details of the nature and scale of phase separation we measured the ρ - H loop area in all the cases and studied their scaling as a function of the external perturbation H. As in the previous case of the ρ - T loop, the area was calculated after normalizing with the zero-filed data, viz. ρ (H=0). The loop area – magnetic field (A – H) scaling is plotted in **Fig. 5.5 (a-c).** In order to have an idea of the scaling behaviour we have employed, instead of the eq. (4) the following eq. to fit the A – H data:

$$\mathbf{A(H) = A_H(H - H_{IM})^{\eta}} \qquad \mathbf{(5.5)}$$

In this eq. the constant H_{IM} is the magnetic field at which the induced AFMI to FMM phase transition appears and is expected to decrease with lowering of the temperature, the exponent 'η' may be taken as a measure of phase separation. The deviation from the scaling eq. (5.5) could be due to the intrinsic phase separated nature and the ensuing H induced AFMI/CO to FMM first order phase transition **[39]**. As seen in **Fig. 5.5 (a)**, the loop area of the ρ - H curves measured at T=185 K remains constant at lower magnetic fields and rises linearly at H higher than ~20 kOe. Eq. (5.5) fits the observed data quite nicely at H ≥30 kOe. In this case the value of the constants yielding the best fit (R^2 = 0.9906) is found to be A_H = 120560 ± 4639, H_{IM} = 27.4 ± 1.3 kOe and η = 0.91 ± 0.03. In case of the ρ - H curves measured at T=150 K shown in **Fig. 5.5 (b)**, the loop area scales non-linearly at H ≥ 20 kOe and the best fitting (R^2 = 0.9973) parameters are found to be A_H = 465052 ± 51206, H_{IM} = 19.6 ± 1 kOe and η = 0.53 ± 0.03. It is interesting to note that the area of the ρ - H loops measured at 110 K, shown in **Fig. 5.5 (c)** below the T_{IM}^{C}=116 K all the observed data points are extremely well fitted by the curve in eq. (4). The best fitting (R^2 = 0.9993) parameters are found to be A_H = 2199 ± 262, H_{IM} = 7.6 ± 0.6 kOe and η = 0.90 ± 0.03. From the fitting parameters, it is clear that the AFMI/CO melting field decreases with lowering of the temperature, that is, the dominance of the FMM over AFMI/CO phase increases. The exponent 'η' is found to be close to unity in the higher temperature region ($T>T_{IM}^{W}$=163 K) which is dominantly AFMI/CO with H induced FMM phase only and in the lower temperature region ($T>T_{IM}^{C}$=116 K) where FMM dominants over AFMI/CO phase (hence less prominent magnetic liquid phase). In the intermediate temperature regime enclosed by the IMTs, which is dominated by the magnetic liquid like phase the value of the exponent is ~ 0.5.

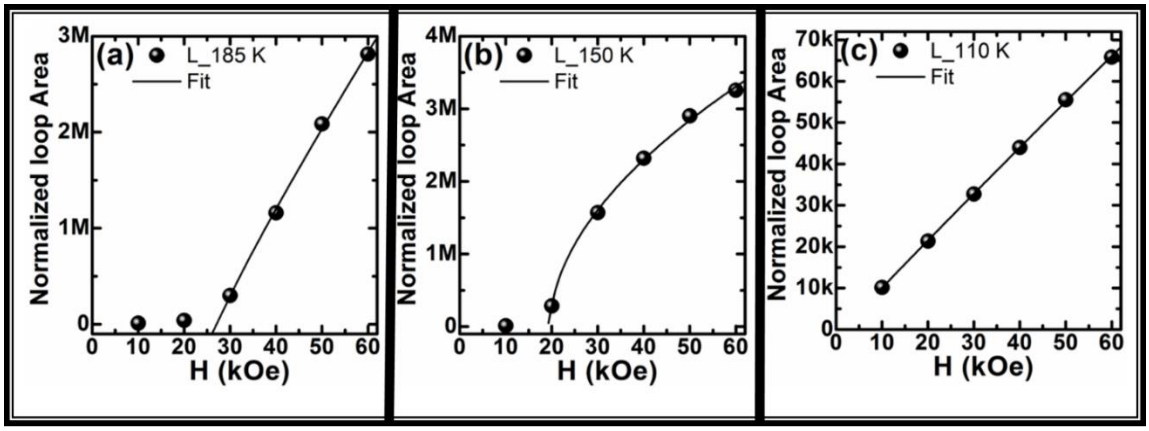

Figure 5.5 : Scaling of normalized loop area enclosed by hysteretic (ρ - H) curves at different H. Solid line represent the fit to equation (5) (see text).

The fact that $H_{IM} \approx 27.4$ kOe, clearly shows that the slow increase in the ρ-H loop area at lower H values is due to weak AFMI to FMM phase fraction. The much sharper and nearly linear rise the loop area at $H>H_{IM}$ is due to the H induced AFMI to FMM phase transition. In this temperature region the magnetic phase dominantly remains a solid like AFMI and hence the nearly linear ρ-H area scaling at $H > H_{IM}$. As the temperature is lowered below the warming cycle T_{IM}^{W}, the magnetic liquid state acquires dominant contribution due to the appearance of FMM clusters and ensuing delicate balance between AFMI and FMM. This enhances the H sensitivity of the resistivity and H induced IMT occurs at much lower field (19.6 kOe) than at T>185 K. The non-linear ρ-H scaling is consistent with the magnetic liquid behaviour at T=150 K. At $T< T_{IM}^{C}$ the magnetic state behaves more like solid FMM with much smaller AFMI phase fraction. Hence the IMT occurs at very small field $H_{IM} \approx 7.6$ kOe and the ρ-H loop area scaling is linear.

In summary, the thermal and magnetic field scaling of the thermomagnetic hysteresis observed in the temperature and magnetic field dependent electric transport properties of ~70 nm thick single crystalline thin films of $La_{0.21}Pr_{0.42}Ca_{0.37}MnO_3$ (LPCMO) grown on STO (110) substrates by RF magnetron sputtering have been investigated. Due to the supercooling of the

magnetic liquid during the cooling cycle and the near equilibrium behaviour during warming results in a pronounced ρ - T hysteresis. The scaling of the IMT with the applied magnetic field during the two thermal cycles is well fitted by the power law of the type $T_{IM}(H) = T_{IM}^{0} + \beta H^{\alpha}$. The fitting parameters β and α are related to the strength of the phase separation and the H induced AFMI to FMM transition. The scaling of the area of the ρ - T hysteresis loop with the magnetic field follows a power law of the type $A_T(H) = A_{T_0} e^{-\Gamma H}$ in the region of strong phase separation. The isothermal ρ - H loop area is found to follow a scaling law of the type $A(H) = A_H(H - H_{IM})^{\eta}$. The constant H_{IM} is the magnetic field at which the induced IMT occurs due to AFMI – FMM phase transition and the exponent η measures the strength of phase separation; being close to unity in the weakly phase separated regimes and ~0.5 in the strongly phase separated or the magnetic liquid regime. The critical ingredients of the phenomenological models used to explain the observed hysteresis in temperature and magnetic field dependent [(ρ-T) and (ρ-H)] loops are the mesoscale phase separation, appearance of magnetic liquid during the cooling cycle, and nearly equilibrium magnetic solid like behaviour while warming.

5.4 References

[1] E. Dagotto, T. Hotta, and A. Moreo, Phys. Rep. **344**, 1 (2001).

[2] E. Dagotto, New J. Phys. **7**, 67 (2005).

[3] Y. Tokura, Rep. Prog. Phys. **69**, 797 (2006).

[4] M. K. Srivastava, A. Kaur, K. K. Maurya, V. P. S. Awana, and H. K. Singh, Appl. Phys. Lett. **102**, 32402 (2013).

[5] L. Ghivelder and F. Parisi, Phys. Rev. B **71**, 184425 (2005).

[6] M. Uehara, S. Mori, C. H. Chen, and S.-W. Cheong, Nature **399**, 560 (1999).

[7] P. A. Sharma, S. B. Kim, T. Y. Koo, S. Guha, and S.-W. Cheong, Phys. Rev. B **71**, 224416 (2005).

[8] W. Wu, C. Israel, N. Hur, S. Park, S.-W. Cheong, and A. de Lozanne, Nat. Mater. **5**, 881 (2006).

[9] V. Agarwal, G. Sharma, P. K. Siwach, K. K. Maurya, and H. K. Singh, Appl. Phys. A **119**, 899 (2015).

[10] V. Agarwal, G. Sharma, P. K. Siwach, K. K. Maurya, V. P. S. Awana, and H. K. Singh, Solid State Commun. **202**, 43 (2015).

[11] V. G. Sathe, A. Ahlawat, R. Rawat, and P. Chaddah, J. Phys. Condens. Matter **22**, 176002 (2010).

[12] D. K. Mishra, V. G. Sathe, R. Rawat, and V. Ganesan, J. Phys. Condens. Matter **25**, 175003 (2013).

[13] T. Z. Ward, S. Liang, K. Fuchigami, L. F. Yin, E. Dagotto, E. W. Plummer, and J. Shen, Phys. Rev. Lett. **100**, 247204 (2008).

[14] H. Jeen and A. Biswas, Phys. Rev. B **88**, 024415 (2013).

[15] V. Podzorov and B. G. Kim, Phys. Rev. B **64**, 140406 (2001).

[16] T. Dhakal, J. Tosado, and A. Biswas, Phys. Rev. B **75**, 92404 (2007).

[17] Y. Tomioka, J. Phys. Soc. Jpn. **64**, 3626 (1995).

[18] Y. Tomioka, A. Asamitsu, H. Kuwahara, Y. Moritomo, and Y. Tokura, Phys. Rev. B **53**, R1689 (1996).

[19] Y. Tomioka, H. Hiraka, Y. Endoh, and Y. Tokura, Phys. Rev. B **74**, 104420 (2006).

[20] Y. Tomioka, A. Asamitsu, H. Kuwahara, and Y. Tokura, J. Phys. Soc. Japan **66**, 302 (1997).

[21] Y. Zhu, K. Du, J. Niu, L. Lin, W. Wei, H. Liu, H. Lin, K. Zhang, T. Yang, Y. Kou, J. Shao, X. Gao, X. Xu, X. Wu, S. Dong, L. Yin, and J. Shen, Nat. Commun. **7**, 11260 (2016).

[22] S. V. Trukhanov, J. Exp. Theor. Phys. **101**, 513 (2005).

[23] S. V. Trukhanov, A. V. Trukhanov, H. Szymczak, R. Szymczak, and M. Baran, J. Phys. Chem. Solids **67**, 675 (2006).

[24] S. V. Trukhanov, J. Exp. Theor. Phys. **100**, 95 (2005).

[25] S. V. Trukhanov, J. Mater. Chem. **13**, 347 (2003).

[26] S. V Trukhanov, A. V Trukhanov, C. E. Botez, A. H. Adair, H. Szymczak, and R. Szymczak, J. Phys. Condens. Matter **19**, 266214 (2007).

[27] S. V. Trukhanov, A. V. Trukhanov, S. G. Stepin, H. Szymczak, and C. E. Botez, Phys. Solid State **50**, 886 (2008).

[28] T. Z. Ward, S. Liang, K. Fuchigami, L. F. Yin, E. Dagotto, E. W. Plummer, and J. Shen, Phys. Rev. Lett. **100**, 247204 (2008).

[29] V. Agarwal, P. K. Siwach, G. D. Varma, V. P. S. Awana, A. K. Srivastava, and H. K. Singh, Mater. Res. Express **1**, 046117 (2014).

[30] S. Sengupta, Y. Marathe, and S. Puri, Phys. Rev. B **45**, 7828 (1992).

[31] P. B. Thomas and D. Dhar, J. Phys. A. Math. Gen. **26**, 3973 (1993).

[32] D. Dhar and P. B. Thomas, J. Phys. A. Math. Gen. **25**, 4967 (1992).

[33] J.-M. Liu, H. L. W. Chan, C. L. Choy, and C. K. Ong, Phys. Rev. B **65**, 014416 (2001).

[34] M. Rao, H. R. Krishnamurthy, and R. Pandit, Phys. Rev. B **42**, 856 (1990).

[35] S. S. Bhattacharyya, M. Rahman, A. Mukherjee, B. K. Chaudhuri, and A. Yoshizawa, Appl. Phys. Lett. **92**, 122909 (2008).

[36] J.-M. Liu, H. L. W. Chan, C. L. Choy, Y. Y. Zhu, S. N. Zhu, Z. G. Liu, and N. B. Ming, Appl. Phys. Lett. **79**, 236 (2001).

[37] J.-M. Liu, B. Pan, H. Yu, and S. T. Zhang, J. Phys. Condens. Matter **16**, 1189 (2004).

[38] W. Y. Lee, B.-C. Choi, J. Lee, C. C. Yao, Y. B. Xu, D. G. Hasko, and J. A. C. Bland, Appl. Phys. Lett. **74**, 1609 (1999).

[39] A. Yadav, S. Singh, A. Vashist, G. Sharma, P. K. Siwach, and H. K. Singh, Mater. Res. Express **4**, 066102 (2017).

6 Consequences of Film Thickness on Structural, Magnetism and Electrical Transport on Epitaxial Phase Separated Manganite Thin Film

6.1 Introduction

The generic perovskite manganese oxides $RE_{1-x}AE_xMnO_3$ (RE being a trivalent rare earth ion and AE a divalent one, commonly an alkaline earth) are metallic and ferromagnetic over a certain range of x-values, which is dependent on the average size of the RE/AE site cations and hence the tolerance factor **[1–4].** The major electronic properties of these compounds are controlled by the 3d orbitals and the simultaneous ferromagnetic and metallic behaviours are explained to a certain extent by the double-exchange (DE) mechanism proposed by Zener, wherein it was considered that the interatomic Hund rule exchange was strong and carriers do not change their spin orientation while hoping from one ion to next. The carriers can only hop if the spins of the two ions are parallel. It was also found through energy minimization that ferromagnetic interactions are favoured when magnetic atoms are well separated and conduction electrons are present. This theory as applied to perovskite manganites which explains the strong correlation between ferromagnetism and conductivity **[1–6]**. The ferromagnetic transition temperature (T_C) in the DE mechanism, scales as **[7]**

$$T_C \sim J \sim t_{dp}^2 \sim S_{dp}^2 \qquad (6.1)$$

Where J is the effective exchange parameter between the adjacent Mn ions, t_{dp} is the Mn_d-O_{2p} transfer integral and S_{dp} is the overlap between the Mn_d and O_{2p}. In such materials the modification of the geometrical surroundings of the Mn e_g orbitals, e.g., $d_{3z^2-r^2}$ and the $d_{x^2-y^2}$ orbitals, offers an extrinsic degree of freedom for physical property tailoring. The manganese e_g shell is doubly degenerate in a regular octahedral surrounding and is only partly occupied.

The Mn^{3+} ions are thus Jahn-Teller (JT) **[8]** active, and small distortions of the oxygen octahedra can shift the relative stability of the two e_g orbitals. A desirous choice between the $d_{3z^2-r^2}$ and the $d_{x^2-y^2}$ orbitals for occupancy could be possible if the Mn ions are subjected to suitable geometric constraints. If $d_{3z^2-r^2}$ is occupied, the DE will take place essentially along the out of plane direction, while the occupation of the $d_{x^2-y^2}$ orbitals strengthens the interlayer DE with concomitant weakening of the interlayer interaction.

In thin films the substrate induced strain modifies the octahedral geometry and therefore is potentially an important extrinsic degree of freedom (in addition the intrinsic ones like lattice, spin, charge degrees of freedom) and has been invoked to tune the physical properties of manganites **[9,10]**. Specifically, a tensile strain causes in-plane stretching of the MnO_6 octahedra in the in-plane direction, which in turn enhances the JT distortion and thus favours the antiferromagnetic (AFM) ordering and the charge ordered insulator (COI) states. An in-plane compression of the MnO_6 octahedra by the compressive strain weakens the JT distortion and favours the ferromagnetic (FM) – double exchange (DE) **[8–12].** The elastic energy released during relaxation of the strain is dissipated through the formation of defects. These defects which comprise mostly of dislocations and stacking faults disrupt the cooperative nature of the JT distortion network. Tensile strain induced in-plane stretching of the MnO_6 octahedra increases in the in-plane Mn-O bond length and therefore it makes occupation of the dx^2-y^2 orbital energetically favourable **[12]**. In-plane compression of the MnO_6 stabilizes the out-of-plane $d3z^2$-r^2 orbital. The above orbital selectivity caused by in-plane compressive and tensile strains has been seen in x-ray absorption **[13]** as well as in angle resolved photoemission **[14]** experiments. The volume conserving tensile strain causes higher occupancy of the in-plane dx^2-y^2 orbital, a larger out-of-plane hopping and smaller in-plane hopping compared to the unstrained values. Thus in-plane tensile strain stabilizes insulators that can have either FM or AFM spin textures **[12].**

In low bandwidth manganites, which exhibit intrinsic tilting/twisting of the MnO_6 octahedra due to smaller average RE/AE site cationic size and have much stronger JT distortion, the role of strain could be more intricate and hence can have novel experimental implications. A prototypical low bandwidth compound which shows very prominent multiorder electronic coupling and therefore has been investigated extensively is $La_{1-x-y}Pr_yCa_xMnO_3$. In such compounds which exhibit nearly isoenergetic existence of multiple electronic phases (like FM and AFM/COI) even the subtle changes in the substrate induced strain (and hence also the variation in the film thickness) can also modify the electronic phase profile and associated phase transitions **[11,15–23]**. In addition to the phase transitions, the strain could also impact the non-equilibrium states like the magnetic liquid and the strain glass (SRG) **[19]**. Although several studies have reported the impact of substrate induced strain in $La_{1-x-y}Pr_yCa_xMnO_3$ at different values of the composition x **[14–20,24,25]**, investigations embodying a wide range of film thickness sufficient to provide a high strain and strain relaxed states are lacking. Jeon et al. **[16],** have studied the impact of the film thickness in $La_{0.35}Pr_{0.35}Ca_{0.30}MnO_3$ in which the composition is far away from the one conducive to the delicate balance between AFM/COI and FMM. A more recent study by V. Agarwal et al. [**19]** demonstrated that in single crystalline $La_{1-x-y}Pr_yCa_xMnO_3$ (x~0.42, y~0.40) thin films on $LaAlO_3$ (001) substrates having thickness in the range 20–140 nm, the multiple magnetic phase transitions, insulator–metal transition (IMT), the supercooling characteristics of the dynamical magnetic liquid and the nature of the glassy state are all sensitive to the compressive strain and its relaxation. The same work also shows that at lower film thickness there is significant depression in the magnetization, possibly due to the formation of a dead layer. However, the impact of in-plane tensile strain in the prototypical strongly phase separated manganite La1-x-yPryCaxMnO3 has not been studied in a systematic way.

Here in this chapter, a systematic study of the consequences of in-plane tensile strain on the correlation between structure/microstructure and magneto-electrical properties of $La_{0.23}Pr_{0.41}Ca_{0.36}MnO_3/SrTiO_3$ (001) thin films (thicknesses in the range 13-81 nm) is presented. Here, composition is so selected that the electronic phase balance is tilted slightly in favour of the FM metal (the bandwidth in the present study is between those investigated in references 19 and 24). Such a selection gives a possibility of the occurrence of FM-metallic behaviour even at sufficiently small film thickness where the tensile strain is very large. It appears quite pertinent to mention here that at very small film thickness such thin films generally show strong insulator behaviour. This work is published in ***AIP Advances 8, 095002 (2018).***

6.2 Experimental Details

In the present case the nominal composition of the target is $La_{0.22}Pr_{0.40}Ca_{0.38}MnO_3$. During all the sputtering depositions the same experimental parameters were employed. The temperature of the (001) oriented STO substrates (three substrates for comparison) of dimension (5 x 3 x 0.5) mm^3 were maintained at ≈ 870 °C. The distance between the target and the substrate was fixed at ≈ 5 cm. The base pressure achieved was $3x10^{-5}$ torr and the dynamic pressure during sputtering was maintained at 200 ± 10 mtorr of Ar~80 % and O_2~20 %. To prepare films of different thickness the depositions were done for ~5, ~10, ~15 and 30 minutes. Post deposition *in-situ* annealing at ~900 °C and ~ 1 atmosphere O_2 for about 4 hrs was done to achieve the optimum oxygen stoichiometry. The magnetization measurements employ the same protocol as discussed in chapter 3. The self-field (in absence of external magnetic field) transport was measured by the standard four contact technique with the Keithley delta mode setup and the temperature of the 6-400 K closed cycle refrigerator was controlled by the lakeshore 332S cryogenic temperature controller at 2K/minute during cooling/warming.

6.3 Results and Discussion

6.3.1 Chemical Composition, Thickness, and Structure

The energy dispersive X-ray spectra recorded from several places on the films were used to evaluate the chemical composition of the film (discussed in chapter 2). The average chemical composition is found to be $La_{0.23}P_{0.41}Ca_{0.36}MnO_3$ and no noticeable spatial variation in the chemical composition of each of the films was observed. The chemical composition of the films did not show any noticeable dependence on the film thickness. In fact films on all the three substrates grown alongside the one investigated during the present study also have the same chemical composition. However, the slight difference in the chemical stoichiometry of the target and the thin films shows the inexact stoichiometry transfer in the RF magnetron sputtering process employed in the present growth process.

The film thickness is estimated from the XRR data of 10 minute RF sputtered films. The XRR data of the 10 minute sputter deposited thin film is plotted in **Fig. 6.1.** The film thickness (d) was calculated from the separation of the Keissig fringes (**Fig. 6.1**) employing the formula: $d=\lambda/2(1/\theta_{m+1} - 1//\theta_m)$; where λ (=1.5406 Å) is the wavelength of the Cu-Kα X-ray employed and θ_m is the angle of incidence of the m^{th} Keissig fringe. The thickness of the 10 minute sputtered film is found to be d ≈27 nm. This yields an average growth rate of ≈ 2.7 nm per minute. From this data thickness of the 15 and 30 minute sputtered films is found to be ≈ 41 nm and 81 nm, respectively.

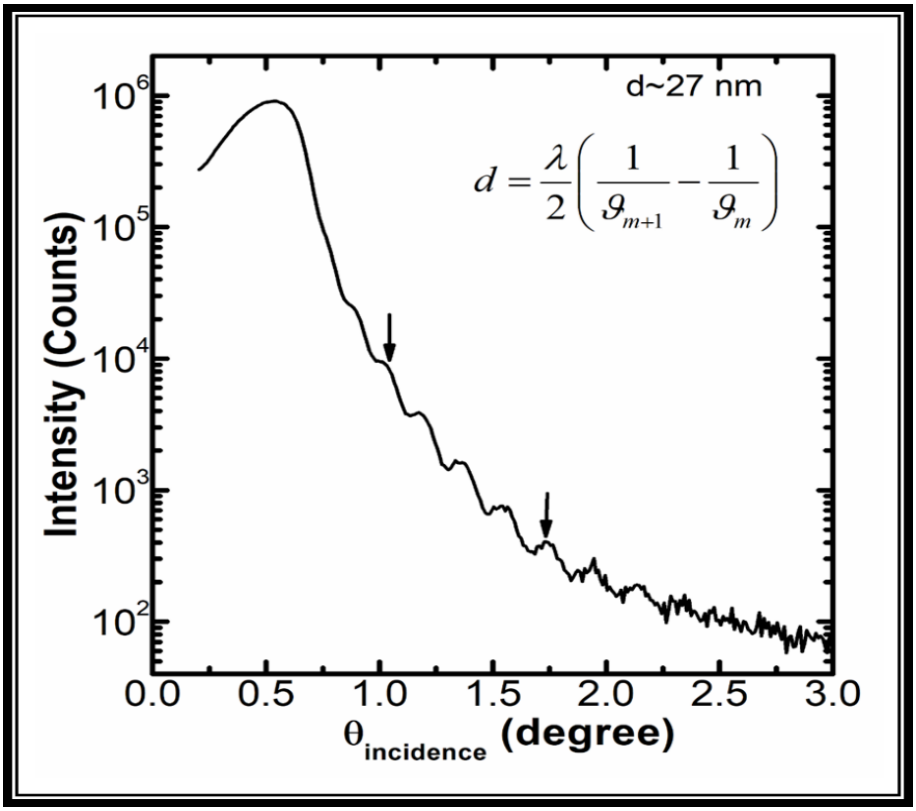

Figure 6.1: X-ray reflectivity plot of 10 minute sputtered deposited $La_{0.23}P_{0.41}Ca_{0.36}MnO_3$ (LPCMO) thin film on (001)-STO substrate. The inset shows the expression used to calculate the thickness of the film.

The bulk target used for sputtering has orthorhombic structure with lattice constants a=5.429 Å, b=7.667 Å and c=5.439 Å. The average in-plane lattice parameter, $a_B = 1/2(a/\sqrt{2} + c/2)$ = 3.836 Å and the out-of-plane lattice constant is a_{CB}=3.846 Å. The (100)-STO has the cubic lattice constant a_{CS} = 3.905 Å. Hence the induced strain is tensile in nature. The strain is calculated using $\varepsilon = (a_S - a_B)*100/a_S$ = 1.77 %. The 2θ/ω scans are depicted in **Fig. 6.2 (a)**. All films show almost identical diffraction patterns with the only visible difference being the shift of the materials peaks towards the substrate with increase in the film thickness. This indicates relaxation of the tensile strain at higher film thickness.

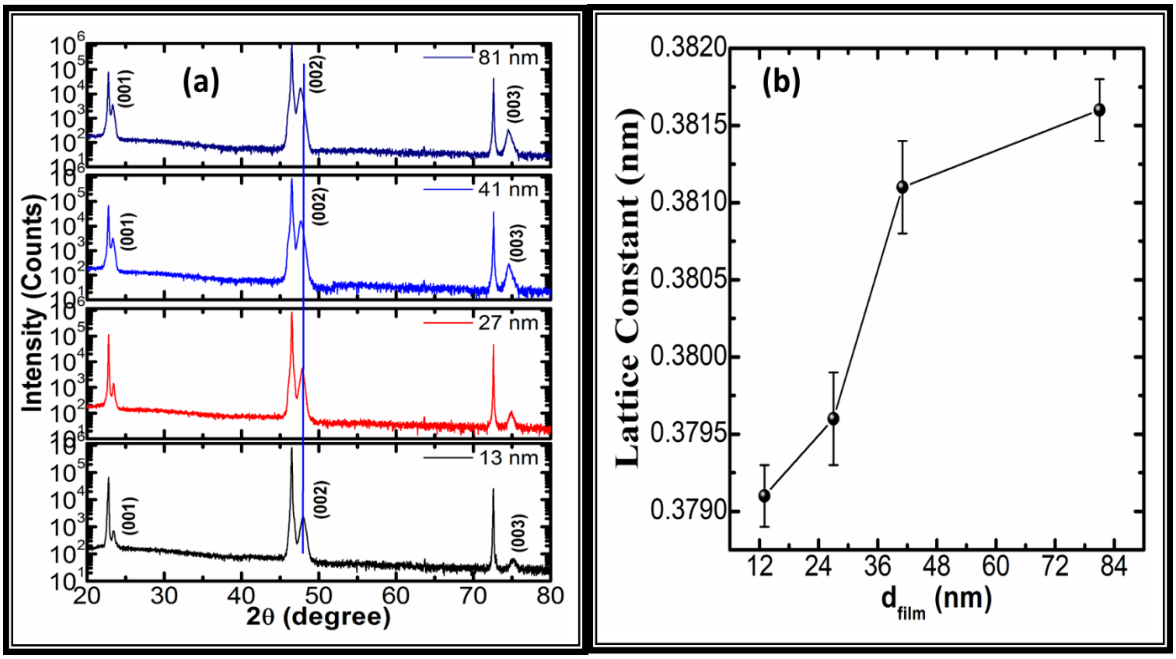

Figure 6.2: (a) $2\theta/\omega$ plot of 13 nm, 27 nm, 41 nm and 81 nm thin films on (001)-STO substrate. The film peaks are indexed. The higher intensity peaks belong to the substrate. (b) Variation of the normal lattice constant with film thickness

The observed 2θ values are used to calculate the out-of-plane (OP) lattice constants (a_c). The thinnest film (13 nm) has a_c=0.3791 ± 0.0002 nm, which is much smaller than the corresponding lattice constant of target (a_{cB} = 0.3846 nm). This marks the presence of large in-plane tensile strain. Given the tensile nature of the in-plane strain, the MnO_6 octahedron stretches along the plane (a-b plane) of the substrate and compress along the normal 'c' direction. This behaviour strengthens the JT distortion, and hence the AFM and CO insulator phases are favoured.

As film thickness rises, the OP lattice parameter shows an abrupt rise as the thickness changes from 27 to 41 nm (**Fig. 6.2 (b)**. Interestingly, except the point corresponding to d_{film} = 41 nm, all the points connect linearly. It is demonstrated that the compression along the 'c' direction (caused by an in-plane tensile strain) (i) makes the $d_{x^2-y^2}$ orbitals energetically favourable, (ii) a larger (smaller) out-of-plane (in-plane) hopping compared to the unstrained

values, (iii) stabilizes the insulating state which may either have FM or AFM spin favour **[12–14,24,25].**

Since the subtle energetic difference between the coexisting FMM and AFMI/COI phases, sizeable tensile strain (as in the case of 13 nm and 27 nm thin films) could lead to a robust insulating state and hence can have dramatic effect on the magnetic-electrical characteristics of the film. Elongation of the OP parameter with increase in film thickness is due to the relaxation of the manganite lattice. As the thickness increases the clamping effect of the substrate which ideally remains fully effective only for the initial few layers of the film, eases up. The trend in the a_C - d_{film} dependence (**Fig. 6.2 (b)**) suggests a linear relaxation of the in-plane tensile strain up to 27 nm. The sudden decrease in a_c beyond 27 nm shows the presence of some curious relaxation process or morphological changes above this thickness. At 81 nm thickness the OP lattice constant is a_C=0.3816 ± 0.0002 nm, which is still appreciably lower as compared to corresponding bulk value. This confirms the substantial strain present at higher thickness may become self-sustained and hence survive at higher film thicknesses.

The rocking curves (RCs) of differently thick films (**Fig. 6.3**) shows that the crystalline nature and in-plane mosaic structure of the films are coupled to the film thickness. The full width at half maximum (FWHM, denoted hereafter by (δω) of the RCs were obtained from the Lorentzian fit to the experimental data. The RC of thinnest film (~13 nm) has δω = 0.277° ± 0.002°. The FWHM then decreases to δω = 0.199° ± 0.001° when the thickness increases to 27 nm. As the film thickness is increase further, the RC again shows broadening and at d = 81 nm, it shows δω=0.269° ±0.003°.

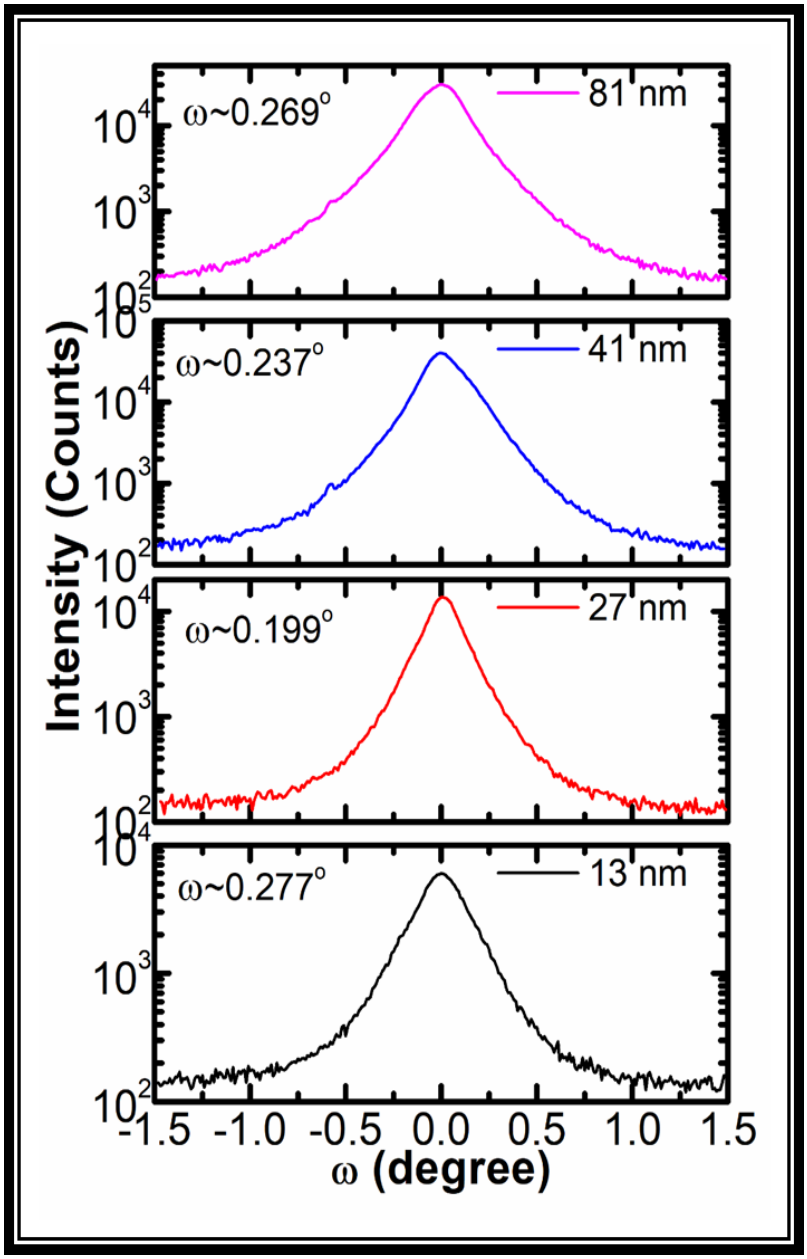

Figure 6.3: Rocking curve (ω-scan) plot of the (002) diffraction peak of 13 nm, 27 nm, 41 nm and 81 nm thick film.

The broadening of RC is influenced by several factors such as (a) strain due to the lattice mismatch between the substrate and the material, (b) a mosaic spread, and (c) variation in the tilt and dilations in crystal due to the presence of dislocations. Since the present measurements were carried out in the triple axis geometry, therefore the contributions of the mosaic spread and that of the strain can be separated **[26]**. The FWHM of the all the films was carried out at

varying beam widths from 1/16° to 1/4°. The 13 nm film did not show any significant change in the FWHM as a function of the beam width. This suggests that in the 13 nm film the profile broadening is mainly due to the strain, which in this case is due to the lattice mismatch. The FWHM of 27 nm film also follows the same trend as a function of the beam width. Hence as the strain is reduced the FWHM also decreases significantly. Strain further relaxes as the film thickness is increased and in view of this the FWHM of 41 and 81 nm thick films should decrease to further lower values. But the contrary happens and the FWHM increases as the film thickness is increased to 81 nm. This clearly shows that the contribution to the mosaic profile broadening in higher thickness films is due to the mosaic spread caused by the dislocation induced tilt and dilations of the lattice. Since the cooperativeness of the JT distortion, which favours the AFM ordering, is disrupted by the presence of lattice defects such as dislocations, the thicker films are expected to have higher FMM phase fraction.

The surface morphology of the films was probed by atomic force microscopy (AFM*). The surface of the 13 nm film shows two distinct kinds of growth features, viz., the terrace like growth and above it small nano-sized platelets spread all over the surface. The presence of holes/vacancies in the under grown terraces suggests that the nano platelets could have come out of them due to lattice and thermal strain during the in-situ annealing. The average surface roughness in this case is 0.388 nm, which is just equal to a unit cell. This shows despite the presence of nano platelets the surface quality of the 13 nm thin film is very good and that bottom layers are epitaxially grown. Almost similar surface features are also observed in the case of 27 nm film except that the surface roughness increases slightly to ~0.42 nm. The surface of the 41 nm film shows weakening of the terrace like features with a simultaneous increase in the nano platelets surface density.

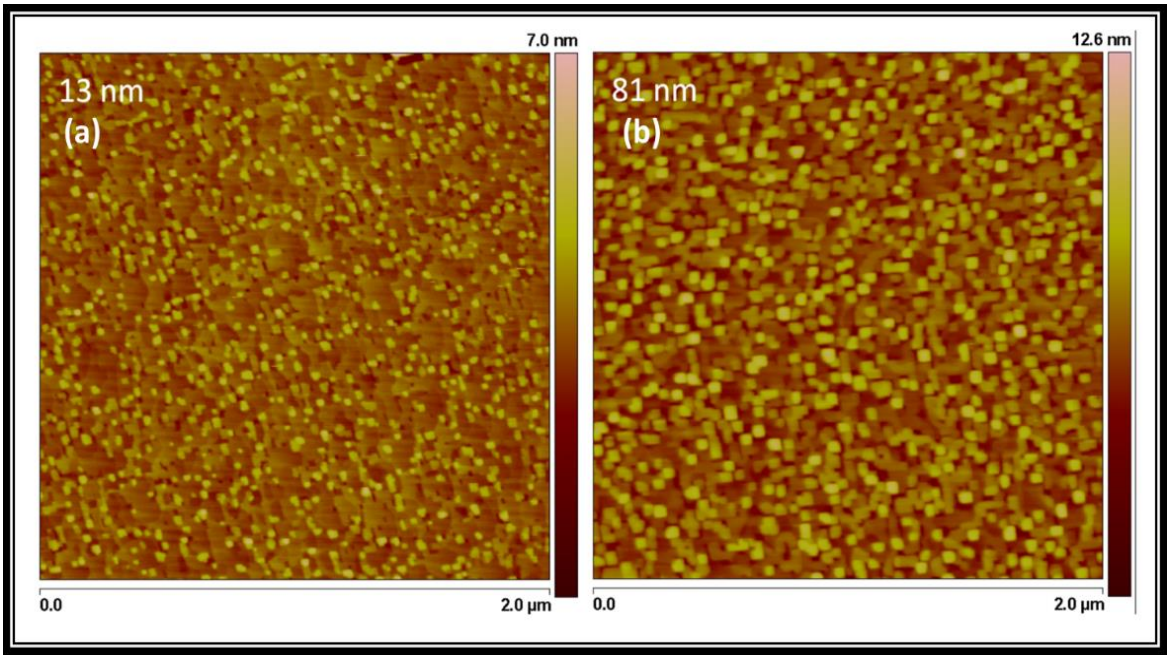

Figure 6.4: Tapping mode representative atomic force microscope images of the LPCMO thin film (13 nm and 81 nm) on STO substrate.

As the strain relaxes rather abruptly at this film thickness, we believe that changes in the surface topography are also due to the elastic energy dissipated during strain relaxation. The surface roughness in the case increases appreciably to ~0.766 nm, which almost two unit cells. Thus at 41 nm the epitaxial nature appears to be under stress and is prone to reorganization as film acquires larger thickness. The surface of 81 nm thick film is found to consist of uniformly distributed platelet like features. The surface roughness in this case is 0.946 nm, which is almost equal to three unit cells. This shows the transition from the epitaxial to disordered brick type single crystalline surface phase. Representative tapping mode AFM images of 13 and 81 nm thick films are shown in **Fig. 6.4**.

6.3.2 Electrical Transport Study

The self-field electrical transport of all the $La_{0.23}P_{0.41}Ca_{0.36}MnO_3$ films was analysed through temperature dependent resistivity (ρ-T) (**Fig. 6.5 (a)**) scaling. The data was acquired at rate of 2K/minute in cooling as well as warming cycles. The 13 nm and 27 nm thin films

showed behaviours characteristic of a good insulator and the resistivity became immeasurable in the lower temperature range. Among these two the 27 nm film has a lower resistivity and the cooling and warming cycle ρ-T of both the films shows complete reversibility over the measured temperature range. We would like to mention that in our earlier study on $La_{0.18}P_{0.40}Ca_{0.42}MnO_3$ thin films we have found similar trend even in compressively strained thin films on $LaAlO_3$ substrates [19]. The ρ(T) of 41 nm film increases from ~$3x10^{-3}$ Ohm-cm at room temperature to ~165 Ohm-cm at ~59 K and then sharp IMT is observed at T_{IM}^{C}=59.3 K. The resistivity drops by more than four orders of magnitude within a very short temperature span below T_{IM}^{C}. During the warming after the initial reversibility, the ρ-T curve shows a minimum at T_m=42.8 K and then increase showing an IMT at T_{IM}^{C}=131.8 K. At higher temperatures it follows temperature dependence of the cooling cycle ρ-T curve. The 81 nm film, after the initial insulating behaviour, which is much weaker as compared that observed in the thinner films, undergoes an IMT at T_{IM}^{C}=111.7 K. The drop in the ρ-T just below the IMT is less sharp (by three orders of magnitude within 15 K range). During the warming cycle a very weak resistivity minimum is seen at T_m=12 K and IMT appears at T_{IM}^{W}= 144.5 K. The above results clearly show that these in-situ annealing thin films do not show any IMT up to a thickness of d= 27 nm. For 41 nm thick film, IMT appears and cooling and warming cycle ρ-T shows colossal thermal hysteresis where the two IMTs differ by 72.5 K. As the thickness rises to 81 K, the IMTs scale up to higher temperatures with a concomitant narrowing of the thermal hysteresis.

To gain more insight into the nature of electrical transport, we analysed the ρ-T data in terms of the adiabatic limit small-polaronic model generally given by **[27,28]**

$$\boldsymbol{\rho(T) = ATe^{E_a/k_bT}} \;\; \boldsymbol{\&} \;\; \boldsymbol{A = \frac{2k_b}{3ne^2a^2\nu}} \qquad \textbf{(6.2)}$$

Here, the polaronic concentration is given by 'n', site-to-site hopping length is 'a', the attempt frequency for overcoming the potential barrier is given by 'ν', and k_b is the Boltzmann constant. The activation energy, E_a is measured by the potential barrier height and is related to the overlap integral 't' through the relation $t = E_P - 2E_a$. However, in general, the overlap integral is so small that it could be neglected and then $E_P = 2E_a$. In all the cases we have used the warming cycle data for fitting with the eq. (6.2).

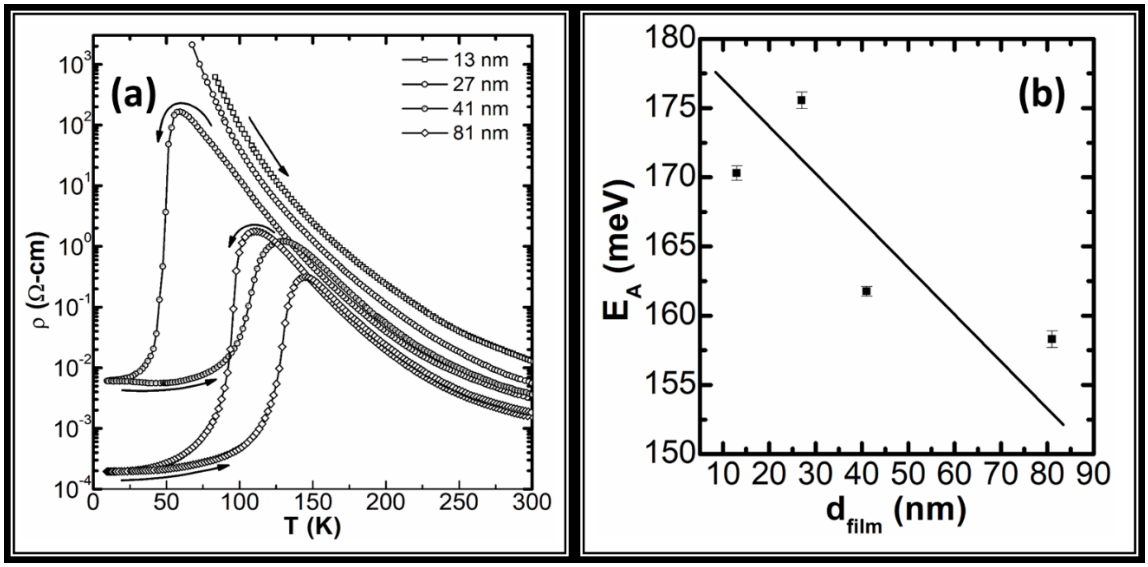

Figure 6.5: (a) Self-field resistivity of the LPCMO thin films of varying thickness measured as a function of temperature (ρ (T) curves). (b) Variation of the small polaron activation energy with film thickness (d_{film}).

The data of the 13 and 27 nm thick films was well fitted from room temperature down to ~180 K (at this temperature the AFM transition generally takes place), while the fitting was good till ~160 K in case of the 41 and 81 nm thick films. From the fitting parameter (the slope $\frac{E_a}{k_b}$ of the $\ln\left(\frac{\rho}{T}\right) = \ln(A) + \left(\frac{E_a}{k_b}\right)\frac{1}{T}$), the E_a was calculated and its dependence on thickness is plotted in **Fig. 6.5 (b)**. The value of the activation energy is found to be 170.30±0.52 meV, 175.56±0.61 meV, 161.75±0.35 meV and 158.30±0.61 meV, respectively for 13, 27, 41 and 81 nm films.

These values show that a decrease in the carrier localization is one of the factors responsible for the appearance of IMT is films having thickness d ≥ 41 nm. These values are much larger than those reported in case of the large BW manganites like $La_{1-x}Sr_xMnO_3$ **[27]**. However, these values are comparable to those observed in case of other low BW manganites like $Sm_{1-x}Sr_xMnO_3$ **[29]** and close to the values reported for nearly similar $La_{1-x-y}Pr_yCa_xMnO_3$ thin films **[30].**

Here, it may be noted that the low temperature electrical resistivity of manganites is generally described in terms of the two major scattering contributions, viz., (i) the electron–electron (e–e) scattering which yields a temperature dependence of the type $\rho_{ee} \propto T^2$ and (ii) the electron–phonon (e–ph) scattering having the form $\rho_{eph} \propto T^5$ **[31]** (related references therein). In addition the contributions of the two magnon process ($\rho_{mag} \propto T^{4.5}$) and small polaron ($\rho_{spol} \propto \sinh^2(\hbar\omega_s/2k_BT)$) to the low temperature resistivity has also been demonstrated **[32,33].** However, as shown by Agarwal et al. **[31]**, in the case of strongly phase separated manganites like $La_{1-x-y}Pr_yCa_xMnO_3$ thin films; the major contribution to the low temperature resistivity is from the e–e scattering. Depending on the degree of phase separation the additional contribution from e–ph and disorder-enhanced strong Coulomb scattering ($\rho_C \propto T^{0.5}$) is also present. In the present case, only the 41 nm and 81 nm thin films show IMT. The cooling cycle low temperature resistivity data of both the films is well described by the $\rho_{ee} \propto T^2$ and $\rho_{eph} \propto T^5$ contributions (data not plotted). The warming cycle data of the 41 nm film is fitted with the two major contributions $\rho_c \propto T^{0.5}$ and $\rho_{ee} \propto T^2$, while the resistivity of the 81 nm film contributions from the e–e and e–ph scatterings. A more detailed study of the low temperature resistivity in all the films (at different magnetic fields) could be a useful separate study.

6.3.3 Magnetic Properties

Since the insulator-metal transition in manganites is simultaneous to the ferromagnetic transition, therefore in order to unravel the magnetic phase profile of the films we measured temperature and magnetic field dependent magnetization (M-T and M-H). The M-T was measured employing the zero filed cooled (ZFC), field cooled cooling (FCC), and field cooled warming (FCW) protocols. M-H was measured after zero- field cooling of the film to the desired temperature (10 K). The final magnetization data was obtained after the subtraction of the substrate contribution. The M-T data is plotted in **Fig. 6.6** shows some interesting features. In case of the thinnest (13 nm) film the magnetization is very small and very noisy throughout the measured temperature range. Despite the small magnetic moment the FCC and FCW curves show FM transition like signature at $T_C \approx 140$ K and the ZFC shows a down turn at $T_P \approx 70$ K. The magnetization at 10 K is found to be ≈8 emu/cm^3. This is much smaller than that recently reported for a ~20 nm thick compressively strained $La_{0.18}Pr_{0.40}Ca_{0.42}MnO_3$ thin film on $LaAlO_3$ substrate **[19]**. One of the factors, apart from the higher film thickness, that could cause difference in the magnetization of the two set of films could also be the difference in the nature of the substrate induced strain. The compressive nature of the strain in the $LaAlO_3$ thin films favours the FMM. The small and noisy magnetization could arise from the magnetic dead layer formed at the various interfaces of the film. On increasing the film thickness to 27 nm, the FCW magnetization increases substantially and 10 K it is ≈35 emu/cm$^{3.}$ The increase in magnetization is accompanied by a much better defined FM transition.

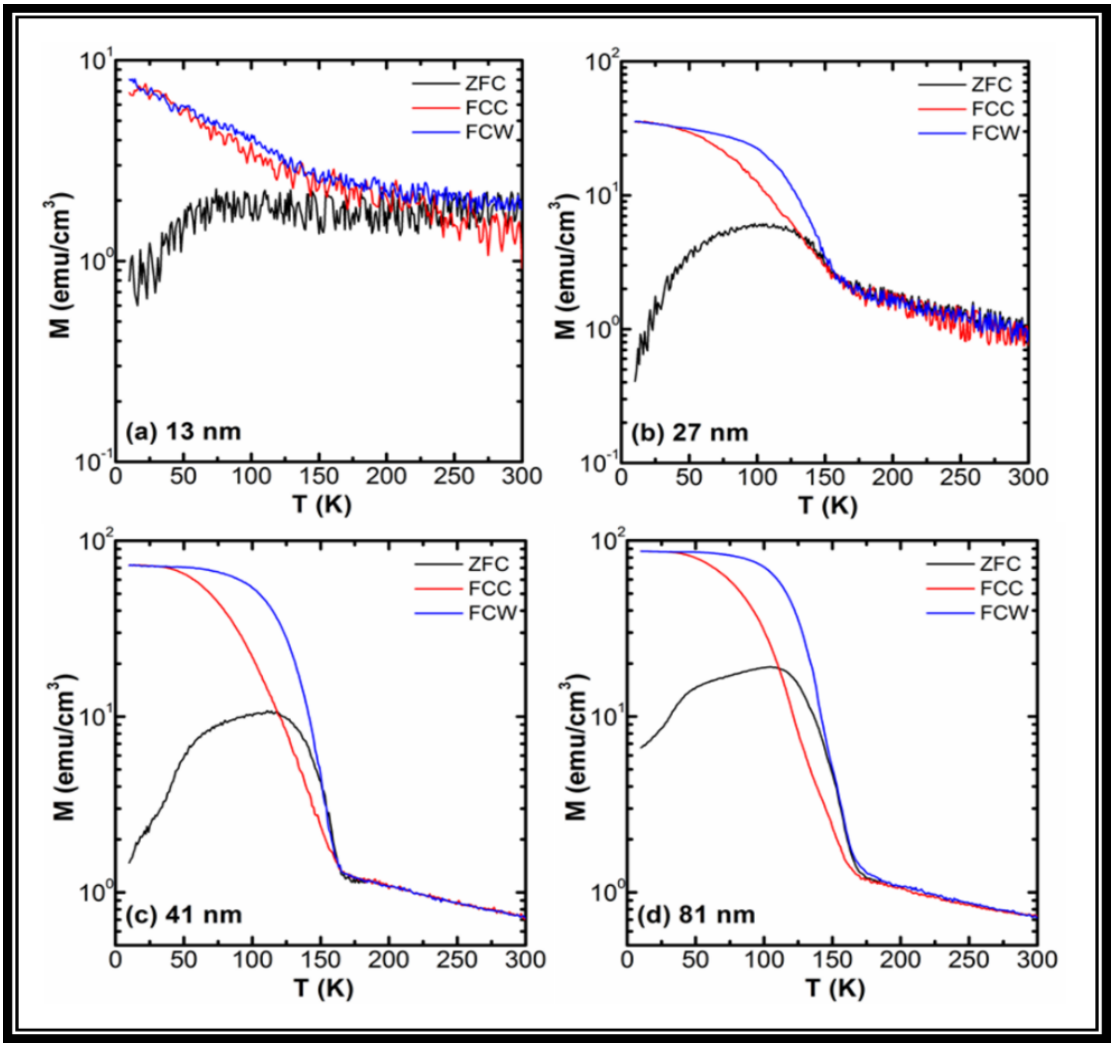

Figure 6.6: ZFC, FCC, and FCW magnetization (M-T) of LPCMO thin films measured at H=100 Oe applied along the longer dimension in plane of the film

The temperature at which the M-T curve starts rising can be taken as the FM transition temperature (T_C). For this film $T_C \approx 158$ K. The magnetization continues to increase with film thickness with a simultaneous sharpening of the FM transition. However, the T_C remains almost constant at ≈160 K for the thicker 41 nm and 81 nm films. The increase in the magnetic moment at higher film thickness is due to the (i) reduced impact of the interfacial electronic reconstruction that forms the dead layer, (ii) relaxation of the substrate induced tensile strain which favours carrier delocalization.

In addition to the increase in magnetization following features are observed in all the films having thickness d≥27 nm: (i) the FCC and FCW curves show hysteresis which widens with increase in the film thickness, (ii) the ZFC and FCW curves show huge divergence that begins just below the T_C. The diverging ZFC-FCW nature differs from that observed in case of canonical spin glass systems but is a common signature of the spin cluster glass **[34].** This kind of cluster glass is common to large bandwidth manganite with low hole doping **[35],** half doped medium bandwidth or low bandwidth manganites **[36]** or over a wide range of divalent doping (x) in low bandwidth manganites **[29,37]** and originates due to the coexistence of FMM and AFM/COI phases below the Neel temperature. The FCC-FCW hysteresis at $T<T_C$ is manifestation of the existence of a magnetic liquid phase consequent to the strong intrinsic electronic phase separation **[15–24].**

The M-H loops measured at T=10 K are depicted in in **Fig. 6.7**. Thinnest film (13 nm) does not show any saturation like behaviour and possesses the lowest magnetic moment. In rest of the films saturation is observed as H approaches ~20 kOe. The remanence (M_r) also increases with increasing film thickness (**inset of Fig. 6.7**). This behaviour confirms that at lower thickness the films have significant fraction of (i) AFM ordered phase, and (ii) magnetically disordered non-FM phase. The thinnest film shows very small coercivity. As the film thickness increases the coercivity (**inset of Fig. 6.7**) first increases for the 27 nm film and then decreases at higher film thicknesses. The increase in the coercivity of the 27 nm film could be due to the pinning of the FM domains by the non-FM matter in the film. At higher film thickness the coercivity decrease is due to the conversion of the non-FM phases into FM ordered phase.

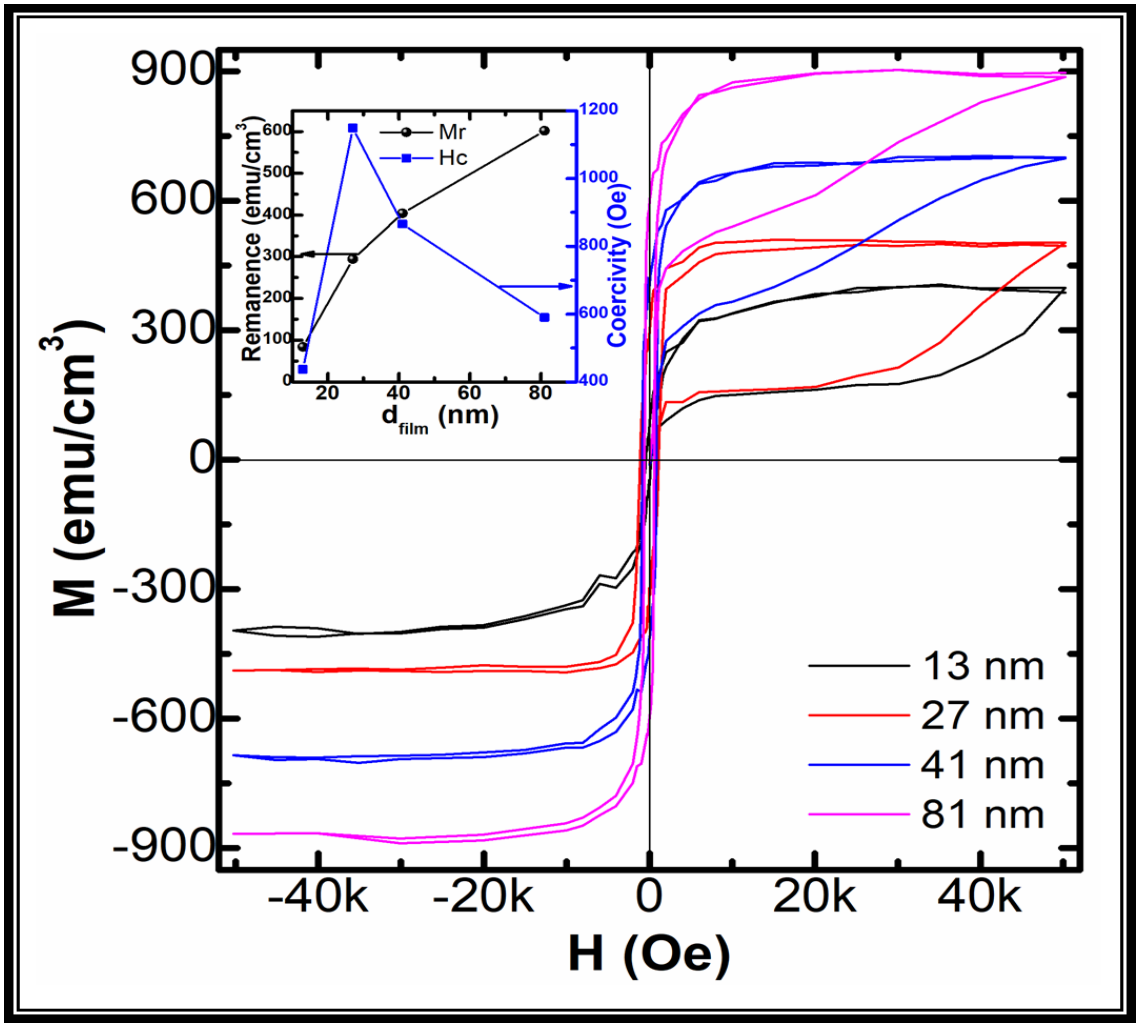

Figure 6.7: Magnetization loops of LPCMO thin films (13 nm, 27 nm, 41nm and 81 nm) measured at 10 K. The magnetic field (H) is along the longer dimension and in plane of the film. Inset shows remanence and coercivity variation with film thickness.

In general a decrease in the magnetic moment is ascribed to electronic phase separation and structural inhomogeneity driven electronic interfacial reconstruction. A magnetic dead layer is the reason of disordered spin structure at the substrate-film interface **[37,38].** The existence of the dead layer is attributed to the decrease in the double exchange energy at the FM (film)/non-FM (Substrate) interface **[39].** However, as emphasized by Bibes et al. **[38]** the dead layer approach alone is not sufficient to explain the scaling of FM/IM transitions with the film thickness. They have demonstrated that in fully tensile strained $La_{2/3}Ca_{1/3}MnO_3$ thin films on (001)-$SrTiO_3$ the T_C/T_{IM} decay rapidly at thickness d<50 nm with significant decrease

(increase) in magnetization (resistivity). Employing the Mn NMR they have established the (i) existence of a prominent non-FM insulator in ultrathin films (d≤5 nm) and (ii) occurrence of a inhomogeneous FM insulator in the range 5 nm<d<40 nm. Abad et al. have also studied $La_{2/3}Ca_{1/3}MnO_3/SrTiO_3$ thin films **[40]** and established the depression in magnetic order and electrical properties as a consequence of strain induced selective e_g orbital occupancy. The variation of magnetic and electrical transport with film thickness is generally different in manganites having different bandwidth (BW), e.g., in large BW compounds like $La_{1-x}Sr_xMnO_3$ even ultrathin films show well defined paramagnetic (PM) – ferromagnetic (FM) and insulator –metal (IM) transitions **[27,33]**. As the bandwidth is lowered by substitution of smaller cations at the RE/AE-site of the perovskite structure (as in case of the presently studied composition), the well-defined PM-FM and IM transitions shift to higher film thickness **[19]**. Hence the dead layer is expected to be significantly thicker in lower BW thin films. However, the minimum/critical thickness at which these transitions appear is not rigorously determined in case of low BW compounds. In view of the presently obtained results and the data reported earlier, we believe that the minimum thickness at which the well-defined transitions appear and hence the thickness of the dead layer is strongly dependent on the (i) bandwidth of the compound (lower sensitivity at higher bandwidths), (ii) the nature of the strain (whether compressive or tensile), (iii) the oxygen stoichiometry. Hence in low bandwidth manganite thin films under tensile strain (like the present one) the dead layer thickness could be larger than in the low bandwidth manganite films. From the above discussion it follows that the existence of magnetic disordered insulator layer results in reduced magnetization and also has adverse effect on the magnetotransport properties. Since the $La_{1-x-y}Pr_yCa_xMnO_3$ has (i) much smaller bandwidth (due to the more dominant presence of Pr^{3+} in the lattice), (ii) higher cationic disorder than $La_{1-x}Ca_xMnO_3$ therefore it has stronger intrinsic tendency towards phase separation. Consequently, the role of interfacial electronic reconstruction as well as the dead

layer effect could be more dramatic in $La_{1-x-y}Pr_yCa_xMnO_3$. Further, in this particular case of the $La_{0.23}P_{0.41}Ca_{0.36}MnO_3$/STO interface the strain that dominates the interface is tensile and this can further accentuate the dead layer effect. The other possible lattice disorder that could yield a depressed magnetic moment could be the strain induced oxygen vacancies **[19].** At lower film thickness the dead layer effect is expected to be more visible.

In this chapter, the impact of tensile strain induced modifications in the structure, microstructure, morphology and their cumulative consequences on the magneto-electrical properties of $La_{0.23}P_{0.41}Ca_{0.36}MnO_3$ thin films deposited on (001) oriented $SrTiO_3$ is studied. At lower thickness (~13 nm) the films bear strong tensile strain and its relaxation even at higher thickness (~81 nm) is partial only. This shows that that higher thickness the tensile strain may remain self-sustained. A sudden jump in the scaling of the out-of-plane lattice constant with films thickness suggests noticeable microstructural changes in films having d≥41 nm. Analysis of the rocking curve broadening shows at lower film thickness (~13 and 27 nm) the microstructure is dominated by the strain, which in this case is due to the lattice mismatch. At higher film thickness the mosaic broadening starts dominating due to the dislocation induced tilt and dilations of the lattice. The degradation of the layer by layer growth and increase in the surface roughness at higher film thickness as observed through the atomic force microscopic measurements also supports the above observations. The lower thickness films (d~13 and ~27 nm) show higher electrical resistivity and insulator like behavior throughout the measured temperature range. At d≥41 nm, an insulator metal transition bearing a strong thermal hysteresis, which narrows down with increase in film thickness is seen. The insulator region electrical conduction in all the films is well described by the Emin-Holstein small polaron hopping, wherein the lower thickness films possess higher activation energies. At lower film thickness a strong depression in the magnetic moment which is accompanied by a broad and diffuse FM transition is observed. The magnetization scaling with the film thickness shows the

possible existence of a spin disordered insulator layer, the associated electronic reconstruction and a sizeable non-ferromagnetic insulator state at d≤27 nm. As thickness increases there is increase in magnetic moment which is attributed to reduced impact of the interfacial electric reconstruction that forms the dead layer and relaxation of the substrate induced tensile strain which favours carrier delocalization.

6.4 References

[1] J. M. D. Coey, M. Viret, and S. von Molnár, Adv. Phys. **48**, 167 (1999).

[2] M. B. Salamon and M. Jaime, Rev. Mod. Phys. **73**, 583 (2001).

[3] E. Dagotto, T. Hotta, and A. Moreo, Phys. Rep. **344**, 1 (2001).

[4] Y. Tokura, Rep. Prog. Phys. **69**, 797 (2006).

[5] C. Zener, Phys. Rev. **81**, 440 (1951).

[6] C. Zener, Phys. Rev. **82**, 403 (1951).

[7] A. Sadoc, B. Mercey, C. Simon, D. Grebille, W. Prellier, and M.-B. Lepetit, Phys. Rev. Lett. **104**, 046804 (2010).

[8] J. B. Goodenough, Annu. Rev. Mater. Sci. **28**, 1 (1998).

[9] W. Prellier, P. Lecoeur, and B. Mercey, J. Phys. Condens. Matter **13**, R915 (2001).

[10] A.-M. Haghiri-Gosnet and J.-P. Renard, J. Phys. D. Appl. Phys. **36**, R127 (2003).

[11] D. Gillaspie, J. X. Ma, H.-Y. Zhai, T. Z. Ward, H. M. Christen, E. W. Plummer, and J. Shen, J. Appl. Phys. **99**, 08S901 (2006).

[12] A. Mukherjee, W. S. Cole, P. Woodward, M. Randeria, and N. Trivedi, Phys. Rev. Lett. **110**, 157201 (2013).

[13] C. Aruta, G. Ghiringhelli, A. Tebano, N. G. Boggio, N. B. Brookes, P. G. Medaglia, and G. Balestrino, Phys. Rev. B **73**, 235121 (2006).

[14] A. Tebano, A. Orsini, P. G. Medaglia, D. Di Castro, G. Balestrino, B. Freelon, A. Bostwick, Y. J. Chang, G. Gaines, E. Rotenberg, and N. L. Saini, Phys. Rev. B **82**, 214407 (2010).

[15] W. Wu, C. Israel, N. Hur, S. Park, S.-W. Cheong, and A. de Lozanne, Nat. Mater. **5**, 881 (2006).

[16] J. Jeon, H. S. Alagoz, R. Boos, J. Jung, and K. H. Chow, Appl. Phys. Lett. **104**, 122405 (2014).

[17] D. K. Mishra, V. G. Sathe, R. Rawat, and V. Ganesan, J. Phys. Condens. Matter **25**, 175003 (2013).

[18] V. G. Sathe, A. Ahlawat, R. Rawat, and P. Chaddah, J. Phys. Condens. Matter **22**, 176002 (2010).

[19] V. Agarwal, L. M. Kandpal, P. K. Siwach, V. P. S. Awana, and H. K. Singh, J. Magn. Magn. Mater. **394**, 299 (2015).

[20] V. Agarwal, G. Sharma, P. K. Siwach, K. K. Maurya, V. P. S. Awana, and H. K. Singh, Solid State Commun. **202**, 43 (2015).

[21] T. Z. Ward, S. Liang, K. Fuchigami, L. F. Yin, E. Dagotto, E. W. Plummer, and J. Shen, Phys. Rev. Lett. **100**, 247204 (2008).

[22] T. Dhakal, J. Tosado, and A. Biswas, Phys. Rev. B **75**, 092404 (2007).

[23] J. Q. He, V. V. Volkov, T. Asaka, S. Chaudhuri, R. C. Budhani, and Y. Zhu, Phys. Rev. B **82**, 224404 (2010).

[24] D. Okuyama, M. Nakamura, Y. Wakabayashi, H. Itoh, R. Kumai, H. Yamada, Y. Taguchi, T. Arima, M. Kawasaki, and Y. Tokura, Appl. Phys. Lett. **95**, 152502 (2009).

[25] Z. Q. Yang, Y. Q. Zhang, J. Aarts, M.-Y. Wu, and H. W. Zandbergen, Appl. Phys. Lett. **88**, 072507 (2006).

[26] B. K. Tanner and D. K. Bowen, *High Resolution X Ray Diffractometry and Topography*

(Taylor & Francis, Bristol, PA, 1998).

[27] R. Prasad, H. K. Singh, M. P. Singh, W. Prellier, P. K. Siwach, and A. Kaur, J. Appl. Phys. **103**, 083906 (2008).

[28] D. Emin and T. Holstein, Ann. Phys. (N. Y). **53**, 439 (1969).

[29] M. K. Srivastava, P. K. Siwach, A. Kaur, and H. K. Singh, Appl. Phys. Lett. **97**, 182503 (2010).

[30] H. S. Alagoz, M. Khan, M. M. Saber, S. T. Mahmud, K. H. Chow, and J. Jung, Appl. Phys. Lett. **102**, 242406 (2013).

[31] V. Agarwal, G. Sharma, P. K. Siwach, K. K. Maurya, and H. K. Singh, Appl. Phys. A **119**, 899 (2015).

[32] G. Zhao, H. Keller, and W. Prellier, J. Phys. Condens. Matter **12**, L361 (2000).

[33] P. Graziosi, A. Gambardella, M. Prezioso, A. Riminucci, I. Bergenti, N. Homonnay, G. Schmidt, D. Pullini, and D. Busquets-Mataix, Phys. Rev. B **89**, 214411 (2014).

[34] J A Mydosh, *Spin Glasses An Experimental Introduction*, 1st Editio (CRC Press, London, 1993).

[35] A. Dutta, N. Gayathri, and R. Ranganathan, Phys. Rev. B **68**, 054432 (2003).

[36] R. Prasad, M. P. Singh, P. K. Siwach, A. Kaur, P. Fournier, and H. K. Singh, Appl. Phys. A **99**, 823 (2010).

[37] J. Z. Sun, D. W. Abraham, R. A. Rao, and C. B. Eom, Appl. Phys. Lett. **74**, 3017 (1999).

[38] M. Bibes, L. Balcells, S. Valencia, J. Fontcuberta, M. Wojcik, E. Jedryka, and S. Nadolski, Phys. Rev. Lett. **87**, 067210 (2001).

[39] M.-B. Lepetit, B. Mercey, and C. Simon, Phys. Rev. Lett. **108**, 087202 (2012).

[40] L. Abad, V. Laukhin, S. Valencia, A. Gaup, W. Gudat, L. Balcells, and B. Martínez, Adv. Funct. Mater. **17**, 3918 (2007).

7 Summary and Future Aspects

7.1 Summary

In the present study a compressive study has been carried out on magnetic and magnetotransport properties of $La_{1-x-y}Pr_yCa_xMnO_3$ thin films grown by RF magnetron sputtering on $SrTiO_3$ (STO) substrates. The studies on the ~42 nm epitaxial thin film of composition $La_{0.22}Pr_{0.40}Ca_{0.38}MnO_3$ on STO (001) substrate, the detailed study of the thermal and magnetic field scaling of the thermomagnetic hysteresis in ~70 nm thick single crystalline thin films of $La_{0.21}Pr_{0.42}Ca_{0.37}MnO_3$ grown on STO (110) and the thickness dependent study on $La_{0.23}P_{0.41}Ca_{0.36}MnO_3$ thin films deposited on (001) oriented $SrTiO_3$ lead to some very interesting conclusions and new findings. The important conclusions and findings are summarized below.

- The electrical transport in a strongly phase separated manganite thin film is extremely sensitive to the relative fraction of the coexisting FMM and AFM/COI phases and has inherent non-ergodicity.
- This non-ergodicity, the origin of which could be traced to the delicate coexistence of FMM and AFM/COI phases leads to the existence of a liquid like behaviour. This liquid like state gets frozen into SRG. The devitrification of the frozen glassy state gives rise to Kondo like resistivity minimum.
- The liquid like behaviour is also confirmed by the large drop in resistivity under moderate magnetic fields.
- The phase separation tendency is weakened when the fraction of AFM/COI phase is reduced.

- The supercooling insulator-metal transition is non-unique and depends on the relative fractions of the FMM and AFM phases at the start of the magneto-thermodynamic process. In contrast, the superheating transition has equilibrium characteristic and remains independent of the ratio of the two ordered phases.
- The relaxation behaviour of the resistivity shows a strong non-Debye type character in the temperature region dominated by the magnetic liquid.
- The competition between co-existing FMM and AFM/COI phases governs the temperature dependent magnetic and transport properties.
- The small polaron activation energy decreases nonlinearly with increase in H and the variation of T_{IM} with the activation energy remains nearly linear in the warming cycle, but it becomes nonlinear in the cooling cycle.
- The analysis of the low temperature ρ-T data reveals the weakening of the electron-lattice coupling under the influence of an external magnetic field as well as during the warming cycle.
- Due to the supercooling of the magnetic liquid during the cooling cycle and the near equilibrium behaviour during warming results in a pronounced ρ - T hysteresis. The scaling of the area of the ρ - T hysteresis loop with the magnetic field follows a power law of the type $A_T(H) = A_{T_0} e^{-\Gamma H}$ in the region of strong phase separation.
- The scaling of the IMT with the applied magnetic field during the two thermal cycles is well fitted by the power law of the type $T_{IM}(H) = T_{IM}^0 + \beta H^{\alpha}$. The fitting parameters β and α are related to the strength of the phase separation and the H induced AFMI to FMM transition.
- The isothermal ρ - H loop area is found to follow a scaling law of the type $A(H) = A_H(H - H_{IM})^{\eta}$. The constant H_{IM} is the magnetic field at which the induced IMT occurs due to AFMI – FMM phase transition and the exponent η measures the strength of

phase separation; being close to unity in the weakly phase separated regimes and ~0.5 in the strongly phase separated or the magnetic liquid regime.

- At lower thickness (~13 nm) the films bear strong tensile strain and its relaxation even at higher thickness (~81 nm) is partial only. This shows that that higher thickness the tensile strain may remain self-sustained. Analysis of the rocking curve broadening shows at lower film thickness (~13 and 27 nm) the microstructure is dominated by the strain, which in this case is due to the lattice mismatch. At higher film thickness the mosaic broadening starts dominating due to the dislocation induced tilt and dilations of the lattice.
- The degradation of the layer by layer growth and increase in the surface roughness at higher film thickness as observed through the atomic force microscopic measurements also supports the above observations.
- The magnetization scaling with the film thickness shows the possible existence of a spin disordered insulator layer, the associated electronic reconstruction and a sizeable non-ferromagnetic insulator state at $d \leq 27$ nm. As thickness increases there is increase in magnetic moment which is attributed to reduced impact of the interfacial electric reconstruction that forms the dead layer and relaxation of the substrate induced tensile strain which favours carrier delocalization.
- The lower thickness films (d~13 and ~27 nm) show higher electrical resistivity and insulator like behavior throughout the measured temperature range. At $d \geq 41$ nm, an insulator metal transition becomes hysteretic.

7.2 Future Scope and Directions

The current study and its findings as summarized above show that there are still some unresolved issues.

- The role of tensile strain induced phase modifications and associated relaxation must be correlated more carefully to the changes in magnetic and magnetotransport properties.
- One such prominent issue appears to be the thermomagnetic hysteresis and its scaling with temperature and magnetic field. For more details regarding its nature and origin the thermomagnetic hysteresis should be studied for a broad range of composition (several values of x and y) in $La_{1-x-y}Pr_yCa_xMnO_3$.
- The time evolution of the resistivity could be very important in determining the size of the competing FMM and AFM/COI clusters. Therefore it should also be conducted for a broad composition as well as in varying magnetic fields, starting from field as low as ~500 Oe to 70 – 90 kOe.
- The time evolution of films having different thickness (different tensile strain) could also provide some very important information about the extrinsic consequences on the nature of phase separation.

Brief Curriculum-Vitae

Sandeep Singh

Technical Officer
Bhartiya Nirdeshak Dravya
(Indian Reference Materials),
CSIR-National Physical Laboratory
e-Mail: singht.npl@nic.in ; sandeepsthakur9@gmail.com
Phone: 011-45721081 (O); 9968424617 (M)

Educational Qualification

Exam. Passed	Year	Board/ University
Phd (Pursuing)	2012 to present	DTU Delhi
M.Sc Physics (Specialization in Applied Electronics)	2007	Gurukula Kangri Vishwavidyalaya Haridwar
B.Sc. (PCM)	2003	Himachal Pradesh University, Shimla

Areas of Interest CMR Manganites, Thin Films, Oxides, Sputtering, Scanning Probe Microscopy

Experience 10 years (In the field of Scanning Probe Microscopy)

Publication: 19 publications

(SANDEEP SINGH)